Interfacial Chemistry of Metal Pnictide Magic-Sized Clusters: Connecting Structure and Function through Ligand Coordination

Soren Sandeno

A dissertation

submitted in partial fulfillment of the

requirements for the degree of

Doctor of Philosophy

University of Washington

2025

Reading Committee:

Brandi M. Cossairt, Chair

Alexandra Velian

Douglas A. Reed

Program Authorized to Offer Degree:

Chemistry

University of Washington

Abstract

Interfacial Chemistry of Metal Pnictide Magic-Sized Clusters: Connecting Structure and Function through Ligand Coordination

Soren Sandeno

Chair of the Supervisory Committee:
Brandi M. Cossairt
Department of Chemistry

Synthesis development of colloidal quantum dots (QDs) has allowed for control over their distinct and unique optoelectronic properties. The continuous tunability in absorbance and emission profiles allowed by their quantum confinement when partnered with the robustness of a colloidal crystalline lattice has led to myriad applications in solid-state lighting, biosensing, photosensitive absorbing devices, and more recently quantum information science. These applications require meticulous and reproducible syntheses to generate materials with highly consistent properties and optoelectronic behaviors. During synthetic investigation toward these ends, researchers have discovered the existence of magic-sized clusters – molecular QDs that form at the early stages of nanocrystal nucleation and growth. Not only do these atomically precise materials serve as important reaction intermediates, but their precision has been heralded as a route toward eliminating heterogeneity from QD syntheses. Despite their presence being sufficiently documented optically, the mechanisms of conversion, true structural identities, and

emissive behaviors remain understudied and ambiguous. This thesis seeks to develop a stronger understanding of magic-sized cluster structure and conversion (Chapters 2 and 3) as well as investigate new avenues for enhancing their emissive properties without disturbing their metastability (Chapters 4 and 5).

After an introduction on the nucleation and growth of magic-sized clusters and QDs (Chapter 1), Chapter 2 focuses on the InP material system. The structural influence of ligand steric pressure on the $In_{37}P_{20}(O_2CR)_{51}$ cluster is investigated using a substituted phenylacetate ligand framework. It is shown that pressure at different angles in the ligand sphere induces structural perturbations in the internal lattice of the cluster. The influence of these structural changes is further investigated through reactions with $P(SiMe_3)_3$ in which para-substituents hinder ingress of reactive species thereby slowing cluster conversion whereas meta-substituents increase surface indium-indium separation distances and enhance cluster conversion rates. Leveraging this knowledge of controlled diffusion through ligand profile allowed for the isolation and complete structural characterization of a new magic-sized cluster intermediate, $In_{26}P_{13}(O_2CR)_{39}$. The relations of the structural motifs present in this new cluster are discussed.

In Chapter 3, these structural conclusions are extended toward the InAs system. The synthesis of InAs QDs has been documented to proceed through a ubiquitous cluster intermediate with a distinct absorbance profile showing features at 425 and 460 nm. Synthetic modifications to reduce conformational flexibility of the surface ligands allowed for isolation and full structural characterization of this predominate magic-sized cluster intermediate thereby identifying it as $In_{26}As_{18}(O_2CR)_{24}(PR'_3)_3$. The crystal structure of this cluster shares important motifs with $In_{26}P_{13}(O_2CR)_{39}$ and $In_{37}P_{20}(O_2CR)_{51}$ in the form of an $In_{14}E_{13}$ (E = P, As) cage yet the overall structure of $In_{26}As_{18}(O_2CR)_{24}(PR'_3)_3$ is more anisotropic. Full characterization also

allows for refinement of the surface suggesting a ligand sparsity in InAs could lead to higher reactivity.

Beyond the structural investigations of magic-sized clusters, Chapter 4 presents a route toward leveraging their homogeneity to achieve narrow emission linewidths. Previous reports have shown that oleate-ligated magic-sized clusters of Cd_3P_2 (Cd_3P_2-450) and Cd_3As_2 (Cd_3As_2-525) have high emissive color purity with <100 meV linewidths but their PLQYs of 7% and 0.5%, respectively, are too low to be considered applicable emitters. In this study, a ligand exchange on these clusters for stronger binding phosphinates was developed. The bidentate coordination motif of the oleate is mimicked by the phosphinate allowing for retention of the internal structure and preservation of stability. The increased binding affinity after exchange increased the PLQY of the Cd_3P_2-450 to 26% and the Cd_3As_2-525 to 9% while maintaining the narrow linewidths. Through time-resolved spectroscopy, the mechanism toward photoluminescent enhancement was determined to be phosphinates shutting down nonradiative recombination pathways.

Following up on the emission augmentation of the Cd_3P_2-450 and Cd_3As_2-525 magic-sized clusters, Chapter 5 describes a synthetic route to introducing continuous tunability in these systems that rely on discrete sizes. The anion sublattice can be alloyed using different ratios of $P(SiMe_3)_3$ and $As(SiMe_3)_3$ to generate $Cd_3P_{2-x}As_x$ clusters while maintaining the internal structure. This alloying allows for continuous tunability between the independent emission profiles of Cd_3P_2-450 and Cd_3As_2-525 with similarly narrow linewidths across the compositional gradient. Further treatment of these materials using the previously developed phosphinate exchange leads to highly emissive, continuously tunable, magic-sized materials with PLQYs reaching as high as 33%. Following the structural investigation, using the ligand-derived

diffusion management that previously resulted in the isolation of $In_{26}P_{13}$, is applied to Cd_3P_2-450 similarly allowing for the isolation of another smaller cluster, Cd_3P_2-390. The structure and conversion of this new magic-sized cluster are investigated showing its direct relation to Cd_3P_2-450.

Overall, this thesis takes a two-pronged approach to investigating the role and behavior of magic-sized clusters in many different materials systems. In the first, structural studies of III-V clusters unveil the identity of multiple previously known and unknown intermediates in the synthesis of QDs. This allows for a rich comparison of structural motifs and identifies the $M_{14}E_{13}$ icosahedral cage as a ubiquitous element in III-V and II-VI nanomaterial growth. In the second, further development of II-V cluster systems increases applicable benchmarks through improving brightness and establishing a synthetic route towards continuous tunability in magic-sized materials. It is demonstrated how the judicious choice in cluster modification can navigate the metastability and simultaneously open new avenues to improved emissive properties.

TABLE OF CONTENTS

LIST OF FIGURES

LIST OF TABLES

ACKNOWLEDGEMENTS

Very rarely are we given clear opportunities to directly and permanently thank the people that have contributed to our lives in a positive way. Completing this degree was (and may remain to be for a long time) the most challenging accomplishment I can claim. Thankfully this section exists to make it abundantly clear that the body of this work and the formalities that go along with it would never have been made possible without significant contribution and support from everyone mentioned here. While the following pages focus on what has occurred at my fume hood, the last four and a half years have incorporated so much beyond the Schlenk line. Each person here has impacted me in a unique and special way, so it is befitting that this section comes at the beginning of this document to first demonstrate how many people are involved in its genesis.

I was first experimentally introduced to cluster chemistry by Dr. Max Friedfeld and it took me all of about 20 minutes to realize I was a padawan training under the likes of a jedi master. Dual-wielding the core tenets of safety and productivity, he taught me how much chemistry is done at your desk and, more importantly, how much chemistry is done in the lab. I have continuously worked throughout my degree to emulate his competence, confidence, and relentless intellectual finesse. On the days when my brain was redlining at 8000 rpm, I owe much to Florence for providing much needed perspective and a nice walk to the Henry. She has helped me in putting some of my more chaotic energy to good use. Truly the Lab Sage. Few things hit harder than being called “Big Dawg” by Forrest. He was a mentor, a friend, and easily the most stylish person in lab. I’m sorry we stole your butter knife to cut sodium in the box but it worked really well and we owe the high reaction yield to you. I owe many thanks to my organic tutor and fellow practitioner of atomic-precision, Diesel Calves. The way in which he presented data at subgroup had a lot in common with the way in which he hiked mailbox peak: gut-wrenching efficiency. I learned a lot from how he so effectively coupled the knowledge of organic and inorganic synthesis which was something that I (naively) sought to imitate in my final years of grad school. Also, his real name is Hunter. One of the most

important facets of scientific communication is the ability to challenge a peer's conclusion with skepticism while avoiding cynicism. Sam has this in spades and her knowledge of photophysics verges on omnipotence. I would have completely lost my mind had it not been for watching Steven Seagal clips between experiments, walking to the Henry, or coming up with absolutely diabolical ghostboat reactions to run (and sometimes actually running them). Let me know when I can come by your new lab and make some silyl pnictides for you (mostly free of charge). A fellow enjoyer of nucleation theory, Helen, your technique in lab and technique on the climbing wall were equally clinical. Hao, your work ethic and accomplishments are unrivaled and I always appreciated how you never hesitated to make time for training and teaching others (though the big thing I learned from you was copying your Blender style and also what to order with Hot Pot). Emily, you taught me everything that I know about E-chem (and that's not an exaggeration) and everything I know about frisbee. I never really completely figured out either of them but I am thankful for the chats that they created. Emi, you were always so good about asking questions at group meetings even if it wasn't directly related to your science. The whole alloying cluster idea came from a question you asked about discrete emission during mine. Also, whenever we were up against each other in fantasy, I got nervous because you know ball. Thank you Jay, for the walks and the lunches we had together. It was really amazing to learn about Korean food from you (even if my chopsticks skills were lackluster). Some of the best memories I have of the outdoors during grad school were made with Grant. Our march up Kaleetan Peak is a core memory and was followed by many other early morning trudges in the service of a sunrise. There are few that can rival my chaos in lab but I acknowledge you as one of them. I had the pleasure of being part of a number of meme chats throughout my graduate school career and it just so happened that Chris was in every single one of them. Could be a coincidence, I happen to think otherwise. You clearly recognized the importance of hard work and honestly should have been logging your laps between 317 and the CD on Strava. You give excellent advice. I have and will continue to hold your opinion in high regard (except when it comes to milk steak). PP (Pedro), seeing how earnestly motivated you were (and are) to grind out lab work was reinvigorating at a time when the glovebox felt like a prison. An elite skiing partner

and camping compatriot, the energy you bring is truly unique and appreciated. I sincerely look forward to talking to you about what you accomplish in the future (if you can still hear after years of 120 dB Knock2 during workup in the box).

My research career would never have been possible without the guidance of my research advisors. Prof. Hendricks was responsible for first instilling in me an interest in nucleation and growth processes at Whitman College (as well as teaching me how to use a Schlenk line). His deft approach to mentorship allowed confidence in independence to manifest alongside synthetic capabilities. It was from Prof. Hendricks that I developed an appreciation and satisfaction with the process of research itself outside of the more concrete benchmarks of experimental progress. Upon moving to the University of Washington, I was repeatedly reminded throughout my degree that there couldn't have been a better mentor for a PhD than Prof. Brandi Cossairt. The freedom to explore a research space is an unparalleled gift and it directly led toward some of the most visceral moments of motivation that I can remember. You have built an environment in which drive, support, intellect, and respect prosper. Among the countless things I have learned from you in the last few years, it was the development of the balance between confidence and concession in research that I will continue to practice. I will always look back on my time in graduate school fondly and I have Prof. Cossairt to thank for that.

This body of work was completed alongside the efforts of many collaborators. First and foremost, all of the crystal structures herein were solved by Sebastian Krajewski. None of the structural conclusions would have been possible without his efforts. Thank you for your patience as I brought down so many samples and then proceeded to go nonverbal when they didn't diffract. When SCXRD wasn't possible, Dylan Ladd and the Toney group were there to do PDF and a whole bunch of other acronyms. You had so many projects and yet, for the love of the game, would still sneak in some of my samples. My time with computational chemistry can be likened to monkeys learning to use tools and Ryan Beck was there to make sure the hammer was facing the right way. So knowledgeable, so patient, thank you. Will Jeffries, your

project vision is 20/20 – I was always in awe of your ability to craft an incredible narrative from the data we were collecting.

Thank you to my committee members, Professor Doug Reed, Professor Alexandra Velian, and Professor David Bergsman for their support, advice and questions.

To my girlfriend, Brooke: Thank you for being there throughout this process. Despite my best efforts, chemistry is not a subject that you particularly enjoy but you were still so supportive and invested because it was special to me. Spending time with you was a meaningful reminder that there is a life outside of science and research even if that's what I was working on while we were together. The healing properties of eating chicken sandwiches and watching North Woods Law with you is otherworldly. Someday you and I will make quantum dots together on the Schlenk line and you will understand why I can get so fired up about it.

Finally, I thank my family. Mom and Dad, from sending you pictures of the InP crystals I've grown, to breakfast at Lost Lake Café, I have always felt your unwavering support. The beginnings of my synthetic explorations began in the kitchen (not making food, mostly just a mess) and soon spread to the garage and despite many of my ideas lacking a grounding in reality, you were always encouraging. I've always felt that however much scientific creativity I have, it is owed to your open-mindedness as I traversed scientific disciplines in the backyard. Olen and Elsa, moments I've spent with you have been the most memorable of the last four and a half years. Our shared sense of humor and sincerity makes for a pretty good time. You guys better read this whole thing front to back. Love you.

DEDICATION

To My Family

for their unwavering understanding and support

Chapter 1. INTRODUCTION TO THE SYNTHESIS AND STRUCTURE OF MAGIC-SIZED CLUSTERS

This chapter aims to provide an introduction to relevant topics in this dissertation.

1.1 THE UTILITY OF SEMICONDUCTORS

Semiconductor materials are the basis of modern technology. Communication in the digital age relies on the controlled manipulation of charge carriers for information transfer. The materials that allow for this control are semiconductors. The functionality of all industrial and consumer electronics is dependent upon their electronic behavior in response to a stimulus. Medical devices such as Magnetic Resonance Imaging machines depend upon semiconductors that supply current to control the superconducting magnetic field and generate radiofrequency pulses for analysis. Solar energy requires converting photon energy into electrical current, which can only be accomplished by semiconductors. The inverse of this process, converting electrical current into visible light, is accomplished by light-emitting diodes (LEDs), the main architectural constituent of which is semiconductors. Most modern environmental sensors measure the electronic response of a semiconductor to its physical environment (i.e., light, heat, gas). More recently, much attention has been focused on the development of quantum information and quantum computers that demand complex semiconductor architectures to generate spin qubits or serve as single photon sources. The technological ubiquity of semiconductor materials is a testament to the commercial indispensability that arises from their reliable electronic response to composition, structure, shape/size, and environment.

1.2 SEMICONDUCTOR ELECTRONIC STRUCTURE

The electronic structure of semiconductors can be rationalized by first considering the bonding in a diatomic molecule. In a simple diatomic, such as H_2, the individual atomic orbitals are brought within proximity of one another, thereby creating two new discrete electronic states. In one instance, the atomic orbitals are in-phase, creating shared electron density between the two bonded atoms and lowering the overall energy of the combined orbitals. In the other, the atomic orbitals are out-of-phase and therefore any electron density in these orbitals will promote repulsion and weaken the atomic bond. Two atomic orbitals result in two molecular orbitals, and this relation must be conserved. The H_2 example is the simplest as it considers two identical atoms, each with a single orbital and a single electron. This bonding picture is complicated but can still be rationalized by introducing more complex atoms with different orbitals and multiple electrons.

Expanding this picture of bonding to a new diatomic, F_2, introduces a new shell of orbitals with different symmetries. The two s-orbitals, similar to how they function for H_2, generate a bonding and an antibonding molecular orbital. However, the new higher energy orbital set, the three p-orbitals (p_x, p_y, p_z), can separately interact with each other to form six new molecular orbitals. Of the six, three are bonding and three are antibonding. In this example, the s-orbitals and p-orbitals energetically exist separately from one another. However, that isn't always the case.

For the diatomic N_2, the same number of orbitals are involved as in F_2. There are two s-orbitals and six p-orbitals total. However, the nuclear charge of nitrogen ($Z = 7$) is less than that of fluorine ($Z = 9$), which allows the energy of electrons in s-orbitals to become much closer to their p-orbital residing counterparts. With some constraints, this allows the s and p_z orbitals to mix together. Due to their similarity in symmetry with respect to the axis of bonding, s and p_z can mix

their respective distributions of electron density to lower the overall energy of bonding electrons. This process is ubiquitous across molecular structures that have atomic orbitals of similar energies.

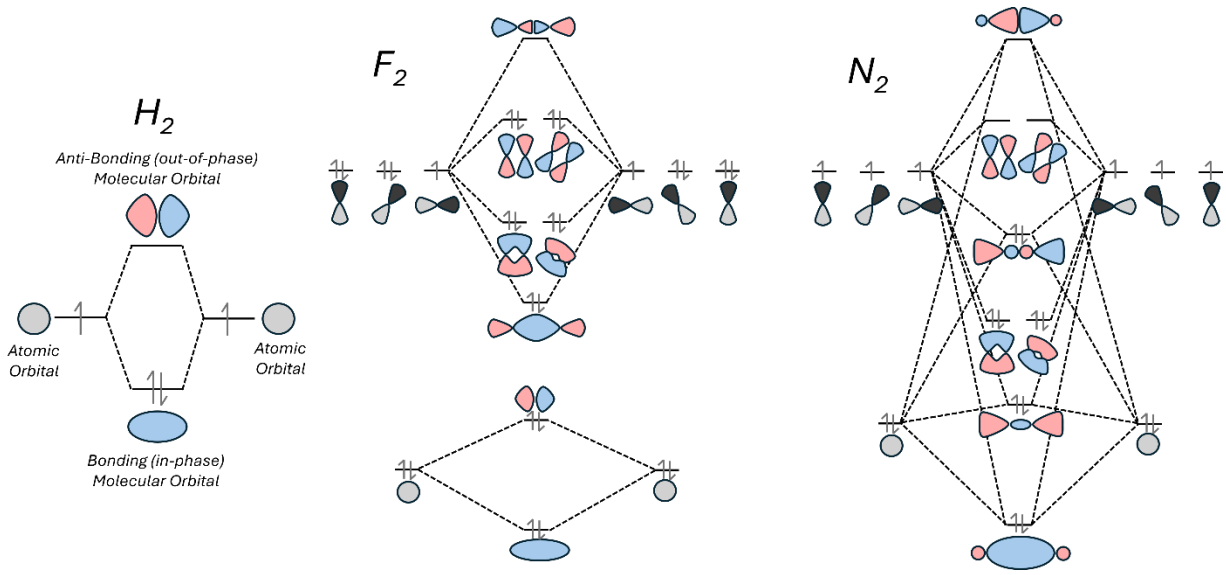

Figure 1.2.1. Molecular orbital diagrams for H_2, F_2, and N_2. H_2 demonstrates the most basic example of molecular bonding. F_2 demonstrates the incorporation of the 2p subshell and N_2 is an example of s and p orbitals mixing to lower the average energy of bonding electrons.

The orbitals that make up semiconductor electronic structure function in very similar ways as in diatomic molecules, but on a much larger scale. Instead of two atoms bonding to generate two orbitals, the extended structure of a bulk semiconductor incorporates approximately anywhere between 10^6 and 10^{22} atoms, each with multiple contributing atomic orbitals. This results in an astronomical number of "molecular" orbitals, each with a distinct combination of in-phase and out-of-phase atomic orbitals that extend across the material. Due to the sheer number of electronic states, each with an inappreciably different energy, it is no longer effective to describe each individual state; there are simply too many. Instead, all the accessible states at their respective

energies are described as a band, and different portions of the band have different numbers of states, a property that is described as the density of states (DOS).

In unary semiconductors such as carbon, silicon, and germanium, these states are generated from s and p orbital mixing. When bonding with adjacent atoms, the interaction can either be bonding (in-phase) or antibonding (out-of-phase) as described before. The effect this has is that it splits the electronic structure into two equal bands: the low energy valence band (bonding), and the high energy conduction band (antibonding). There then exists a defined energetic gap between the bands, which is analogous to the gap between molecular orbitals in the diatomic case. Furthermore, before bonding, each atom has 2 electrons and 4 orbitals that will participate in the electronic structure. The number of states must equal the number of participating orbitals, and half of these orbitals will form the valence band. It happens that the number of electrons is also half the number of orbitals, and therefore, all the lower energy states are filled with electrons. It is these two characteristics that define semiconductor electronic structure: 1) there is a pronounced energy gap between orbital bands, and 2) the lower energy valence band is filled with electrons, while the higher energy conduction band is totally unoccupied.

While unary semiconductors provide the most basic example, there are other, more complex materials with the same two electronic characteristics. Binary semiconductors, made up of two different elements, further extend the applicability beyond what can be accomplished with unary semiconductors. These binary materials are mainly referred to by the numbers of the columns on the periodic table that describe their constituent atoms. III-V (ex. InP, InAs, GaN, GaP, GaAs), II-VI (ex. CdS, CdSe, CdTe, ZnS, ZnSe), and IV-VI (ex. PbS, PbSe, PbTe, SnS, SnSe, SnTe) are common binary material types for semiconducting applications. The significant degree of material variability allows for wide variation in the bandgap energy of these materials

from ~0.2 eV to ~3.5 eV. It then follows that materials with different bandgaps are suited for different applications. For example, the 3.4 eV bandgap of GaN is well suited for blue/UV emission in LEDs, whereas the 0.4 eV bandgap of PbS makes for efficient infrared detectors.[1,2]

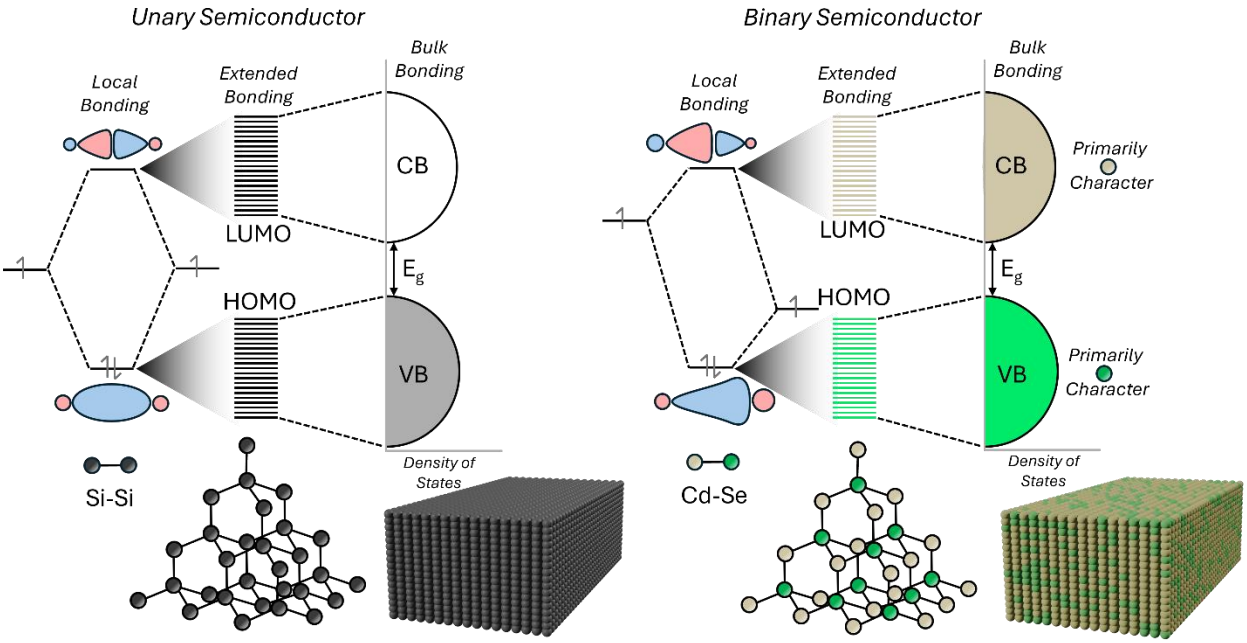

Figure 1.2.2. Transition from the local bonding of a diatomic to the extended bonding of a macromolecule to the bonding of a bulk solid. In binary semiconductors, the two bonding elements do not introduce electrons at the same energy level, causing the valence band to have primarily anion character and the conduction band to have primarily cationic character.

The bandgap represents the energy input required to elicit a measurable electronic change in the material. In other words, the bandgap generally defines the minimum energy that a material can absorb and the maximum that it can emit. With electrons filling the valence band, the material cannot absorb energy until that energy meets or exceeds the bandgap energy as there are no lower available states. When this requirement is met, the material absorbs that energy and, in doing so, promotes an electron into the lowest lying state of the conduction band. The promotion of the

electron leaves a positively charged hole in its place in the valence band. While the hole is not a real, physical particle, it has become important nomenclature to track a position for the lack of an electron upon excitation. Quickly, the electron recombines with the hole, returning to the valence band, and releases energy that is approximately equal to the energy of the bandgap. If the energy provided is significantly higher than the bandgap energy, the electron is free to move throughout the conduction band before recombining. But in many instances, the stimulus energy is very similar to the energy of the bandgap. In this case, the electron and hole are not completely separated, and instead, there remains an attractive coulombic interaction between them. In this instance, the electron-hole pair is referred to as an exciton. The charge carriers have been separated, but they cannot be considered independent; they are still partially bound to one another through this coulombic force. Excitons versus free carriers are preferred depending on the application. When carrier recombination is the functional process, as is the case with LEDs, lasers, and single-photon sources, it is preferred to form excitons. Conversely, if the application is focused on charge extraction, like in solar cells, transistors, and thermoelectrics, free carriers must be generated for efficient utility.

While the current information age has been built on a contemporary understanding of semiconductor electronic structure, there are certain areas where increased functionality would open the horizon to new utilities and applications. This has led to and will maintain the Herculean research effort into new semiconductor behaviors.

1.3 Semiconductor Quantum Dots

One of these new behaviors has arisen from taking semiconductor structures and making them much smaller. If we consider a structure with ~10^{22} atoms (millimeter length scale), and

remove atoms until we are only left with a few hundred to a few thousand, we will likely be left with something that is measured on the nanometer length scale. On the nanoscale, it is observed that the energy of light absorbed and emitted by a semiconductor becomes size-dependent.[3,4] As the semiconductor becomes progressively smaller, the energy that the material interacts with becomes progressively larger relative to the intrinsic bandgap. As the particle becomes larger, the energy lowers and eventually approaches the intrinsic bandgap energy. This phenomenon can be rationalized through the behavior of charge carriers confined to a predetermined volume.

One of the inherent properties of semiconductor materials is the Bohr radius (r_B) which describes the distance between an electron and hole when excited to form an exciton. Originally, the term Bohr radius refers to the most probable distance of an electron from the nucleus of a hydrogen atom. Seeing the analogous conditions where in the case of hydrogen, the center point is the nucleus and with semiconductors, it is the location of the hole, Bohr radius can be applied in both scenarios. This distance (r_B) is material dependent and on the order of nanometers as seen with InP (r_B = ~10 nm), CdSe (r_B = ~6 nm), and PbS (r_B = ~18 nm) as a few examples.[5] Based on lattice covalency and the dielectric constant of the material, the bound electron and hole will prefer a certain distance apart before reaching a barrier in the potential of the lattice. Interestingly, the physical dimensions of a nanocrystal can be smaller than this intrinsic Bohr radius of the material. In this instance, as the wavefunction of the exciton faces a potential barrier outside of the particle, it cannot extend to encompass the Bohr radius. Instead, it is confined to the smaller dimensions of the nanocrystal. It follows that larger particles will confine the exciton wavefunction less and smaller particles will provide greater confinement. This size-dependent restriction of the exciton influences its energy through the Heisenberg uncertainty principle.

$$\Delta x \Delta p \geq \hbar$$

Decreasing the uncertainty in the position must result in an increase in the uncertainty of the momentum. The broader distribution in electron momentum leads to an increase in the kinetic energy of the exciton. Therefore, confining excitons to a smaller volume increases their kinetic energy. Furthermore, as described above, the exciton cannot exist outside of the particle and therefore its wavefunction must reach a probability of zero at the edges of the particle's dimensions. Only specific standing waves with discrete energies can satisfy this requirement which manifests in the material as isolated, quantized energy levels instead of bands. The concept of particle size causing these two characteristics, a size-dependent bandgap and appearance of discrete states at the band edges, is referred to as quantum confinement. Semiconductor nanocrystals that are small enough to fall in this regime are then given a special, colloquial name: quantum dots.

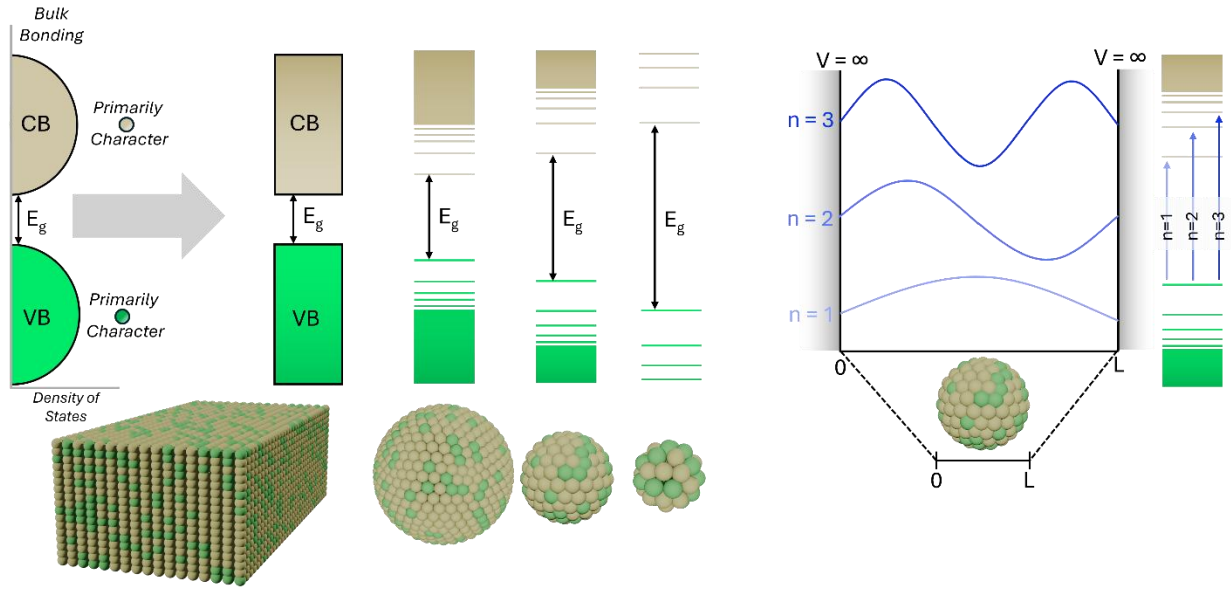

Figure 1.3.1. Semiconductors on the nanoscale show size-dependent band gaps due to the quantum confinement of the exciton wavefunction. The dimensions of a particle of length L force the wavefunction to reach a probability of zero outside of the particle dimensions. This causes the appearance of quantized electronic states.

1.4 Introducing Solution Processability

As so far described, QDs would be materials that are extremely challenging to manipulate. They are constructed from semiconductors with high dielectric constants and their surface is covered in uncoordinated, charged atoms leading to a high charge density. These characteristics in conjunction would make them reactive and impossible to dissolve in common solvents. Furthermore, the actual generation of these particles would have to be done through molecular beam epitaxy or plasma synthesis, neither of which can be easily scaled. Therefore, it would be of great benefit to functionalize these nanocrystals such that they can exist in solution.

This functionalization is done through the inclusion of molecules that bind to the surface, referred to as ligands, that incorporate functional groups with varying stereoelectronics. When carefully selected, these ligands can passivate the surface charge density and improve solubility through ligand-solvent interactions. This allows QDs to exist as stable solution phase colloids, thereby opening a wide horizon of new commercial applicability. Established processing techniques such as spin coating, roll-to-roll processing and a variety of printing methods become accessible. Furthermore, the addition of ligands alongside reactive metal and anion precursors allows QDs to be reliably synthesized in solution as well. This solution processability promises lower manufacturing costs, milder, more efficient synthesis methods as well as improved scalability and integration potential. The solution-phase also introduces synthetic versatility in the form of altering precursor identity, solution temperature and concentration which presents a significantly more tunable parameter space for modifying properties. Because of this, most research efforts investigate QDs as solution-processable materials.

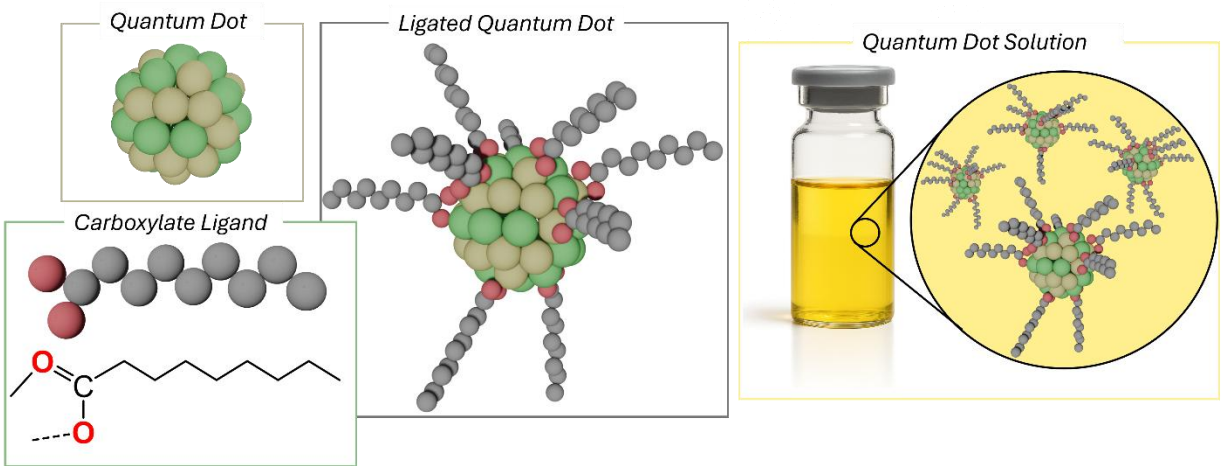

Figure 1.4.1. The ligation of a QD with aliphatic ligands allows them to be dispersed in nonpolar solvents for solution processability.

1.5 Understanding Nucleation and Growth

The ability to synthesize QDs in solution invokes a particularly unique mechanism for particle formation. Individual precursors react to form nanoscale crystals that maintain their solubility. The individual atoms in each precursor must react together to form these larger, crystalline particles while maintaining colloidal stability. This phase change can be understood through the perspective of nucleation and growth. Understanding and controlling this fundamental mechanism of nanocrystal reactions became an important subfield of QD chemistry due to the significance of synthesizing homogeneous nanocrystal populations.[6] Arguably, the two areas with the greatest promise of QD contribution are solid-state emitters (classical light) and single photon emitters (quantum light). The unique electronic structure of QDs is designed to allow efficient charge carrier recombination due to the exciton's spatial confinement. Other semiconductor applications that are based on charge extraction are poised to compete with the increased recombination rate that comes from confinement. Seeing as the structure of QDs is best suited for

recombination, applications in emission should be targeted. These two main applications, solid-state emitters and single photon emitters, albeit for different reasons, depend on the photon purity from emission. Nanocrystals of different sizes, morphologies and phases can emit photons of varying energies and therefore it is imperative to synthesize QDs with the highest precision possible.[7–10] Due to the confinement of the wavefunction inside the particle, nearly every atom is contributing in some way to the photophysical characteristics. Therefore, structural deviations influencing even single atoms can cause a degree of heterogeneity that will poison photon purity across the sample.[11] Due to these stringent requirements on ensemble-level nanocrystal precision, there has been and continues to be a field-wide drive to synthesize reproducible, homogeneous QD samples. With the ultimate goal of generating synthetic design rules that can explain and produce homogeneous ensembles, the chemical mechanisms underlying the QD nucleation and growth processes that govern particle formation has been the subject of intensive investigation.

At a basic level, the process of nucleation and growth begins with the assembly of discrete atoms to generate a small repeating unit of solid (nucleation) after which further atoms add to the surface of the particle thereby increasing its size (growth). Empirical observations of systems that follow this description show that growth is almost always energetically favored. For example, snowflakes grow rapidly after the initial formation of ice nuclei, hydroxyapatite in the bones will favor further deposition over the creation of a new structure, and growing sugar crystals often involves the addition of an already formed seed crystal to bypass the energy penalty of nucleation. This is to say that the formation of nuclei requires more energy than the growth of existing particles, which is a fundamental principle that guides many of the models that seek to describe these processes.[12] To rationalize this bias in particle formation, the overall stability of crystals can

be described through two separate characteristics: 1) the internal energy, and 2) the surface energy.[13]

The internal energy is derived from the favorability of bond formation and crystallinity. It is conceptually similar to the lattice energy, or bonding strength in a crystal, but internal energy is more generalizable as it incorporates deviations in crystallinity. Crystals are extremely stable due to the repetitive formation of strong chemical bonds with very little variation. As the internal energy is based on the number and quality of those bonds in the crystal, it varies with the volume of the particle and is stabilizing.

The surface energy comes from the atoms in the outer layer of the particle that form the interface between the particle and its surroundings. As these atoms are on the outside of the particle, they lack the one or more bonds required by the crystal structure and are therefore incompletely passivated and inherently unstable. Because of this, the surface energy is destabilizing and varies with the surface area of the particle.[14,15]

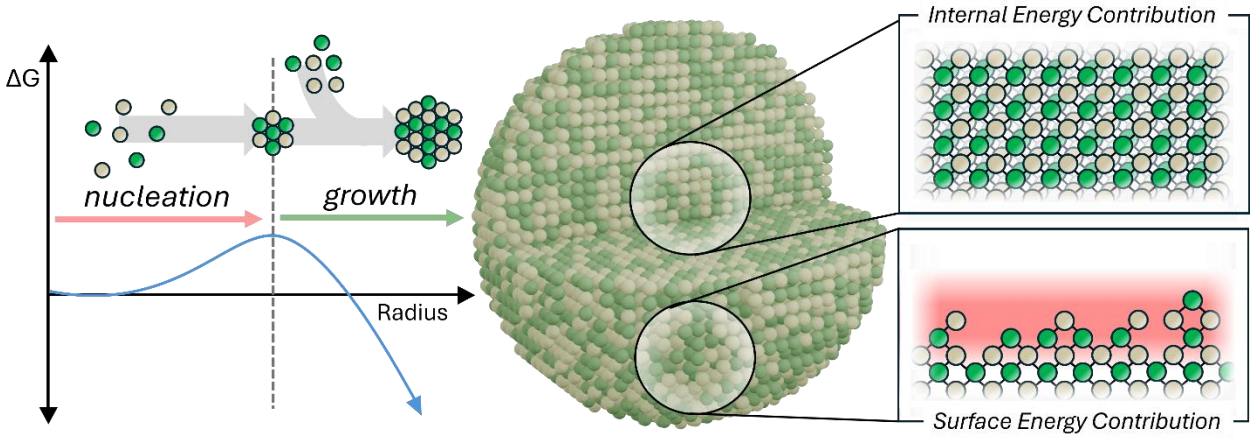

Figure 1.5.1. The energetic barrier of nucleation must be overcome before the more favorable growth process can occur. This is due to the energetic penalty of undercoordinated surface atoms competing with the stabilization of crystallized internal atoms within a lattice.

While a simplification, it is the addition of the internal and surface energies that dictate the total energy of the system. Smaller particles have higher surface area to volume ratios and therefore the surface energy dominates the overall stability, thereby making the particles unstable. But as particles continue to grow, the internal energy from the increase in volume stabilizes and allows for further growth. The interplay of surface and internal energies controlling stability during particle formation is encompassed by Classical Nucleation Theory (CNT).[16–18]

Applying these ideas to QD formation and growth is relatively intuitive. The different molecular precursors that react to form nanocrystals begin in the solution-phase and, at high temperatures, generate nuclei that then continue to grow from the same precursors. As QDs form, they must overcome the surface energy to create stable particles and with time these particles grow to benefit the stabilizing internal energy. However, as is the case with all experimental systems, models cannot account for all necessary variables to perfectly describe the real, physical process. The synthesis of QDs is no exception.

For example, CNT does not take ligands into account. As different ligand types can passivate undercoordinated atoms, they play a substantial role in modulating the surface energy of particles during growth.[19] This decrease in surface energy can stabilize particles that would otherwise submit to dissolution as described by CNT and can be imperative in promoting growth at specific particle facets. Furthermore, as QDs are colloidal species and form at high temperatures, there is more than enough energy to drive particle rearrangement during synthesis. Solute that has bonded to the surface to grow QDs can repeatedly detach and rearrange which leads to an equilibrium between solution-phase solute and QDs.[20,21] The stability as dictated by the internal and surface energies is therefore constantly in flux and can change over time, unlike what CNT describes. *However, the foremost inaccuracy of CNT as applied to nanocrystals is that it uses*

purely thermodynamics to describe a system that is very much governed by kinetics.[22–26] The initial formation of QDs can happen on the millisecond time scale due to the high temperatures and reactive precursors that are often used in the reactions.[27] Due to this rate, products that can be accessed faster have lower activation energy barriers and are favored over those that are generally more thermodynamically stable. While the internal and surface energies can theoretically describe the most stable particle, the reaction rate pushes the system towards less stable, kinetically favored atomic arrangements in particles. Because it neglects kinetics, CNT assumes that the process of nucleation is instantaneous, that there is no time component in the initial formation of particles.

Despite these complications, CNT has been invoked to describe many nanocrystal reactions with relative success especially in the cases of metal chalcogenides.[6,28–33] Arguably, the most pertinent example of this was using LaMer and Dinegar's nucleation and growth model, developed to explain hydrosol formation, as a framework for interpreting nanocrystal synthesis results.[34] The foundation of this model being that the concentration of reactive solute will dictate the reaction regime. Whether nucleation or growth is favored at a specific point in the reaction can be simply interpreted through the number of solute molecules present. High solute concentration drives up the chemical potential required for nucleation and after some of it is consumed in the process, the lower resulting potential pushes the reaction into the growth regime. At a certain point, the equilibrium solubility of the solute in the solvent is reached and these processes are discontinued.

Initial QD syntheses successful at generating respectfully homogeneous ensembles could be interpreted through this model. Fast injections at high temperatures result in narrow size distributions as the high chemical potential is reached rapidly, supposedly resulting in an instantaneous, single nucleation event. The short timescale would ensure homogeneous nuclei as

they are all generated at the same time and under the same conditions. This solute-concentration driven model was effectively applied to several CdSe and PbS systems,[6,28] however, many other materials and precursor systems never seemed to follow the reaction trajectory as predicted by CNT and LaMer. This could very well be due to differences in ionicity and covalency across materials.[35] In the field of binary semiconductors, the lattices of cadmium and lead chalcogenides are considered to be quite ionic. As a result, the individual bonds are weaker when compared to the more covalent lattices of indium and gallium pnictides. During synthesis, this allows more reversibility in ionic materials and therefore reactive solute is a more reasonable concept in these systems. There indeed may be some form of solute equilibrium that drives particle nucleation and growth as described by CNT. In contrast, covalent materials with stronger bonds participate much less in any equilibrium that might exist between a particle and solute in solution. With particle formation being driven by bond strength over concentration, covalent materials cannot be accurately described by a variable concentration model.

Despite the empirical accuracy of LaMer's findings in ionic materials, further study has shown that narrow size distributions can still be obtained through nucleation events that extend far into the growth stage.[36,37] This homogeneity has been rationalized through size-dependent growth kinetics where smaller particles that nucleate late in the reaction promote a faster growth rate. With smaller particles growing faster and larger particles growing slower, the particle sizes converge over extended reaction times. The full mechanistic rationale for why smaller particles can develop a faster growth rate remains ambiguous. Furthermore, these observations emphasize the tendency for generalized models to be applied to empirically developed data sets. While initially explanatory, the foundation of the CNT model can be found inadequate at describing more complex perturbations on a simpler process.

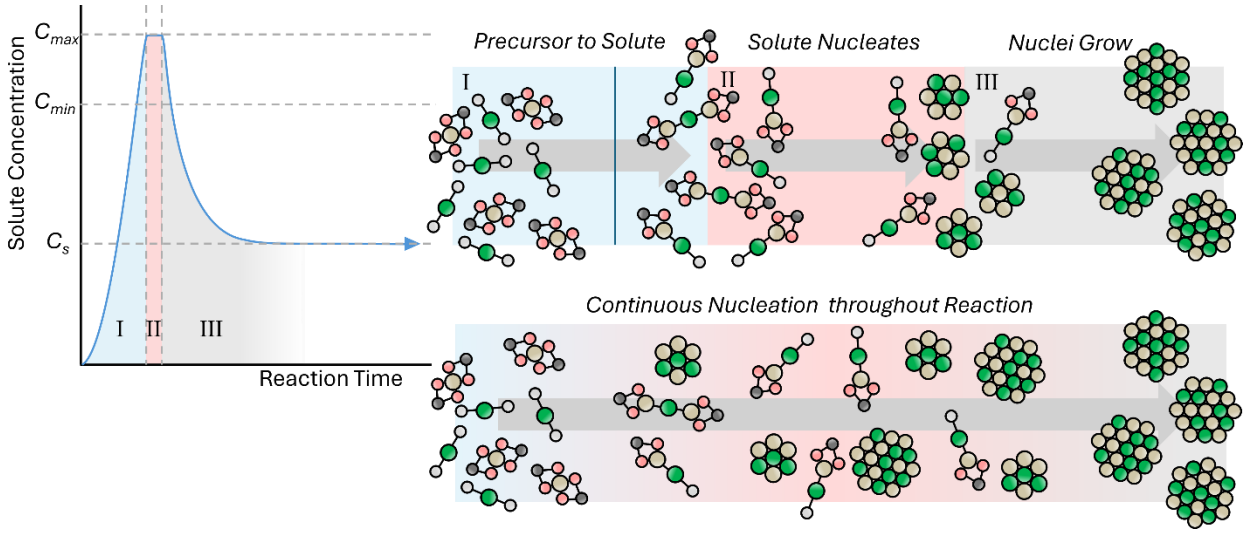

Figure 1.5.2. The basis behind many nanocrystal formation models is how concentration dictates the synthetic regime. I) Precursors combine at high temperature together to begin forming reactive solute. II) The formation of reactive solute eventually reaches a high enough concentration (or chemical potential) to cause a nucleation event. III) The decrease in solute concentration upon nucleation decreases the chemical potential pushing the reaction into the growth stage. While this can be a strong educational framework for considering the variables that contribute to nanocrystal synthesis, the three regimes in most cases occur continuously throughout the synthesis.

Nevertheless, these observations and conclusions put into context how chemists have contributed to rethinking the extent to which the CNT framework is accurate in the analysis of nanocrystal growth processes. This resulted in an emphasis on and deeper interest in investigating *nonclassical nucleation* processes in nanocrystal synthesis.

1.6 Molecular Species Documented in QD Reactions

Quite soon after the development of solution-phase QD synthesis, it became apparent that transient, metastable species were forming during the synthesis.[38–47] Here, metastable species were

identified by discrete optical absorption features forming during the initial stages of QD reactions across a wide temperature range. As mentioned with QDs, generally larger sizes are more stable as they maximize the enthalpy gain from crystallinity and minimize the ratio of surface area to volume. Consequently, QDs will continuously grow as an ensemble as temperature increases and the reaction proceeds. Seeing as these new discrete optical absorbance features do not shift with moderate changes in temperature, they are therefore suggestive of a single, molecular particle, the stability of which is uncharacteristically high for a crystal of that particular size. In some way, the internal and surface energies of these species have serendipitously balanced to form a stable, atomically-precise structure. This made them easy to identify and optically characterize during syntheses.

As QD synthesis developed, the documentation of these metastable, atomically-precise particles continued across different materials, precursor systems, temperatures, and many other levers of reaction variance.[48–60] However, despite their appearance in a seemingly ubiquitous range of material compositions, the knowledge required to rationalize their existence of unique stability was severely lacking. This earned them the name magic-sized clusters (MSCs).

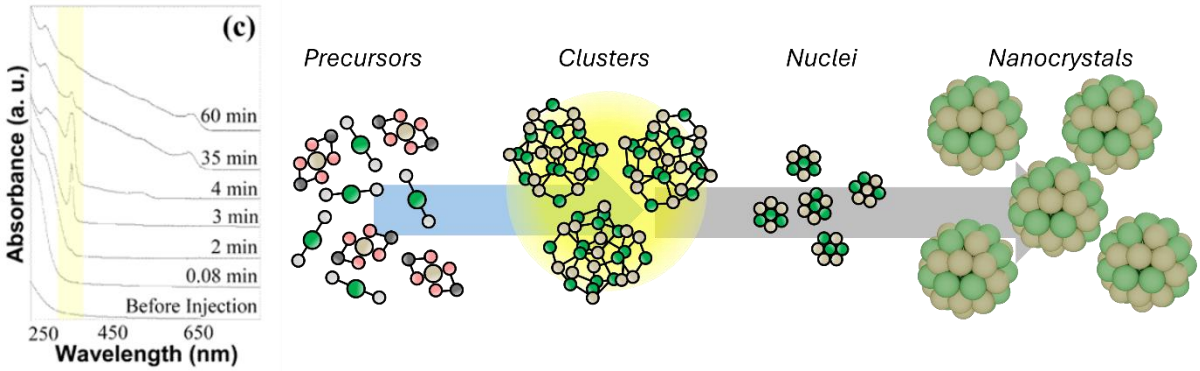

Figure 1.6.1. Sharp optical features appear in absorbance spectra at early reaction times which are indicative of MSC formation. Absorbance traces from reference 38.

The classical understanding of nucleation suggests a continuous process in which precursors react to form solute, which generates nuclei that grow into nanocrystals. The presence of discrete, persistent, metastable intermediates not only defies the continuity of this process but also breaks the classical notions of interpreting stability. Larger particles should be more stable than smaller particles but now suddenly there is a seemingly arbitrary bias towards a single, typically small, crystal size. The foundations of their existence and how they might influence or participate in QD formation mechanisms were completely unknown.

The research interest that developed for MSCs was then two-fold. Firstly, the relationship between their atomic structure and conversion pathways. Through extensive optical characterization during QD reactions, it became clear that these molecular structures can function as metastable intermediates and sources of solute during nanocrystal formation.[39,61–63] However, the vast majority of documented MSCs have only been characterized by their absorbance profile. Their stability, conversion pathways, and optoelectronic properties are all derived from their atomic structure and yet these structures are, for the most part, completely unknown. There is simply no available rationale for why and how these intermediates form since there is a lack of structural information required to establish these conclusions. The second pronounced area of research interest is derived from the inherent sample homogeneity that MSCs provide. As mentioned previously, achieving atomistic precision in QD synthesis is what will augment their already established usage in photonic applications. In some ways, this precision has already been achieved through the MSC system. They are molecular species and atomically precise thereby reaching the highest achievable standard of ensemble homogeneity as every magic-sized cluster has the exact same atomic arrangement. The inherent ensemble-level homogeneity underscores the significant potential for unprecedentedly narrow emission linewidths and the opportunity for

these materials to be viewed as atomically precise models of QDs. However, there are complications in the emission profiles of MSCs that have so far challenged the application of these materials as homogeneous emitters.

To begin to understand the intrinsic structural stability of semiconductor MSCs, it is important to put their existence in the context of other, more well-developed molecular clusters. Investigating structure-function relationships in defined cluster species will allow for the rationalization of their unique stability and design rules for their synthesis and resultant properties.

1.7 The Metallic Roots of Molecular Cluster Stability

The existence of high nuclearity clusters of atoms with distinctive stabilities is not unique to semiconductors. In fact, the rubric for the behavior of metallic MSCs has long been in development. The formation of molecular cluster species in the context of nanomaterial synthesis began from M_6 complexes of Nb and Ta as Nb_6Cl_{14} and Ta_6Cl_{15}.[64] While the structure of tri- and tetranuclear complexes were common at this point, the M_6 can generally be considered as the starting point of cluster species. This area of analysis was continued to generate the library of $[Pt_3(CO)_6]_n^{2-}$ (n = 1, 2, 3, 4, 5, 6, 10) clusters.[65] These provided experimental proof for significantly larger clusters and furthered the complexity of metal-metal bonded polyhedra. Grown from the consecutive addition of trinulear platinium units, this could also be considered the first example of quantized (non-continuous) growth in this context.

Meanwhile, in a similar timeline, clusters of other noble metals were being developed, namely the 1,2-bis(diphenylphosphino)ethane-ligated Au_6 cluster and its relation to $Au_{11}(PPh_3)_7(SCN)_3$.[66,67] As documented cluster sizes and corresponding nuclearity grew larger, it became apparent that there were unknown rules governing the stability of these materials that

could not be interpreted through the same lens as organic molecules. This crescendoed with the full structural characterization of $Au_{102}(SR)_{44}$, which featured a 49 gold atom Marks decahedron core, two 20 atom "caps" at opposing vertices and a 13 atom belt around the equator of the structure.[68] Synthesizing homogeneous materials is very challenging, especially as particles become larger. In those cases, the internal energy dominates stability and therefore growth, by addition of solute to the surface, contributes inconsequentially to the overall stability of the particle. There is no energetic bias between larger and smaller particles and thus heterogeneity manifests. A structure as large as $Au_{102}(SR)_{44}$ proved that homogeneity on a molecular level can exist at very large size scales. The atomically-resolved characterization of this structure inspired a field of efforts that sought to fully understand the rules by which noble metal clusters form with distinct and discrete stabilities.

Following the momentum of $Au_{102}(SR)_{44}$, came a slew of crystallographically characterized gold clusters including $Au_{23}(SR)_{16}$, $Au_{25}(SR)_{18}$, $Au_{28}(SR)_{20}$, $Au_{36}(SR)_{24}$, $Au_{38}(SR)_{24}$, Au_{130}, and Au_{144}.[69–75] This has since been expanded even further to the largest gold cluster that has been crystallographically characterized, $Au_{246}(SR)_{80}$.[76] It was the full structural characterization of all these clusters followed by a rigorous analysis of their structural motifs that has allowed for the formation of a structure-based rubric that can explain the discrete stability of these materials. Firstly, a geometric closed-shell structure is required. That is to say that the atomic arrangement must be based on a platonic solid of close-packed atoms with no vacancies. Secondly, a full-shell electron configuration must be satisfied, analogous to the electronic structure of noble gases.[77–79]

The rules governing noble metal cluster stability have been developed due to the vast, rich structural library generated from years of synthesis and characterization. Each new structure provides an additional data point through which the structure-based rubric is refined. It is

noteworthy that not all structures of noble metal clusters can be simply rationalized through the perspective of closed geometric and electronic shells. Notably, Au_{68} is a structural outlier in this sense which emphasizes that while incredibly well-developed, the stipulations placed on structural stability must continuously be adapted to incorporate contemporary experimentation.[80]

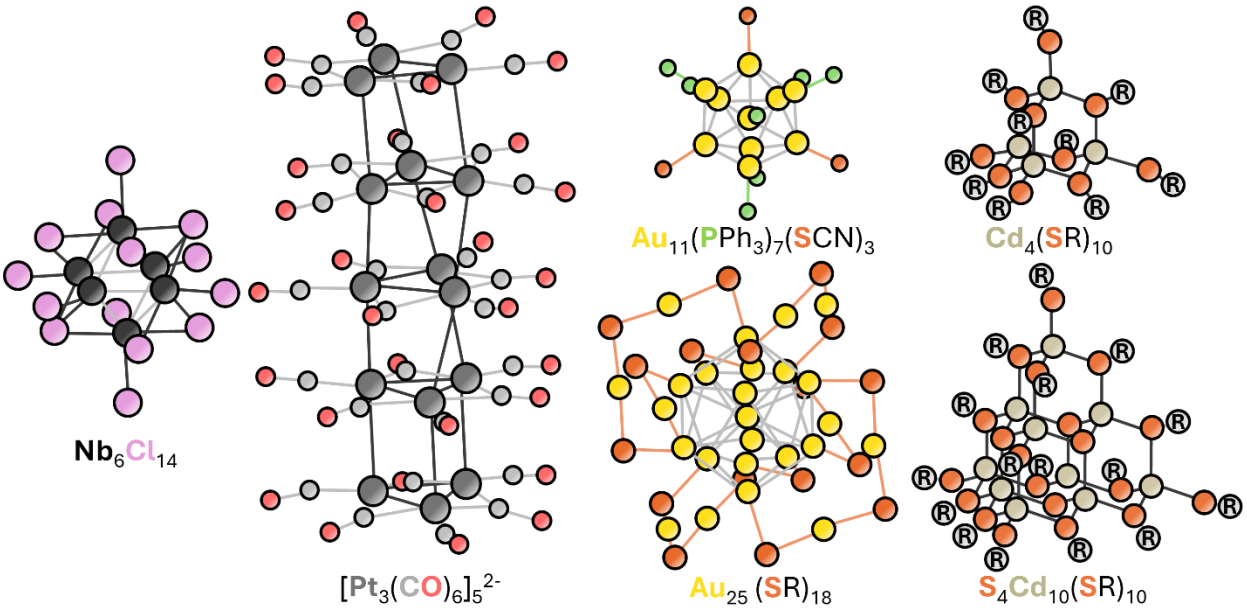

Figure 1.7.1. Structures of some of the most influential molecular clusters mentioned in the text. These materials provided a rubric for interpreting the stability of MSCs in QD synthesis in the future.

Subsequent studies of molecular clusters following the structural observations of the noble metals targeted the common binary semiconductor systems that are used with QDs. The reaction between a metal nitrate salt and benzenethiol in the presence of tetramethylammonium chloride led to the formation of $(R_4N)_2[M_4(SPh)_{10}]$ and the subsequent addition of powdered chalcogen resulted in $(Me_4N)_4[M_{10}E_4(SPh)_{16}]$ (E = Se, S; M = Cd, Zn).[81,82] While cadmium and zinc chalcogenides are semiconducting materials, these clusters weren't viewed through the lens of

quantum confinement and nanochemistry but instead were targeted as potential analogues to thiolate-ligated cobalt and iron complexes that served a biological context.[83,84]

Further study of the $(Me_4N)_4[S_4M_{10}(SPh)_{16}]$ clusters resulted in the charge neutral analogue, $M_{10}S_4(SPh)_{12}$, as well as $Cd_{17}S_4(SPh)_{26}$, $Cd_{54}S_{28}(SPh)_{52}$, and $Cd_{32}S_{14}(SPh)_{36}$.[85,86] The isolation and structural characterization of these binary clusters closely mirrored the efforts in the noble metal cluster space. But the tetrahedral coordination of metal and chalcogen in these semiconductor materials created a distinct separation from the structural behavior of the noble metals which prefer the 12 nearest-neighbor configuration of face-centered cubic lattices. The atomic arrangement in these binary clusters can be described as a cubic zincblende core with the addition of hexagonal wurtzite corners in larger clusters. These being the thermodynamically stable phases of these materials left few open questions as to their distinct stability. Interestingly, many years later, the $M_{10}Se_4(SPh)_{16}$ clusters were used as single-source precursors to CdSe and ZnSe QDs through thermolysis.[87] While the structural characterization of these II-VI clusters provided the first framework for understanding molecular stability of semiconductors, they were not directly, mechanistically related to QDs. Their synthesis was born of inorganic coordination chemistry at low temperatures in polar solvents, so while the structures provide important context for interpreting MSC behavior in QD systems, they themselves remain as a separate brand of molecular semiconductors.

As the enigma of stability appeared for MSC intermediates in QD reactions, the knowledge to be applied in interpreting their behavior is built on the foundational studies of unary metallic clusters and the inorganic complexation reactions of metal chalcogenide molecules.

1.8 Atomic Structure and Conversion Pathways of MSCs

The initial investigations of MSCs as reaction intermediates unveiled that they were a kinetic trap for reactive precursors. In this mechanism, QD precursors are combined at high temperature resulting in the rapid formation of MSCs as evidenced by sharp absorbance features at early timepoints in the reaction. With the high temperature maintained, the MSCs will destabilize thereby producing reactive solute species, distinct from the initial solute produced from precursors, that can re-nucleate and grow nanocrystals. This effectively decouples the direct reaction between precursors and QD formation.[61,88] MSCs function as a potential well that breaks the kinetic chain normally connecting precursors and QDs. With this functioning as the standard mechanism for cluster behavior, there are other routes for cluster conversion as well. MSCs have also been used as synthetic tools to make more complex nanomaterials such as nanorods, nanoplatelets, and quantum belts.[89–92] These investigations led to the conceptualization of three growth pathways for MSCs: 1) dissolution and renucleation, 2) cluster assembly, and 3) quantized growth.[93,94]

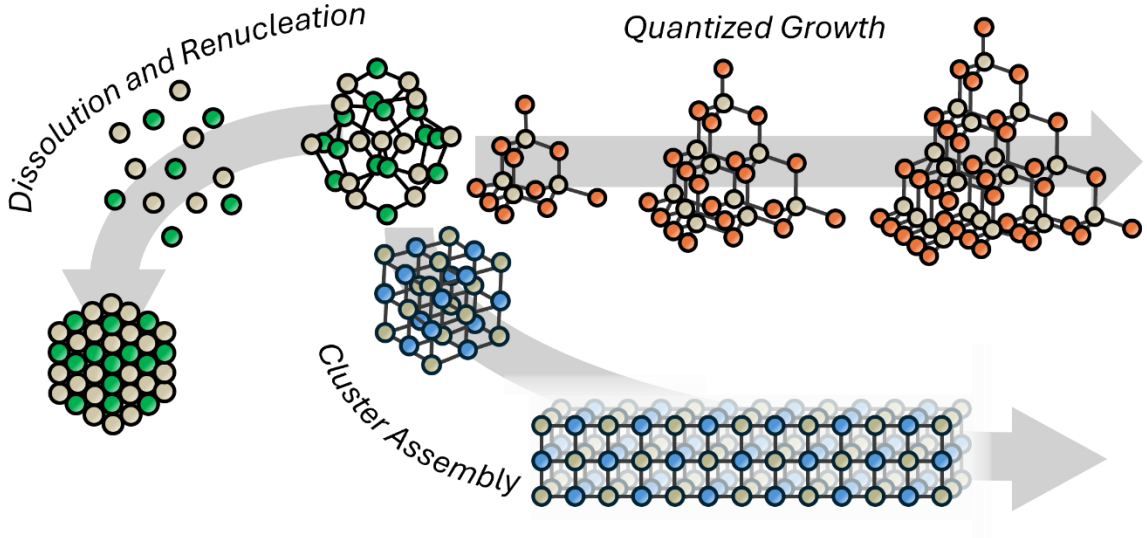

Figure 1.8.1. The three growth pathways of MSCs.

Invoking cluster assembly involves the spontaneous organization of MSCs into a larger structure followed by an annealing step or the addition of more precursor to completely crystallize the larger structure. This method has been used to great effect in synthesizing large, highly crystalline nanosheets and quantum belts.[89–92] Cluster aggregation is induced by the van der Waals forces of interdigitated ligand tails which causes the high degree of ordering. Following this, the annealing does not disturb the assembled structure so large structures with precise dimensions, as predetermined by the cluster size, can be achieved.

Quantized growth occurs when one MSC converts into a larger, more stable MSC of a similar morphology. This can occur during thermolysis of MSCs and is most clearly demonstrated by the system of CdSe tetrahedra in which one of four facets is extended by a singular layer resulting in a tetrahedron of the next largest size.[47,95–98] This has allowed for the growth of clusters across a wide range of visible wavelengths while still maintaining homogeneity. While the direct conversion of any homogeneous ensemble into another larger ensemble while maintaining homogeneity can be considered quantized growth, it is the facet-based mechanism of CdSe tetrahedra that has received the most study.[99]

The growth pathway is partially dictated by the general reaction conditions where higher temperatures benefit dissolution/renucleation, primary straight-chain alkyl amines promote cluster assembly, and mild temperature increases stimulate quantized growth. However, the primary variable that controls cluster growth behavior is atomic structure. Less crystalline MSCs, with atomic structures that do not contain repeating, ordered atomic arrangements, undergo thermolysis at lower temperatures.[100–102] Surface atom spacing, as defined by atomic structure, controls epitaxy and therefore assembly, and the cluster structure must have a well-defined high energy, reactive facet to allow quantized growth to occur.[103–105] It is the atomic structure of the MSC that defines

not just the chemical behavior during conversion but also the photophysical behavior upon excitation. Put simply, the function of a material is defined by its structure. Despite the empirical mechanistic developments of MSCs, knowledge of their structure and therefore a fundamental understanding of their properties has remained difficult to access. Furthermore, the underlying rationale for their "magic" stability must be interpreted through their structure. It is clear that certain atomic arrangements lead to unpredictable wells of stability, but we lack actual characterization of those arrangements. With more structural information we can begin to understand and develop intuition as to why these materials achieve atomic precision and apply that to synthetic mechanisms to better understand fundamental nanomaterial behavior and, in the process, generate precise and applicable colloidal materials.

As a final thought in this section, it is interesting to compare the formation pathways of QDs versus MSCs. The basics of nucleation and growth have been described above and can be accurately applied to QD nucleation and growth in most cases. In this instance, a concentration dependence governs the regime of the reaction thereby transitioning between nucleation, growth, and equilibrium. However, MSCs do not necessarily obey these regulations. Studies have shown that instead of following nucleation kinetics, the formation of these particles seems to follow chemical kinetics in which the direct reaction between precursors overcomes an activation energy to produce the product.[40] While this may seem unsurprising at face value as MSCs are indeed formed from molecules and are molecules themselves, the formation of thermodynamic phases still requires some semblance of crystallization. MSCs then cannot be considered to form through nucleation kinetics but their structure precludes them from forming only through chemical kinetics. So, both in mechanism and in structure, they exist as a bridge between the precise, molecular realm and the crystalline regime of nanomaterials.

1.9 Previous Characterization of MSCs in QD Systems

As the general study of QD synthesis developed, the presence of MSCs continued to build momentum. Persistent absorbance features were documented in the synthesis of CdSe,[38,41,42] CdS,[106] InP,[40,61,62] InAs,[52,62,107,108] ZnSe,[109–111] ZnS,[49,112] and Cd_3As_2.[56,57] Syntheses were also developed to specifically target and isolate MSCs which would allow for optoelectronic studies of their properties separate from their heterogeneous parent nanomaterial. This was the case for many CdSe and CdS clusters as well as InP, PbSe, and Cd_3P_2.[55,58,59,61,95,113,114] As the presence of MSCs as synthetic tools became ubiquitous, the observation or isolation of one became less impactful. Instead, their existence transformed under the lens of noble metal clusters, as questions focused more on why they were stable as opposed to simply documenting their existence. The information that structural characterization can provide opens avenues to rationalize MSC behavior at the atomic level. Despite the library of MSCs with well-documented absorbance profiles, the corresponding structures are understudied and remain completely ambiguous. Therefore, justifying and understanding chemical and photophysical behavior through structure is nearly impossible. That being said, it is not a dramatic oversight nor lack of effort in the QD field that has led to the lack of structural information regarding MSCs. Procuring a sample that allows for this structural omniscience is arduous.

Full structural refinement by single-crystal x-ray diffraction methods requires the growth of diffraction quality crystals. Molecules of interest must be controllably crystallized from a solution resulting in highly ordered crystals preferably of a large size.* Any imperfections in the

* To be clear, this is separate from the crystallization process that occurs to grow QDs and MSCs. Nucleation and growth occur from precursors as described to produce nanocrystals, and in this case, more specifically MSCs. For these MSCs to be structurally characterized, they themselves must be crystallized to form a crystal of crystals. While the terminology can overlap, the conditions under which each process occurs is very different.

form of misaligned crystal planes, atomic disorder, or structural twinning will disrupt the electron-density map that is built from the diffracted x-rays.[115] If the crystal is too small, there simply aren't enough atoms to allow for adequate constructive interference of x-rays that provide signal.[116] The growth of these crystals can be extremely challenging for even small molecules made up of only 10 to 50 atoms. There are simply too many conformational degrees of freedom in solution which result in imperfections as the crystal grows. Applying this to magic-sized clusters, in many instances simply just the inorganic core of the cluster is already approaching 50 atoms and with the addition of ligands, the total structure can be well over 1100 atoms. Due to the hindrance conformational freedom has on diffraction signal, judicious choices must be made as to the ligand set that is employed during crystallization. Rigid substituents are used in place of their common, more soluble aliphatic counterparts. The synthesis of the clusters must then be adapted for the usage of a different, more rigid ligand set without disturbing the structural integrity of the product. These challenges work in tandem during attempts to structurally refine reported MSCs and can explain why, despite their ubiquitous presence, severely lack in structural information. Despite the formidable effort required for this encompassing analysis, there are still MSCs that have been characterized in this fashion.

The first of which is a tetrahedral CdSe MSC with the formula $Cd_{35}Se_{20}(X)_{30}(L)_{30}$ ($X = O_2CC_6H_5$, $L = H_2NC_4H_9$).[95] It's relation to the previously described collection of phenylthiolate-ligated II-VI clusters (i.e. $M_{10}Se_4(SPh)_{16}$) was immediately apparent as both present a zincblende core and a tetrahedral morphology. The important distinction here is that the precursors used, cadmium carboxylate, primary amine, and $Se(SiMe_3)_2$, were relevant to QD synthesis. Along with the structure, extended heating of this cluster led to the quantized growth into larger tetrahedral

clusters, $Cd_{56}Se_{35}$ and $Cd_{84}Se_{56}$, the structures of which could not be resolved by SCXRD and were instead analyzed by pair distribution function analysis.

After the isolation of the three CdSe tetrahedra came the full structural characterization of an InP magic-sized cluster, $In_{37}P_{20}(O_2CR)_{51}$.[117] Formed from indium carboxylate and $P(SiMe_3)_3$, the principal conclusion from this investigation was that the atomic arrangement of In and P in this cluster is not zincblende or wurtzite, the stable crystalline phases of bulk InP. The previously documented II-VI clusters are all in the zincblende crystalline phase so while the number of constituent atoms in these materials was novel information, the atomic arrangement was unsurprising. This was not the case for $In_{37}P_{20}(O_2CR)_{51}$ and emphasized that there are unknown rules dictating the formation of many of these materials.

Following $In_{37}P_{20}$, a $Cd_{14}Se_{13}$ cluster ligated by tetramethylethylenediamine was crystallized.[118] It had a cage-like structure generated from 2- and 3-coordinate Se bound to Cd surrounding a central, 4-coordinate Se atom. It was recognized that this atomic arrangement also deviated from bulk phases of CdSe but what remained unrecognized was the structural similarities with the $In_{37}P_{20}$ cluster which is a topic of discussion in Chapter 2. The characterization of this cluster showed that especially CdSe, but materials in general, can adopt multiple forms on the nanoscale to achieve a local minimum of stability. These minima are not only size-dependent but also phase-dependent suggesting that stability at this length scale is a highly complex potential energy surface.

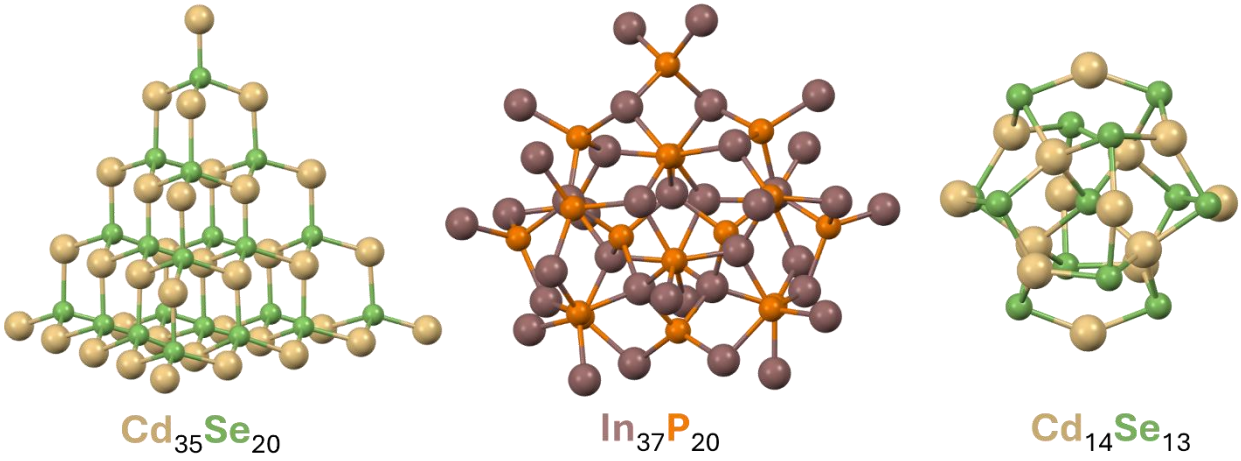

Figure 1.9.1. Three MSC structures resolved by SCXRD.

As of 2022, these were the only MSCs that had been structurally characterized. While these three structures formed the basis on which cluster stability could later be interpreted, on their own not enough information was accessible to begin to explain trends in stability. In order to build out an understanding of the rules and motifs that dictate the stability of binary semiconductor MSCs, the library of MSC structures must be expanded.

1.10 The Usage of MSCs as Homogeneous Colloidal Emitters

Structural studies of MSCs dug into the foundational existence of discrete crystal sizes but did not result in application-focused improvements. As particle size controls absorbance and emission wavelengths within the quantum confinement regime, the molecular nature of MSCs poses promise for homogeneous emission. As with QDs, this leads to two primary applications: 1) emitters for solid-state lighting, and 2) single photon emitters for quantum information science (QIS). These routes are both contingent upon nearly-perfect sample homogeneity.[7,119–121]

Any heterogeneity or deviation in atomic structure as a part of the ensemble will negatively impact implementation. In the case of solid-state lighting, this decreases color purity as slightly different wavelengths of light will contribute to the emission. This has the added effect of reducing efficiency since unwanted portions of the emission spectrum must be filtered out and therefore any excitation energy leading to unwanted emission wavelengths is wasted. For Quantum Information Science (QIS), QDs can be used as single-photon emitters, which rely on photon indistinguishability. A heterogeneous ensemble will emit photons of slightly different energies thereby precluding indistinguishability. Furthermore, broader emission is directly correlated with photon decoherence times.[122–124] For photons to maintain their encoded quantum information for as long as possible, they must remain coherent. Having photons of different energies emitted from the same sample drastically reduces coherence times leading to the loss of encoded information.

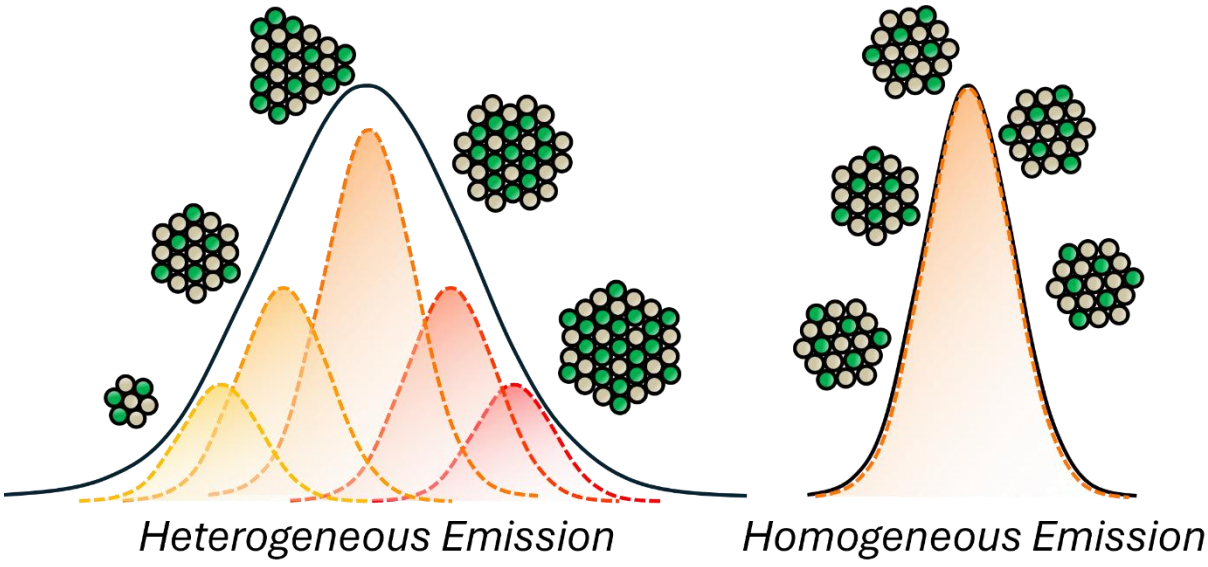

Figure 1.10.1. Variation in particle size causes variation in emission wavelength leading to heterogeneous emission. A homogeneous samples has no particle variations leading to homogeneous emission.

Seeing how imperative sample homogeneity is to the usage of QDs, it would follow that implementing MSCs would remove all possible heterogeneity resulting in the perfect candidate for homogeneous, narrow emission. However, the analysis of emission profiles from MSCs shows that instead, the emission is very dim and normally quite broad.[59,95,118,125] Excitation of these materials results in significant nonradiative recombination and the recombination that is radiative occurs at a wide variety of different wavelengths. This apparent discrepancy in nanomaterial behavior can be generally attributed to two different factors: 1) strong confinement leading to surface vibrational coupling and, 2) lattice softness allowing emission from structurally distorted states. In the first case, seeing as most clusters exist on the 1-2 nanometer scale, the small size ensures that clusters are much smaller than the Bohr radii of common semiconductor materials. Clusters are therefore extremely confined in most cases and the disparity between r_B and their size allows for the exciton wavefunction to couple easily with the particle surface.[126–128] This increases the probability of overlap with surface vibrational modes leading to vibronic coupling and nonradiative recombination. Beyond the strength of confinement, clusters do not have the same extent of lattice periodicity as their larger, QD counterparts, so large nuclear distortions can occur after excitation that severely distort the atomic geometry.[129–132] These distortions can facilitate previously disallowed electronic transitions that are much lower in energy, resulting in massive Stokes shifts and very broad emission. This behavior in semiconductors is oftentimes referred to as a self-trapped exciton.[133] The formation of the exciton causes such a large distortion in the lattice that an entirely different molecular orbital set is accessed from the excited state that is much lower in energy. The emission then comes from this newly accessed electronic state. The large Stokes shift comes from the decrease in energy prior to emission and the broad linewidths occur due to

the vibronic coupling of the emission. It is arguable whether applying the "self-trapped exciton" nomenclature to cluster behavior makes chemical sense, but at the very least, the overall emissive behaviors of the systems are very similar.

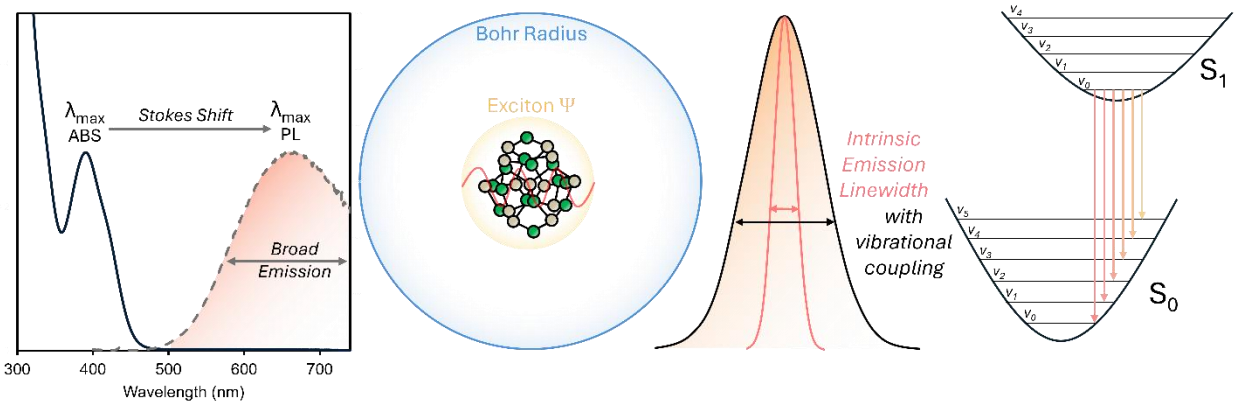

Figure 1.10.2. Despite atomic precision, the emission of many MSCs is characterized by very broad and dim with a large Stokes shift. This can be attributed to stronger confinement leading to the exciton interacting with the surface as well as a high degree of vibrational coupling.

MSCs suffering from nonradiative recombination and large nuclear distortions cause their emission to fall below the threshold of applicability (photoluminescence quantum yield (PLQY) <10%). While certain clusters achieve higher radiative efficiency, most have PLQY values of <5%.[55,59,95,118,125,134] It becomes evident that improving emission of MSCs will come from enhancing the rigidity of the molecule, but this must not come at the sacrifice of the distinctive energetic balance that allows for atomic precision. QDs have also suffered from weak emission where unpassivated surface atoms cause carrier trapping and radiative losses occur through vibrational coupling.[135–140] These issues have been addressed in a variety of different ways in the QD system. Primarily, a coating of a different material with a larger bandgap, called a shell, can

be grown around the QD to passivate surface atoms and confine the exciton wavefunction to the core disallowing surface interaction.[141–143] While this route has been applied to great effect with QDs, the shelling procedures require high temperatures and cause significant surface disruptions during growth. The unique balance between surface and internal energies of MSCs that allow for discrete stability would be strongly perturbed by the removal of surface ligands and subsequent shell growth. Similarly, exchanging the native QD ligands for a set with a different head group can influence emission.[144–148] However, once again, this can severely perturb the free energy balance that dictates the stability of MSCs.

The ligand network on MSCs adopts a specific distribution of binding modes that is imperative for stability.[149,150] Perturbance of the ligand sphere results in a propagation of modes likely resulting in a loss of stability and dissolution. This emphasizes the metastability of these materials and highlights that the same approaches to enhance QD emission will inevitably result in either heterogeneity or complete instability when applied to MSCs. Improvements to emission must then come from the result of judicious choices in modification routes.

The final complication in achieving applicable, homogeneous emission with MSCs is derived from their intrinsic properties. While QDs undergo continuous growth allowing for emission at any wavelength based on their size, MSCs do not have this luxury. They are atomically-precise due to the inherent structural bias that causes certain sizes and atomic arrangements to be more stable than others.[88,151,152] Therefore, continuous growth is impossible with MSCs, as only discrete, independent species are stable. The emission from these materials is therefore predetermined and uncontrollable as the structures and sizes of MSCs are also predetermined. Lacking the ability to target any emission wavelength significantly reduces the usability. However, similar to the complications with the surface, the inorganic core of the cluster

cannot be perturbed without the immediate loss of atomic precision. Methods must then be developed to circumvent this apparently intrinsic complication.

1.11 What to Expect from this Thesis

Through the introduction of the binary semiconductor MSC system, it is evident that there are two major areas meriting further study. The first seeks to develop the cluster structural library to diagnose the underlying origins of discrete stability. Despite the challenges of full structural refinement, previous endeavors have proven that crystallization of these macromolecules is possible. With a concerted effort, the rubric of magic-sized stability may be expanded to include the complex behavior of colloidal, binary systems and thereby allowing a rich analysis of what motifs allow for atomic precision at the nanoscale. The second area focuses on applying MSCs to technologies that require homogeneous ensemble emission. This is contingent upon improving the emissive properties by narrowing photoluminescence linewidths and eliminating nonradiative recombination pathways. While there is clearly much to learn from the surface modifications of QDs, sagacious choices must be made to ensure retention of the precise atomic arrangements that are the hallmark of these unique materials.

In this thesis, these two areas of MSC research are explored. In Chapter 2, the steric profile of the ligand shell on an InP cluster is engineered to control reactivity, eventually resulting in the isolation and full structural characterization of a new InP cluster. In Chapter 3, structural refinement of a ubiquitous InAs cluster is accomplished and, when analyzed in tandem with existing cluster structures, allows for the beginnings of rationalizing the atomic-precision of binary clusters. In Chapter 4, significant emission enhancement of II-V clusters is documented by leveraging the similarity in coordination motifs of carboxylate and phosphinate ligands. In Chapter

5, continuous tunability in absorption and emission wavelengths is accomplished by alloying P and As in II-V MSCs. Through these studies, a rationalization of nanoscale molecular stability was developed and has allowed for functionalization of metastable materials through the interfacial chemistry of metal pnictide magic-sized clusters.

1.12 REFERENCES

(1) Meneghini, M.; De Santi, C.; Abid, I.; Buffolo, M.; Cioni, M.; Khadar, R. A.; Nela, L.; Zagni, N.; Chini, A.; Medjdoub, F.; Meneghesso, G.; Verzellesi, G.; Zanoni, E.; Matioli, E. GaN-Based Power Devices: Physics, Reliability, and Perspectives. *J. Appl. Phys.* **2021**, *130* (18), 181101. https://doi.org/10.1063/5.0061354.

(2) H. Patel, M.; K. Chaudhuri, T.; K. Patel, V.; Shripathi, T.; Deshpande, U.; P. Lalla, N. Dip-Coated PbS/PVP Nanocomposite Films with Tunable Band Gap. **2017**. https://doi.org/10.1039/C6RA25935A.

(3) Rossetti, R.; Nakahara, S.; Brus, L. E. Quantum Size Effects in the Redox Potentials, Resonance Raman Spectra, and Electronic Spectra of CdS Crystallites in Aqueous Solution. *J. Chem. Phys.* **1983**, *79* (2), 1086–1088. https://doi.org/10.1063/1.445834.

(4) Ekimov, A.; Onushchenko, A.; Tsekhomskii, V. Exciton Absorption by Copper (I) Chloride Crystals in a Glassy Matrix. *Fiz Khim Stekla* **1980**, *6*, 511–512.

(5) Lin, X.; Ye, Z.; Cao, Z.; Qin, H.; Peng, X. Colloidal Nanocrystals: A Promising Semiconductor Platform for Photon/Exciton Manipulation. *Acc. Mater. Res.* **2024**, *5* (8), 884–895. https://doi.org/10.1021/accountsmr.3c00286.

(6) Murray, C. B.; Norris, D. J.; Bawendi, M. G. Synthesis and Characterization of Nearly Monodisperse CdE (E = Sulfur, Selenium, Tellurium) Semiconductor Nanocrystallites. *J. Am. Chem. Soc.* **1993**, *115* (19), 8706–8715. https://doi.org/10.1021/ja00072a025.

(7) Nguyen, H. A.; Dixon, G.; Dou, F. Y.; Gallagher, S.; Gibbs, S.; Ladd, D. M.; Marino, E.; Ondry, J. C.; Shanahan, J. P.; Vasileiadou, E. S.; Barlow, S.; Gamelin, D. R.; Ginger, D. S.; Jonas, D. M.; Kanatzidis, M. G.; Marder, S. R.; Morton, D.; Murray, C. B.; Owen, J. S.; Talapin, D. V.; Toney, M. F.; Cossairt, B. M. Design Rules for Obtaining Narrow Luminescence from Semiconductors Made in Solution. *Chem. Rev.* **2023**, *123* (12), 7890–7952. https://doi.org/10.1021/acs.chemrev.3c00097.

(8) Wolf, M.; Berezovsky, J. Homogeneous and Inhomogeneous Sources of Optical Transition Broadening in Room Temperature CdSe/ZnS Nanocrystal Quantum Dots. *Appl. Phys. Lett.* **2014**, *105* (14), 143105. https://doi.org/10.1063/1.4897347.

(9) Cui, J.; Beyler, A. P.; Marshall, L. F.; Chen, O.; Harris, D. K.; Wanger, D. D.; Brokmann, X.; Bawendi, M. G. Direct Probe of Spectral Inhomogeneity Reveals Synthetic Tunability of Single-Nanocrystal Spectral Linewidths. *Nat. Chem.* **2013**, *5* (7), 602–606. https://doi.org/10.1038/nchem.1654.

(10) Gellen, T. A.; Lem, J.; Turner, D. B. Probing Homogeneous Line Broadening in CdSe Nanocrystals Using Multidimensional Electronic Spectroscopy. *Nano Lett.* **2017**, *17* (5), 2809–2815. https://doi.org/10.1021/acs.nanolett.6b05068.

(11) Senellart, P.; Solomon, G.; White, A. High-Performance Semiconductor Quantum-Dot Single-Photon Sources. *Nat. Nanotechnol.* **2017**, *12* (11), 1026–1039. https://doi.org/10.1038/nnano.2017.218.

(12) Oxtoby, D. W. Nucleation of First-Order Phase Transitions. *Acc. Chem. Res.* **1998**, *31* (2), 91–97. https://doi.org/10.1021/ar9702278.

(13) Kashchiev, D. *Nucleation*; Elsevier, 2000.

(14) Magomedov, M. N. The Surface Energy of Nanocrystals. **2005**, *79* (5).

(15) Vollath, D.; Fischer, F. D.; Holec, D. Surface Energy of Nanoparticles – Influence of Particle Size and Structure. *Beilstein J. Nanotechnol.* **2018**, *9*, 2265–2276. https://doi.org/10.3762/bjnano.9.211.

(16) Gibbs, J. W. *The Collected Works of J. Willard Gibbs*; New York : Longmans, Green and Co., 1928; Vol. 1.

(17) Volmer, M.; Weber, A. Keimbildung in übersättigten Gebilden. *Z. Für Phys. Chem.* **1926**, *119U* (1), 277–301. https://doi.org/10.1515/zpch-1926-11927.

(18) Becker, R.; Döring, W. Kinetische Behandlung Der Keimbildung in Übersättigten Dämpfen. *Ann. Phys.* **1935**, *416* (8), 719–752. https://doi.org/10.1002/andp.19354160806.

(19) Calvin, J. J.; Brewer, A. S.; Crook, M. F.; Kaufman, T. M.; Alivisatos, A. P. Observation of Negative Surface and Interface Energies of Quantum Dots. *Proc. Natl. Acad. Sci.* **2024**, *121* (18), e2307633121. https://doi.org/10.1073/pnas.2307633121.

(20) Wang, D.; Xing, M.; Wei, Y.; Wang, L.; Wang, R.; Shen, Q. Modeling of Nucleation and Growth in the Synthesis of PbS Colloidal Quantum Dots Under Variable Temperatures. *ACS Omega* **2021**, *6* (5), 3701–3710. https://doi.org/10.1021/acsomega.0c05223.

(21) Lazzari, S.; Abolhasani, M.; F. Jensen, K. Modeling of the Formation Kinetics and Size Distribution Evolution of II–VI Quantum Dots. **2017**. https://doi.org/10.1039/C7RE00068E.

(22) Thanh, N. T. K.; Maclean, N.; Mahiddine, S. Mechanisms of Nucleation and Growth of Nanoparticles in Solution. *Chem. Rev.* **2014**, *114* (15), 7610–7630. https://doi.org/10.1021/cr400544s.

(23) Gebauer, D.; Kellermeier, M.; Gale, J. D.; Bergström, L.; Cölfen, H. Pre-Nucleation Clusters as Solute Precursors in Crystallisation. *Chem. Soc. Rev.* **2014**, *43* (7), 2348–2371. https://doi.org/10.1039/C3CS60451A.

(24) Vekilov, P. G. Two-Step Mechanism for the Nucleation of Crystals from Solution. *J. Cryst. Growth* **2005**, *275* (1), 65–76. https://doi.org/10.1016/j.jcrysgro.2004.10.068.

(25) Whitehead, C. B.; Özkar, S.; Finke, R. G. LaMer's 1950 Model for Particle Formation of Instantaneous Nucleation and Diffusion-Controlled Growth: A Historical Look at the Model's Origins, Assumptions, Equations, and Underlying Sulfur Sol Formation Kinetics Data. *Chem. Mater.* **2019**, *31* (18), 7116–7132. https://doi.org/10.1021/acs.chemmater.9b01273.

(26) Shchukin, V.; Schöll, E.; Kratzer, P. Thermodynamics and Kinetics of Quantum Dot Growth. In *Semiconductor Nanostructures*; Bimberg, D., Ed.; Springer: Berlin, Heidelberg, 2008; pp 1–39. https://doi.org/10.1007/978-3-540-77899-8_1.

(27) Lignos, I.; Stavrakis, S.; Kilaj, A.; deMello, A. J. Millisecond-Timescale Monitoring of PbS Nanoparticle Nucleation and Growth Using Droplet-Based Microfluidics. *Small* **2015**, *11* (32), 4009–4017. https://doi.org/10.1002/smll.201500119.

(28) Hendricks, M. P.; Campos, M. P.; Cleveland, G. T.; Plante, I. J.-L.; Owen, J. S. A Tunable Library of Substituted Thiourea Precursors to Metal Sulfide Nanocrystals. *Science* **2015**, *348* (6240), 1226–1230. https://doi.org/10.1126/science.aaa2951.

(29) Vreeland, E. C.; Watt, J.; Schober, G. B.; Hance, B. G.; Austin, M. J.; Price, A. D.; Fellows, B. D.; Monson, T. C.; Hudak, N. S.; Maldonado-Camargo, L.; Bohorquez, A. C.; Rinaldi, C.; Huber, D. L. Enhanced Nanoparticle Size Control by Extending LaMer's Mechanism. *Chem. Mater.* **2015**, *27* (17), 6059–6066. https://doi.org/10.1021/acs.chemmater.5b02510.

(30) Peng, X.; Wickham, J.; Alivisatos, A. P. Kinetics of II-VI and III-V Colloidal Semiconductor Nanocrystal Growth: "Focusing" of Size Distributions. *J. Am. Chem. Soc.* **1998**, *120* (21), 5343–5344. https://doi.org/10.1021/ja9805425.

(31) van Embden, J.; Mulvaney, P. Nucleation and Growth of CdSe Nanocrystals in a Binary Ligand System. *Langmuir* **2005**, *21* (22), 10226–10233. https://doi.org/10.1021/la0510811.

(32) Bullen, C. R.; Mulvaney, P. Nucleation and Growth Kinetics of CdSe Nanocrystals in Octadecene. *Nano Lett.* **2004**, *4* (12), 2303–2307. https://doi.org/10.1021/nl0496724.

(33) Owen, J. S.; Chan, E. M.; Liu, H.; Alivisatos, A. P. Precursor Conversion Kinetics and the Nucleation of Cadmium Selenide Nanocrystals. *J. Am. Chem. Soc.* **2010**, *132* (51), 18206–18213. https://doi.org/10.1021/ja106777j.

(34) LaMer, V. K.; Dinegar, R. H. Theory, Production and Mechanism of Formation of Monodispersed Hydrosols. *J. Am. Chem. Soc.* **1950**, *72* (11), 4847–4854. https://doi.org/10.1021/ja01167a001.

(35) Phillips, J. C. Ionicity of the Chemical Bond in Crystals. *Rev. Mod. Phys.* **1970**, *42* (3), 317–356. https://doi.org/10.1103/RevModPhys.42.317.

(36) McMurtry, B. M.; Qian, K.; Teglasi, J. K.; Swarnakar, A. K.; De Roo, J.; Owen, J. S. Continuous Nucleation and Size Dependent Growth Kinetics of Indium Phosphide

Nanocrystals. *Chem. Mater.* **2020**, *32* (10), 4358–4368. https://doi.org/10.1021/acs.chemmater.0c01561.

(37) Abécassis, B.; Greenberg, M. W.; Bal, V.; McMurtry, B. M.; Campos, M. P.; Guillemeney, L.; Mahler, B.; Prevost, S.; Sharpnack, L.; Hendricks, M. P.; DeRosha, D.; Bennett, E.; Saenz, N.; Peters, B.; Owen, J. S. Persistent Nucleation and Size Dependent Attachment Kinetics Produce Monodisperse PbS Nanocrystals. *Chem. Sci.* **2022**, *13* (17), 4977–4983. https://doi.org/10.1039/D1SC06134H.

(38) Peng, Z. A.; Peng, X. Nearly Monodisperse and Shape-Controlled CdSe Nanocrystals via Alternative Routes: Nucleation and Growth. *J. Am. Chem. Soc.* **2002**, *124* (13), 3343–3353. https://doi.org/10.1021/ja0173167.

(39) Jiang, Z.-J.; Kelley, D. F. Role of Magic-Sized Clusters in the Synthesis of CdSe Nanorods. *ACS Nano* **2010**, *4* (3), 1561–1572. https://doi.org/10.1021/nn100076f.

(40) Xie, R.; Li, Z.; Peng, X. Nucleation Kinetics vs Chemical Kinetics in the Initial Formation of Semiconductor Nanocrystals. *J. Am. Chem. Soc.* **2009**, *131* (42), 15457–15466. https://doi.org/10.1021/ja9063102.

(41) Peng, X. Mechanisms for the Shape-Control and Shape-Evolution of Colloidal Semiconductor Nanocrystals. *Adv. Mater.* **2003**, *15* (5), 459–463. https://doi.org/10.1002/adma.200390107.

(42) Peng, Z. A.; Peng, X. Mechanisms of the Shape Evolution of CdSe Nanocrystals. *J. Am. Chem. Soc.* **2001**, *123* (7), 1389–1395. https://doi.org/10.1021/ja0027766.

(43) Pradhan, N.; Xu, H.; Peng, X. Colloidal CdSe Quantum Wires by Oriented Attachment. *Nano Lett.* **2006**, *6* (4), 720–724. https://doi.org/10.1021/nl052497m.

(44) Ouyang, J.; Zaman, Md. B.; Yan, F. J.; Johnston, D.; Li, G.; Wu, X.; Leek, D.; Ratcliffe, C. I.; Ripmeester, J. A.; Yu, K. Multiple Families of Magic-Sized CdSe Nanocrystals with Strong Bandgap Photoluminescence via Noninjection One-Pot Syntheses. *J. Phys. Chem. C* **2008**, *112* (36), 13805–13811. https://doi.org/10.1021/jp803845n.

(45) Chen, H. S.; Kumar, R. V. Discontinuous Growth of Colloidal CdSe Nanocrystals in the Magic Structure. *J. Phys. Chem. C* **2009**, *113* (1), 31–36. https://doi.org/10.1021/jp809360n.

(46) Kasuya, A.; Sivamohan, R.; Barnakov, Y. A.; Dmitruk, I. M.; Nirasawa, T.; Romanyuk, V. R.; Kumar, V.; Mamykin, S. V.; Tohji, K.; Jeyadevan, B.; Shinoda, K.; Kudo, T.; Terasaki, O.; Liu, Z.; Belosludov, R. V.; Sundararajan, V.; Kawazoe, Y. Ultra-Stable Nanoparticles of CdSe Revealed from Mass Spectrometry. *Nat. Mater.* **2004**, *3* (2), 99–102. https://doi.org/10.1038/nmat1056.

(47) Kudera, S.; Zanella, M.; Giannini, C.; Rizzo, A.; Li, Y.; Gigli, G.; Cingolani, R.; Ciccarella, G.; Spahl, W.; Parak, W. J.; Manna, L. Sequential Growth of Magic-Size CdSe Nanocrystals. *Adv. Mater.* **2007**, *19* (4), 548–552. https://doi.org/10.1002/adma.200601015.

(48) Dagtepe, P.; Chikan, V.; Jasinski, J.; Leppert, V. J. Quantized Growth of CdTe Quantum Dots; Observation of Magic-Sized CdTe Quantum Dots. *J Phys Chem C* **2007**, *111* (41), 14977–14983. https://doi.org/10.1021/jp072516b.

(49) Liu, S.; Yu, Q.; Zhang, C.; Zhang, M.; Rowell, N.; Fan, H.; Huang, W.; Yu, K.; Liang, B. Transformation of ZnS Precursor Compounds to Magic-Size Clusters Exhibiting Optical Absorption Peaking at 269 Nm. *J. Phys. Chem. Lett.* **2020**, *11* (1), 75–82. https://doi.org/10.1021/acs.jpclett.9b02999.

(50) Wegner, K. D.; Häusler, I.; Knigge, X.; Hodoroaba, V.-D.; Emmerling, F.; Reiss, P.; Resch-Genger, U. One-Pot Heat-Up Synthesis of ZnSe Magic-Sized Clusters Using Thiol Ligands. *Inorg. Chem.* **2022**, *61* (19), 7207–7211. https://doi.org/10.1021/acs.inorgchem.2c00041.

(51) Ning, J.; Banin, U. Magic Size InP and InAs Clusters: Synthesis, Characterization and Shell Growth. *Chem. Commun.* **2017**, *53* (17), 2626–2629. https://doi.org/10.1039/C6CC09778B.

(52) Xie, R.; Peng, X. Synthetic Scheme for High-Quality InAs Nanocrystals Based on Self-Focusing and One-Pot Synthesis of InAs-Based Core–Shell Nanocrystals. *Angew. Chem. Int. Ed.* **2008**, *47* (40), 7677–7680. https://doi.org/10.1002/anie.200802867.

(53) Yu, Q.; Liu, C.-Y. Study of Magic-Size-Cluster Mediated Formation of CdS Nanocrystals: Properties of the Magic-Size Clusters and Mechanism Implication. *J. Phys. Chem. C* **2009**, *113* (29), 12766–12771. https://doi.org/10.1021/jp903199y.

(54) Wang, R.; Ouyang, J.; Nikolaus, S.; Brestaz, L.; Zaman, M. B.; Wu, X.; Leek, D.; Ratcliffe, C. I.; Yu, K. Single-Sized Colloidal CdTe Nanocrystals with Strong Bandgap Photoluminescence. *Chem. Commun.* **2009**, No. 8, 962–964. https://doi.org/10.1039/B818967F.

(55) Wang, R.; Ratcliffe, C. I.; Wu, X.; Voznyy, O.; Tao, Y.; Yu, K. Magic-Sized Cd3P2 II−V Nanoparticles Exhibiting Bandgap Photoemission. *J. Phys. Chem. C* **2009**, *113* (42), 17979–17982. https://doi.org/10.1021/jp907642b.

(56) Harris, D. K.; Allen, P. M.; Han, H.-S.; Walker, B. J.; Lee, J.; Bawendi, M. G. Synthesis of Cadmium Arsenide Quantum Dots Luminescent in the Infrared. *J. Am. Chem. Soc.* **2011**, *133* (13), 4676–4679. https://doi.org/10.1021/ja1101932.

(57) Huang, M.; Hickey, S. G.; Höfer, B.; Ding, F.; He, S.; Schmidt, O. G.; Eychmüller, A.; Miao, S. Band-Emission Evolutions from Magic-Sized Clusters to Nanosized Quantum Dots of Cd3As2 in the Hot-Bubbling Synthesis. *J. Phys. Chem. C* **2015**, *119* (28), 16390–16395. https://doi.org/10.1021/acs.jpcc.5b04437.

(58) Nevers, D. R.; Williamson, C. B.; Savitzky, B. H.; Hadar, I.; Banin, U.; Kourkoutis, L. F.; Hanrath, T.; Robinson, R. D. Mesophase Formation Stabilizes High-Purity Magic-Sized Clusters. *J. Am. Chem. Soc.* **2018**, *140* (10), 3652–3662. https://doi.org/10.1021/jacs.7b12175.

(59) Evans, C. M.; Guo, L.; Peterson, J. J.; Maccagnano-Zacher, S.; Krauss, T. D. Ultrabright PbSe Magic-Sized Clusters. *Nano Lett.* **2008**, *8* (9), 2896–2899. https://doi.org/10.1021/nl801685a.

(60) Dukes, A. D. I.; McBride, J. R.; Rosenthal, S. J. Synthesis of Magic-Sized CdSe and CdTe Nanocrystals with Diisooctylphosphinic Acid. *Chem. Mater.* **2010**, *22* (23), 6402–6408. https://doi.org/10.1021/cm102370a.

(61) Gary, D. C.; Terban, M. W.; Billinge, S. J. L.; Cossairt, B. M. Two-Step Nucleation and Growth of InP Quantum Dots via Magic-Sized Cluster Intermediates. *Chem. Mater.* **2015**, *27* (4), 1432–1441. https://doi.org/10.1021/acs.chemmater.5b00286.

(62) Li, Y.; Hou, X.; Shen, Y.; Dai, N.; Peng, X. Tuning the Reactivity of Indium Alkanoates by Tertiary Organophosphines for the Synthesis of Indium-Based Quantum Dots. *Chem Mater* **2021**, *33* (23), 9348–9356. https://doi.org/10.1021/acs.chemmater.1c03219.

(63) Friedfeld, M. R.; Stein, J. L.; Cossairt, B. M. Main-Group-Semiconductor Cluster Molecules as Synthetic Intermediates to Nanostructures. *Inorg. Chem.* **2017**, *56* (15), 8689–8697. https://doi.org/10.1021/acs.inorgchem.7b00291.

(64) Simon, A.; Georg Schnering, H.; Wöhrle, H.; Schäfer, H. Beiträge Zur Chemie Der Elemente Niob Und Tantal. 44. Nb_6 Cl_{14} Synthese, Eigenschaften, Struktur. *Z. Für Anorg. Allg. Chem.* **1965**, *339* (3–4), 155–170. https://doi.org/10.1002/zaac.19653390306.

(65) Longoni, G.; Chini, P. Synthesis and Chemical Characterization of Platinum Carbonyl Dianions [Pt3(CO)6]N2- (n = .Apprx.10,6,5,4,3,2,1). A New Series of Inorganic Oligomers. *J. Am. Chem. Soc.* **1976**, *98* (23), 7225–7231. https://doi.org/10.1021/ja00439a020.

(66) Naldini, L.; Cariati, F.; Simonetta, G.; Malatesta, L. Gold–Tertiary Phosphine Derivatives with Intermetallic Bonds. *Chem Commun Lond.* **1966**, *0* (18), 647–648. https://doi.org/10.1039/C19660000647.

(67) McPartlin, M.; Mason, R.; Malatesta, L. Novel Cluster Complexes of Gold(0)–Gold(I). *J Chem Soc D* **1969**, *0* (7), 334–334. https://doi.org/10.1039/C29690000334.

(68) Jadzinsky, P. D.; Calero, G.; Ackerson, C. J.; Bushnell, D. A.; Kornberg, R. D. Structure of a Thiol Monolayer-Protected Gold Nanoparticle at 1.1 Å Resolution. *Science* **2007**, *318* (5849), 430–433. https://doi.org/10.1126/science.1148624.

(69) Tlahuice-Flores, A.; Santiago, U.; Bahena, D.; Vinogradova, E.; Conroy, C. V.; Ahuja, T.; Bach, S. B. H.; Ponce, A.; Wang, G.; José-Yacamán, M.; Whetten, R. L. Structure of the Thiolated Au130 Cluster. *J. Phys. Chem. A* **2013**, *117* (40), 10470–10476. https://doi.org/10.1021/jp406665m.

(70) Das, A.; Li, T.; Nobusada, K.; Zeng, C.; Rosi, N. L.; Jin, R. Nonsuperatomic [Au23(SC6H11)16]− Nanocluster Featuring Bipyramidal Au15 Kernel and Trimeric Au3(SR)4 Motif. *J. Am. Chem. Soc.* **2013**, *135* (49), 18264–18267. https://doi.org/10.1021/ja409177s.

(71) Heaven, M. W.; Dass, A.; White, P. S.; Holt, K. M.; Murray, R. W. Crystal Structure of the Gold Nanoparticle [N(C8H17)4][Au25(SCH2CH2Ph)18]. *J. Am. Chem. Soc.* **2008**, *130* (12), 3754–3755. https://doi.org/10.1021/ja800561b.

(72) Zeng, C.; Li, T.; Das, A.; Rosi, N. L.; Jin, R. Chiral Structure of Thiolate-Protected 28-Gold-Atom Nanocluster Determined by X-Ray Crystallography. *J. Am. Chem. Soc.* **2013**, *135* (27), 10011–10013. https://doi.org/10.1021/ja404058q.

(73) Qian, H.; Eckenhoff, W. T.; Zhu, Y.; Pintauer, T.; Jin, R. Total Structure Determination of Thiolate-Protected Au38 Nanoparticles. *J. Am. Chem. Soc.* **2010**, *132* (24), 8280–8281. https://doi.org/10.1021/ja103592z.

(74) Bahena, D.; Bhattarai, N.; Santiago, U.; Tlahuice, A.; Ponce, A.; Bach, S. B. H.; Yoon, B.; Whetten, R. L.; Landman, U.; Jose-Yacaman, M. STEM Electron Diffraction and High-Resolution Images Used in the Determination of the Crystal Structure of the Au144(SR)60 Cluster. *J. Phys. Chem. Lett.* **2013**, *4* (6), 975–981. https://doi.org/10.1021/jz400111d.

(75) Zeng, C.; Qian, H.; Li, T.; Li, G.; Rosi, N. L.; Yoon, B.; Barnett, R. N.; Whetten, R. L.; Landman, U.; Jin, R. Total Structure and Electronic Properties of the Gold Nanocrystal Au36(SR)24. *Angew. Chem. Int. Ed.* **2012**, *51* (52), 13114–13118. https://doi.org/10.1002/anie.201207098.

(76) Zeng, C.; Chen, Y.; Kirschbaum, K.; Lambright, K. J.; Jin, R. Emergence of Hierarchical Structural Complexities in Nanoparticles and Their Assembly. *Science* **2016**, *354* (6319), 1580–1584. https://doi.org/10.1126/science.aak9750.

(77) Negishi, Y.; Nakazaki, T.; Malola, S.; Takano, S.; Niihori, Y.; Kurashige, W.; Yamazoe, S.; Tsukuda, T.; Häkkinen, H. A Critical Size for Emergence of Nonbulk Electronic and

Geometric Structures in Dodecanethiolate-Protected Au Clusters. *J. Am. Chem. Soc.* **2015**, *137* (3), 1206–1212. https://doi.org/10.1021/ja5109968.

(78) Qian, H.; Zhu, M.; Wu, Z.; Jin, R. Quantum Sized Gold Nanoclusters with Atomic Precision. *Acc. Chem. Res.* **2012**, *45* (9), 1470–1479. https://doi.org/10.1021/ar200331z.

(79) Lee, J.; Yang, J.; Kwon, S. G.; Hyeon, T. Nonclassical Nucleation and Growth of Inorganic Nanoparticles. *Nat. Rev. Mater.* **2016**, *1* (8), 16034. https://doi.org/10.1038/natrevmats.2016.34.

(80) Azubel, M.; Koivisto, J.; Malola, S.; Bushnell, D.; Hura, G. L.; Koh, A. L.; Tsunoyama, H.; Tsukuda, T.; Pettersson, M.; Häkkinen, H.; Kornberg, R. D. Electron Microscopy of Gold Nanoparticles at Atomic Resolution. *Science* **2014**, *345* (6199), 909–912. https://doi.org/10.1126/science.1251959.

(81) Choy, A.; Craig, D.; Dance, I.; Scudder, M. $[S_4 M_{10} (SPh)_{16}]^{4-}$ (M□Zn, Cd), a Molecular Fragment of the Sphalerite Ms Lattice: Structural Congruence of Metal Sulphides and Metal Thiolates. *J Chem Soc Chem Commun* **1982**, No. 21, 1246–1247. https://doi.org/10.1039/C39820001246.

(82) Dance, I. G.; Choy, A.; Scudder, M. L. Syntheses, Properties, and Molecular and Crystal Structures of (Me4N)4[E4M10(SPh)16] (E = Sulfur or Selenium; M = Zinc or Cadmium): Molecular Supertetrahedral Fragments of the Cubic Metal Chalcogenide Lattice. *J. Am. Chem. Soc.* **1984**, *106* (21), 6285–6295. https://doi.org/10.1021/ja00333a030.

(83) Dance, I. G. Synthesis, Crystal Structure, and Properties of the Hexa(.Mu.-Benzenethiolato)Tetra(Benzenethiolatocobaltate(II)) Dianion, the Prototype Cobalt(II)-Thiolate Molecular Cluster. *J. Am. Chem. Soc.* **1979**, *101* (21), 6264–6273. https://doi.org/10.1021/ja00515a018.

(84) Hagen, K. S.; Reynolds, J. G.; Holm, R. H. Definition of Reaction Sequences Resulting in Self-Assembly of [Fe4S4(SR)4]2- Clusters from Simple Reactants. *J. Am. Chem. Soc.* **1981**, *103* (14), 4054–4063. https://doi.org/10.1021/ja00404a013.

(85) Bendova, M.; Puchberger, M.; Schubert, U. Characterization of "Cd10S4(SPh)12", the Thermal Decomposition Product of (NMe4)4[Cd10S4(SPh)16]: Synthesis of a Neutral Cd54 Sulfide Cluster and of a Polymeric Chain of Thiolate-Bridged Cd17 Sulfide Clusters. *Eur. J. Inorg. Chem.* **2010**, *2010* (21), 3299–3306. https://doi.org/10.1002/ejic.201000454.

(86) Herron, N.; Calabrese, J. C.; Farneth, W. E.; Wang, Y. Crystal Structure and Optical Properties of Cd32S14(SC6H5)36. DMF4, a Cluster with a 15 Angstrom CdS Core. *Science* **1993**, *259* (5100), 1426–1428. https://doi.org/10.1126/science.259.5100.1426.

(87) Cumberland, S. L.; Hanif, K. M.; Javier, A.; Khitrov, G. A.; Strouse, G. F.; Woessner, S. M.; Yun, C. S. Inorganic Clusters as Single-Source Precursors for Preparation of CdSe, ZnSe, and CdSe/ZnS Nanomaterials. *Chem. Mater.* **2002**, *14* (4), 1576–1584. https://doi.org/10.1021/cm010709k.

(88) Busatto, S.; de Mello Donega, C. Magic-Size Semiconductor Nanostructures: Where Does the Magic Come From? *ACS Mater. Au* **2022**, *2* (3), 237–249. https://doi.org/10.1021/acsmaterialsau.1c00075.

(89) Wang, Y.; Zhou, Y.; Zhang, Y.; Buhro, W. E. Magic-Size II–VI Nanoclusters as Synthons for Flat Colloidal Nanocrystals. *Inorg. Chem.* **2015**, *54* (3), 1165–1177. https://doi.org/10.1021/ic502637q.

(90) Baek, W.; Bootharaju, M. S.; Lorenz, S.; Lee, S.; Stolte, S.; Fainblat, R.; Bacher, G.; Hyeon, T. Nanoconfinement-Controlled Synthesis of Highly Active, Multinary

Nanoplatelet Catalysts from Lamellar Magic-Sized Nanocluster Templates. *Adv. Funct. Mater.* **2021**, *31* (49), 2107447. https://doi.org/10.1002/adfm.202107447.

(91) Wang, F.; Wang, Y.; Liu, Y.-H.; Morrison, P. J.; Loomis, R. A.; Buhro, W. E. Two-Dimensional Semiconductor Nanocrystals: Properties, Templated Formation, and Magic-Size Nanocluster Intermediates. *Acc. Chem. Res.* **2015**, *48* (1), 13–21. https://doi.org/10.1021/ar500286j.

(92) Liu, Y.-H.; Wang, F.; Wang, Y.; Gibbons, P. C.; Buhro, W. E. Lamellar Assembly of Cadmium Selenide Nanoclusters into Quantum Belts. *J Am Chem Soc* **2011**, *133* (42), 17005–17013. https://doi.org/10.1021/ja206776g.

(93) Friedfeld, M. R.; Stein, J. L.; Ritchhart, A.; Cossairt, B. M. Conversion Reactions of Atomically Precise Semiconductor Clusters. *Acc. Chem. Res.* **2018**, *51* (11), 2803–2810. https://doi.org/10.1021/acs.accounts.8b00365.

(94) Friedfeld, M. R.; Stein, J. L.; Cossairt, B. M. Main-Group-Semiconductor Cluster Molecules as Synthetic Intermediates to Nanostructures. *Inorg. Chem.* **2017**, *56* (15), 8689–8697. https://doi.org/10.1021/acs.inorgchem.7b00291.

(95) Beecher, A. N.; Yang, X.; Palmer, J. H.; LaGrassa, A. L.; Juhas, P.; Billinge, S. J. L.; Owen, J. S. Atomic Structures and Gram Scale Synthesis of Three Tetrahedral Quantum Dots. *J. Am. Chem. Soc.* **2014**, *136* (30), 10645–10653. https://doi.org/10.1021/ja503590h.

(96) Pun, A. B.; Mazzotti, S.; Mule, A. S.; Norris, D. J. Understanding Discrete Growth in Semiconductor Nanocrystals: Nanoplatelets and Magic-Sized Clusters. *Acc. Chem. Res.* **2021**, *54* (7), 1545–1554. https://doi.org/10.1021/acs.accounts.0c00859.

(97) Mule, A. S.; Mazzotti, S.; Rossinelli, A. A.; Aellen, M.; Prins, P. T.; van der Bok, J. C.; Solari, S. F.; Glauser, Y. M.; Kumar, P. V.; Riedinger, A.; Norris, D. J. Unraveling the

Growth Mechanism of Magic-Sized Semiconductor Nanocrystals. *J. Am. Chem. Soc.* **2021**, *143* (4), 2037–2048. https://doi.org/10.1021/jacs.0c12185.

(98) Mazzotti, S.; Mule, A. S.; Pun, A. B.; Held, J. T.; Norris, D. J. Growth Synchronization and Size Control in Magic-Sized Semiconductor Nanocrystals. *ACS Nano* **2023**, *17* (14), 13232–13240. https://doi.org/10.1021/acsnano.3c00585.

(99) Ripberger, H. H.; Schnitzenbaumer, K. J.; Nguyen, L. K.; Ladd, D. M.; Levine, K. R.; Dayton, D. G.; Toney, M. F.; Cossairt, B. M. Navigating the Potential Energy Surface of CdSe Magic-Sized Clusters: Synthesis and Interconversion of Atomically Precise Nanocrystal Polymorphs. *J. Am. Chem. Soc.* **2023**, *145* (50), 27480–27492. https://doi.org/10.1021/jacs.3c08897.

(100) Peng, H. R.; Gong, M. M.; Chen, Y. Z.; Liu, F. Thermal Stability of Nanocrystalline Materials: Thermodynamics and Kinetics. *Int. Mater. Rev.* **2017**, *62* (6), 303–333. https://doi.org/10.1080/09506608.2016.1257536.

(101) Suryanarayana, C. Nanocrystalline Materials. *Int. Mater. Rev.* **1995**, *40* (2), 41–64. https://doi.org/10.1179/imr.1995.40.2.41.

(102) Murty, B. S.; Datta, M. K.; Pabi, S. K. Structure and Thermal Stability of Nanocrystalline Materials. *Sadhana* **2003**, *28* (1), 23–45. https://doi.org/10.1007/BF02717124.

(103) Mule, A. S.; Mazzotti, S.; Rossinelli, A. A.; Aellen, M.; Prins, P. T.; van der Bok, J. C.; Solari, S. F.; Glauser, Y. M.; Kumar, P. V.; Riedinger, A.; Norris, D. J. Unraveling the Growth Mechanism of Magic-Sized Semiconductor Nanocrystals. *J. Am. Chem. Soc.* **2021**, *143* (4), 2037–2048. https://doi.org/10.1021/jacs.0c12185.

(104) Cho, K.-S.; Talapin, D. V.; Gaschler, W.; Murray, C. B. Designing PbSe Nanowires and Nanorings through Oriented Attachment of Nanoparticles. *J. Am. Chem. Soc.* **2005**, *127* (19), 7140–7147. https://doi.org/10.1021/ja050107s.

(105) Schliehe, C.; Juarez, B. H.; Pelletier, M.; Jander, S.; Greshnykh, D.; Nagel, M.; Meyer, A.; Foerster, S.; Kornowski, A.; Klinke, C.; Weller, H. Ultrathin PbS Sheets by Two-Dimensional Oriented Attachment. *Science* **2010**, *329* (5991), 550–553. https://doi.org/10.1126/science.1188035.

(106) Zhu, T.; Zhang, B.; Zhang, J.; Lu, J.; Fan, H.; Rowell, N.; Ripmeester, J. A.; Han, S.; Yu, K. Two-Step Nucleation of CdS Magic-Size Nanocluster MSC–311. *Chem. Mater.* **2017**, *29* (13), 5727–5735. https://doi.org/10.1021/acs.chemmater.7b02014.

(107) Harris, D. K.; Bawendi, M. G. Improved Precursor Chemistry for the Synthesis of III–V Quantum Dots. *J. Am. Chem. Soc.* **2012**, *134* (50), 20211–20213. https://doi.org/10.1021/ja309863n.

(108) Franke, D.; Harris, D. K.; Xie, L.; Jensen, K. F.; Bawendi, M. G. The Unexpected Influence of Precursor Conversion Rate in the Synthesis of III–V Quantum Dots. *Angew. Chem. Int. Ed.* **2015**, *54* (48), 14299–14303. https://doi.org/10.1002/anie.201505972.

(109) Li, Y.; Zhang, M.; He, L.; Rowell, N.; Kreouzis, T.; Zhang, C.; Wang, S.; Luan, C.; Chen, X.; Zhang, S.; Yu, K. Manipulating Reaction Intermediates to Aqueous-Phase ZnSe Magic-Size Clusters and Quantum Dots at Room Temperature. *Angew. Chem. Int. Ed.* **2022**, *61* (39), e202209615. https://doi.org/10.1002/anie.202209615.

(110) Wang, W.; Shen, Q.; Yang, Y.; Sapelkin, A.; Wang, S.; Luan, C.; Yu, K. Formation of Prenucleation Clusters and Transformation to ZnSe Quantum Dots and Magic-Size Clusters. **2025**. https://doi.org/10.1039/D5NR00265F.

(111) Cunningham, P. D.; Coropceanu, I.; Mulloy, K.; Cho, W.; Talapin, D. V. Quantized Reaction Pathways for Solution Synthesis of Colloidal ZnSe Nanostructures: A Connection between Clusters, Nanowires, and Two-Dimensional Nanoplatelets. *ACS Nano* **2020**, *14* (4), 3847–3857. https://doi.org/10.1021/acsnano.9b09051.

(112) Kim, H.; Kittilstved, K. R. Coalescence-Induced Growth Doping in a II–VI Magic Size Cluster. *J. Phys. Chem. A* **2025**, *129* (36), 8324–8336. https://doi.org/10.1021/acs.jpca.5c04100.

(113) Harrell, S. M.; McBride, J. R.; Rosenthal, S. J. Synthesis of Ultrasmall and Magic-Sized CdSe Nanocrystals. *Chem. Mater.* **2013**, *25* (8), 1199–1210. https://doi.org/10.1021/cm303318f.

(114) Lee, K.; Deng, G.; Bootharaju, M. S.; Hyeon, T. Synthesis, Assembly, and Applications of Magic-Sized Semiconductor (CdSe)13 Cluster. *Acc. Chem. Res.* **2023**, *56* (9), 1118–1127. https://doi.org/10.1021/acs.accounts.3c00061.

(115) Krivoglaz, M. A.; Azároff, L. V. *Theory of X-Ray and Thermal Neutron Scattering by Real Crystals*. *Phys. Today* **1970**, *23* (3), 78–79. https://doi.org/10.1063/1.3022033.

(116) Holton, J. M.; Frankel, K. A. The Minimum Crystal Size Needed for a Complete Diffraction Data Set. *Acta Crystallogr. D Biol. Crystallogr.* **2010**, *66* (4), 393–408. https://doi.org/10.1107/S0907444910007262.

(117) Gary, D. C.; Flowers, S. E.; Kaminsky, W.; Petrone, A.; Li, X.; Cossairt, B. M. Single-Crystal and Electronic Structure of a 1.3 Nm Indium Phosphide Nanocluster. *J. Am. Chem. Soc.* **2016**, *138* (5), 1510–1513. https://doi.org/10.1021/jacs.5b13214.

(118) Bootharaju, M. S.; Baek, W.; Deng, G.; Singh, K.; Voznyy, O.; Zheng, N.; Hyeon, T. Structure of a Subnanometer-Sized Semiconductor Cd14Se13 Cluster. *Chem* **2022**, *8* (11), 2978–2989. https://doi.org/10.1016/j.chempr.2022.06.025.

(119) Orfield, N. J.; McBride, J. R.; Wang, F.; Buck, M. R.; Keene, J. D.; Reid, K. R.; Htoon, H.; Hollingsworth, J. A.; Rosenthal, S. J. Quantum Yield Heterogeneity among Single Nonblinking Quantum Dots Revealed by Atomic Structure-Quantum Optics Correlation. *ACS Nano* **2016**, *10* (2), 1960–1968. https://doi.org/10.1021/acsnano.5b05876.

(120) Ollivier, H.; Maillette de Buy Wenniger, I.; Thomas, S.; Wein, S. C.; Harouri, A.; Coppola, G.; Hilaire, P.; Millet, C.; Lemaître, A.; Sagnes, I.; Krebs, O.; Lanco, L.; Loredo, J. C.; Antón, C.; Somaschi, N.; Senellart, P. Reproducibility of High-Performance Quantum Dot Single-Photon Sources. *ACS Photonics* **2020**, *7* (4), 1050–1059. https://doi.org/10.1021/acsphotonics.9b01805.

(121) Chen, O.; Zhao, J.; Chauhan, V. P.; Cui, J.; Wong, C.; Harris, D. K.; Wei, H.; Han, H.-S.; Fukumura, D.; Jain, R. K.; Bawendi, M. G. Compact High-Quality CdSe–CdS Core–Shell Nanocrystals with Narrow Emission Linewidths and Suppressed Blinking. *Nat. Mater.* **2013**, *12* (5), 445–451. https://doi.org/10.1038/nmat3539.

(122) Tighineanu, P.; Dreeßen, C. L.; Flindt, C.; Lodahl, P.; Sørensen, A. S. Phonon Decoherence of Quantum Dots in Photonic Structures: Broadening of the Zero-Phonon Line and the Role of Dimensionality. *Phys. Rev. Lett.* **2018**, *120* (25), 257401. https://doi.org/10.1103/PhysRevLett.120.257401.

(123) Schimpf, C.; Reindl, M.; Klenovský, P.; Fromherz, T.; Silva, S. F. C. D.; Hofer, J.; Schneider, C.; Höfling, S.; Trotta, R.; Rastelli, A. Resolving the Temporal Evolution of

Line Broadening in Single Quantum Emitters. *Opt. Express* **2019**, *27* (24), 35290–35307. https://doi.org/10.1364/OE.27.035290.

(124) Proppe, A. H.; Berkinsky, D. B.; Zhu, H.; Šverko, T.; Kaplan, A. E. K.; Horowitz, J. R.; Kim, T.; Chung, H.; Jun, S.; Bawendi, M. G. Highly Stable and Pure Single-Photon Emission with 250 Ps Optical Coherence Times in InP Colloidal Quantum Dots. *Nat. Nanotechnol.* **2023**, *18* (9), 993–999. https://doi.org/10.1038/s41565-023-01432-0.

(125) Rosson, T. E.; Claiborne, S. M.; McBride, J. R.; Stratton, B. S.; Rosenthal, S. J. Bright White Light Emission from Ultrasmall Cadmium Selenide Nanocrystals. *J. Am. Chem. Soc.* **2012**, *134* (19), 8006–8009. https://doi.org/10.1021/ja300132p.

(126) Jasrasaria, D.; Weinberg, D.; Philbin, J. P.; Rabani, E. Simulations of Nonradiative Processes in Semiconductor Nanocrystals. *J. Chem. Phys.* **2022**, *157* (2), 020901. https://doi.org/10.1063/5.0095897.

(127) Vasilevskiy, M. I.; Anda, E. V.; Makler, S. S. Electron-Phonon Interaction Effects in Semiconductor Quantum Dots: A Nonperturabative Approach. *Phys. Rev. B* **2004**, *70* (3), 035318. https://doi.org/10.1103/PhysRevB.70.035318.

(128) Jasrasaria, D.; Rabani, E. Interplay of Surface and Interior Modes in Exciton–Phonon Coupling at the Nanoscale. *Nano Lett.* **2021**, *21* (20), 8741–8748. https://doi.org/10.1021/acs.nanolett.1c02953.

(129) Beecher, A. N.; Dziatko, R. A.; Steigerwald, M. L.; Owen, J. S.; Crowther, A. C. Transition from Molecular Vibrations to Phonons in Atomically Precise Cadmium Selenide Quantum Dots. *J. Am. Chem. Soc.* **2016**, *138* (51), 16754–16763. https://doi.org/10.1021/jacs.6b10705.

(130) Xie, Y.; Yu, S.; Zhang, L.; Du, N.; Yang, M. Radiative and Non-Radiative Decay Kinetics of (CdSe)N (N = 3 and 4) Clusters. *J. Chem. Phys.* **2019**, *151* (6), 064306. https://doi.org/10.1063/1.5109068.

(131) Kelley, A. M. Exciton-Optical Phonon Coupling in II-VI Semiconductor Nanocrystals. *J. Chem. Phys.* **2019**, *151* (14), 140901. https://doi.org/10.1063/1.5125147.

(132) Lin, C.; Gong, K.; Kelley, D. F.; Kelley, A. M. Size-Dependent Exciton–Phonon Coupling in CdSe Nanocrystals through Resonance Raman Excitation Profile Analysis. *J. Phys. Chem. C* **2015**, *119* (13), 7491–7498. https://doi.org/10.1021/acs.jpcc.5b00774.

(133) Tan, J.; Li, D.; Zhu, J.; Han, N.; Gong, Y.; Zhang, Y. Self-Trapped Excitons in Soft Semiconductors. **2022**. https://doi.org/10.1039/D2NR03935D.

(134) Williamson, C. B.; Nevers, D. R.; Nelson, A.; Hadar, I.; Banin, U.; Hanrath, T.; Robinson, R. D. Chemically Reversible Isomerization of Inorganic Clusters. *Science* **2019**, *363* (6428), 731–735. https://doi.org/10.1126/science.aau9464.

(135) Giansante, C.; Infante, I. Surface Traps in Colloidal Quantum Dots: A Combined Experimental and Theoretical Perspective. *J. Phys. Chem. Lett.* **2017**, *8* (20), 5209–5215. https://doi.org/10.1021/acs.jpclett.7b02193.

(136) Wei, H. H.-Y.; Evans, C. M.; Swartz, B. D.; Neukirch, A. J.; Young, J.; Prezhdo, O. V.; Krauss, T. D. Colloidal Semiconductor Quantum Dots with Tunable Surface Composition. *Nano Lett.* **2012**, *12* (9), 4465–4471. https://doi.org/10.1021/nl3012962.

(137) Kumar, S.; Cocchi, C.; Steenbock, T. Surface Defects and Symmetry Breaking Impact on the Photoluminescence of InP Quantum Dots. *Nano Lett.* **2025**, *25* (26), 10588–10593. https://doi.org/10.1021/acs.nanolett.5c02317.

(138) Lin, C.; Gong, K.; Kelley, D. F.; Kelley, A. M. Electron–Phonon Coupling in CdSe/CdS Core/Shell Quantum Dots. *ACS Nano* **2015**, *9* (8), 8131–8141. https://doi.org/10.1021/acsnano.5b02230.

(139) Kennehan, E. R.; Munson, K. T.; Grieco, C.; Doucette, G. S.; Marshall, A. R.; Beard, M. C.; Asbury, J. B. Exciton–Phonon Coupling and Carrier Relaxation in PbS Quantum Dots: The Case of Carboxylate Ligands. *J. Phys. Chem. C* **2021**, *125* (41), 22622–22629. https://doi.org/10.1021/acs.jpcc.1c05803.

(140) Lifshitz, E. Evidence in Support of Exciton to Ligand Vibrational Coupling in Colloidal Quantum Dots. *J. Phys. Chem. Lett.* **2015**, *6* (21), 4336–4347. https://doi.org/10.1021/acs.jpclett.5b01567.

(141) Won, Y.-H.; Cho, O.; Kim, T.; Chung, D.-Y.; Kim, T.; Chung, H.; Jang, H.; Lee, J.; Kim, D.; Jang, E. Highly Efficient and Stable InP/ZnSe/ZnS Quantum Dot Light-Emitting Diodes. *Nature* **2019**, *575* (7784), 634–638. https://doi.org/10.1038/s41586-019-1771-5.

(142) Dabbousi, B. O.; Rodriguez-Viejo, J.; Mikulec, F. V.; Heine, J. R.; Mattoussi, H.; Ober, R.; Jensen, K. F.; Bawendi, M. G. (CdSe)ZnS Core−Shell Quantum Dots: Synthesis and Characterization of a Size Series of Highly Luminescent Nanocrystallites. *J. Phys. Chem. B* **1997**, *101* (46), 9463–9475. https://doi.org/10.1021/jp971091y.

(143) Hines, M. A.; Guyot-Sionnest, P. Synthesis and Characterization of Strongly Luminescing ZnS-Capped CdSe Nanocrystals. *J. Phys. Chem.* **1996**, *100* (2), 468–471. https://doi.org/10.1021/jp9530562.

(144) Jin, S.; Harris, R. D.; Lau, B.; Aruda, K. O.; Amin, V. A.; Weiss, E. A. Enhanced Rate of Radiative Decay in CdSe Quantum Dots upon Adsorption of an Exciton-Delocalizing Ligand. *Nano Lett.* **2014**, *14* (9), 5323–5328. https://doi.org/10.1021/nl5023699.

(145) Schiettecatte, P.; Giordano, L.; Cruyssaert, B.; Bonifas, G.; De Vlamynck, N.; Van Avermaet, H.; Zhao, Q.; Vantomme, A.; Nayral, C.; Delpech, F.; Hens, Z. Enhanced Surface Passivation of InP/ZnSe Quantum Dots by Zinc Acetate Exposure. *Chem. Mater.* **2024**, *36* (12), 5996–6005. https://doi.org/10.1021/acs.chemmater.4c00492.

(146) Cho, E.; Lee, J.; Kim, T.-G.; Son, W.-J.; Jang, I.; Kim, D. S. Theoretical Investigation of Organic Ligands on the Surface Structure of InP Quantum Dots: Implications for Display Materials with Enhanced Surface Stability. *ACS Appl. Nano Mater.* **2023**, *6* (23), 21548–21555. https://doi.org/10.1021/acsanm.3c03356.

(147) Balan, A. D.; Olshansky, J. H.; Horowitz, Y.; Han, H.-L.; O'Brien, E. A.; Tang, L.; Somorjai, G. A.; Alivisatos, A. P. Unsaturated Ligands Seed an Order to Disorder Transition in Mixed Ligand Shells of CdSe/CdS Quantum Dots. *ACS Nano* **2019**, *13* (12), 13784–13796. https://doi.org/10.1021/acsnano.9b03054.

(148) Stein, J. L.; Mader, E. A.; Cossairt, B. M. Luminescent InP Quantum Dots with Tunable Emission by Post-Synthetic Modification with Lewis Acids. *J. Phys. Chem. Lett.* **2016**, *7* (7), 1315–1320. https://doi.org/10.1021/acs.jpclett.6b00177.

(149) Shim, D.; Lee, J.; Kang, J. Multiscale Isomerization of Magic-Sized Inorganic Clusters Chemically Driven by Atomic-Bond Exchanges. *Chem Mater* **2022**, *34* (21), 9527–9535. https://doi.org/10.1021/acs.chemmater.2c02018.

(150) Shim, D.; Kang, J. Enhanced Reactivity of Magic-Sized Inorganic Clusters by Engineering the Surface Ligand Networks. *Chem Mater* **2023**, *35* (2), 700–708. https://doi.org/10.1021/acs.chemmater.2c03394.

(151) He, L.; Luan, C.; Rowell, N.; Zhang, M.; Chen, X.; Yu, K. Transformations Among Colloidal Semiconductor Magic-Size Clusters. *Acc. Chem. Res.* **2021**, *54* (4), 776–786. https://doi.org/10.1021/acs.accounts.0c00702.

(152) Ripberger, H. H.; Sandeno, S. F.; Eagle, F. W.; Nguyen, H. A.; Cossairt, B. M. Structure and Reactivity of II–VI and III–V Magic-Sized Clusters: Understanding and Expanding the Scope of Accessible Form and Function. *Acc. Mater. Res.* **2024**, *5* (6), 726–738. https://doi.org/10.1021/accountsmr.4c00064.

Chapter 2. TUNING THE REACTIVITY OF INDIUM PHOSPHIDE CLUSTERS USING LIGAND STERIC PROFILE

2.1 INTRODUCTION

The development of colloidal quantum dot (QD) syntheses has allowed for control over their attractive optoelectronic properties. Many of these synthetic methods begin empirically with a limited understanding of the underlying nucleation and growth mechanisms. InP QDs have emerged as a commercially relevant, emissive material and as such their formation pathways have been the subject of deep investigation. Today, the state-of-the-art method for producing InP QDs involves the combination of indium carboxylates ($In(O_2CR)_3$) and tris(trimethylsilyl)phosphine ($P(SiMe_3)_3$) to generate the core QDs before shelling with ZnSe and ZnS.[1,2] While InP QD synthesis has been optimized to the point of commercial production, one of the characteristics that still hinders progress on color purity is the monodispersity of the InP cores. It is now well-known that InP QDs do not proceed through a classical nucleation pathway and instead stray from the La Mer model of nucleation in two ways. The first involves the intermediacy of atomically-precise

magic-sized clusters (MSCs) that have been observed to nucleate, and then fully or partially redissolve before QD growth proceeds.[3–5] This effectively decouples precursor reactivity from the QD growth rate as any changes in reactivity only affect MSC formation. The second important consideration is the observation of a prolonged nucleation period that substantially overlaps with the growth period.[6] Burst nucleation can no longer be invoked to control monodisperity and instead InP systems are thought to undergo size-focusing growth over long time windows. This limits the accessible size window for which narrow polydispersity can be achieved. With an understanding of these limitations, the isolation and study of InP MSCs have provided new avenues towards controlling the synthesis of InP QD cores with the potential to advance mechanisms for control over QD growth.

The most well-studied InP MSC is $In_{37}P_{20}(O_2CR)_{51}$ which is amenable to gram-scale synthesis and was structurally characterized by single crystal X-ray diffraction (SCXRD) in the case of R = $CH_2C_6H_5$.[7] While other InP MSCs have been optically identified, the lack of structural knowledge has hindered further investigation.[3,8–10] The isolation of $In_{37}P_{20}(O_2CR)_{51}$ led to the development of multiple synthetic routes towards obtaining InP QDs with unprecedented characteristics. Hot-injection of the cluster at temperatures greater than 200 °C results in conversion as a single-source precursor producing zinc-blende InP quantum dots.[3,4] This method was expanded to incorporate Zn^{2+} and Ga^{3+} dopants within the cluster that then allowed for a similar single-source precursor approach towards doped InP QDs.[11] Both of these conversions were suggested to proceed through cluster dissolution into reactive monomer species, followed by renucleation and subsequent growth of InP QDs. The temperature was found to dictate the quality of the resulting QDs with lower temperatures (<200°C) causing cluster degradation with little to no successive, productive crystal growth. However, at higher reaction temperatures (>200°C) the

mechanism of dissolution and subsequent growth resulted in high-quality InP QDs.[3,4] Beyond hot-injection, the InP cluster has also been documented to template the formation of quasi-wurtzite phase InP QDs. This work represented the first time the phase of the cluster had been documented on that size scale and sets the stage for potential anisotropic InP nanostructure growth.[12]

While these studies are examples of the successful application of InP clusters as isolable single source precursors and seeds for the growth of larger nanostructures, an unresolved question is how it functions in-situ to produce high quality InP QD cores. Multiple studies have documented its presence when synthesizing cores using indium carboxylate and $P(SiMe_3)_3$,[3,5] and it is thought that dissolution follows in-situ cluster formation, but the extent of dissolution and pathways of regrowth to form high-quality QDs still largely remain a mystery. Optical characterization of potential intermediates has been documented but the lack of extensive structural analysis hinders deterministic knowledge of MSC growth and dissolution routes.[13]

Computational studies of $In_{37}P_{20}$ have revealed important features that relate its reactivity and structure. Kulik and coworkers developed multiple connections between the carboxylate ligands and the surface reactivity of the InP cluster, leading to the conclusion that the bridging syn-anti binding mode is the most reactive when subjected to P^{3-}.[14] Furthermore, the distance between surface In atoms is the primary descriptor that dictates their susceptibility to displacement by P^{3-}, where longer separations correlate with higher carboxylate dissociation energies. Beyond the study of surface attack driven conversion, *ab initio* molecular dynamics calculations have been performed to better understand the initial mechanistic steps in the thermally induced conversion of clusters.[15] Kang and coworkers identified three indium carboxylate units on the cluster surface whose release is what initiates cluster dissolution. Once again, the carboxylate network on the cluster surface is cited as the culprit for directing structural rearrangement.

The structural and reactivity comparisons made by Kang and coworkers also highlight the developing juxtaposition of InP and Cd-chalcogenide clusters. Claims of structural homologies have been made by Robinson and coworkers regarding an α-CdS cluster and the $In_{37}P_{20}$ cluster.[16] This spurred two computational studies by Kang and coworkers investigating the possibility of analogous structures in the two materials systems and why InP does not show the bond exchange isomerization under the same conditions that are observed for CdS.[15,17] Despite these computational efforts, there has yet to be definitive experimental validation of this structural relationship between III-V and II-VI clusters.

In this work, we sought to experimentally investigate cluster surface chemistry as a powerful leverage point for controlling conversion reactivity and mechanisms. By synthesizing the $In_{37}P_{20}(O_2CR)_{51}$ cluster with a family of substituted phenylacetate ligands possessing differing steric profiles, it is shown that the surface reactivity can be both hindered and accelerated when compared to the parent phenylacetate-ligated cluster. The steric profile is also found to modulate cluster thermolysis reactions by extending nucleation periods at high temperatures (>200 °C) leading to nanocrystal sizes that are ligand dependent. Furthermore, these studies allowed for the single-crystal X-ray diffraction study of a smaller member in the InP cluster family that is not only implicated as an intermediate in the reported $P(SiMe_3)_3$-induced conversions, but also serves as the first structurally-defined InP homolog to a $Cd_{14}Se_{13}$ cluster recently reported by Hyeon and coworkers.[18]

2.2 Structural Characterization

All $In_{37}P_{20}(O_2CR)_{51}$ clusters were synthesized by combining indium carboxylate, carboxylic acid, and $P(SiMe_3)_3$ according to the previously reported procedure by replacing

phenylacetic acid with the same stoichiometry of the substituted phenylacetic acid (**Figure 2.2.2A**).[7] The local environments of the phosphorus atoms within the clusters were probed with ^{31}P NMR spectroscopy (**Figure 2.2.2B**). The placement of a *tert*-butyl group in the para-position leads to a similar overall pattern as observed in the case of the parent phenylacetate cluster, but coalescence of signals at -190 ppm and a loss in symmetry evidenced by signal splitting at -235 ppm and -238 ppm is observed in addition to a significant shift in the most downfield resonance at -176 ppm. As steric bulk is increased near the core through meta-substitution, we see significant broadening that makes the assignment of specific P-signals difficult. However, the general shape and range of the ^{31}P resonances remain the same, suggesting that the overall connectivity is preserved. An assignment of the ^{31}P resonances in the parent phenylacetate-ligated cluster spectrum to individual atoms in the crystal structure is provided in the supplemental information (**Figure 2.2.1**).

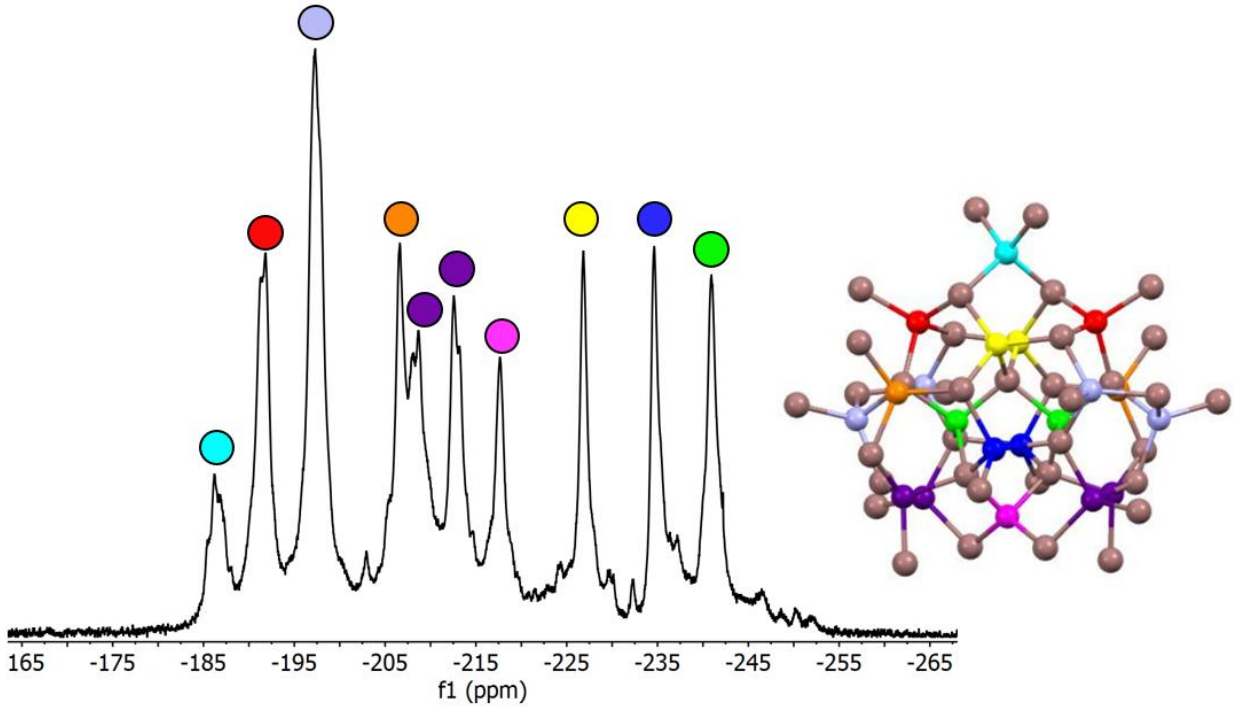

Figure 2.2.1. Assignment of ^{31}P-NMR resonances to P atoms in the phenylacetate-ligated $In_{37}P_{20}$ crystal structure.

These changes in chemical shift and peak coalescence or splitting indicate internal perturbations in the structure of the $In_{37}P_{20}$ cluster that are induced by steric pressure in the ligand sphere. In general, the two factors governing a ^{31}P resonance are the electron density around the P nucleus and the shielding cones of unsaturated systems.[19] We do not anticipate shielding cones from π-networks making any substantial contribution to the overall resonances given their physical distance from the core P atoms. The aromatic rings in the carboxylate ligands are decoupled from the carboxylate through a CH_2 and all substituents are aliphatic so there should be no significant electronegativity differences between ligands. The frequency of the carbonyl stretch of the carboxylic acid can be used to assess the electron density at the head group, which should correlate with binding affinity. We measured the frequency of this stretch as 1693 cm^{-1}, 1692 cm^{-1}, 1695 cm^{-1}, and 1710 cm^{-1} for phenylacetic acid, *m*-tolylacetic acid (3-Me), 3,5-dimethylphenylacetic acid (3,5-Me_2), and 4-*tert*-butylphenylacetic acid (tBu), respectively. While the FTIR of the bound carboxylate is discussed further below, we see no meaningful differences in the frequencies associated with the asymmetric stretch of the bound carboxylate. Finally, while we believe the FTIR signature is a better representation of electronegativity differences at the binding site, the reported pKa values of similar acids can provide further context. While there is no reported pKa value for 3-Me or 3,5-Me_2, it has been reported as 4.31 for phenylacetic acid, 4.37 for *p*-tolylacetic acid, and both 4.42 and 4.37 for tBu.[20–22]

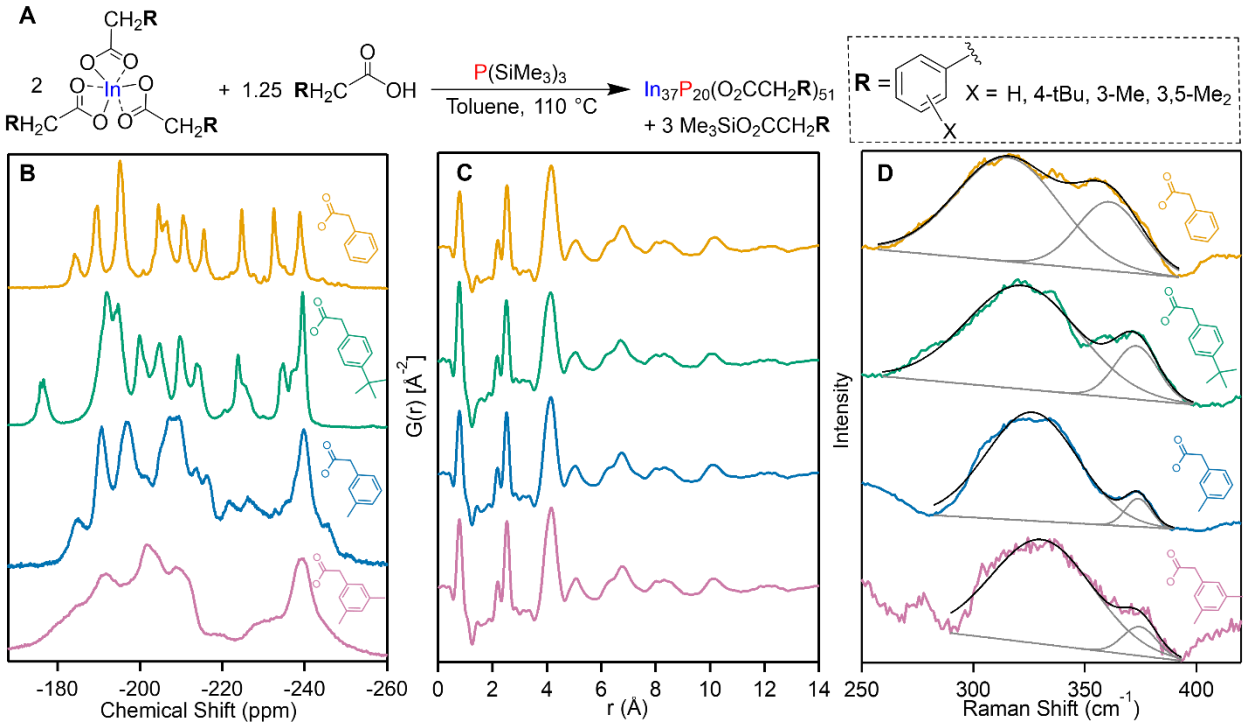

Figure 2.2.2. A) Synthetic scheme for $In_{37}P_{20}(O_2CCH_2R)$ clusters with substituted phenylacetate ligands. B) ^{31}P NMR spectra of phenylacetate-ligated $In_{37}P_{20}$ clusters with H, 4-tBu, 3-Me, and 3,5-Me_2 substituents. C) Pair distribution function for all clusters from X-ray total scattering (offset for clarity). D) Raman spectra for all clusters using λ_{exc} = 785 nm. The 290-390 cm^{-1} region was fit to two Gaussian distributions representing two collections of vibrations involving In and P atoms.

This leaves the In-P-In bond angles as the primary culprit for controlling and changing the observed resonances. Bond angles impact the resonance by modulating the s-orbital character, with increased s-orbital character resulting in better shielding of the observed nucleus and an upfield shift. For molecular phosphines, a wider Tolman cone angle correlates with more s-orbital character and further upfield resonances.[23] We conclude that the structural modifications induced by the ligand sphere manifest as In-P-In bond angle changes. For instance, the downfield shift

observed for the apical phosphorus resonance in the 4-*tert*-butylphenylacetate-ligated cluster is consistent with more acute bonding at that phosphorus atom induced by ligand steric pressure that causes the angles to surface indium atoms to become more acute. Finally, as surface-directed ligand pressure increases, we observe considerable increases in the linewidths of the ^{31}P resonances. This trend can be interpreted through the lens of the characterization of proteins using NMR spectroscopy where structural rigidity is correlated with linewidth.[24] We believe that the meta-substituents greatly enhance the rigidity of the surface indium carboxylate through hindered ligand rotation, thereby interfering with the nuclear relaxation rate which is known to vary inversely with molecular mobility. These broadened resonances then suggest that the meta-substituents hinder the structural flexibility leading to a more rigid cluster structure.

The structure of the $In_{37}P_{20}$ cores were investigated with X-ray pair distribution function (PDF) analysis generated from total scattering data using PDFgetX3 (**Figure 2.2.2C**).[25] The reduced PDF, G(r), reveals only minor structural differences between ligand substituents, shown with residual calculations in **Figure 2.2.3**, confirming that the core $In_{37}P_{20}$ average stoichiometry and connectivity is left unchanged. Nearest neighbor peaks in G(r) represent In-O, and In-P pair distances centered at 2.19 Å and 2.53 Å, respectively (**Figure 2.2.4**).[7]

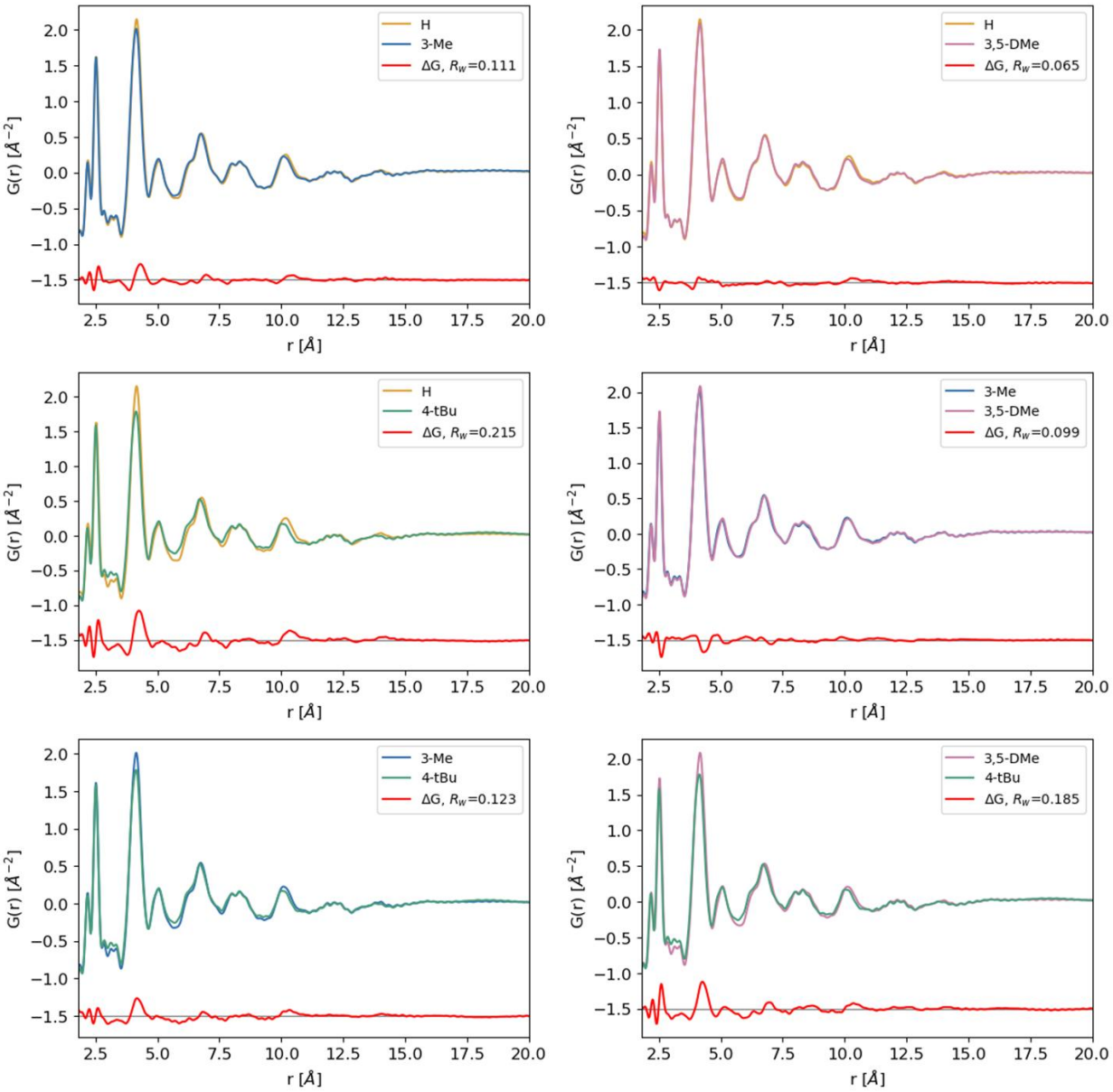

Figure 2.2.3. Overlaid G(r) and resulting ΔG comparing each ligand type.

Relative to peak positions of the phenylacetate-ligated cluster, G(r) peaks of each other ligand substituent shift to shorter interatomic distances in real space. We quantitatively estimate the magnitude of the cluster core's response to the pressure of the ligand sphere by comparing first-neighbor peak centers of each ligand substituent to those of the H-substituent phenylacetate

cluster.[26] General variance in the In-P bond lengths range from approximately 0% for 3,5-Me_2 to 0.7% for 4-tBu. In-O bonds at the surface are also subject to deviation as dictated by ligand steric pressure (**Table 2.2.1**).

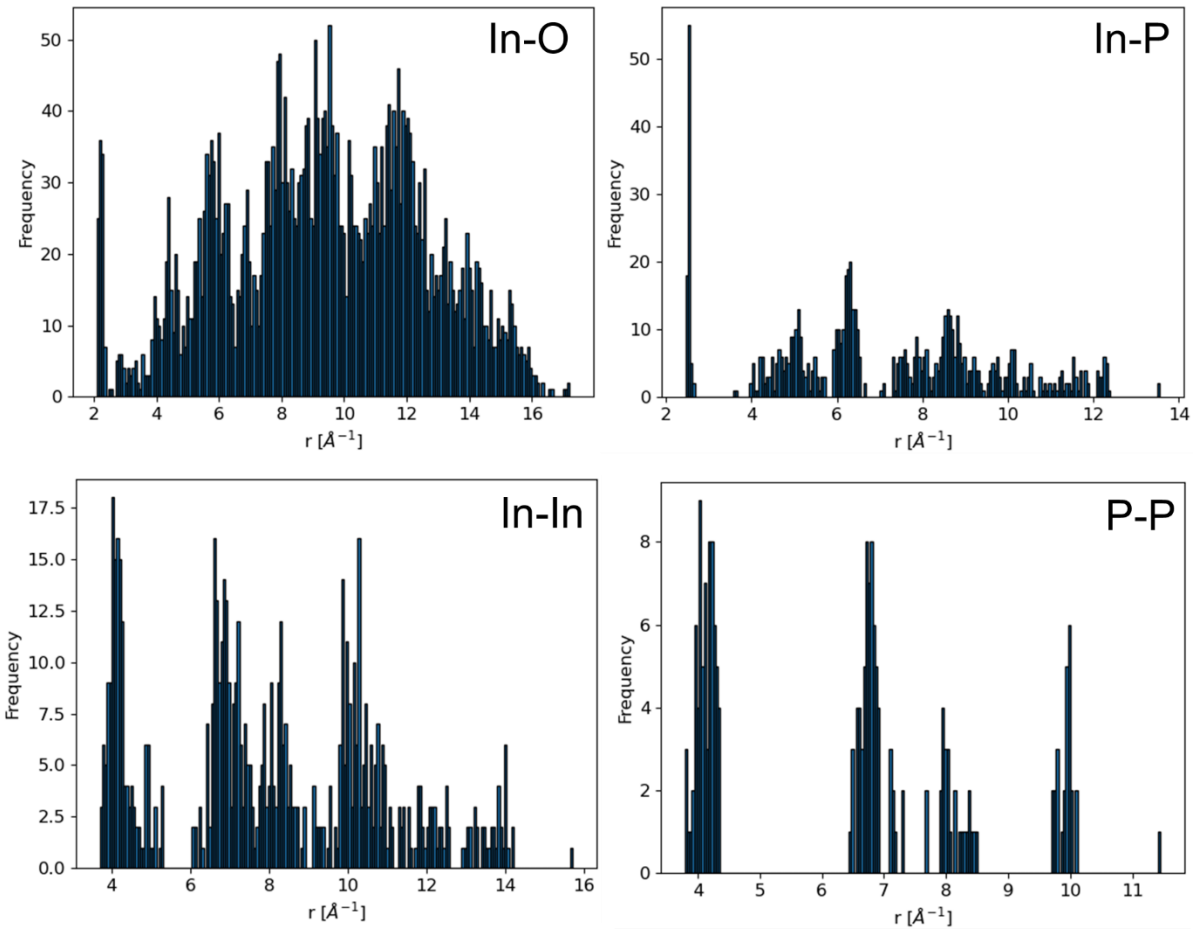

Figure 2.2.4. Distribution of interatomic correlation distances by atom as measured from the $In_{37}P_{20}(O_2CCH_2Ph)_{51}$ crystal structure.

Substituent	r_{In-P}	Δr_{InP}	In-P Diff. %	r_{In-O}	Δr_{InO}	In-O Diff. %
H	2.533	0	0	2.192	0	0
3-Me	2.522	-0.011	-0.43	2.181	-0.011	-0.50
3,5-DMe	2.532	-0.001	-0.03	2.191	-0.002	-0.07
4-tBu	2.515	-0.018	-0.69	2.173	-0.019	-0.88

Table 2.2.1. Calculated first neighbor G(r) peak positions and bond length deviations for InP clusters.

The second-nearest neighbor peak at 4.15 Å and the peaks at higher r predominantly represent In-In distances due to stronger X-ray scattering by this atom pair. The 4.15 Å peak shows a similar shift to lower distances from the phenylacetate to the 3-Me and tBu (**Figure 2.2.5A**). The 4.15 Å peak of 3,5-Me_2 does not show a clear shift relative to the phenylacetate but does change shape and broaden toward shorter distances as seen in the ΔG of the two PDFs (**Figure 2.2.5B**). Shape changes and static broadening may suggest that a subpopulation of In-In pair distances varies, perhaps due to anisotropic strain imparted on the low-symmetry cluster structure. A final demonstrative peak is positioned at 10.18 Å representing longer interatomic distances, generally between core and surface In atoms. This broad peak again shifts to increasingly shorter distances from phenylacetate to 3,5-Me_2, 3-Me and finally tBu. These changes at longer correlation distances (≥10 Å) approach the particle diameter and suggest variability in surface In geometries (**Figure 2.2.5C, D, E**). For clarity, the peak at 0.9 Å that is present for all the clusters is an unphysical artifact arising from the Fourier transformation applied through PDFgetX3.

A

G_{exp1} \ G_{exp2}	Ligand	H	3-Me	3,5-Me_2	4-tBu
	H	0	0.111	0.065	0.215
	3-Me	0.116	0	0.099	0.123
	3,5-Me_2	0.065	0.095	0	0.185
	4-tBu	0.242	0.133	0.208	0

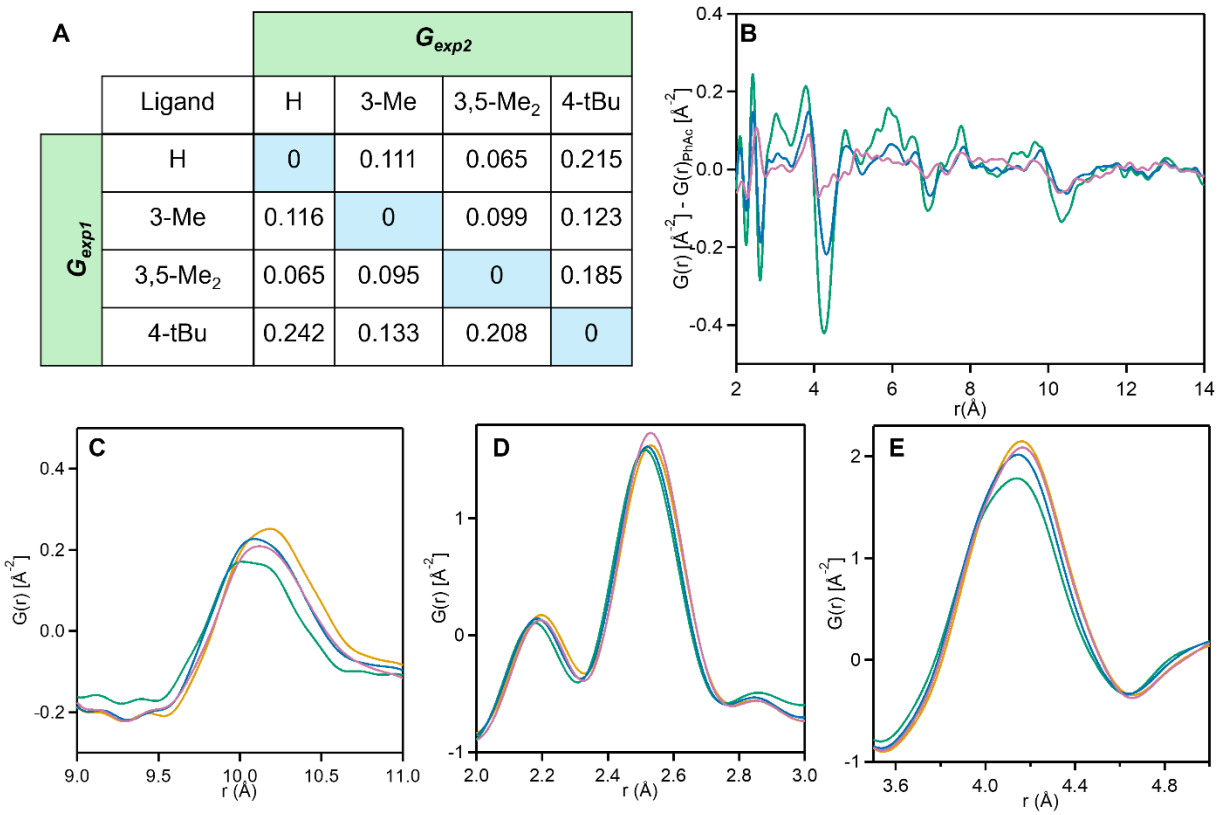

Figure 2.2.5. A) Agreement factors R_w comparing each ligand substituent. B) ΔG(r) plots comparing the signal from all ligated clusters to the phenylacetate ligated cluster. tBu (green), 3-Me (blue), 3,5-Me_2 (pink). C,D,E) Important features in the PDF with more detail. Core-to-surface correlation (C), In-In and P-P correlations (D), In-P and In-O correlations (E). Phenylacetate (yellow), 3-Me (blue), tBu (green), and 3,5-Me_2 (pink).

The isolated and purified clusters were further characterized by Raman spectroscopy to investigate ensemble behavior arising from ligand-induced structural perturbations. Previous characterization of myristate-ligated InP clusters has approximated the Raman signal from the clusters as two separate vibrational modes centered at 320 cm^{-1} and 365 cm^{-1}.[12] These vibrations are distinct from the transverse and longitudinal optical modes (TO and LO) at 306 and 348 cm^{-1} respectively, reported for bulk zinc-blende InP.[27] On the nanoscale, both the TO and LO phonons

are distinct and represented in InP QDs with the relative TO peak intensity increasing with smaller QDs and the LO-TO peak separation increasing with increasing QD size.[28,29] These trends do not extend into the InP cluster regime as the quasi-wurtzite phase is cluster specific and has an entirely different atomic arrangement compared to the common zinc-blende QDs. This leads to a distinct spectrum of InP-based Raman-active vibrations in clusters that can be approximately fit by two gaussians representing a low frequency region and a high frequency region (**Figure 2.2.2D**). A similar spectral shape has been reported in the Raman spectra of atomically precise CdSe clusters, with the lower and higher frequencies attributed to surface and interior modes, respectively.[30] For the phenylacetate-ligated cluster, these regions are centered at 315 cm^{-1} and 361 cm^{-1}. With steric pressure increasing from 4-tBu to 3-Me and 3,5-Me_2, the low frequency center shifts to 322 cm^{-1}, 326 cm^{-1}, and 330 cm^{-1} respectively (**Table 2.2.2**). A similar but reduced trend is seen with the high frequency region shifting to 373 cm^{-1}, 374 cm^{-1}, and 375 cm^{-1}. Comparing the relative integration of low and high frequency regions between clusters shows 70% and 30% contributions from each respective region for phenylacetate, 80% and 20% for 4-tBu, and finally 90% and 10% for both 3-Me and 3,5-Me_2. This behavior is reminiscent of reported phonon mode modulation in graphene through pressure-induced strain.[31–33] In these reports, the induced strain results in a shift to lower frequency of Raman-active phonon modes. Similar softening behavior of vibrations that contribute to the high frequency region would produce a shift in the center of both high and low frequency regions to higher wavenumber. This would then be coupled with an increase in the overall signal at low frequency that is compensated for by a decrease in the signal at higher frequency. These phenomena are indeed experimentally observed as described above. This corroborates the trend observed in the ^{31}P NMR linewidths and suggests the rigidity of the meta-

substituted ligand sphere is imparting strain on the interior of the cluster, causing modulation of the Raman-active InP-based vibrational modes.

		H	3-tBu	3-Me	3,5-Me$_2$
Low Frequency Region	A1	3.159e+5± 6.55e+3	5.070e+5 ±6.33e+3	9.496e+5 ±1.11e+4	3.491e+5 ±7.98e+3
	w1	314.45 ±0.544	322.05 ±0.343	314.45 ±0.544	314.45 ±0.544
	fwhm1	54.647 ±0.544	58.905 ±0.906	47.799 ±0.691	52.912 ±1.54
High Frequency Region	A2	1.300e+5± 6.16e+3	1.010e+5 ±4.66e+3	6.925e+4 ±6.23e+3	3.294e+4 ±5.37e+3
	w2	361.00 ±0.487	373.04 ±0.359	373.95 ±0.526	374.63 ±0.937
	fwhm2	33.848 ±0.957	22.689 ±0.898	13.441 ±1.28	17.941 ±2.45
	m	-10.54	-15.86	-21.7	-15.96
	y0	7200	12500	18500	63800

$$f(w) = A_1 \frac{2}{fwhm_1}\sqrt{\frac{ln2}{\pi}}\exp\left(\frac{-4\,ln2\,(w-w_1)^2}{{fwhm_1}^2}\right) + A_2 \frac{2}{fwhm_2}\sqrt{\frac{ln2}{\pi}}exp\left(\frac{-4\,ln2\,(w-w_2)^2}{{fwhm_2}^2}\right) + m * w + y0$$

Table 2.2.2. Low and high frequency vibrational mode fits for all Raman spectra of $In_{37}P_{20}$ clusters along with the fit function for two gaussian distributions.

While the vibrations of the cluster core can be observed in the Raman spectra, the ligands can be more readily analyzed with FTIR spectroscopy. The ability to approximate carboxylate binding mode populations on the InP cluster surface has been developed previously.[34,35] The single crystal structural characterization and subsequent IR studies of molecular zinc carboxylate complexes has allowed for the determination of binding mode-dependent symmetric and

asymmetric carboxylate stretch frequencies as $\Delta\omega = \omega_{asymmetric} - \omega_{symmetric}$.[36] These can be applied to indium carboxylates on the surface of the cluster to follow the general order: $\Delta\omega_{chelating} < \Delta\omega_{bridging\ (syn\text{-}anti)} < \Delta\omega_{bridging\ (syn\text{-}syn)} < \Delta\omega_{monodentate}$. Using this approach to approximate the relative binding mode populations on the InP cluster surface showed that, in solution, the bridging (syn-anti) is the predominant configuration followed by bridging (syn-syn) and finally, chelating and monodentate.[34] This approach was implemented in this study to observe approximate distributions of particular binding motifs and any correlations with the ligand steric profile in solution (**Figure 2.2.6**). We acknowledge the inherent uncertainty in a 4 gaussian fit to a narrow wavenumber range with little peak definition so the distribution of binding modes can only roughly be quantified. However, the general peak shape and structure in the asymmetric carboxylate stretching region appears remarkably similar across the ligand suite. The bridging modes make up the majority of passivation with some minor contributions from the chelating and monodentate binding modes which corroborates previous binding mode assignments though FTIR analysis of the oleate-capped $In_{37}P_{20}$ cluster.[34] Overall, the solution-phase FTIR serves to indicate that the binding mode distributions are remarkably similar, if not identical, across different degrees of ligand steric profiles. This indicates that the structural differences observed across the ligand suite is not in response to a binding mode reorganization and instead is a direct result of steric pressure in the ligand sphere.

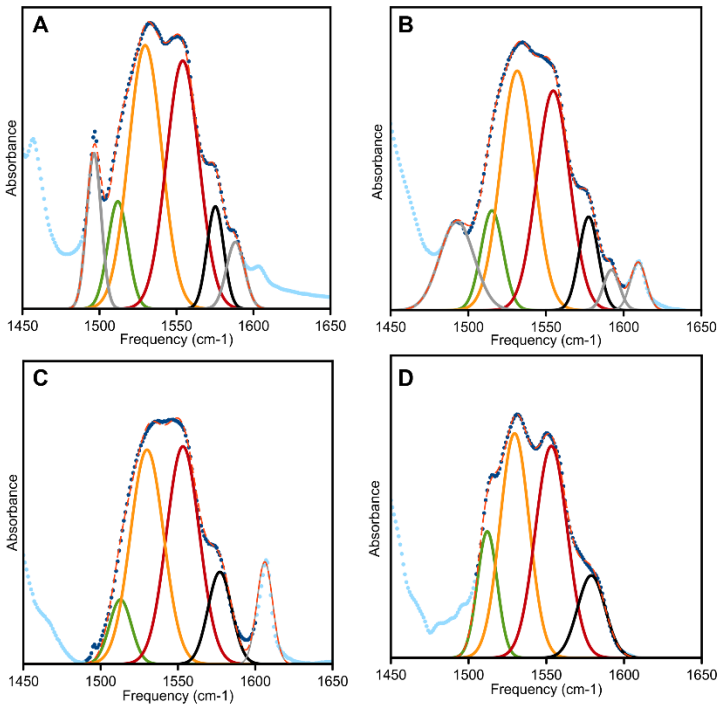

E

		Ligand Identity			
		PhAc	3-Me	3,5-Me_2	tBu
Chelating	a	0.1674	0.1645	0.0639	0.146
	x_0	1512	1515	1513	1512
	dx	7.690	8.37	8.37	7.52
Bridging (syn-anti)	a	0.4108	0.395	0.212	0.260
	x_0	1530	1531	1530	1530
	dx	12.650	12.657	12.67	11.05
Bridging (syn-syn)	a	0.3867	0.3621	0.2155	0.245
	x_0	1554	1555	1553	1553
	dx	12.500	12.497	12.50	12.08
Monodentate	a	0.1596	0.1541	0.091	0.095
	x_0	1575	1577	1577	1579
	dx	6.36	7.35	9.04	10.45

Figure 2.2.6. Solution-state FTIR of $In_{37}P_{20}$ cluster with phenylacetate (A), m-tolylacetate (B), 3,5-dimethylphenylacetate (C), and 4-tert-butylphenylacetate (D) in tetrachloroethylene with each binding mode, chelating (green), bridging syn-anti (orange), bridging syn-syn (red), and monodentate (black), fit to a gaussian curve. All residual ligand signals from ring modes are shown in grey traces. E) Table summarizing best fit parameters for each binding mode (a = curve amplitude, x_0 = peak position, dx = half width at half max).

2.3 Conversion and Reactivity

After characterizing the ligand-induced structural perturbations, we turned to testing the reactivity of all clusters. It is worth noting at this point that we also explored the synthesis of *o*-tolylacetate and 3,5-di-*tert*-butylphenylacetate-ligated clusters providing early clues about reactivity differences as a function of ligand steric profile. With *o*-tolylacetate, the cluster transiently formed and could be characterized by UV-Vis spectroscopy, but over the course of a few hours

destabilized into smaller, insoluble species (**Figure 2.3.1A**). Using 3,5-di-*tert*-butylphenylacetic acid in the reaction may have formed the cluster, but it was quickly bypassed before spectroscopic characterization could confirm the presence of cluster, forming larger quantum dots and thus again, the cluster was not stable enough to be isolated (**Figure 2.3.1B**). Previous studies of MSC surface chemistry have shown control over both structural and electronic characteristics but few extend these studies to investigate implications for stability and reactivity.[16,37–42]

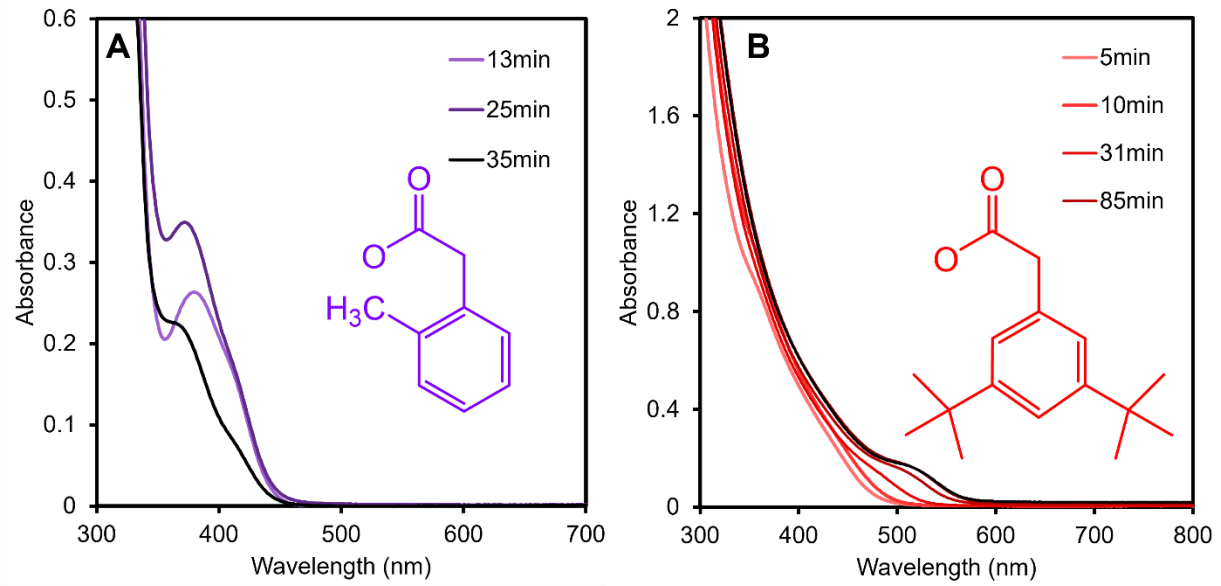

Figure 2.3.1. A) Absorbance progression of a typical $In_{37}P_{20}$ cluster synthesis using *o*-tolylacetic acid (purple). B) Absorbance progression of a typical $In_{37}P_{20}$ cluster synthesis using 3,5-di-tert-butylphenylacetic acid (red).

Previously our group has shown that further addition of $P(SiMe_3)_3$ induces partial fragmentation of the InP cluster followed by templated growth of quasi-wurtzite QDs.[12] This is initiated by $P(SiMe_3)_3$ reacting with indium-bound carboxylates to liberate silyl ester with formation of a new In-P bond. Through the sequential removal of carboxylates, the cluster eventually fragments, forming a higher symmetry core intermediate along with the liberation of

InP monomer species. The monomers then add back to the core, forming larger nanocrystals. Computational work from Kulik and coworkers has suggested that a vital parameter governing the ease of carboxylate displacement by P^{3-} is the In-In separation distance.[14] Furthermore, as a part of the same study, a computational comparison between phenylacetate and acetate-ligated InP clusters suggested that π-π stacking between adjacent phenyl groups can create negative deviations in In-O dissociation energies. While the ring is decoupled from the carboxylate by the methylene group, there is still an electronic effect from the ring that can be augmented by π-π stacking. We hypothesized that the variations in steric profile and substitution of the phenyl ring could modulate surface indium separation and direct surface π-π stacking thereby tuning the susceptibility of carboxylate displacement by $P(SiMe_3)_3$.

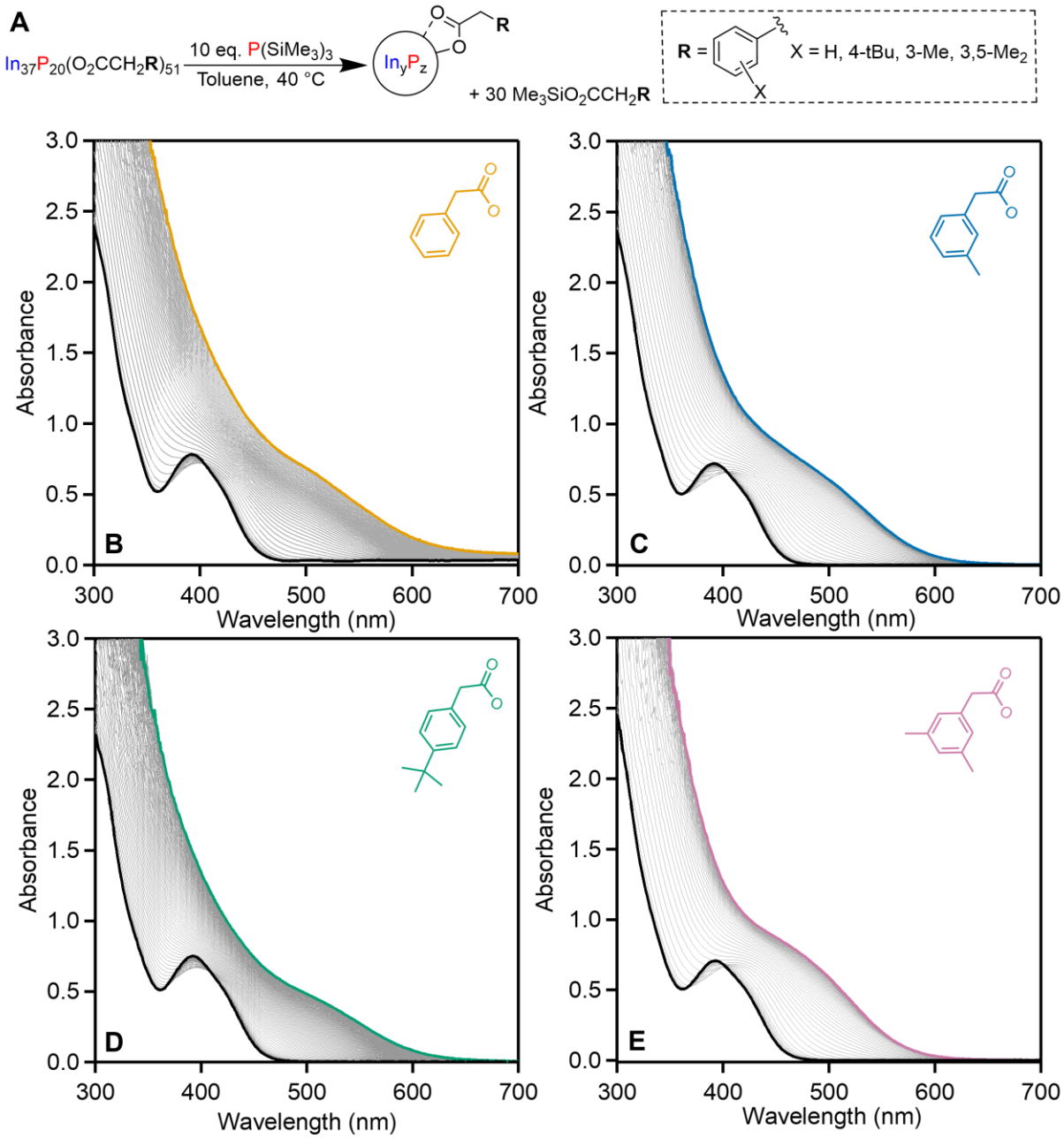

Figure 2.3.2. A) Reaction scheme for the formation of quasi-wurtzite phase InP nanocrystals through the addition of $P(SiMe_3)_3$ to $In_{37}P_{20}(O_2CCH_2R)_{51}$ clusters. B, C, D, E) Example 10 eq. $P(SiMe_3)_3$ conversion reactions at 40 °C for all $In_{37}P_{20}$ clusters with the first trace shown in black and last trace shown in color. H (PhOAc) (A, yellow, 0-118 min), 3-Me (B, blue, 0-118 min), tBu (C, green, 0-238 min), 3,5-Me_2 (D, pink, 0-108 min).

To observe the kinetics of conversion, a solution containing 10 equivalents of $P(SiMe_3)_3$ was injected into a solution of cluster in toluene at 40 °C (**Figure 2.3.2A**). The rate of growth was then measured by tracking absorbance changes over time for cluster conversion to QD as shown in **Figure 2.3.2B, C, D, E**. The change in absorbance over time monitored at multiple wavelengths is shown in **Figure 2.3.3A, B, C**. The inflection point for growth was found through the maximum of the first derivative and the progression of the reaction up to this point we refer to as the induction period (**Figure 2.3.4**). The reaction beyond the inflection point is referred to as the growth region. Fitting the growth region of these traces to a single exponential allows for an approximate k_{obs} value to be extracted from each conversion reaction. With fitting across multiple wavelengths, the induction period from shortest to longest follows the order 3,5-Me_2 (31.3 ± 1.2 min), H (41.0 ± 2.0 min), 3-Me (42.7 ± 1.2 min), and 4-tBu (89.0 ± 20.6 min). Across the same wavelengths, the growth rate from fastest to slowest is 3,5-Me_2 (0.048 ± 0.001), 3-Me (0.035 ± 0.002), H (0.028 ± 0.004) and 4-tBu (0.014 ± 0.002) (**Figure 2.3.3D, E, F**). The phenylacetate-ligated cluster conversion products aggregate and begin to lose colloidal stability at the 82nd minute due to less favorable solvent-ligand interactions leading to a linear region in the absorbance vs time plots. This region was excluded when calculating k_{obs} from the growth region for the phenylacetate cluster.

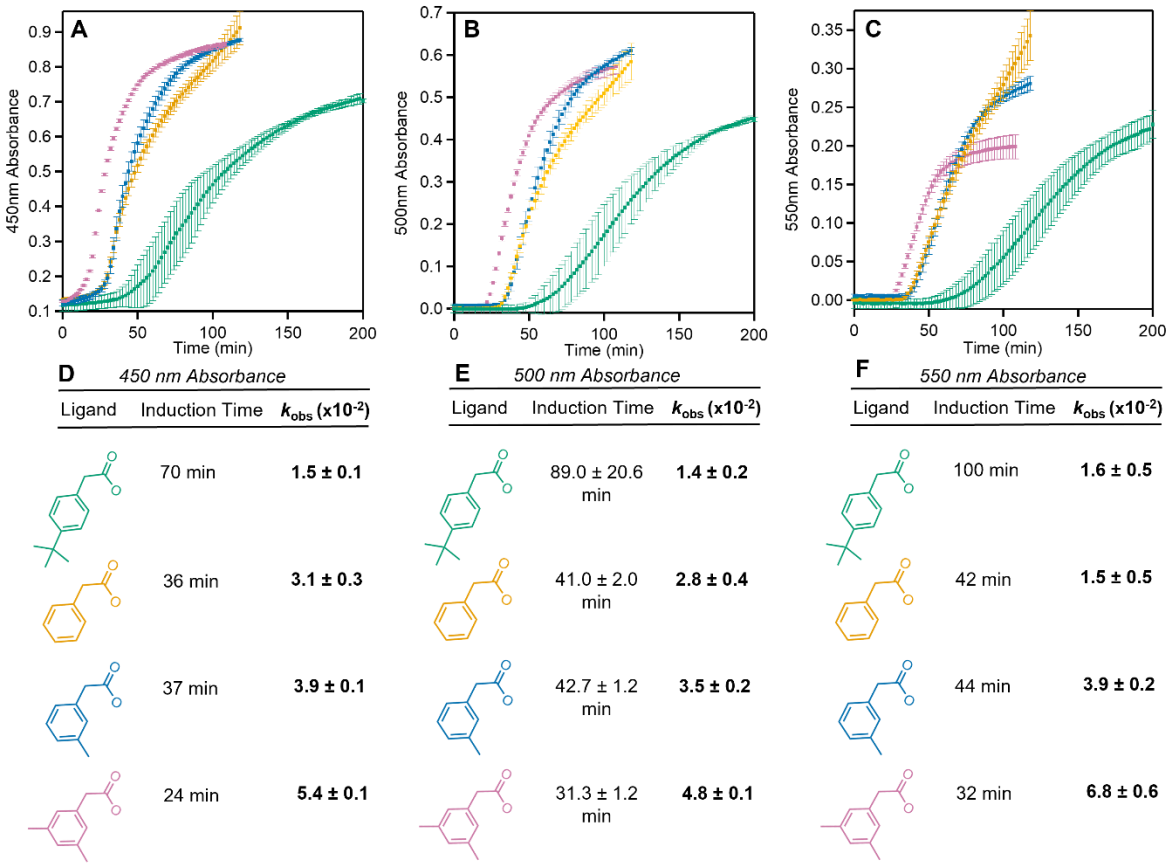

Figure 2.3.3. A,B,C) Absorbance over time monitored at three different wavelengths: 450 nm (A), 500 nm (B), and 550 nm (C) after the addition of 10 eq. of $P(SiMe_3)_3$ to each cluster. H (yellow), 3-Me (blue), 3,5-Me_2 (pink), 4-tBu (green). D,E,F) Induction time and k_{obs} as measured from the trajectory at each monitored wavelength of absorbance.

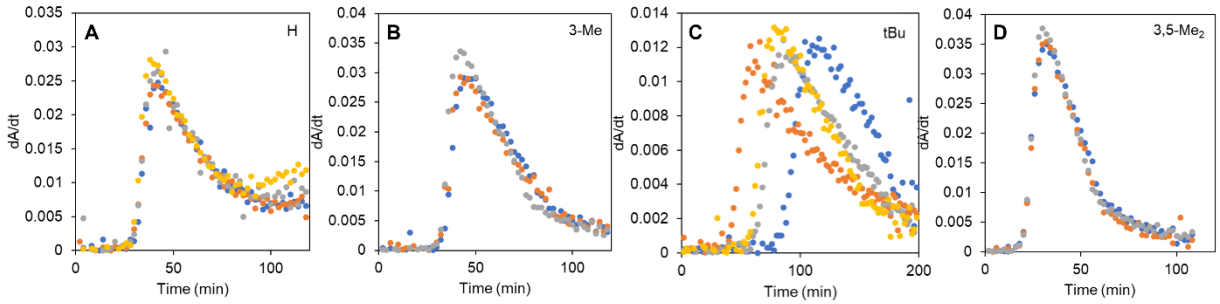

Figure 2.3.4. A, B, C, D) First derivative graphs of all 10 eq $P(TMS)_3$ cluster conversions for induction period time determination. H (A), 3-Me (B), 4-tBu (C), 3,5-Me_2 (D).

These trends clearly show a substantial increase in reactivity from the 4-tBu substituted cluster to the 3,5-Me_2 cluster. A direct comparison of the phenylacetate and 3-Me ligands shows that while the induction periods are nearly identical, the growth rates are different. We rationalize this by introducing two processes that make up the induction period, diffusion and displacement. The addition of a methyl group hinders the diffusion of $P(SiMe_3)_3$ through the ligand shell to the cluster surface but simultaneously augments the reactivity of In-O bonds. The balance between hindering diffusion and augmenting reactivity is what determines the induction period. This is why the phenylacetate-ligated cluster may begin liberating monomer at a similar time as the 3-Me cluster but overall has a slower growth rate. In the case of 3,5-Me_2, the drastic increase in the reactivity of the surface more than compensates for any restricted diffusion giving it the shortest induction period and highest reactivity. For 4-tBu, the steric profile leads to a vastly slower diffusion rate which dominates the slower reactivity of the cluster. We have also confirmed by *in-situ* solution-phase FTIR that the bridging syn-anti carboxylate binding sites are indeed the most reactive on the cluster being selectively displaced by $P(SiMe_3)_3$ to induce fragmentation (**Figure 2.3.5**).

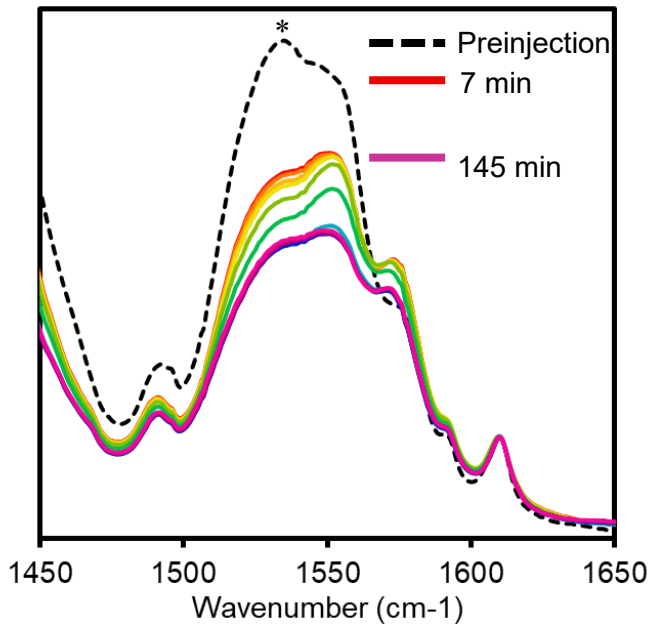

Figure 2.3.5. Solution-phase FTIR in the asymmetric carboxylate stretching region of the 3-Me $In_{37}P_{20}$ cluster reacting with 5 eq. of $P(TMS)_3$. The bridging syn-anti carboxylate stretch (*), centered at 1531 cm^{-1}, decreases in intensity the most compared to the other three binding modes.

This pattern of reactivity shows that both the placement and extent of substitution are important factors in engineering the surface for controlling reactivity. With meta-substituents directed at one another, steric crowding on the surface could force bridging carboxylates to shorten In-In separation distances thereby increasing the reactivity (**Figure 2.3.6A**) as predicted by the computational model from Kulik and coworkers.[14] The bulky para-substituent greatly hinders reactivity by slowing phosphine ingress (**Figure 2.3.6B**). Furthermore, the meta-substituted phenyl groups could also selectively organize with π-π stacking to minimize the steric pressure from adjacent substituents (**Figure 2.3.6C**). These three processes likely occur constructively with all ligands to determine the overall reactivity.

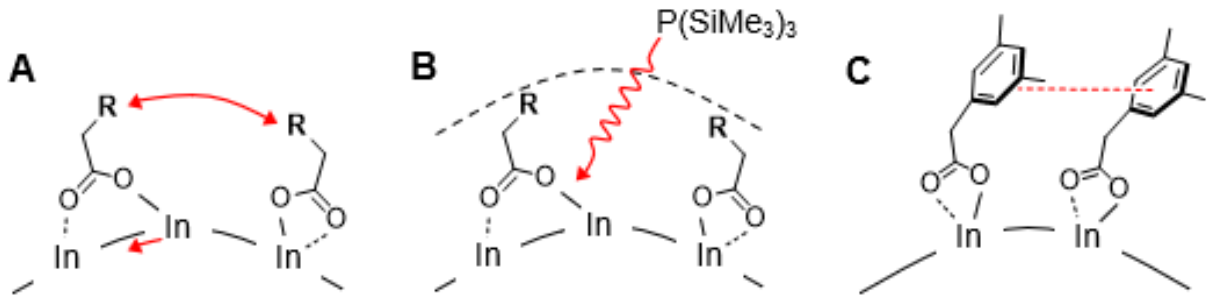

Figure 2.3.6. A) Steric pressure between ligands shortens indium separation distances to enhance reactivity. B) A larger steric profile discourages $P(SiMe_3)_3$ diffusion to the cluster surface to decrease reactivity C) Meta-substituents direct the alignment of π-π stacking to favor ligand dissociation and enhance reactivity.

The reactivity differences between these clusters were also tested by thermolysis. As mentioned above, it is thought that thermally induced cluster to QD conversion proceeds through complete dissolution and renucleation to generate narrow size distributions.[3,43–45] For these hot-injection studies using the clusters as single-source precursors, it is unlikely that the thermally induced conversions will have much dependence on surface reactivity. The dissolution of cluster into monomers at these temperatures likely does not involve any appreciable amount of surface attack as there is no secondary species to induce destabilization. Instead, the cluster dissolution is likely brought on by thermally instigated bond vibrations exceeding a critical distortion similar to the Lindemann melting criterion.[46] The conversion of clusters with different ligands to QDs through this mechanism is then dependent upon two factors: the thermal stability of the cluster and the steric profile of the ligand. Monitoring the change in absorbance at 500 nm throughout the hot-injection reactions suggests that the conversion of these clusters at 240 °C is very much ligand dependent. With less bulky substituents, H and 3-Me, there is a significant degree of QD growth shown by an increase in absorbance at 500 nm within 3 minutes of the injection. This is

accompanied by a disappearance of the cluster absorbance feature at 386 nm. Comparatively, the bulkier substituents, 3,5-Me_2 and tBu, show less development at 500 nm during early time points suggesting a slower growth rate (**Figure 2.3.7, Figure 2.3.8A**). There is not a profound difference in the persistence of the 386 nm feature with bulkier substituents suggesting that the monomer production rate across different ligands is similar. These conversions result in the final absorbance

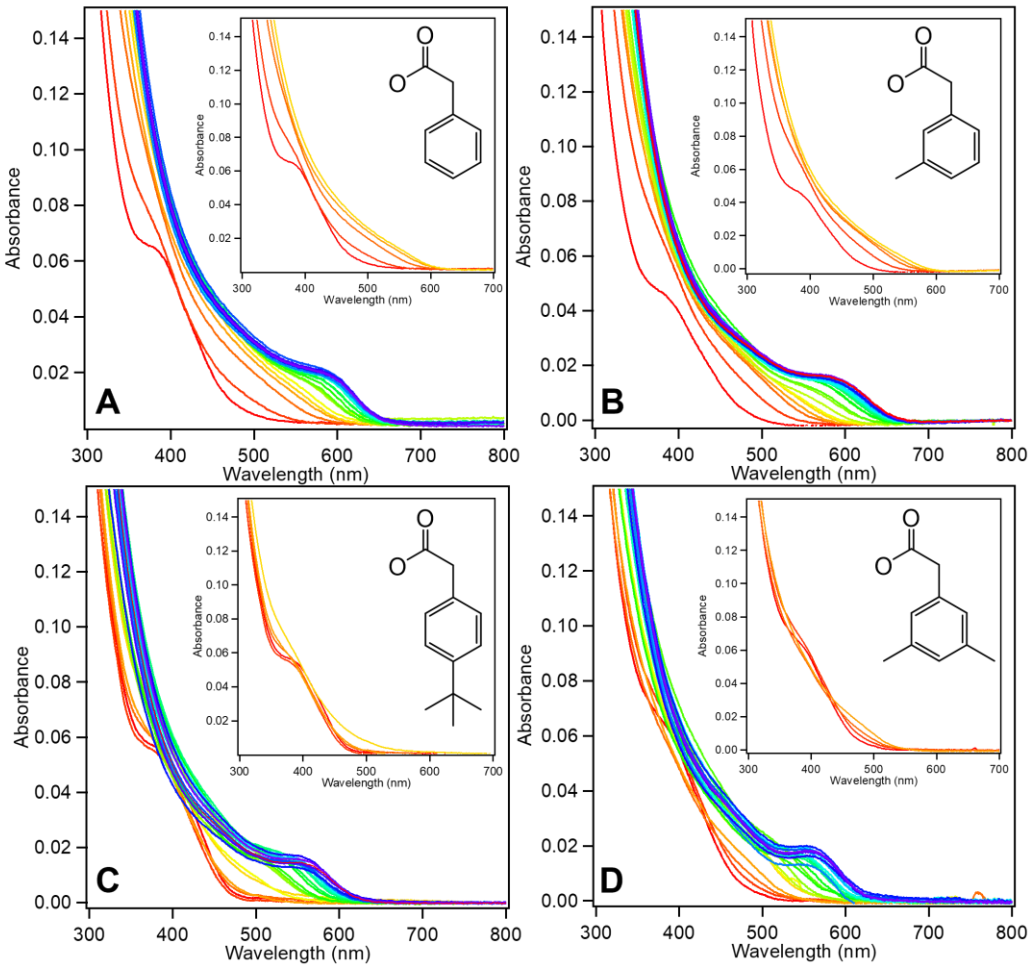

Figure 2.3.7. Full UV-Vis aliquot tracking for 240 °C thermolysis conversions of all $In_{37}P_{20}$ clusters from 0 min (red) to 126 min (purple). H (A), 3-Me (B), 4-tBu (C), 3,5-Me_2 (D). Each inset shows the early timepoint aliquots taken at 30s, 1min, 1min30s, 2min30s, and 3min from red to yellow at 240 °C.

traces shown in **Figure 2.3.8B**, which demonstrate that the initial rate of growth can be correlated with the λ_{max} of the final QDs where bulkier substituents converge on a shorter λ_{max} (**Figure 2.3.8B, C**). The size trend observed in the absorbance was corroborated by TEM (**Figure 2.3.8D, E**).

Many previous studies have documented the correlation between carboxylate chain length and resulting size of nanocrystals where longer chain lengths direct smaller QDs.[47–49] These results were rationalized by asserting that longer fatty acid chains slow nucleation and growth. This interpretation was reinvestigated by De Nolf et al. to determine that the size control with long chain fatty acids can also be explained by chain length changing the rate of diffusion as well as the solubility of the monomer species during nucleation and growth.[50] Using these studies as a framework to interpret our observed size-dependence provides three possible rationales. Firstly, aligned with the study of De Nolf et al., there could be a difference in the diffusion and solubility of monomer species generated from cluster dissolution. Secondly, the substitution of the phenyl group could direct different degrees of surface tension from interligand interactions. Finally, the ligand steric profile may impact the kinetic balance between nucleation and growth leading to different sizes. Now addressing these interpretations, we do not anticipate any impactful differences in diffusion and solubility between ligands. Especially using 3-Me and 3,5-Me_2 as points of comparison, the addition of a single methyl group should not substantially affect diffusion or solubility to generate a size difference of this magnitude. While we do anticipate differences in surface tension across the suite of ligands, the observable size trend does not follow what we would predict to be the trend in surface tension. Seeing that meta-substituents greatly enhance the rigidity of the cluster surface, it would follow that the 3-Me and 3,5-Me_2 ligated QDs should have the highest surface tension which should correlate with larger nanocrystals but this trend is not experimentally observed. Finally, the relationship can be rationalized by the steric profile altering

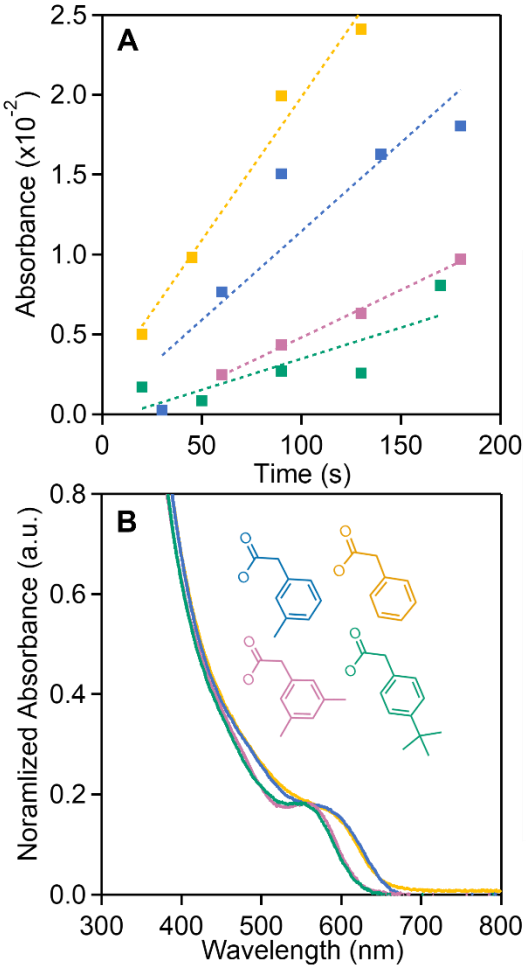

C	H	4-tBu	3-Me	3,5-Me$_2$
m ($\frac{Abs}{s}$x10^{-4})	1.99	0.355	1.14	0.509
R^2	0.992	0.872	0.955	0.995
λ_{max} (nm)	580	552	584	559

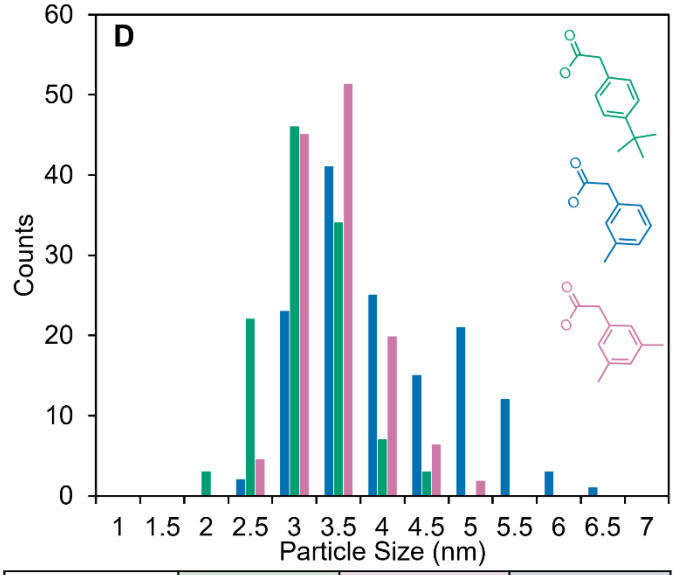

E	4-tBu	3,5-Me$_2$	3-Me
Avg Size	3.13 nm	3.47 nm	4.04 nm
Std. Dev.	0.51	0.45	0.85

Figure 2.3.8. A) Dependence of QD growth rate on ligand substitution by monitoring the change in absorbance at 500 nm over early time points. H (yellow), 4-tBu (green), 3-Me (blue), and 3,5-Me_2 (pink). The dotted lines are linear best fits but serve to primarily guide the eye. B) Absorbance of final QDs after complete conversion synthesized from thermolysis of clusters at 240 °C for 120 min. C) Summary table documenting initial growth rates (Abs/s), R^2 values for linear fitting of initial growth, and the λ_{max} of final QDs for each ligand. D) TEM-based size analysis of final reaction products from 240 °C thermolysis reactions of $In_{37}P_{20}$ clusters based on at least 100 measured particles. E) Summary table of average size and distributions based on measurements from A.

the balance between nucleation and growth after cluster dissolution. A larger steric profile of monomer species and nanocrystal surface should reasonably hinder growth thereby maintaining a high monomer concentration for longer time periods. Considering higher monomer concentrations favor nucleation over growth, steric hindrance restricting growth should benefit the production of nuclei resulting in a larger number of nuclei and a smaller average particle radius. This rationale fits the observed experimental trend, so while diffusion, solubility and surface tension may contribute, we conclude that the mechanism of $In_{37}P_{20}$ thermolysis is dominated by restricted surface growth.

2.4 $In_{26}P_{13}$ Synthesis and Characterization

After tracking and characterizing the ligand-dependent cluster conversions both through thermolysis and $P(SiMe_3)_3$ addition, we sought to further explore the implications of the hindered precursor diffusion that the tBu group provides. While investigating the routes toward generating the indium carboxylate, we found that when neatly reacting the 4-*tert*-butylphenylacetic acid with indium acetate to form the indium carboxylate precursor in an $In_{37}P_{20}$ cluster synthesis, the result is a partially soluble indium precursor. However, when the indium carboxylate is made through the reaction between trimethylindium and 4-*tert*-butylphenylacetic acid, the resulting precursor is completely soluble in toluene at room temperature. Using the indium carboxylate made through trimethylindium in the cluster synthesis leads to a new species absorbing at 350 nm, indicative of a smaller cluster (InP-350, **Figure 2.4.1A, B, Figure 2.4.3**). Using any of the other carboxylic acids and trimethylindium to generate the indium carboxylate did not result in the same 350 nm absorption when reacted with $P(SiMe_3)_3$. Instead, the 386 nm absorbance of the $In_{37}P_{20}$ cluster is observed. It is likely that this difference in speciation is due to the increased surface protection of

the tBu group leading to hindered diffusion to the cluster surface. This slows further growth of the intermediate InP-350 cluster as reactive solute species preferentially nucleate instead of adding onto already existing cluster. It is noteworthy that both $In_{37}P_{20}$ and InP-350 can be made with 4-*tert*-butylphenylacetate ligands so there is a difference in speciation that is dependent upon the preparation route of the indium carboxylate. We believe that the difference in precursor solubility and morphology is what drives the difference in reaction products. A less soluble indium carboxylate, such as the one that forms through the indium acetate route, likely has a much larger degree of bridging carboxylates to form an oligomerized, insoluble complex. The insolubility then results in aggregation between oligomers. This artificially increases the reactive equivalents of $P(SiMe_3)_3$ as it will react faster with the fewer equivalents of indium carboxylate that is actually dissolved in solution. With the trimethylindium route, all of the precursor is dissolved leading to a slightly different reaction stoichiometry. Prolonged exposure of a 3-Me $In_{37}P_{20}$ crude reaction solution to acetonitrile allowed for crystallization of the corresponding indium carboxylate precursor. This structure does not have the same substituent that results in the formation of $In_{26}P_{13}$ but it illustrates the vast degree of bridging and oligomerization that is likely responsible for the differing degrees of indium carboxylate solubility (**Figure 2.4.2**).

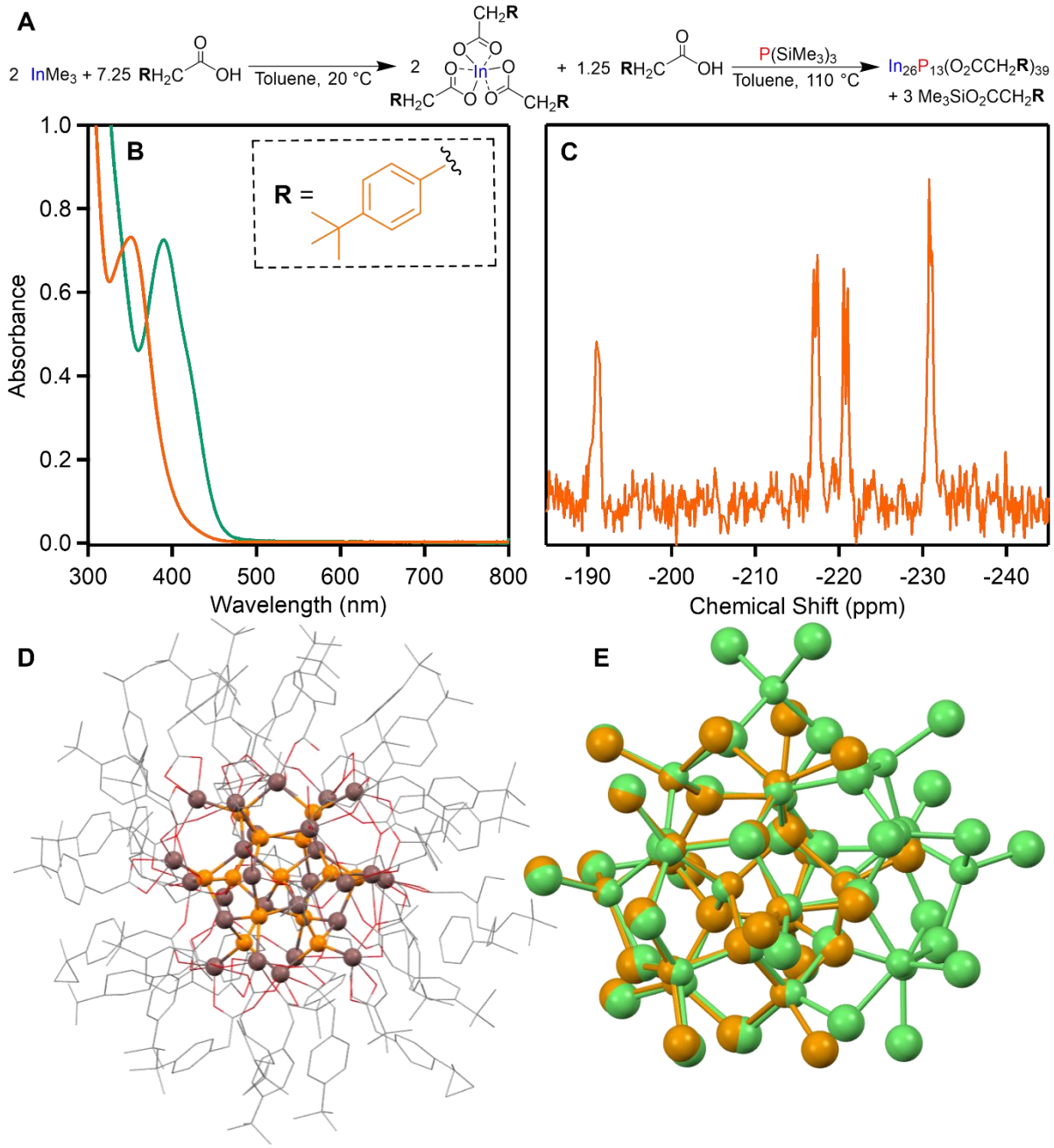

Figure 2.4.1. A) Synthesis of $In_{26}P_{13}$ cluster fragment leveraging the enhanced stability of the 4-tBu substituent. B) Absorbance comparison between isolated $In_{26}P_{13}$ cluster (orange) showing a λ_{max} at 350 nm and isolated $In_{37}P_{20}$ cluster (green) showing a λ_{max} at 386 nm. C) ^{31}P NMR spectrum of $In_{26}P_{13}(O_2CCH_2C_6H_4\text{-}tBu)_{39}$ cluster fragment. D) Single-crystal XRD structure of $In_{26}P_{13}(O_2CCH_2C_6H_4\text{-}tBu)_{39}$ with hydrogen atoms removed for clarity. E) Structural overlay of $In_{37}P_{20}$ (green) and $In_{26}P_{13}$ (orange) showing a high degree of overlap of like atoms.

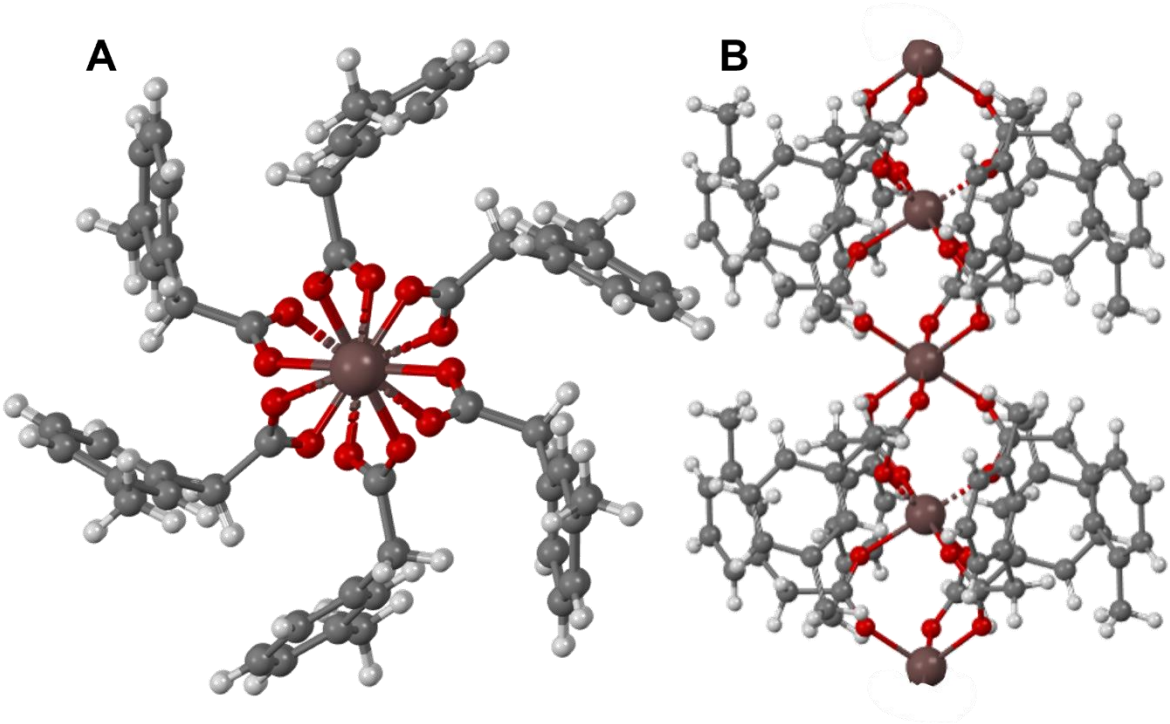

Figure 2.4.2. A) View down the C_3 symmetry axis of the $In(O_2CH_2C_6H_4CH_3)_3$ crystal structure. B) View of the extended bridging carboxylate network in the $In(O_2CH_2C_6H_4CH_3)_3$ along the c axis (right). Color legend: indium (brown), oxygen (red), carbon (grey), hydrogen (white).

The previous study done by our group investigating the reaction between $In_{37}P_{20}$ and $P(SiMe_3)_3$ found that the addition of 1-2 equivalents of $P(SiMe_3)_3$ with respect to cluster led to fragmentation and no subsequent growth.[12] Under these conditions, the fragmentation resulted in a new molecular structure that could only be characterized by UV-Vis and ^{31}P-NMR spectroscopy. In particular, the ^{31}P-NMR spectrum showed four sharp resonances in the -195 to -230 ppm region. Further investigation using myristate ligands showed that the smaller structure could be synthesized bottom-up under select conditions and lower temperatures but never in quantities large enough to allow for isolation and characterization.[12] Interestingly, characterizing the new cluster made through 4-*tert*-butylphenylacetic acid absorbing at 350 nm with ^{31}P-NMR showed the same

four sharp resonances previously documented (**Figure 2.4.1C**). Seeing that near stoichiometric equivalents of $P(SiMe_3)_3$ leads to fragmentation into the smaller cluster and any further amounts of phosphine result in templated growth, we hypothesize that this smaller cluster functions as an intermediate in the $P(SiMe_3)_3$-induced conversion mechanism. Furthermore, previous work has shown the final product to be temperature dependent but completely independent of cluster concentration.[12] This is further evidence for a reaction mechanism that proceeds by conversion through this intermediate.

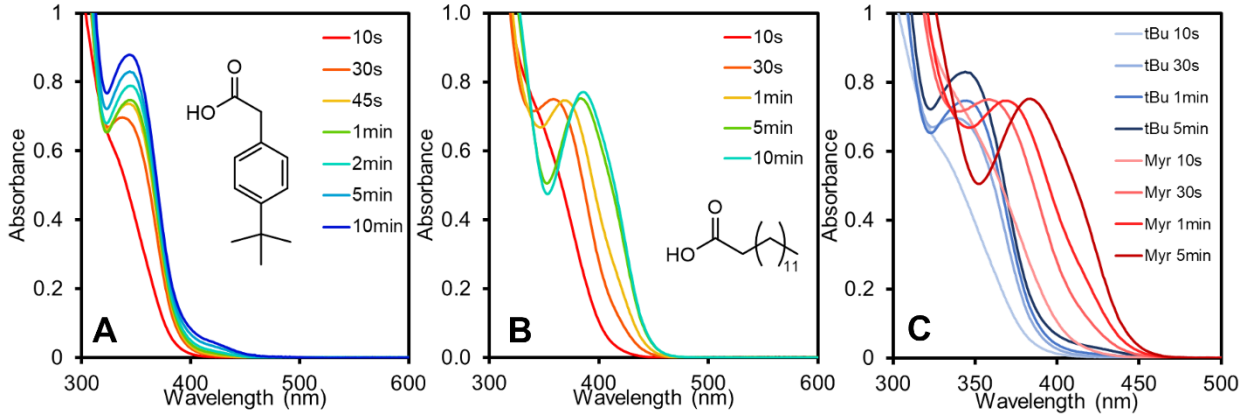

Figure 2.4.3. Comparison of synthesis progression using 4-tert-butylphenylacetic acid (top left) and myristic acid (top right) in identical synthetic conditions as described above for the synthesis of $In_{26}P_{13}$. Aliquots at equivalent time points are compared showing that myristic acid leads to more growth and larger species throughout (bottom right).

The rigidity of the *tert*-butyl group not only stabilized the cluster and modulated diffusion of $P(SiMe_3)_3$ but also allowed for growth of X-ray quality single-crystals and full structural determination at a resolution of 0.84 Å and R_1 and wR_2 values of 13.91% and 29.63% respectively. This revealed the intermediate to have the formula $In_{26}P_{13}(O_2CR)_{39}$ (**Figure 2.4.1D**). In previous work our group had provided an initial guess of the composition of this intermediate as $In_{29}P_{14}(O_2CR)_{45}$.[12] This initial hypothesis was very close to the true identity but assumed that the

fragment would be a symmetric subset of the original $In_{37}P_{20}$ species maintaining the central indium.

The structure was elucidated to be a higher-symmetry fragment of the $In_{37}P_{20}$ cluster with a central P atom. Structural overlay shows that the root mean squared deviation between paired atoms in $In_{26}P_{13}$ versus $In_{37}P_{20}$ is 0.438 Å, which emphasizes the strong similarities between these two structures (**Figure 2.4.1E**). Even the dangling surface In atoms are positioned as they would be for integration into the cluster core upon growth. The five ligand binding modes, monodentate, chelating, bidentate dative, symmetric bridging, and asymmetric bridging, represented on the surface of the $In_{37}P_{20}$ cluster are all also represented on the surface of $In_{26}P_{13}$ but with a different distribution. Of the 39 carboxylates, 7 are chelating, 10 are symmetric bridging, 21 are asymmetric bridging, and 1 is forced into a monodentate configuration by a bound water molecule. Trace water from polar solvents used in crystallization were found to bind readily to the surface of the cluster similar to the previously reported $In_{37}P_{20}(O_2CR)_{51}(H_2O)$ structure that was generated when the original InP cluster was exposed to humid conditions.[7] The average In-In separation distance in bridging carboxylates for the $In_{37}P_{20}$ cluster is found to be 4.75 Å. For $In_{26}P_{13}$ this metric was determined to be 4.46 Å. The decrease in In-In separation distance suggests a more reactive surface as predicted by Kulik and coworkers and reinforces the trend of surface In separation increasing from early-stage clusters to quantum dots.[14] In the case of $In_{37}P_{20}(O_2CR)_{51}(H_2O)$, water is found to displace a chelating ligand thereby forcing it to adopt a monodentate configuration. This occurs selectively on an indium passivating the apical phosphorus atom of the cluster. Despite the local ligand rearrangement, the bound H_2O is found to have negligible effect on the average In-In separation distances (also found to be 4.75 Å) and binding mode populations which remain unchanged hold the displaced chelating carboxylate. This is true even for the In-In separation

distances directly involving the In that binds the H_2O. Finally, the four ^{31}P resonances in the NMR spectrum can be assigned to environments in the crystal structure where the three most downfield signals are the sets of four P atoms that superimpose under each of the three C_2 axes and the final most upfield environment being the center P atom (**Figure 2.4.1C**).

Analyzing the $[In_{14}P_{13}]^{3+}$ core of the $In_{26}P_{13}$ cluster reveals T point group symmetry (**Figure 2.4.4**). Furthermore, with the surface In atoms removed, the $[In_{14}P_{13}]^{3+}$ core is structurally homologous to the TMEDA and Cl ligated $Cd_{14}Se_{13}$ reported by Hyeon and coworkers.[18] This is strong evidence for the similarities in structure between the many reported II-VI MSCs and the carboxylate-ligated III-V clusters. The comparative cation-richness of the InP is derived from the requirement for complete 4-coordination of P atoms, which is behavior not seen with analogous CdSe structures. Computational comparisons between III-V and II-VI nanomaterials show that with CdSe, the Se atoms can exist as 2-coordinate without restructuring whereas with InP materials, the P atoms almost exclusively exist as 3- or 4-coordinate.[51]

Within the $Cd_{14}Se_{13}$ cluster, all Se atoms are 3-coordinate except for the central, 4-coordinate atom. This relaxed requirement for chalcogen passivation drives the wider horizon of stoichiometries documented in II-VI materials whereas the 4-coordinate requirement of InP restricts the known cluster stoichiometries to being cation rich. These structural comparisons can be extended further to the observed conversion of $Cd_{14}Se_{13}$ to CdSe-420 whose structure lacks full determination but it has been posited that the underlying geometry of CdSe-420 is homologous to that of the $In_{37}P_{20}$ cluster with minor differences in stoichiometry.[18,52] The recently reported structure of $Cd_{26}Se_{17}$ synthesized through the cation exchange of $Cu_{26}Se_{13}$ furthers this analysis.[53,54] Both of these clusters show the same general anion sublattice as the $In_{26}P_{13}$ cluster and by extension, $In_{37}P_{20}$ and $Cd_{14}Se_{13}$. It is noteworthy that the growth of the anion sublattice

that occurs from $Cu_{26}Se_{13}$ to $Cd_{26}Se_{17}$ does not follow the same progression of growth as $In_{26}P_{13}$ to $In_{37}P_{20}$ despite the same initial sublattice structure. $In_{26}P_{13}$ requires asymmetric growth off of one side of the cluster to form the $In_{37}P_{20}$ structure. In comparison, the 4 Se atoms that are added upon cation exchange all grow off of geometrically equivalent sites. These structural differences between the III-V and II-VI materials could potentially be derived from the difference in ligand type where the mixed environment of L-type phosphines and X-type iodides of the $Cd_{26}Se_{17}$ direct a more stoichiometric ratio compared to the only X-type carboxylates of the InP-based clusters.

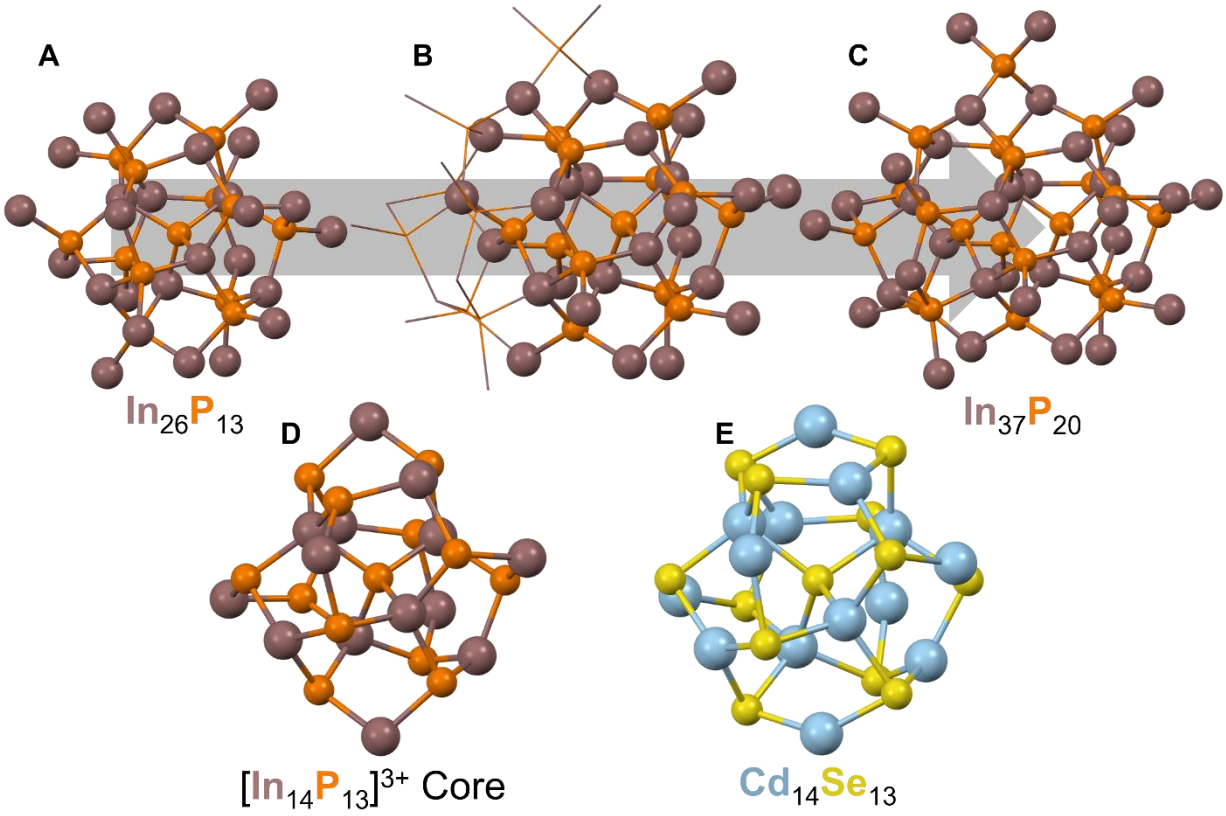

Figure 2.4.4. Structural comparisons of $In_{37}P_{20}$, $In_{26}P_{13}$, and $Cd_{14}Se_{13}$. A) $In_{26}P_{13}(O_2CCH_2C_6H_4\text{-}tBu)_{39}$ with all carboxylate ligands removed. B) Crystal model of $In_{37}P_{20}$ showing the sub-portion that makes up the $In_{26}P_{13}$ cluster. C) $In_{37}P_{20}(O_2CCH_2C_6H_5)_{51}$ with all carboxylate ligands removed. D) $[In_{14}P_{13}]^{3+}$ core presenting T-symmetry and structural analogy to $[Cd_{14}Se_{13}]^{2+}$ core. E) Structure of $[Cd_{14}Se_{13}]^{2+}$ core without ligands.[18]

To further investigate the electronic structure of $In_{26}P_{13}$, we performed TDDFT calculations using TD-HSE06/LANDL2DZ with the ligands truncated to acetate to decrease computational cost. The predicted energies of the first transitions show good agreement with the experimentally acquired spectrum (**Figure 2.4.5A**). Analyzing the leaving and arriving orbitals shows that the electronic ground state is essentially entirely composed of phosphorus 3p orbitals (**Figure 2.4.5B**). The arriving orbital shows a significant degree of delocalization across the cluster and is primarily composed of phosphorus 4s and indium 5s orbitals (**Figure 2.4.5C**). This stands as an interesting comparison with the arriving orbital of $In_{37}P_{20}$ which shows a much larger degree of localization and a smaller contribution from indium 5s to make up the NTO. The five discrete transitions that make up the overall peak shape arise from leaving orbitals that are all some arrangement of electron density distributed across different localized phosphorus 3p orbitals (**Figure 2.4.5D, Figure 2.4.6A**). This causes the leaving orbitals of the five lowest energy transitions to be very close to degenerate. Furthermore, these transitions all have the same arrival orbital which is isolated energetically from the next two higher energy arriving orbitals. Both of these higher energy arriving orbitals show much larger degrees of surface localization which result in higher relative energies. Simulated Raman modes of $In_{26}P_{13}$ match well with those computed and measured for $In_{37}P_{20}$ (**Figure 2.4.6B**).

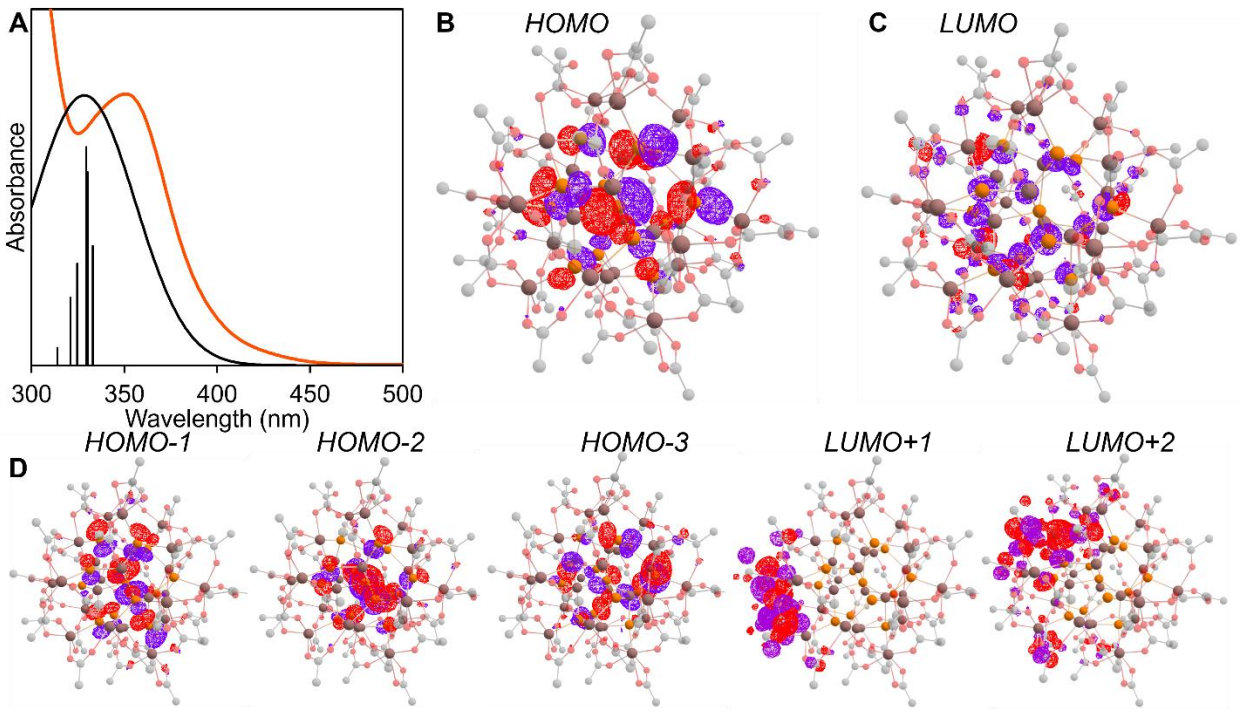

Figure 2.4.5. A) Experimental absorption of $In_{26}P_{13}$ (orange) compared to the first 5 electronic transitions as predicted by TDHSE06/LANDL2DZ for the simulated acetate-capped cluster (black). B) Visualization of the leaving NTO of the lowest energy transition. C) Visualization of the arriving NTO of the lowest energy transition. D) Extended occupied and unoccupied NTOs for $In_{26}P_{13}(O_2CR)_{39}$. NTOs were plotted with an isosurface value of 0.025 which, when combined with the high degree of orbital mixing, causes the traditional atomic orbital picture to not be present so atomic orbital specific nodes are not visible.

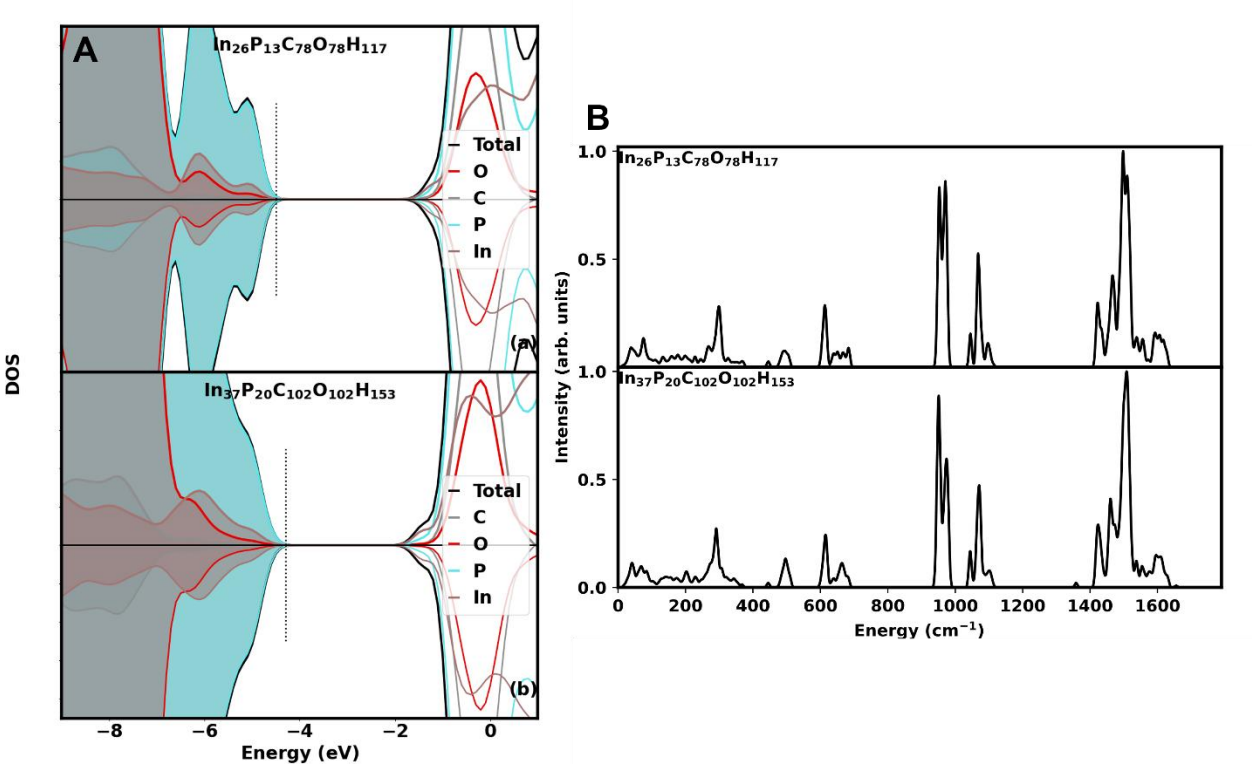

Figure 2.4.6. A) Computed density of states for electronic transitions in $In_{26}P_{13}(O_2CR)_{39}$ (top) and $In_{37}P_{20}(O_2CR)_{51}$ (bottom). B) Computed Raman Spectra for $In_{26}P_{13}(O_2CR)_{39}$ (top) and $In_{37}P_{20}(O_2CR)_{51}$ (bottom).

2.5 CONCLUSIONS

The addition of sterically hindered phenylacetate ligands to the surface of $In_{37}P_{20}$ clusters modifies the local structural environment of phosphorus atoms without a change in atomic connectivity as evidenced by ^{31}P-NMR spectroscopy and PDF analysis. The addition of para and meta-alkyl substituents to the phenylacetate ligand shell also dampen Raman-active InP-ensemble vibrations through the rigidity of surface indium carboxylates. We were also able to identify the substituent extremes that do not allow for cluster isolation in the form of *o*-tolylacetate and 3,5-di-*tert*-butylphenylacetate.

We have further shown that the surface reactivity of $In_{37}P_{20}$ clusters can be modulated by the steric profile of the phenylacetate-derived ligands. Steric substitution in the para-position was observed to protect the surface against $P(SiMe_3)_3$ attack thereby reducing the rate of conversion to QDs. In contrast, meta-positioned substituents enhanced the reactivity by shortening the separation distance between surface indium atoms and directing π-π stacking among ligand phenyl groups. Both of these phenomena function to lower the dissociation energy of bridged carboxylates thereby increasing the surface reactivity. Additionally, the ligands were found to direct different growth rates in thermolysis reactions using the clusters as single source precursors by hindering the rate of surface addition to extend the nucleation period. The mapping of relationships between these reactions is summarized in **Figure 2.5.1**.

Finally, we have leveraged the diffusion control and stability of the 4-*tert*-butylphenylacetate ligand to kinetically trap an intermediate InP cluster fragment. Complete structural characterization was carried out by SCXRD confirming the identity of the fragment to be $In_{26}P_{13}(O_2CR)_{39}$ and allowed for the observation that the core of this cluster fragment is homologous to the $Cd_{14}Se_{13}$ cluster ligated with TMEDA and chloride.

These observations have powerful implications for control over cluster-based nanocrystal systems and act as the first definitive evidence for the structural similarities between III-V and II-VI clusters.

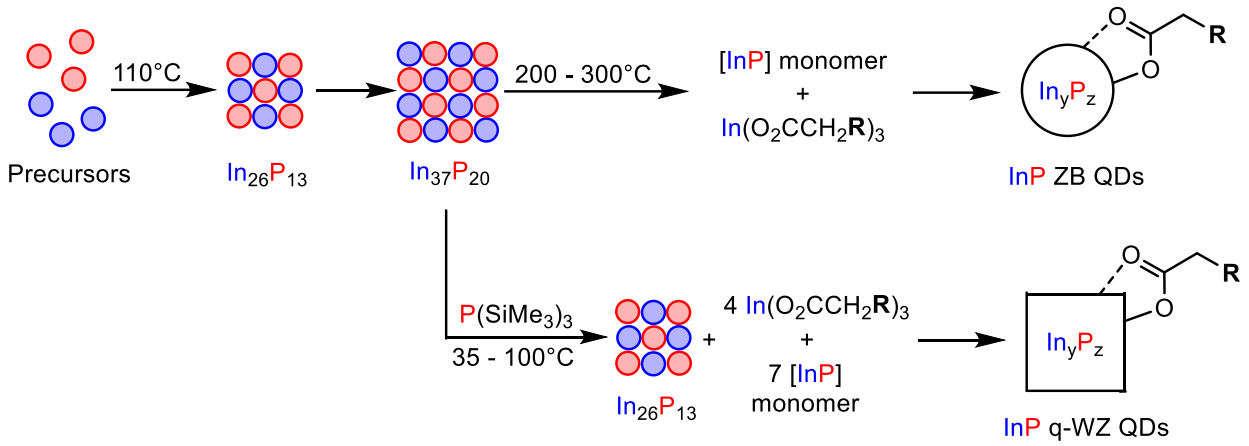

Figure 2.5.1. Summary of investigated reaction pathways of InP magic-sized clusters. The $In_{26}P_{13}$ cluster precedes formation of $In_{37}P_{20}$ which then undergoes dissolution to generate monomers to renucleate zinc-blende QDs. The addition of $P(SiMe_3)_3$ to $In_{37}P_{20}$ induces fragmentation to form $In_{26}P_{13}$ which is the nucleus from which quasi-wurtzite QDs are grown.

2.6 Outlook

The majority of the work in this study was dedicated to the cluster-to-QD conversion mechanisms and how the ligand structure and interface influenced the kinetics and outcome. While it was satisfying to have some experimental proof for the computational work done by Kulik and coworkers, the conclusions that most contributed to the broader knowledge of the field were those that concerned cluster structure. It was (and still remains) an open question: how rigid are the requirements for cluster structure to maintain atomic precision. In other words, how deep is the stability well of the cluster before conversion to larger QDs. Through the ^{31}P NMR and PDF, it became clear that rather substantial internal structural modifications can be made to the cluster but the metastability is still maintained. The requirements for structural stability are therefore not as stringent as I previously thought. Changes at the surface as well as changes in the atomic

arrangement can occur without complete destabilization and dissolution. This contributed to proof that clusters don't need to be treated as a molecule with a single identity with pre-set inflexible properties. Instead, they allow for a respectable degree of functionalization that can lead to tunable properties such as reactivity.

While reconsidering the robustness of clusters was a fascinating, fundamental concept, it is important to put cluster conversion in perspective with the rest of the QD synthesis literature. While the direct thermolysis of clusters has resulted in QDs with decent properties, most of the literature does not use them as single-source precursors when synthesizing QDs.[3,4,55–58] Instead, the trend is very much towards the direct reaction between precursors at temperatures where most clusters will be quickly destabilized (>190 °C).[1,2,59–61] It then remains an open question: to what degree are molecular clusters participating in the QD growth mechanism and is their formation benefiting sample quality or is it a pernicious process that should be avoided? At least for InP QDs, effort has been dedicated to purposefully destabilizing clusters in-situ to grow high-quality nanocrystals.[62] The rationale being that having metastable, pseudo-crystalline clusters leads to unfavorable kinetics as more energy is required to destabilize the cluster than to nucleate and grow directly from precursors. However, the reactions that result in the highest quality InP QDs occur under conditions that would be suitable for the transient formation of clusters at the beginning of the reaction. Unfortunately, there is simply an inherent challenge in gathering high-resolution structural information on short time scales so assessing to what degree clusters are forming in these reactions is extremely challenging. The closest to direct characterization has come in the form of MALDI-TOF proving that materials with a molecular weight in the cluster regime are persistent throughout the course of InP QD reactions.[63] But while the mechanistic role of clusters in industrially-applicable QD reactions remains ambiguous, the study of their crystalline structures

provides unique information about their formation and stability. These conclusions provide guidance towards understanding how atomically-precise clusters form and how they differ between material classes.

It is rare that a magic-sized cluster that is directly related to a known QD synthesis receives full structural characterization via SCXRD. The isolation and subsequent identification of the $In_{26}P_{13}(O_2CR)_{39}$ intermediate was therefore an exciting result that allowed for a synergistic analysis of cluster growth when placed alongside the $In_{37}P_{20}(O_2CR)_{51}$ structure. Specifically, how does the $In_{26}P_{13}$ structure grow into the $In_{37}P_{20}$ structure? The perspective that the SCXRD results provides here really challenged my preconceived notions about nanomaterial growth. It showed that $In_{26}P_{13}$ grows into $In_{37}P_{20}$ through the addition of an asymmetric facet of sorts. I had always assumed that a structure like this would grow outward symmetrically similar to a QD. The core of the cluster, the $[In_{14}P_{13}]^{3+}$ cage, is just so symmetric and so if reaction conditions cause one side of the cluster surface to grow, why wouldn't any equivalent surface also undergo growth (**Figure 2.6.1**)?

The obvious hypothesis for why the cluster wouldn't grow further is that the surface energy of the cluster changes upon the first growth step to become $In_{37}P_{20}$. While this is a strong possibility, especially when considering the small size of this material, it has been difficult for me to completely accept this. The addition of another "facet" to generate $In_{48}P_{27}$ wouldn't influence the symmetry of the cluster but would benefit the internal energy. I still can't completely rationalize why a larger structure doesn't exist.

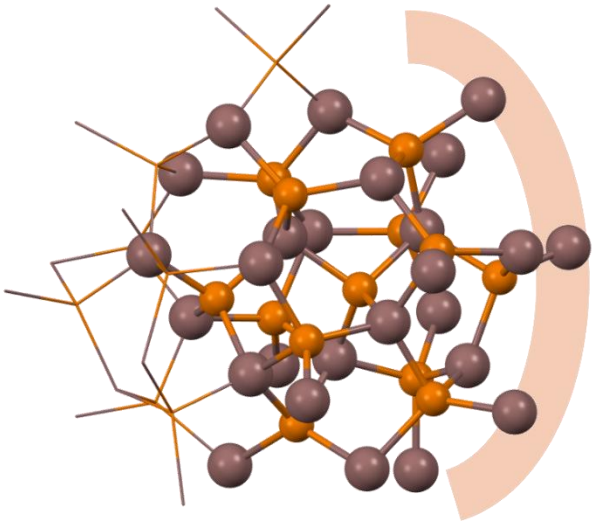

Figure 2.6.1. $In_{26}P_{13}$ cluster shown as a ball-and-stick model with the additional atoms that form the $In_{37}P_{20}$ cluster shown in wireframe. The orange arc shows that region of the $In_{26}P_{13}$ cluster where an additional set of equivalent atoms could be added to generate a hypothetical larger cluster, $In_{48}P_{27}$.

Towards investigating this growth process, I spent some time trying to directly convert the $In_{26}P_{13}$ into the $In_{37}P_{20}$ cluster through the further addition of $P(SiMe_3)_3$. If I could find the conditions under which $In_{26}P_{13}$ becomes $In_{37}P_{20}$, perhaps the same conditions would further lead to the growth of $In_{48}P_{27}$. Despite this conversion seemingly happening readily in-situ for standard $In_{37}P_{20}$ reactions, no further additions of $P(SiMe_3)_3$ led to any further growth of $In_{26}P_{13}$ until the clusters eventually destabilized into QDs. Upon further reflection, potentially it isn't too surprising that the $In_{26}P_{13}$ cannot be so easily converted.

It could be that upon complete formation of $In_{26}P_{13}$, the surface reaches a point of stability that does not allow for further growth. This would be the case when using the 4-*tert*-butylphenylacetate ligands alongside trimethylindium (**Figure 2.6.2A**). The $In_{26}P_{13}$ cluster forms a stable species with well-defined surface chemistry. However, when using other ligands, the

ligand shell of $In_{26}P_{13}$ never reaches a point of stability due to the faster kinetics and thus the smaller cluster is only a transient intermediate in these reactions (**Figure 2.6.2B**). This would suggest that if $In_{26}P_{13}$ forms completely, disturbing the ligand shell won't lead to discrete growth into $In_{37}P_{20}$ and instead, the clusters will lose atomic precision and convert into QDs which is indeed what is observed.

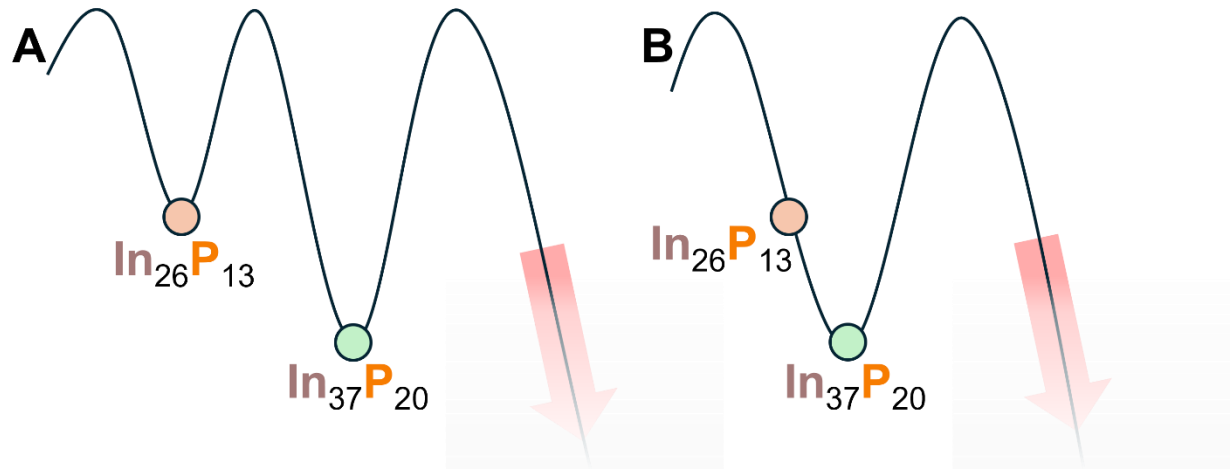

Figure 2.6.2. A) Reaction coordinate diagram for InP cluster reactions using 4-*tert*-butylphenylacetate ligands. B) Reaction coordinate diagram for InP cluster reactions using long alkyl chain carboxylate ligands.

The final structural concept that deserves discussion is the structural homology between the $Cd_{14}Se_{13}$ cluster and $In_{26}P_{13}$, especially in regard to the similarity from the $[In_{14}P_{13}]^{3+}$ cage. Seeing as the bulk phases of CdSe and InP are both zincblende and wurtzite, it is not entirely surprising that their nanoscale cluster structures would be similar as well. Furthermore, the 4-coordinate requirement of phosphorus leading to a more cation rich stoichiometry ($Cd_{14}Se_{13}$ versus $In_{26}P_{13}$) can be understood through p orbital diffusivity. The 4p shell of Se^{2-} is quite soft and diffuse allowing for larger deviations in bond angles and geometry where the 3p shell of P^{3-} is much harder

and more rigid leading to stringent bonding requirements. Furthermore, the TMEDA ligands used in the isolation of the $Cd_{14}Se_{13}$ would promote a more stoichiometric cluster anyways seeing as they are L-type and uncharged. However, while the differences between the two structures can be rationalized, it is much more challenging to explain why these systems arrive at the $M_{14}E_{13}$ geometry.

The main structural motif of the $M_{14}E_{13}$ cage is that the surrounding anions form an icosahedron around the central anion. The icosahedron is not an unfamiliar shape in cluster chemistry although it normally appears in a different context. The noble metal cluster literature has extensive structural and electronic characterization of icosahedral magic-sized clusters of different sizes. These observations were kicked off after the discovery of the $[Au_{25}(SCH_2CH_2Ph)_{18}^-][N(C_8H_{17})_4^+]$ structure in which 12 outer gold atoms form the vertices of an icosahedron around a central gold atom.[64] The icosahedral cluster is then ligated with six $Au_2(SCH_2CH_2Ph)_3$ "staple" units. The general rationale for this particular shape forming is that the icosahedron has a low SA:V ratio thereby minimizing the destabilizing surface energy while maximizing the stabilizing internal energy. Furthermore, this atomic arrangement satisfies the full-shell configuration of electronic energy levels. If all 25 Au atoms are contributing a 6s valence electron, 18 of them will be tied up in thiolate bonding which leaves seven electrons in the core as well as one additional electron from the total charge of the cluster resulting in eight total. This satisfies the closed-shell requirement for noble gases that leads to their stability. Now while the low SA:V and closed electronic shell provide an acceptable rationale for why noble metallic clusters form the way they do, this can't necessarily be directly applied to the formation of the $M_{14}E_{13}$ cage.

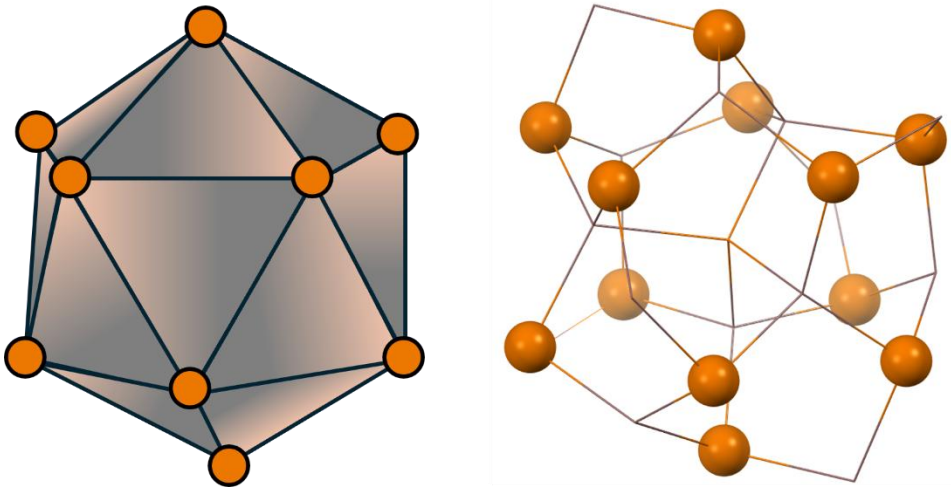

Figure 2.6.3. Platonic icosahedron (left) with orange circles at each visible vertex. $[In_{14}P_{13}]^{3+}$ (right) with the surrounding phosphorus atoms that generate the icosahedral sublattice shown as spheres and all other atoms shown in wireframe.

The first and most important distinction is that the binary cluster structures are not icosahedral, they simply contain a sublattice that is icosahedral. This doesn't completely negate a contribution that the shape might have to the overall stability but it confirms that the structural preferences of these binary clusters cannot be interpreted in the exact same way as the unary, metallic clusters. If the surface is not made from the vertices of the icosahedron then it's especially low SA:V ratio is not contributing to the overall stability of the cluster. Why then would that particular shape incorporate itself into the structure?

Another possible hypothesis to explain the presence of the icosahedron takes into account the tetrahedral coordination of the binary lattice in InP and CdSe. Both zincblende and wurtzite, the two stable crystalline phases of InP and CdSe, involve consistent tetrahedral coordination of both metal and anion in the lattice. The first step in nucleating these clusters is then generating a 4-coordinate, central phosphorus atom (**Figure 2.6.4A**) via carboxylate-ligated indium. The four indium atoms must then be 4-coordinate and tetrahedral via phosphorus. This generates four

tetrahedra around a central phosphorus atom with each vertex being a surrounding phosphorus (**Figure 2.6.4B**). These surrounding phosphorus atoms are the 12 atoms that make up the vertices of the icosahedron. Therefore, following this logic, the icosahedron is not preferential due to a lowering of the surface energy, but instead happens to be generated by the tetrahedral coordination of four tetrahedra. The final cage structure is then formed through the passivation of these 12 phosphorus vertices by indium (**Figure 2.6.4C**).

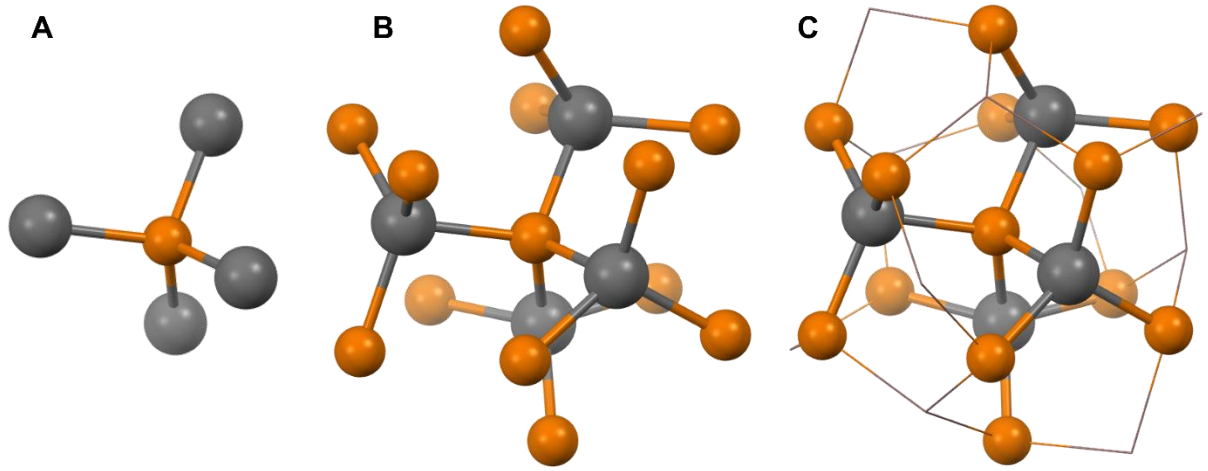

Figure 2.6.4. A) The central 4-coordinate phosphorus of the $In_{26}P_{13}$ cluster. B) Expanding the coordination so that the four internal indium atoms are themselves 4-coordinate leads to the 12 surrounding phosphorus atoms that create the vertices of the icosahedral structure. C) Further coordination of the 12 surrounding phosphorus atoms leads to the $[In_{14}P_{13}]^{3+}$ cage structure.

The structural similarity unveiled here between the smaller InP and CdSe clusters could also be extended to their larger structures as well. Seeing as the $In_{26}P_{13}$ cluster converts into the $In_{37}P_{20}$, it would follow that the $Cd_{14}Se_{13}$ could grow into a more stoichiometric version of the $In_{37}P_{20}$, most likely $Cd_{21}Se_{20}$. In the same study that documents the crystal structure of the $Cd_{14}Se_{13}$, it is shown that cluster can be converted into a larger magic-sized cluster, $CdSe_{420}$

(named for its absorbance λ_{max} at 420 nm), through a simple ligand exchange (tetramethylethylenediamine for (trifluoromethyl)benzylamine).[18] This larger cluster has a very distinct absorbance profile (**Figure 2.6.5A**) with λ_{max} values reported between 410 and 420 nm. Since the $In_{26}P_{13}$ converts into the $In_{37}P_{20}$ and the $Cd_{14}Se_{13}$ converts into the $CdSe_{420}$, we thought it highly plausible that the $CdSe_{420}$ is the stoichiometric version of $In_{37}P_{20}$, $Cd_{21}Se_{20}$ (**Figure 2.6.5B**). This hypothesis was published as a part of a study investigating the interconversion of CdSe magic-sized clusters.[52] To this date, the $CdSe_{420}$ still has not received full structural characterization by SCXRD and thus this structural assignment remains a hypothesis.

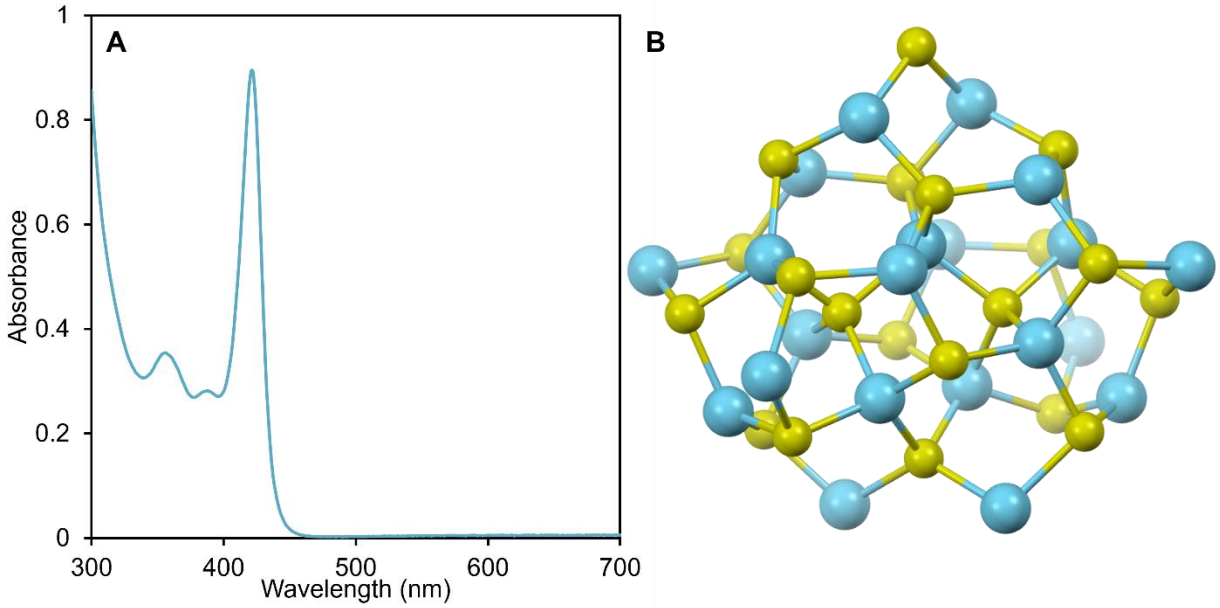

Figure 2.6.5. A) Absorbance spectrum of $CdSe_{420}$ with a λ_{max} at 420 nm. B) Hypothesized crystal structure of the $CdSe_{420}$ cluster with a $Cd_{21}Se_{20}$ stoichiometry and a core structure that is homologous to the $In_{37}P_{20}$.

Full structural characterization of the $In_{26}P_{13}$ magic-sized cluster in this study allowed for many new conclusions about the formation, stability, and structural similarities in cluster systems. The next step in furthering the ideas presented here was then to expand on the list of magic-sized

clusters that have been characterized by SCXRD. A great candidate for this goal was an InAs magic-sized cluster, the presence and absorbance spectrum of which had been reported in the literature for many years.

2.7 Experimental Section

2.7.1 *General Considerations.*

Indium acetate (99.99%), phenylacetic acid (99%), *o*-tolylacetic acid (99%), potassium cyanide (96%), anhydrous octane (>99%), anhydrous tetrachloroethylene (>99%) and diphenyl ether (99%) were obtained from Sigma Aldrich and used without further purification. 4-*tert*-butylphenylacetic acid (>98%) and *m*-tolylacetic acid (>98%) were obtained from TCI and used without further purification. Trimethyl indium (98%) was obtained from Strem Chemicals and used as received. 1-(Bromomethyl)-3,5-di-*tert*-butylbenzene (>95%) was obtained from Synthonix and used without further purification. Biphenyl (99%) was obtained from Acros Organics and used without further purification. 2-(3,5-Dimethylphenyl)acetic acid (99.85%) was obtained from Chemscene and used without further purification. 1,2-difluorobenzene was obtained from Sigma Aldrich, dried over P_2O_5 and distilled prior to use. Deuterated benzene (C_6D_6) was obtained from Cambridge Isotope Laboratories, dried over CaH_2 and distilled prior to use. Tris(trimethylsilyl)phosphine ($P(SiMe_3)_3$) was prepared according to literature procedures.[65] All manipulations were performed under an inert atmosphere of dry N_2 using standard Schlenk line or glovebox techniques unless otherwise indicated. Optical spectra were acquired on Cary 5000 and Cary 60 UV-Vis spectrophotometers from Agilent Technologies. NMR spectra were acquired on 300 and 500 MHz Bruker Avance spectrometers in C_6D_6. All Raman spectra were collected with a Renishaw InVia equipped with the Leica DMIRBE inverted optical microscope, exciting at 785 nm, using samples drop cast from solution onto Si wafer. Samples were prepared in a glovebox

and remained air-free until mounting on the sample stage of the Raman microscope. Spectra were typically acquired within 0.5 – 1 hour of exposure to air, though control experiments show excellent agreement between Raman spectra following 0.5 – 1 hour and 24 – 48 hours exposure to air at room temperature. Diffractograms were collected on a Bruker D8 powder x-ray diffractometer with a Pilatus 100K large-area 2D detector using a 1 mm collimator.

2.7.2 *Synthesis of $In_{37}P_{20}(O_2CH_2R)_{51}$.*

$In_{37}P_{20}(O_2CH_2R)_{51}$ clusters were prepared through a reported procedure for phenylacetate-capped particles using $In(O_2CCH_3)_3$ (934 mg, 3.20 mmol) and substituted phenylacetic acid (11.6 mmol) in toluene (10 mL) and $P(SiMe_3)_3$ (465 uL, 1.60 mmol) in toluene (5 mL).[7] All toluene is removed by vacuum and the clusters are flocculated 3 times with toluene and acetonitrile followed by purification through a gel permeation chromatography column. In the case of the parent phenylacetate-ligated cluster, the flocculation is performed with toluene and pentane. In a typical synthesis, $In_{37}P_{20}(O_2CCH_2R)_{51}$ is isolated in 25% yield (0.02 mmol) based on $P(SiMe_3)_3$ as the limiting reagent.

2.7.3 *Synthesis of $In_{26}P_{13}(O_2CH_2C_6H_4C(CH_3)_3)_{39}$.*

$In_{26}P_{13}(O_2CH_2C_6H_4C(CH_3)_3)_{39}$ clusters were prepared by adapting the synthesis of $In_{37}P_{20}(O_2CH_2R)_{51}$ particles. In a typical synthesis, 4-*tert*-butylphenylacetic acid (2.23 g, 11.6 mmol) is added to an oven-dried 50 mL 3-neck round-bottom flask fitted with a thermowell, t-adapter, and septum. The flask is placed under vacuum at 50 mtorr for 1.5 hours after which anhydrous toluene (5 mL) is injected into the flask. Trimethyl indium (512 mg, 3.20 mmol) is

dissolved in 8 mL of toluene and added dropwise to the flask with 800 rpm stirring at 2 drops per second. The solution is left to stir for 5 minutes after which the temperature is increased to 105 °C. A solution of $P(SiMe_3)_3$ (460 uL, 1.58 mmol) in anhydrous toluene (2 mL) is then promptly injected into the flask. After 20 minutes at 105 °C, the reaction is allowed to cool to room temperature and all toluene is removed under vacuum. The $In_{26}P_{13}(O_2CH_2C_6H_4C(CH_3)_3)_{39}$ particles are isolated as a white, crystalline solid by successive precipitation from toluene using acetonitrile.

For crystallization, under a nitrogen atmosphere, 15 mg of isolated cluster is dissolved in 400 µL of 1,2-difluorobenzene and layered with acetonitrile in an oven-dried NMR tube. Colorless crystals grew after 5 days at the liquid boundary.

2.7.4 *Crystallization of $In(O_2CH_2C_6H_4CH_3)_3$.*

$In_{37}P_{20}(O_2CH_2R)_{51}$ clusters were synthesized with *m*-tolylacetate (3-Me) ligands as described above. A sample of the crude reaction mixture (3 mL) before purification was brought to the point of crash out by dropwise addition of acetonitrile. The solution was put through a 0.45 µm PTFE filter into a 20 mL scintillation vial. The vial was left sealed and after 8 months colorless crystals had formed at the bottom of the vial.

2.7.5 *Conversion of $In_{37}P_{20}$ to Quasi-Wurtzite QDs.*

Under a nitrogen atmosphere, a 2.82×10^{-5} M solution of $In_{37}P_{20}$ cluster is made up in toluene. A cuvette is charged with 3.5 mL of stock solution and sealed under nitrogen with a cap and septum. The cuvette is then placed in a preheated cryostat at 40 °C and the temperature is

allowed to equilibrate for 10 min. During temperature equilibration, $P(SiMe_3)_3$ (5.7 µL) is combined with anhydrous octane (0.703 g) and 50 µL of this solution is stoppered in a gas-tight syringe. The $P(SiMe_3)_3$ solution is promptly injected into the cuvette with stirring after which UV-Vis monitoring begins immediately.

2.7.6 *Thermolysis of $In_{37}P_{20}$ to Zinc-blende QDs.*

A 70% diphenyl ether and 30% biphenyl eutectic (4.5 mL) is injected into an oven-dried 15 mL 3-neck round-bottom flask and brought to 240 °C. During heating, $In_{37}P_{20}$ cluster (0.00237 mmol) is dissolved in 1 mL of the eutectic mixture along with 10 drops of toluene to ensure complete solubility. Once at 240 °C, the cluster solution is promptly injected and the reaction progression monitored by UV-Vis aliquots (20 µL in 3 mL).

2.7.7 *Synthesis of 3,5-di-tert-butylphenylacetic acid.*

3,5-di-tert-butylbenzyl bromide (9.921 g), KCN (2.279 g), and 18-crown-6 (9.354 g) were placed in a 250 mL round-bottom flask and 110 mL of acetonitrile was added. The solution was refluxed for 4.5 hours, then diluted with water (200 mL). The product was extracted with 3 x 100 mL of ether which was then removed by rotary evaporation to yield 9.3315 g of crude product (98% conversion bromoalkane to nitrile by NMR). The crude product was then dissolved in ethanol (300 mL) and to this solution 12.5 M NaOH (100 mL) was added. This solution was brought to reflux and left to react for 16.5 hours which resulted in a biphasic mixture. Conc. HCl was added to the organic layer with stirring until pH 0.5 after which the solution was concentrated by rotary evaporation to yield a white solid. This was redissolved in ether, filtered, and the ether

from the filtrate was removed by rotary evaporation. The resulting white solid was suspended in cold pentane and filtered. White crystals were washed with cold pentane and then pumped down at 50 mtorr overnight to remove any residual solvent. The final product was a fluffy white solid (3.300 g, mp = 113 C -120 C)

2.7.8 *Single Crystal X-ray Diffraction Methods.*

For crystallization of $In_{26}P_{13}(O_2CH_2C_6H_4C(CH_3)_3)_{39}$, a colorless piece, measuring 0.32 x 0.13 x 0.10 mm^3 was mounted on a loop with oil. For $In(O_2CH_2C_6H_4CH_3)_3$, a colorless shard, measuring 0.10 x 0.07 x 0.06 mm^3 was mounted on a loop with oil. Data was collected at -173 °C on a Bruker APEX II single crystal X-ray diffractometer, Mo-radiation, equipped with a Miracol X-ray optical collimator. The data was integrated and scaled using SAINT, SADABS within the APEX2 software package by Bruker.[66] Solution by direct methods (SHELXT[67] or SIR97[68]) produced a complete heavy atom phasing model consistent with the proposed structure. The structure was completed by difference Fourier synthesis with SHELXL.[67,69] Scattering factors are from Waasmair and Kirfel.[70] Hydrogen atoms were placed in geometrically idealized positions and constrained to ride on their parent atoms with C---H distances in the range 0.95-1.00 Angstrom. Isotropic thermal parameters U_{eq} were fixed such that they were $1.2U_{eq}$ of their parent atom Ueq for CH's and $1.5U_{eq}$ of their parent atom U_{eq} in case of methyl groups. All non-hydrogen atoms were refined anisotropically by full-matrix least-squares. While all C and O atoms were restraint with ISOR to help keep the displacement parameter matrices positive definite, the disordered ones were restraint with SIMU. Some difluorobenzene solvent molecules were found, but the contribution of additional unidentified solvent was removed with SQUEEZE.[71–73] The crystallographic data for the $In_{26}P_{13}(O_2CH_2C_6H_4C(CH_3)_3)_{39}$ structure and the $In(O_2CH_2C_6H_4CH_3)_3$

structure have been deposited in the Cambridge Crystallographic Database under deposition numbers 2261840 and 2306934 respectively.

2.7.9 *Computational Methods.*

Computational studies were performed using the Gaussian[74] electronic structure package. The HSE064-6[75–77] range-separated hybrid DFT functional was used to perform the linear-response TDDFT absorption spectra. This method has been used previously by our group to characterize the electronic structure of the $In_{37}P_{20}$ cluster.[7,34,78] Initial structures were taken from XRD, optimized until the total and root mean squared displacement and force were under $1.80*10^{-3}$ and $1.20*10^{-3}$ Bohr, and $4.50*10^{-4}$ and $3.00*10^{-4}$ Har/Bohr, respectively. TDDFT[79–81] was used to compute both the excitation energies and corresponding oscillator strengths of the first 20 electronic transitions. For all these calculations the water molecule was removed from the structure as we believe it is a result of prolonged contact with polar solvents containing trace water.

2.7.10 *Solution Phase FTIR Methods.*

All solution phase FT-IR measurements were acquired on a PerkinElmer Frontier FT-IR spectrometer using a CaF_2 window liquid cell with the sample dissolved in tetrachloroethylene. The solvent signal was subtracted before gaussian peak fitting by linear least squares. Quantitative differences were assessed by comparing the integrated intensity of peaks of interest.

2.7.11 *Kinetic Rate Determination Methods.*

For each trial, at wavelengths 450, 500, and 550 nm, the first derivative of absorbance versus time was taken. To standardize all fitting widths across ligands, the time point where the maximum of that first derivative occurs, representing the inflection point of the absorbance versus time graph, was used as the induction time. For the reported values and standard errors, the induction times of all trials at a specific wavelength were averaged and the standard deviation was taken. For k_{obs}, a single exponential function of the form $f(x) = y_0 + Ae^{-k_{obs}(x-x_0)}$ was applied as global least squares fit to all absorbance versus time trials at a particular wavelength.

2.7.12 *X-ray Total Scattering Methods.*

Excess solvent was evaporated off of InP MSC samples in inert atmosphere and dried samples were sealed in quartz capillaries. X-ray total scattering data was obtained at the NSLS-II beamline 28-ID-1 at Brookhaven National Laboratory as reported previously.[52] Sample scans consisted of 600 1-second exposures to a 74.5 keV incident beam. Each scan was background subtracted and corrected for percent transmission. Sample transmission ranging from 66-76% was measured on a silicon photodiode with impedance amplifying circuit.

2.7.13 *Pair Distribution Function.*

Reduced pair distribution function was calculated using PDFgetX3.[25] PDFgetX3 inputs used to generate G(r) from scattered intensity I(Q) are listed in **Table 2.7.1**. A Qmin of 0.5 $Å^{-1}$ is chosen to avoid any scattering of the direct X-ray beam around the beamstop. Qmax is chosen as the maximum Q value before the scattering signal becomes exceedingly noisy. Rpoly is left at the

software's default value of 0.9Å which is below the first relevant peak in the PDF and, with Qmaxinst=23.6 $Å^{-1}$ results in the weighted use of 7th and 8th order correction polynomials and unphysical error in our G(r) up to r=0.9 Å. Full $In_{37}P_{20}(O_2CR)_{51}$ elemental composition was used to calculate each sample's average atomic scattering factor. G(r) for each sample was generated from the Fourier transform of F(Q)) from Q=0.5-23.6 $Å^{-1}$. Full details on the workings of PDFgetX3 are reported in reference 25.

Param.	Rmin [Å]	Rmax [Å]	Rstep [Å]	Qmax [$Å^{-1}$]	Qmin [$Å^{-1}$]	Qmaxinst [$Å^{-1}$]	Rpoly
Value	0.0	30	0.01	23.6	0.5	26.0	0.9

Table 2.7.1. PDFgetX3 Transform Parameters

Formalized equations in this analysis are defined as follows:

Structure Function $$S(Q) = \frac{I(Q)}{<f(q)>^2} + \frac{<f(q)>^2 - <f(q)^2>}{<f(q)>^2}$$

Reduced Structure Function $$F(Q) = Q[S(Q) - 1]$$

Reduced Pair Distribution Function $$G(r) = \left(\frac{2}{\pi}\right) \int_{Q_{min}}^{Q_{max}} F(Q) \sin(Qr)\, dQ$$

2.7.14 *G(r) Peak Center Determination.*

Bond length variation for sterically hindered substituent ligands was calculated with respect to the phenylacetate ligated cluster. Simple double Gaussian fits were applied to describe the first neighbor In-O and In-P G(r) peaks. Each Gaussian peak center was extracted and assigned as the average bond length for In-O and In-P respectively. While the cluster structures are low-symmetry with high degrees of static disorder, an approximate difference is calculated from the

average bond lengths with the equation below where $r_{In\text{-}P\_Subst.}$ represents the In-P peak position of the 3-Me, 3,5-Me_2 or 4-tBu substituents, and $r_{In\text{-}P\_H}$ is that of the phenylacetate cluster:

$$Difference\ \% = 100\% * \frac{r_{In-P\_Subst} - r_{In-P\_H}}{r_{In-P\_H}}$$

ΔG Analysis. ΔG and R_w were calculated with the expression used for structural disorder in CdSe nanoparticles[26] using a second experimental G(r) in lieu of a calculated G(r) to understand the differences between experimental PDFs.

$$R_w = \sqrt{\frac{\sum_{i=1}^{N}[G_{exp1}(r_i) - G_{exp2}(r_i)]^2}{\sum_{i=1}^{N}[G_{exp1}(r_i)]^2}}$$

2.8 REFERENCES

(1) Kim, Y.; Ham, S.; Jang, H.; Min, J. H.; Chung, H.; Lee, J.; Kim, D.; Jang, E. Bright and Uniform Green Light Emitting InP/ZnSe/ZnS Quantum Dots for Wide Color Gamut Displays. *ACS Appl Nano Mater* **2019**, *2* (3), 1496–1504. https://doi.org/10.1021/acsanm.8b02063.

(2) Won, Y.-H.; Cho, O.; Kim, T.; Chung, D.-Y.; Kim, T.; Chung, H.; Jang, H.; Lee, J.; Kim, D.; Jang, E. Highly Efficient and Stable InP/ZnSe/ZnS Quantum Dot Light-Emitting Diodes. *Nature* **2019**, *575* (7784), 634–638. https://doi.org/10.1038/s41586-019-1771-5.

(3) Gary, D. C.; Terban, M. W.; Billinge, S. J. L.; Cossairt, B. M. Two-Step Nucleation and Growth of InP Quantum Dots via Magic-Sized Cluster Intermediates. *Chem. Mater.* **2015**, *27* (4), 1432–1441. https://doi.org/10.1021/acs.chemmater.5b00286.

(4) Friedfeld, M. R.; Johnson, D. A.; Cossairt, B. M. Conversion of InP Clusters to Quantum Dots. *Inorg. Chem.* **2019**, *58* (1), 803–810. https://doi.org/10.1021/acs.inorgchem.8b02945.

(5) Xie, L.; Shen, Y.; Franke, D.; Sebastián, V.; Bawendi, M. G.; Jensen, K. F. Characterization of Indium Phosphide Quantum Dot Growth Intermediates Using MALDI-TOF Mass Spectrometry. *J. Am. Chem. Soc.* **2016**, *138* (41), 13469–13472. https://doi.org/10.1021/jacs.6b06468.

(6) McMurtry, B. M.; Qian, K.; Teglasi, J. K.; Swarnakar, A. K.; De Roo, J.; Owen, J. S. Continuous Nucleation and Size Dependent Growth Kinetics of Indium Phosphide Nanocrystals. *Chem. Mater.* **2020**, *32* (10), 4358–4368. https://doi.org/10.1021/acs.chemmater.0c01561.

(7) Gary, D. C.; Flowers, S. E.; Kaminsky, W.; Petrone, A.; Li, X.; Cossairt, B. M. Single-Crystal and Electronic Structure of a 1.3 Nm Indium Phosphide Nanocluster. *J. Am. Chem. Soc.* **2016**, *138* (5), 1510–1513. https://doi.org/10.1021/jacs.5b13214.

(8) Ning, J.; Banin, U. Magic Size InP and InAs Clusters: Synthesis, Characterization and Shell Growth. *Chem. Commun.* **2017**, *53* (17), 2626–2629. https://doi.org/10.1039/C6CC09778B.

(9) Gary, D. C.; Petrone, A.; Li, X.; Cossairt, B. M. Investigating the Role of Amine in InP Nanocrystal Synthesis: Destabilizing Cluster Intermediates by Z-Type Ligand Displacement. *Chem Commun* **2016**, *53* (1), 161–164. https://doi.org/10.1039/C6CC07952K.

(10) Kwon, Y.; Oh, J.; Lee, E.; Lee, S. H.; Agnes, A.; Bang, G.; Kim, J.; Kim, D.; Kim, S. Evolution from Unimolecular to Colloidal-Quantum-Dot-like Character in Chlorine or Zinc Incorporated InP Magic Size Clusters. *Nat Commun* **2020**, *11* (1), 3127. https://doi.org/10.1038/s41467-020-16855-9.

(11) Friedfeld, M. R.; Stein, J. L.; Johnson, D. A.; Park, N.; Henry, N. A.; Enright, M. J.; Mocatta, D.; Cossairt, B. M. Effects of Zn2+ and Ga3+ Doping on the Quantum Yield of Cluster-Derived InP Quantum Dots. *J Chem Phys* **2019**, *151* (19). https://doi.org/10.1063/1.5126971.

(12) Ritchhart, A.; Cossairt, B. M. Templated Growth of InP Nanocrystals with a Polytwistane Structure. *Angew. Chem. Int. Ed.* **2018**, *57* (7), 1908–1912. https://doi.org/10.1002/anie.201711539.

(13) Gazis, T. A.; Matthews, P. D. Reeling Them in: Ph2PSiMe3 in the Sequential Formation of InP Magic-Sized Clusters. *Chem Commun* **2022**, *58* (99), 13799–13802. https://doi.org/10.1039/D2CC06204F.

(14) Zhao, Q.; Kulik, H. J. Electronic Structure Origins of Surface-Dependent Growth in III–V Quantum Dots. *Chem. Mater.* **2018**, *30* (20), 7154–7165. https://doi.org/10.1021/acs.chemmater.8b03125.

(15) Shim, D.; Kang, J. Enhanced Reactivity of Magic-Sized Inorganic Clusters by Engineering the Surface Ligand Networks. *Chem. Mater.* **2023**, *35* (2), 700–708. https://doi.org/10.1021/acs.chemmater.2c03394.

(16) Williamson, C. B.; Nevers, D. R.; Nelson, A.; Hadar, I.; Banin, U.; Hanrath, T.; Robinson, R. D. Chemically Reversible Isomerization of Inorganic Clusters. *Science* **2019**, *363* (6428), 731–735. https://doi.org/10.1126/science.aau9464.

(17) Shim, D.; Lee, J.; Kang, J. Multiscale Isomerization of Magic-Sized Inorganic Clusters Chemically Driven by Atomic-Bond Exchanges. *Chem Mater* **2022**, *34* (21), 9527–9535. https://doi.org/10.1021/acs.chemmater.2c02018.

(18) Bootharaju, M. S.; Baek, W.; Deng, G.; Singh, K.; Voznyy, O.; Zheng, N.; Hyeon, T. Structure of a Subnanometer-Sized Semiconductor Cd14Se13 Cluster. *Chem* **2022**, *8* (11), 2978–2989. https://doi.org/10.1016/j.chempr.2022.06.025.

(19) Kühl, O. *The Range of Chemical Shifts, Coupling Constants, and What Influences Each. In Phosphorus-31 NMR Spectroscopy: A Concise Introduction for the Synthetic Organic and Organometallic Chemist*; Kühl, O., Ed.; Springer: Berlin Heidelberg: Berlin, Heidelberg, 2008. https://doi.org/10.1007/978-3-540-79118-8_2.

(20) Dippy, J. F. J.; Hughes, S. R. C.; Laxton, J. W. Chemical Constitution and the Dissociation Constants of Monocarboxylic Acids. Part XIII. Some Alkylbenzoic Acids Exhibiting Steric Effects. *J Chem Soc* **1954**, No. 0, 1470–1476. https://doi.org/10.1039/JR9540001470.

(21) Baker, J. W.; Dippy, J. F. J.; Page, J. E. The Dissociation Constants of Alkyl-Substituted Benzoic and Phenylacetic Acids. *J Chem Soc* **1937**, No. 0, 1774–1779. https://doi.org/10.1039/JR9370001774.

(22) Hoefnagel, A. J.; Wepster, B. M. Further Studies an the Extended Hammett Equation Comprising the Hydrophobic Constant: Reactivity Data for Benzoic Acids, Arylacetic Acids, β-Arylpropionic Acids, Trans- and Cis-Cinnamic Acids, Methyl Benzoates; Dissociation Constants, DDM Reaction and Alkaline Hydrolysis in Various Water-Organic Solvent Mixtures. *Collect Czech Chem Commun* **1990**, *55* (1), 119–135. https://doi.org/10.1135/cccc19900119.

(23) Tolman, C. A. Steric Effects of Phosphorus Ligands in Organometallic Chemistry and Homogeneous Catalysis. *Chem Rev* **1977**, *77* (3), 313–348. https://doi.org/10.1021/cr60307a002.

(24) Marion, D. An Introduction to Biological NMR Spectroscopy. *Mol Cell Proteomics* **2013**, *12* (11), 3006–3025. https://doi.org/10.1074/mcp.O113.030239.

(25) Juhás, P.; Davis, T.; Farrow, C. L.; Billinge, S. J. L. PDFgetX3: A Rapid and Highly Automatable Program for Processing Powder Diffraction Data into Total Scattering Pair Distribution Functions. *J. Appl. Crystallogr.* **2013**, *46* (2), 560–566. https://doi.org/10.1107/S0021889813005190.

(26) Yang, X.; Masadeh, A. S.; McBride, J. R.; Božin, E. S.; Rosenthal, S. J.; Billinge, S. J. L. Confirmation of Disordered Structure of Ultrasmall CdSe Nanoparticles from X-Ray Atomic Pair Distribution Function Analysis. *Phys. Chem. Chem. Phys.* **2013**, *15* (22), 8480–8486. https://doi.org/10.1039/C3CP00111C.

(27) Bedel, E.; Landa, G.; Carles, R.; Redoules, J. P.; Renucci, J. B. Raman Investigation of the InP Lattice Dynamics. *J Phys C Solid State Phys* **1986**, *19* (10), 1471–1479. https://doi.org/10.1088/0022-3719/19/10/004.

(28) Vasilevsky, M. I.; Rolo, A. G.; Gomes, M. J. M.; Gaponik, N. P.; Talapin, D. V.; Rogach, A. L. Raman and FIR Studies of Optical Phonons Confined in InP Quantum Dots. In *Conference Proceedings. 14th Indium Phosphide and Related Materials Conference (Cat. No.02CH37307*; 2002; pp 67–70. https://doi.org/10.1109/ICIPRM.2002.1014108.

(29) Seong, M. J.; Mićić, O. I.; Nozik, A. J.; Mascarenhas, A.; Cheong, H. M. Size-Dependent Raman Study of InP Quantum Dots. *Appl. Phys. Lett.* **2003**, *82* (2), 185–187. https://doi.org/10.1063/1.1535272.

(30) Beecher, A. N.; Dziatko, R. A.; Steigerwald, M. L.; Owen, J. S.; Crowther, A. C. Transition from Molecular Vibrations to Phonons in Atomically Precise Cadmium Selenide Quantum Dots. *J Am Chem Soc* **2016**, *138* (51), 16754–16763. https://doi.org/10.1021/jacs.6b10705.

(31) Huang, M.; Yan, H.; Heinz, T. F.; Hone, J. Probing Strain-Induced Electronic Structure Change in Graphene by Raman Spectroscopy. *Nano Lett* **2010**, *10* (10), 4074–4079. https://doi.org/10.1021/nl102123c.

(32) Neumann, C.; Reichardt, S.; Venezuela, P.; Drögeler, M.; Banszerus, L.; Schmitz, M.; Watanabe, K.; Taniguchi, T.; Mauri, F.; Beschoten, B.; Rotkin, S. V.; Stampfer, C. Raman Spectroscopy as Probe of Nanometre-Scale Strain Variations in Graphene. *Nat Commun* **2015**, *6* (1), 8429. https://doi.org/10.1038/ncomms9429.

(33) Huang, M.; Yan, H.; Chen, C.; Song, D.; Heinz, T. F.; Hone, J. Phonon Softening and Crystallographic Orientation of Strained Graphene Studied by Raman Spectroscopy. *Proc. Natl. Acad. Sci. 2009 106* (18), 7304–7308. https://doi.org/10.1073/pnas.0811754106.

(34) Leger, J. D.; Friedfeld, M. R.; Beck, R. A.; Gaynor, J. D.; Petrone, A.; Li, X.; Cossairt, B. M.; Khalil, M. Carboxylate Anchors Act as Exciton Reporters in 1.3 Nm Indium Phosphide Nanoclusters. *J. Phys. Chem. Lett.* **2019**, *10* (8), 1833–1839. https://doi.org/10.1021/acs.jpclett.9b00602.

(35) Klein, M. D.; Bisted, C. H.; Dou, F. Y.; Sandwisch, J. W.; Cossairt, B. M.; Khalil, M. Measuring Relative Energies of Ligand Binding Conformations on Nanocluster Surfaces with Temperature-Dependent FTIR Spectroscopy. *J. Phys. Chem. C* **2023**, *127* (34), 16970–16978. https://doi.org/10.1021/acs.jpcc.3c03951.

(36) Zeleňák, V.; Vargová, Z.; Györyová, K. Correlation of Infrared Spectra of Zinc(II) Carboxylates with Their Structures. *Spectrochim. Acta. A. Mol. Biomol. Spectrosc.* **2007**, *66* (2), 262–272. https://doi.org/10.1016/j.saa.2006.02.050.

(37) Newton, J. C.; Ramasamy, K.; Mandal, M.; Joshi, G. K.; Kumbhar, A.; Sardar, R. Low-Temperature Synthesis of Magic-Sized CdSe Nanoclusters: Influence of Ligands on

Nanocluster Growth and Photophysical Properties. *J Phys Chem C* **2012**, *116* (7), 4380–4389. https://doi.org/10.1021/jp2086818.

(38) Kilina, S.; Ivanov, S.; Tretiak, S. Effect of Surface Ligands on Optical and Electronic Spectra of Semiconductor Nanoclusters. *J Am Chem Soc* **2009**, *131* (22), 7717–7726. https://doi.org/10.1021/ja9005749.

(39) Cossairt, B. M.; Juhas, P.; Billinge, S. J. L.; Owen, J. S. Tuning the Surface Structure and Optical Properties of CdSe Clusters Using Coordination Chemistry. *J Phys Chem Lett* **2011**, *2* (24), 3075–3080. https://doi.org/10.1021/jz2013769.

(40) Liu, Y.-H.; Wang, F.; Wang, Y.; Gibbons, P. C.; Buhro, W. E. Lamellar Assembly of Cadmium Selenide Nanoclusters into Quantum Belts. *J Am Chem Soc* **2011**, *133* (42), 17005–17013. https://doi.org/10.1021/ja206776g.

(41) Del Ben, M.; Havenith, R. W. A.; Broer, R.; Stener, M. Density Functional Study on the Morphology and Photoabsorption of CdSe Nanoclusters. *J Phys Chem C* **2011**, *115* (34), 16782–16796. https://doi.org/10.1021/jp203686a.

(42) Nevers, D. R.; Williamson, C. B.; Hanrath, T.; Robinson, R. D. Surface Chemistry of Cadmium Sulfide Magic-Sized Clusters: A Window into Ligand-Nanoparticle Interactions. *Chem Commun* **2017**, *53* (19), 2866–2869. https://doi.org/10.1039/C6CC09549F.

(43) Jiang, Z.-J.; Kelley, D. F. Role of Magic-Sized Clusters in the Synthesis of CdSe Nanorods. *ACS Nano* **2010**, *4* (3), 1561–1572. https://doi.org/10.1021/nn100076f.

(44) Cumberland, S. L.; Hanif, K. M.; Javier, A.; Khitrov, G. A.; Strouse, G. F.; Woessner, S. M.; Yun, C. S. Inorganic Clusters as Single-Source Precursors for Preparation of CdSe, ZnSe, and CdSe/ZnS Nanomaterials. *Chem Mater* **2002**, *14* (4), 1576–1584. https://doi.org/10.1021/cm010709k.

(45) Jawaid, A. M.; Chattopadhyay, S.; Wink, D. J.; Page, L. E.; Snee, P. T. Cluster-Seeded Synthesis of Doped CdSe:Cu4 Quantum Dots. *ACS Nano* **2013**, *7* (4), 3190–3197. https://doi.org/10.1021/nn305697q.

(46) Chakravarty, C.; Debenedetti, P. G.; Stillinger, F. H. Lindemann Measures for the Solid-Liquid Phase Transition. *J. Chem. Phys.* **2007**, *126* (20), 204508. https://doi.org/10.1063/1.2737054.

(47) Battaglia, D.; Peng, X. Formation of High Quality InP and InAs Nanocrystals in a Noncoordinating Solvent. *Nano Lett* **2002**, *2* (9), 1027–1030. https://doi.org/10.1021/nl025687v.

(48) Lucey, D. W.; MacRae, D. J.; Furis, M.; Sahoo, Y.; Cartwright, A. N.; Prasad, P. N. Monodispersed InP Quantum Dots Prepared by Colloidal Chemistry in a Noncoordinating Solvent. *Chem Mater* **2005**, *17* (14), 3754–3762. https://doi.org/10.1021/cm050110a.

(49) Ouyang, J.; Kuijper, J.; Brot, S.; Kingston, D.; Wu, X.; Leek, D. M.; Hu, M. Z.; Ripmeester, J. A.; Yu, K. Photoluminescent Colloidal CdS Nanocrystals with High Quality via Noninjection One-Pot Synthesis in 1-Octadecene. *J Phys Chem C* **2009**, *113* (18), 7579–7593. https://doi.org/10.1021/jp900252e.

(50) Nolf, K.; Capek, R. K.; Abe, S.; Sluydts, M.; Jang, Y.; Martins, J. C.; Cottenier, S.; Lifshitz, E.; Hens, Z. Controlling the Size of Hot Injection Made Nanocrystals by Manipulating the Diffusion Coefficient of the Solute. *J Am Chem Soc* **2015**, *137* (7), 2495–2505. https://doi.org/10.1021/ja509941g.

(51) Dümbgen, K. C.; Zito, J.; Infante, I.; Hens, Z. Shape, Electronic Structure, and Trap States in Indium Phosphide Quantum Dots. *Chem. Mater.* **2021**, *33* (17), 6885–6896. https://doi.org/10.1021/acs.chemmater.1c01795.

(52) Ripberger, H. H.; Schnitzenbaumer, K. J.; Nguyen, L. K.; Ladd, D. M.; Levine, K. R.; Dayton, D. G.; Toney, M. F.; Cossairt, B. M. Navigating the Potential Energy Surface of CdSe Magic-Sized Clusters: Synthesis and Interconversion of Atomically Precise Nanocrystal Polymorphs. *J. Am. Chem. Soc.* **2023**, *145* (50), 27480–27492. https://doi.org/10.1021/jacs.3c08897.

(53) Ma, F.; Abboud, K. A.; Zeng, C. Precision Synthesis of a CdSe Semiconductor Nanocluster via Cation Exchange. *Nat. Synth.* **2023**, *2* (10), 949–959. https://doi.org/10.1038/s44160-023-00330-6.

(54) Deveson, A.; Dehnen, S.; Fenske, D. Syntheses and Structures of Four New Copper(I)–Selenium Clusters: Size Dependence of the Cluster on the Reaction Conditions. *J Chem Soc Dalton Trans* **1997**, No. 23, 4491–4498. https://doi.org/10.1039/A705750D.

(55) Shin, J.; Choi, M.; Shim, D.; Ziehl, T. J.; Park, S.; Cho, E.; Zhang, P.; Lee, H.; Kang, J.; Jeong, S. Unveiling the Nanocluster Conversion Pathway for Highly Monodisperse InAs Colloidal Quantum Dots. *JACS Au* **2024**, *4* (3), 1097–1106. https://doi.org/10.1021/jacsau.3c00809.

(56) Li, Y.; Hou, X.; Shen, Y.; Dai, N.; Peng, X. Tuning the Reactivity of Indium Alkanoates by Tertiary Organophosphines for the Synthesis of Indium-Based Quantum Dots. *Chem Mater* **2021**, *33* (23), 9348–9356. https://doi.org/10.1021/acs.chemmater.1c03219.

(57) Lee, E.; Kwon, Y.; Agnes, A.; Ryu, Y.; Kim, S. Multiple Roles of Magic-Sized Clusters in Quantum Dot Synthesis. *J. Phys. Chem. C* **2024**, *128* (4), 1809–1818. https://doi.org/10.1021/acs.jpcc.3c07189.

(58) Tiwari, N.; Liang, Q.; Fedin, I. Cd3P2 QDs Emitting in the SWIR through Overgrowth of Cadmium Phosphide Clusters. *Nanoscale* **2025**, *17* (20), 12654–12659. https://doi.org/10.1039/D5NR00002E.

(59) Ramasamy, P.; Kim, N.; Kang, Y.-S.; Ramirez, O.; Lee, J.-S. Tunable, Bright, and Narrow-Band Luminescence from Colloidal Indium Phosphide Quantum Dots. *Chem. Mater.* **2017**, *29* (16), 6893–6899. https://doi.org/10.1021/acs.chemmater.7b02204.

(60) Stam, M.; Almeida, G.; Ubbink, R. F.; van der Poll, L. M.; Vogel, Y. B.; Chen, H.; Giordano, L.; Schiettecatte, P.; Hens, Z.; Houtepen, A. J. Near-Unity Photoluminescence Quantum Yield of Core-Only InP Quantum Dots via a Simple Postsynthetic InF3 Treatment. *ACS Nano* **2024**, *18* (22), 14685–14695. https://doi.org/10.1021/acsnano.4c03290.

(61) Shen, C.; Zhu, Y.; Li, Z.; Li, J.; Tao, H.; Zou, J.; Xu, X.; Xu, G. Highly Luminescent InP–In(Zn)P/ZnSe/ZnS Core/Shell/Shell Colloidal Quantum Dots with Tunable Emissions Synthesized Based on Growth-Doping. *J. Mater. Chem. C* **2021**, *9* (30), 9599–9609. https://doi.org/10.1039/D1TC01664D.

(62) Xu, Z.; Li, Y.; Li, J.; Pu, C.; Zhou, J.; Lv, L.; Peng, X. Formation of Size-Tunable and Nearly Monodisperse InP Nanocrystals: Chemical Reactions and Controlled Synthesis. *Chem. Mater.* **2019**, *31* (14), 5331–5341. https://doi.org/10.1021/acs.chemmater.9b02292.

(63) Xie, L.; Shen, Y.; Franke, D.; Sebastián, V.; Bawendi, M. G.; Jensen, K. F. Characterization of Indium Phosphide Quantum Dot Growth Intermediates Using MALDI-TOF Mass Spectrometry. *J. Am. Chem. Soc.* **2016**, *138* (41), 13469–13472. https://doi.org/10.1021/jacs.6b06468.

(64) Heaven, M. W.; Dass, A.; White, P. S.; Holt, K. M.; Murray, R. W. Crystal Structure of the Gold Nanoparticle [N(C8H17)4][Au25(SCH2CH2Ph)18]. *J. Am. Chem. Soc.* **2008**, *130* (12), 3754–3755. https://doi.org/10.1021/ja800561b.

(65) Gary, D. C.; Cossairt, B. M. Role of Acid in Precursor Conversion During InP Quantum Dot Synthesis. *Chem. Mater.* **2013**, *25* (12), 2463–2469. https://doi.org/10.1021/cm401289j.

(66) Bruker. APEX2, 2007.

(67) Sheldrick : A short history of SHELX. *Acta Cryst* **2008**, *A64*, 112–122.

(68) Altomare, A.; Burla, M. C.; Camalli, M.; Cascarano, G. L.; Giacovazzo, C.; Guagliardi, A.; Moliterni, A. G. G.; Polidori, G.; Spagna, R. SIR97: A New Tool for Crystal Structure Determination and Refinement. *J. Appl. Crystallogr.* **1999**, *32* (1), 115–119. https://doi.org/10.1107/S0021889898007717.

(69) MaXus: A Computer Program for the Solution and Refinement of Crystal Structures from Diffraction Data.

(70) Waasmaier, D.; Kirfel, A. New Analytical Scattering Factor Functions for Free Atoms and Ions, 1995.

(71) Spek A. *J Appl Cryst* **2003**, *36*, 7–13.

(72) Sluis; Spek, A. L. Acta Cryst, 1990, *A46*, 194–201.

(73) Spek, A. L. Acta. *Cryst* **2009**, *D65*, 148–155.

(74) Gaussian 16, Revision C.01, Frisch, M. J.; Trucks, G. W.; Schlegel, H. B.; Scuseria, G. E.; Robb, M. A.; Cheeseman, J. R.; Scalmani, G.; Barone, V.; Petersson, G. A.; Nakatsuji, H.; Li, X.; Caricato, M.; Marenich, A. V.; Bloino, J.; Janesko, B. G.; Gomperts, R.; Mennucci, B.; Hratchian, H. P.; Ortiz, J. V.; Izmaylov, A. F.; Sonnenberg, J. L.; Williams-Young, D.;

Ding, F.; Lipparini, F.; Egidi, F.; Goings, J.; Peng, B.; Petrone, A.; Henderson, T.; Ranasinghe, D.; Zakrzewski, V. G.; Gao, J.; Rega, N.; Zheng, G.; Liang, W.; Hada, M.; Ehara, M.; Toyota, K.; Fukuda, R.; Hasegawa, J.; Ishida, M.; Nakajima, T.; Honda, Y.; Kitao, O.; Nakai, H.; Vreven, T.; Throssell, K.; Montgomery, J. A., Jr.; Peralta, J. E.; Ogliaro, F.; Bearpark, M. J.; Heyd, J. J.; Brothers, E. N.; Kudin, K. N.; Staroverov, V. N.; Keith, T. A.; Kobayashi, R.; Normand, J.; Raghavachari, K.; Rendell, A. P.; Burant, J. C.; Iyengar, S. S.; Tomasi, J.; Cossi, M.; Millam, J. M.; Klene, M.; Adamo, C.; Cammi, R.; Ochterski, J. W.; Martin, R. L.; Morokuma, K.; Farkas, O.; Foresman, J. B.; Fox, D. J. Gaussian, Inc., Wallingford CT, 2016.

(75) Heyd, J.; Scuseria, G. E. Efficient Hybrid Density Functional Calculations in Solids: Assessment of the Heyd–Scuseria–Ernzerhof Screened Coulomb Hybrid Functional. *J. Chem. Phys.* **2004**, *121* (3), 1187–1192. https://doi.org/10.1063/1.1760074.

(76) Heyd, J.; Scuseria, G. E.; Ernzerhof, M. Hybrid Functionals Based on a Screened Coulomb Potential. *J. Chem. Phys.* **2003**, *118* (18), 8207–8215. https://doi.org/10.1063/1.1564060.

(77) Vydrov, O. A.; Heyd, J.; Krukau, A. V.; Scuseria, G. E. Importance of Short-Range versus Long-Range Hartree-Fock Exchange for the Performance of Hybrid Density Functionals. *J. Chem. Phys.* **2006**, *125* (7), 074106. https://doi.org/10.1063/1.2244560.

(78) Cho, E.; Jang, H.; Lee, J.; Jang, E. Modeling on the Size Dependent Properties of InP Quantum Dots: A Hybrid Functional Study. *Nanotechnology* **2013**, *24* (21), 215201. https://doi.org/10.1088/0957-4484/24/21/215201.

(79) Casida, M. E.; Jamorski, C.; Casida, K. C.; Salahub, D. R. Molecular Excitation Energies to High-Lying Bound States from Time-Dependent Density-Functional Response Theory: Characterization and Correction of the Time-Dependent Local Density Approximation

Ionization Threshold. *J. Chem. Phys.* **1998**, *108* (11), 4439–4449. https://doi.org/10.1063/1.475855.

(80) Furche, F.; Ahlrichs, R. Adiabatic Time-Dependent Density Functional Methods for Excited State Properties. *J. Chem. Phys.* **2002**, *117* (16), 7433–7447. https://doi.org/10.1063/1.1508368.

(81) Stratmann, R. E.; Scuseria, G. E.; Frisch, M. J. An Efficient Implementation of Time-Dependent Density-Functional Theory for the Calculation of Excitation Energies of Large Molecules. *J. Chem. Phys.* **1998**, *109* (19), 8218–8224. https://doi.org/10.1063/1.477483.

Chapter 3. SYNTHESIS AND SINGLE CRYSTAL X-RAY DIFFRACTION STRUCTURE OF AN INDIUM ARSENIDE NANOCLUSTER

Components of this chapter were republished with permission of the American Chemical Society, from Synthesis and Single Crystal X-ray Diffraction Structure of an Indium Arsenide Nanocluster", Soren F. Sandeno, Sebastian M. Krajewski, Ryan A. Beck, Werner Kaminsky, Xiaosong Li, and Brandi M. Cossairt; *ACS Central Science.* **2024**, *10* (3), 744–751; Copyright 2024 American Chemical Society.

3.1 INTRODUCTION

Ever since the initial discovery of quantum dots (QDs), the mechanism by which they nucleate and grow has been the subject of intense experimental and theoretical study.[1–9] While some nanocrystal syntheses have been rationalized through a model of classical nucleation involving a temporally discrete nucleation event, followed by growth,[10,11] further investigation has shown that many systems deviate in complex ways from this classical model.[12,13] One of the most important departures from the classical model of nucleation and growth is the formation of magic-sized clusters during the early stages of precursor conversion.[14–17]

Magic-sized clusters are atomically-precise molecules that form as intermediates during the transition from precursors to nanocrystals. Their documentation in the literature is pervasive across QD chemistries and has led to a deeper understanding of the complexities in nanocrystal growth mechanisms.[12,13,18–23] The formation of these clusters as intermediates breaks the kinetic

chain linking precursor reactivity to nanocrystal nucleation and growth meaning precursor tuning cannot be invoked to control size, shape or morphology.[12] While this generates synthetic challenges in controlling these material systems, some of the most impressive, industrially-relevant syntheses of QDs use precursors that are known to result in intermediate cluster formation.[24,25] The link between magic-sized clusters and superb QD quality continues to be under investigation to provide an understanding for why these two features are inextricably linked.

To understand the pathways of cluster formation and conversion, syntheses have been developed to allow for isolation and characterization of these intermediates.[12,22,26,27] The study of cluster intermediates not only informs the mechanism by which the ensuing QDs form, but also produces a molecular platform upon which post-synthetic chemistry can be studied, including ligand exchange, doping, conversion to QDs, and even cluster interconversions and self-assembly.[28–37] Many of the isolated clusters have been characterized optically but the premier characterization of these materials has come in the form of single-crystal X-ray diffraction (SCXRD), which can allow for complete structural determination. This method has been used extensively in the characterization of metallic nanoclusters to unveil a deep, refined understanding of intermediate structures, growth pathways, and surface chemistry in those systems.[38] While the number of reported semiconductor clusters is not as substantial, crystallography has demonstrated unprecedented phases that are not observable in the bulk, precise surface analysis of ligand binding modes and stoichiometries, and a more nuanced insight into the differences between clusters made up of different semiconducting materials.[18,22,39,40] With a tenacious approach to structural characterization, the QD field will benefit from the same insights that have allowed for great progress with metallic nanoclusters. Towards that end, the structures of clusters as QD intermediates have been determined for a wide variety of the most common semiconducting QD

materials such as CdSe, CdS, and InP.[18,22,39,40] However, there are many other material systems that have identified the presence of magic-sized clusters spectroscopically but still lack full structural characterization of those intermediates.[20,27,41–45]

One of the QD material systems that is known to form clusters but lacks structural characterization is InAs. The synthesis of high quality InAs QDs has been reported and improved upon for more than 20 years with much attention paid to the final monodispersity and less towards the formation mechanisms.[20,26,41,42,46–51] The vast majority of the reported syntheses use indium carboxylate, a tertiary alkylphosphine and a reactive silylarsine to nucleate and grow InAs QDs. In the process of studying this precursor system, magic-sized clusters were observed as an intermediate with a characteristic absorption doublet with maxima at 425 and 460 nm.[20,41,42,51] Even when investigating the usage of germylarsines to improve nanocrystal monodispersity, this characteristic cluster persists.[42] Since the initial optical characterization of the InAs magic-sized cluster, the use of this precursor system has continued to be the standard for the synthesis of high quality InAs QDs. However, the synthesis, isolation, and structural characterization of the cluster intermediate has remained elusive.

Herein we report a synthesis of InAs magic-sized clusters that allows for isolation of the material with a variety of carboxylate and phosphine ligands. Further characterization of the isolated material by SCXRD has shown the structure to be $In_{26}As_{18}(O_2CR)_{24}(PR_3)_3$ with a mixed carboxylate and phosphine ligand environment on the surface and a relatively anisotropic core structure with pseudo-C_3 symmetry that persists to the ligand shell. This represents the first full structural characterization of an InAs magic-sized cluster and provides new insights into the comparative structures and structural evolution of III-V and II-VI clusters.

3.2 Synthesis and Isolation

Previous syntheses of InAs magic-sized clusters have shown that there are 3 essential precursors to allow for cluster formation: indium carboxylate, tertiary alkylphosphine, and silylarsine.[20,41,51] This stands in comparison to InP cluster syntheses which do not require an alkylphosphine for cluster formation or high-quality QD growth. The role of the tertiary alkylphosphine is understood to be twofold as it has been cited to function as a Lewis base to activate the indium carboxylate precursor as well as decrease the apparent reactivity of silylpnictides through solvation effects similar to reports of amines.[42,51,52] This suggests that the alkylphosphine requirement for InAs syntheses is likely a result of the higher reactivity of $As(SiMe_3)_3$ compared to $P(SiMe_3)_3$. The more reactive arsine precursor requires an increase in the reactivity of the indium carboxylate to achieve balanced reactivity and controlled nucleation. This can be accomplished by the inclusion of the alkylphosphine to activate the indium while simultaneously hindering the diffusion of the $As(SiMe_3)_3$.

In a typical synthesis, the indium carboxylate is generated through the reaction between indium acetate and carboxylic acid under vacuum or using trimethylindium and carboxylic acid in solution. The phosphine is then added to the indium precursor and the temperature is raised to 110 °C (**Figure 3.2.1A**). Once at the reaction temperature, a solution of $As(SiMe_3)_3$ is injected which immediately starts the reaction as shown in **Figure 3.2.1B**. We have found that hot-injection of $As(SiMe_3)_3$ into just indium carboxylate at 110 °C results in no productive cluster or QD formation and furthermore, the injection of the phosphine into this mixture immediately initiates cluster formation with no noticeable differences in absorbance (**Figure 3.2.2**). This result corroborates the findings on the role of the phosphine mentioned above and implicates the phosphine as necessary for balancing the precursor consumption rates that promote kinetic trapping and cluster formation.

As clusters evolve at 110 °C, there is a substantial amount of QD that forms as a side-product in these reactions. The relative stoichiometry of phosphine appears to have a consequential effect on the yield of cluster with respect to the amount of unproductive QD growth. When using myristate ligands, outside the range of 1 and 3 equivalents of phosphine relative to indium, there is a noticeable increase in the amount of undesirable QD formation. We propose that if the amount of phosphine is too low, not enough of the indium precursor is activated, leading to $As(SiMe_3)_3$ reacting with lower equivalents of activated indium. If the amount of phosphine approaches and exceeds 3 equivalents, the equilibrium is pushed towards a different surface ligand stoichiometry as the cluster forms causing destabilization and QD growth.

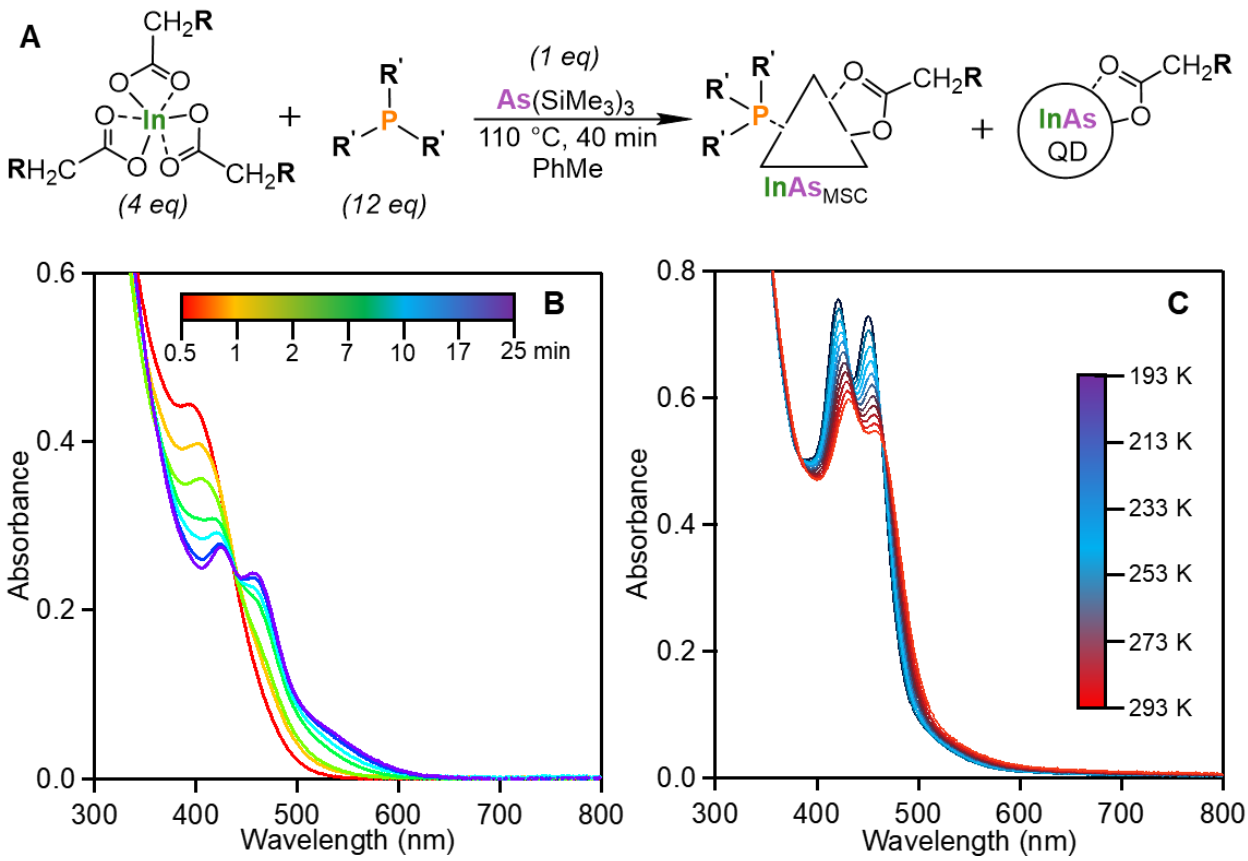

Figure 3.2.1. A) Reaction scheme for the synthesis of myristate and trioctylphosphine ligated InAs clusters. B) Absorbance progression of a typical InAs cluster synthesis using indium myristate and trioctylphosphine. C) Variable temperature absorbance of InAs clusters from 20 °C (red) to -80 °C (dark blue) in 10 °C increments in toluene.

While investigating ligand rigidity on the cluster surface to promote single crystal growth, we have concluded that the carboxylate chain is also important in directing cluster formation. The myristate-based indium precursor with a long chain hydrocarbon tail seems to promote the best control, yield, and robustness of the InAs cluster reaction. When transitioning to the use of phenylacetate, we document that the equivalents of organophosphine with respect to indium must be adapted. The 1-3 equivalent window is no longer accurate for indium phenylacetate and instead we find that not only does 1 equivalent of phosphine promote the best cluster growth but 3 eq. of

phosphine shows no cluster evolution. This difference in phosphine requirement between carboxylates is likely a function of the phosphine-bound indium carboxylate precursor speciation that has been found to vary with phosphine concentration.[51,53] We therefore suggest that while rigid ligands such as phenylacetate allow for structural determination by crystal growth as described below, the most robust InAs cluster syntheses are those that are heavily modulated by hindering diffusion of $As(SiMe_3)_3$ using long chain fatty acids.

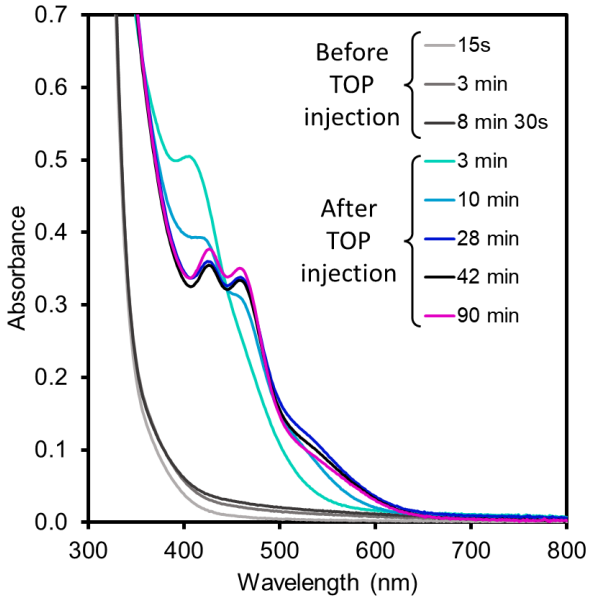

Figure 3.2.2. $As(SiMe_3)_3$ was injected into indium carboxylate in toluene as described in the synthesis of $In_{26}As_{18}(Myr)_{24}(TOP)_3$ in the absence of phosphine. With no development of recognizable absorbance features, 1.4 equivalents of trioctylphosphine with respect to indium was injected into the reaction causing the immediate formation of InAs clusters.

Further synthetic alterations to allow for single-crystal growth involved the use of diethylphenylphosphine (Et_2PhP) in place of the n-alkylphosphines. The yield of InAs cluster decreased substantially when using Et_2PhP as evidenced by an increase in the QD absorbance as well as a decrease in the peak-to-trough ratio of the cluster in the crude reaction. We observe no

significant synthetic differences in the InAs cluster synthesis when using tri-n-octylphosphine or tri-n-butylphosphine which suggests that there isn't an appreciable change with diffusion rate as modulated by the phosphine (**Figure 3.2.3**). Furthermore, the cone angle of the n-alkylphosphines (~132°) is quite similar to that of the Et_2PhP (136°). The electronic parameters reported for these phosphines are different however with tri-n-butylphosphine reported as 2060.3 cm^{-1} and Et_2PhP as 2063.7 cm^{-1}.[54] We suggest then that the binding affinity of the phosphine plays a valuable role in regulating the reactivity.

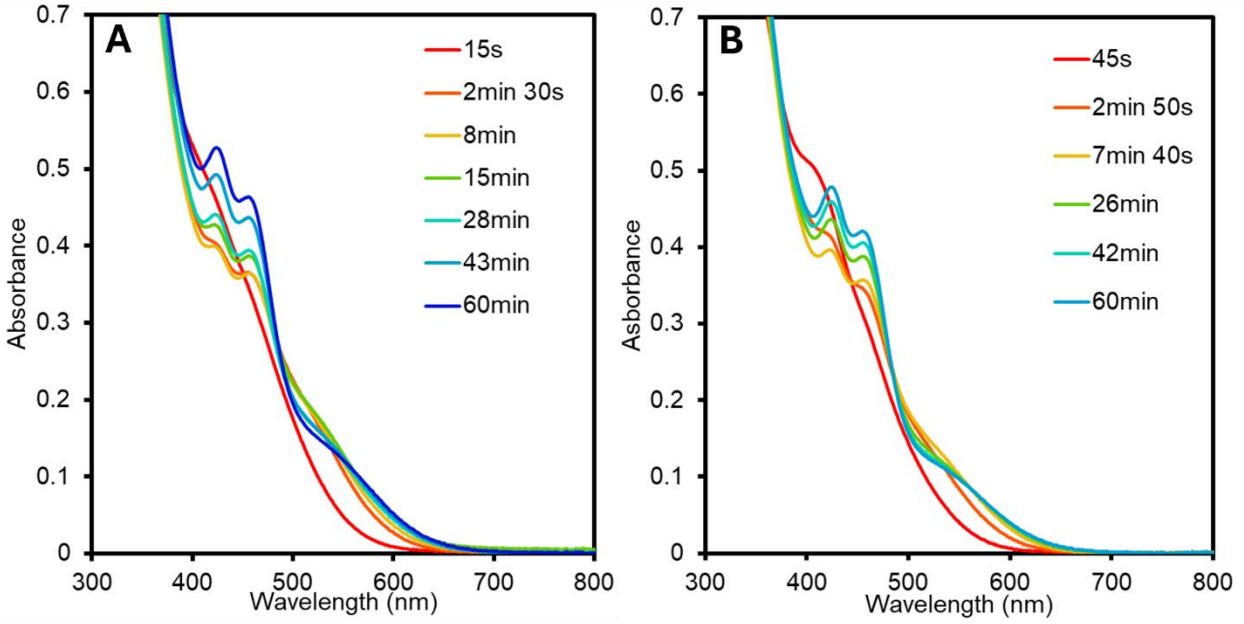

Figure 3.2.3. Equivalent $In_{26}As_{18}$ cluster reactions using phenylacetate and two different phosphine ligands: A) tributylphosphine, B) trioctylphosphine. The overall outcome of the synthesis as well as the kinetics of conversion do not seem to vary with n-alkylphosphine chain length.

With the absorbance progression of the InAs cluster synthesis shown in **Figure 3.2.1B**, we also document the formation of an initial absorbance feature at 395 nm within the first 20 seconds

of $As(SiMe_3)_3$ injection. This then converts through an isosbestic point giving way to the 425 nm and 460 nm features that are characteristic of the final InAs cluster. The rate of conversion of InAs-395 to InAs-460 is concentration dependent, which would suggest a conversion process based on growth as opposed to a structural rearrangement (**Figure 3.2.4**). It would then seem that the InAs-395 is substantially smaller compared to InAs-460 based on the energy of the first excitonic feature. Despite the concentration dependence of the cluster conversion rate, we document no significant difference in the overall yield of InAs cluster or the cluster to QD ratio when varying total reaction concentration (**Figure 3.2.4**).

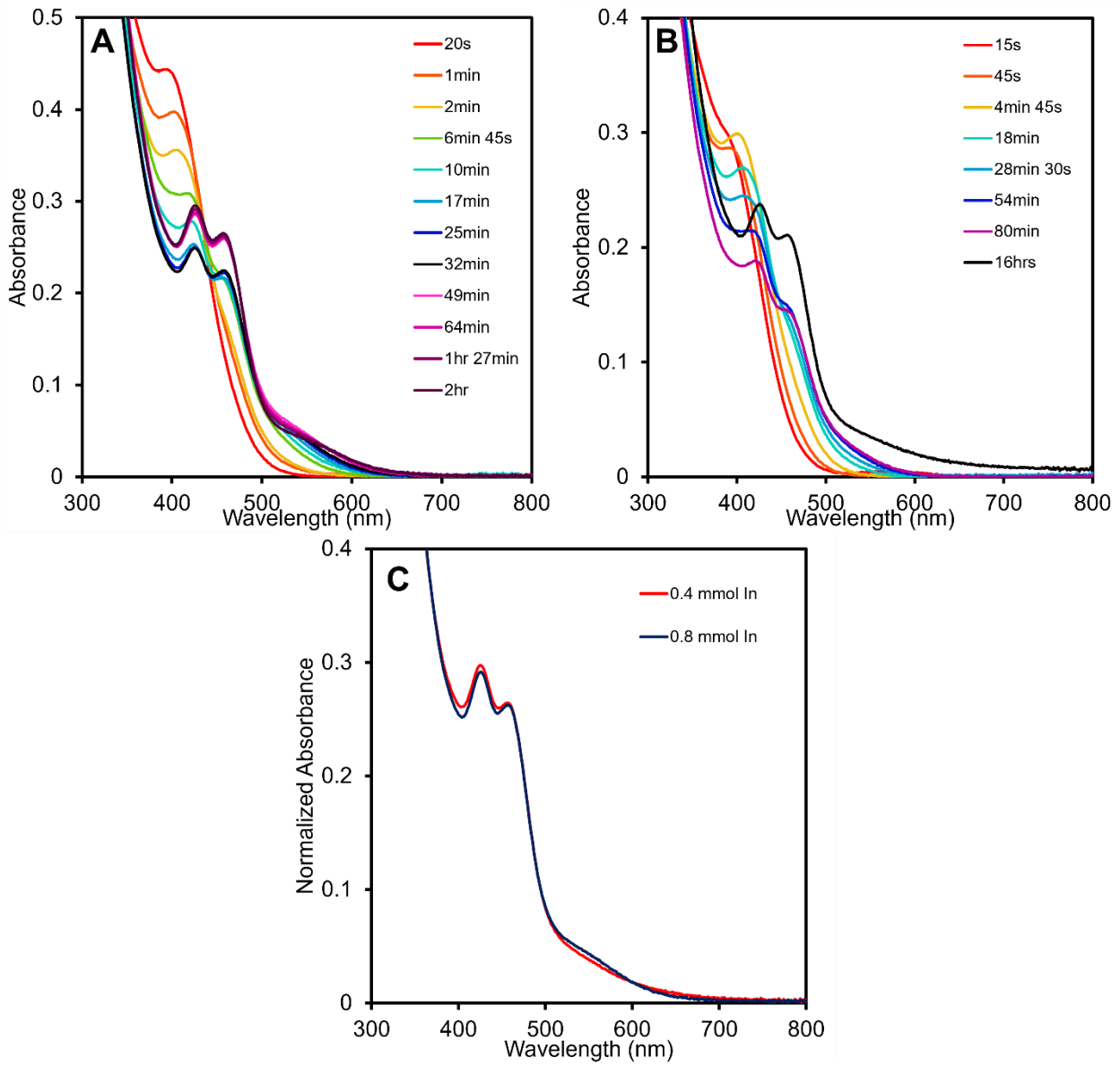

Figure 3.2.4. A) Absorbance progression for the synthesis of $In_{26}As_{18}(Myr)_{24}(TOP)_3$ clusters (0.8 mmol In, left). B) Absorbance progression for the synthesis of $In_{26}As_{18}(Myr)_{24}(TOP)_3$ clusters with all reagents at half concentration in toluene (0.4 mmol In, right). C) Final absorbance traces from the reactions in A and B normalized at 350 nm suggesting the reaction outcome does not correlate meaningfully with concentration despite the differences in conversion kinetics.

Purification of the InAs-460 cluster by size-exclusion chromatography allowed for further optical characterization through variable temperature absorbance measurements. From 20 °C down to -80 °C we observe significant spectral line narrowing that is consistent with vibronic coupling causing the line broadening at room temperature (**Figure 3.2.1C**). The narrowing, along with no absorbance changes upon returning to 20 °C, is consistent with previous variable temperature measurements on III-V cluster materials.[18,55] Along similar lines, the isolated cluster shows no measurable photoluminescence at room temperature and when cooled to 77 K shows broad emission ranging from 550 nm to beyond 700 nm (**Figure 3.2.5**).

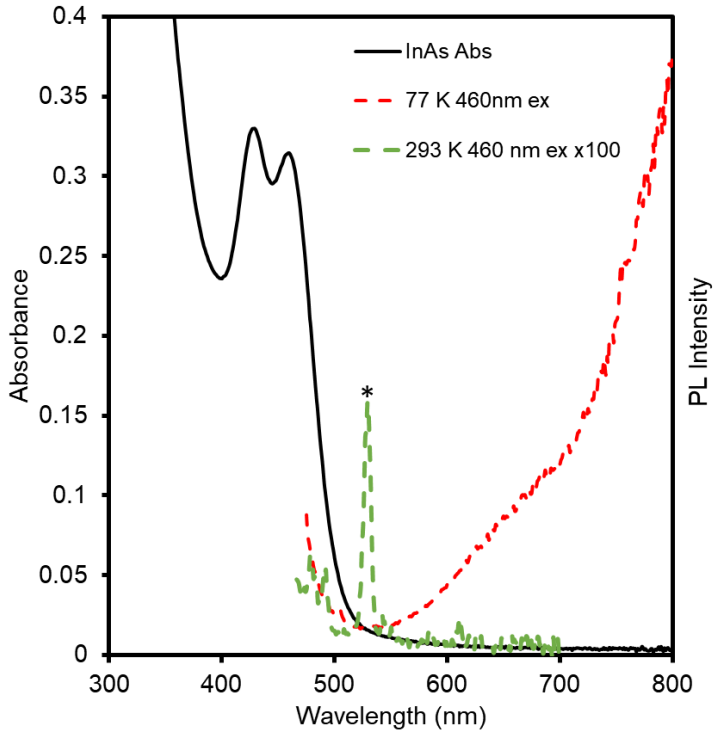

Figure 3.2.5. Photoluminescence of $In_{26}As_{18}(O_2CCH_2Ph)_{24}(PBu_3)_3$ at room temperature (green) and 77 K (red) with the absorbance shown in black. The sharp feature at 530 nm in the room temperature spectrum designated by the asterisk is a Raman feature from the solvent and does not represent photoluminescence from the sample.

This is not unexpected as the relatively low effective electron mass in bulk InAs (m_e = 0.023)[56] should allow for many nonradiative recombination pathways through exciton-surface interactions. The narrow absorbance features at room temperature for quantum-confined InAs combined with the high degree of monodispersity as evidenced by spontaneous superlattice formation upon preparation of films for transmission electron microscopy analysis (**Figure 3.2.6**) suggested atomic precision, motivating our pursuit of diffraction quality crystals of InAs-460 for single crystal X-ray analysis.

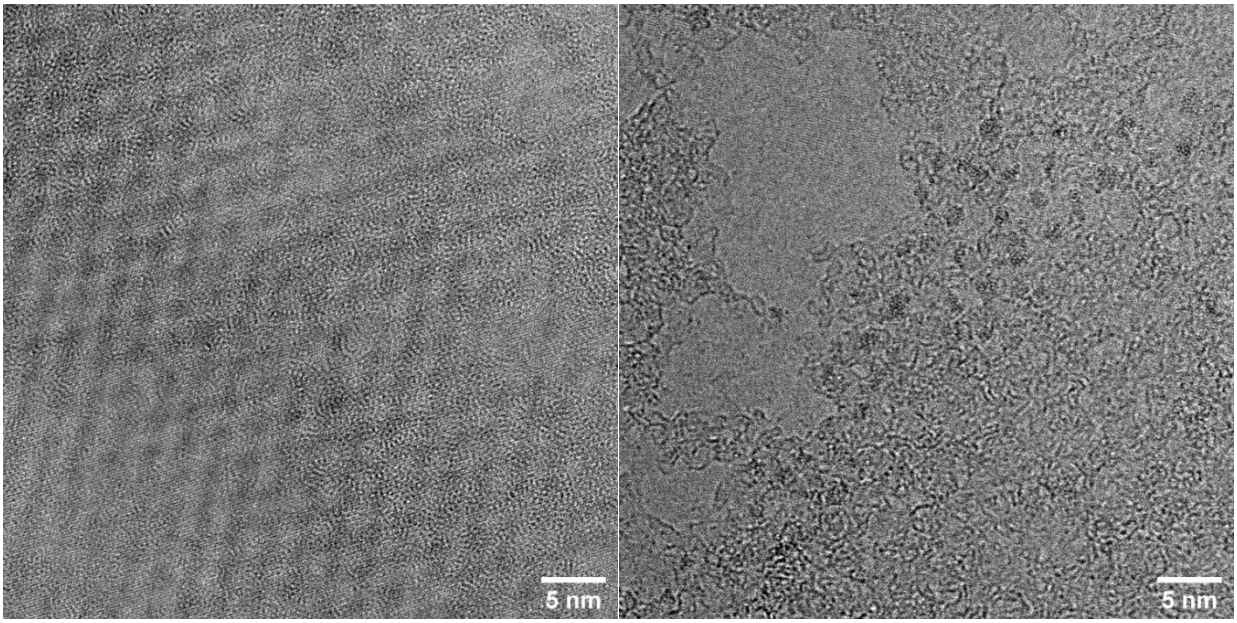

Figure 3.2.6. TEM micrographs of InAs clusters in a superlattice assembled by slow evaporation of toluene (left) and as discrete particles (right).

3.3 Crystal Growth and Structural Analysis

Modifying the synthesis of InAs clusters using indium phenylacetate and diethylphenylphosphine as ligands (**Figure 3.3.1**) allowed for the growth of X-ray quality single crystals from vapor diffusion (**Figure 3.3.2A, B**). Diffraction at a resolution of 0.86 Å with R_1 and

R_w values of 14.09% and 28.02%, respectively, allowed for a high-quality structural solution, providing the assignment $In_{26}As_{18}(O_2CR)_{24}(PR_3)_3$ (**Figure 3.3.6A**). Full crystallographic details are provided in the appendix.

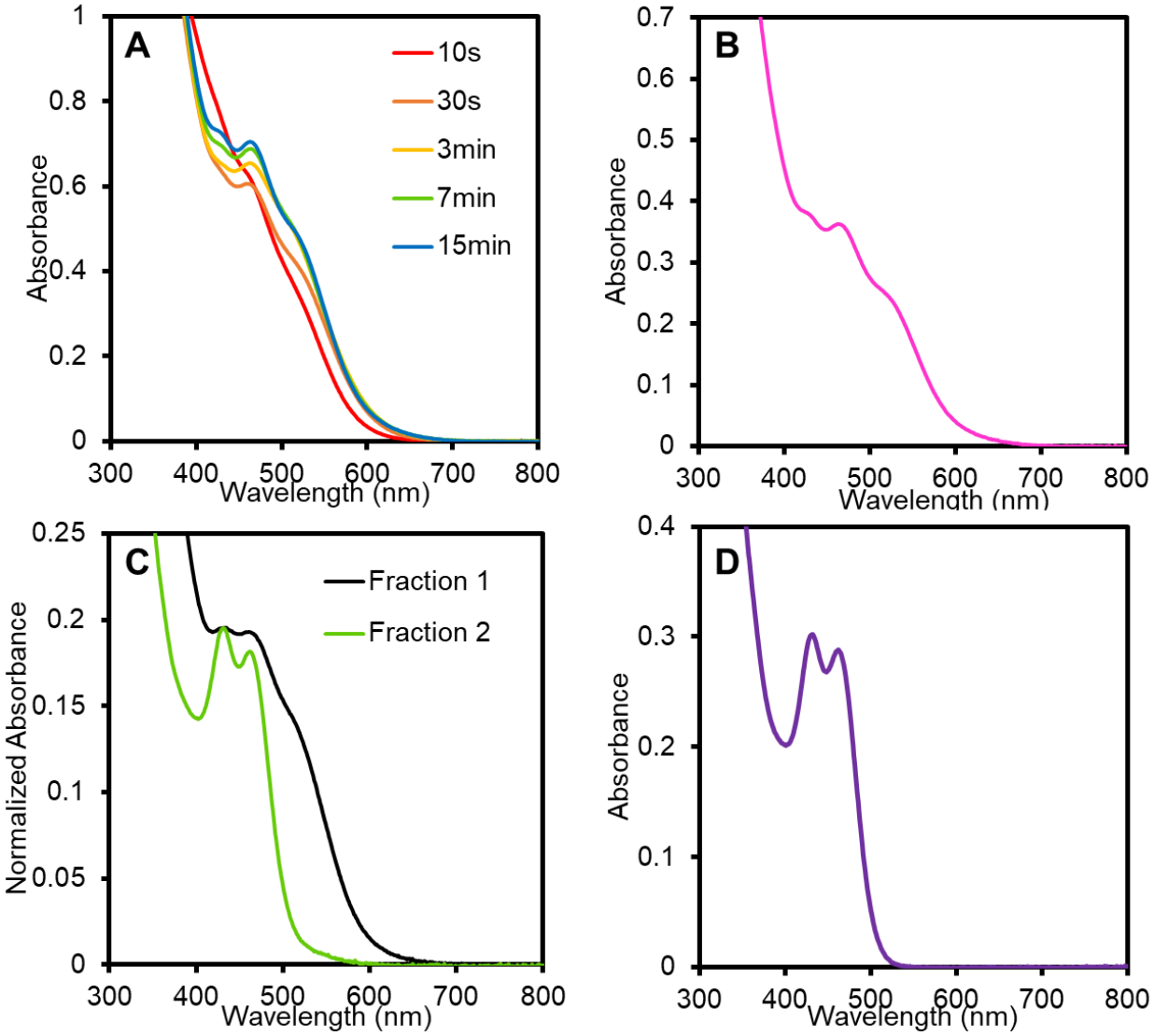

Figure 3.3.1. A) $In_{26}As_{18}(O_2CCH_2Ph)_{24}(PEt_2Ph)_3$ reaction progression. B) Final $In_{26}As_{18}(O_2CCH_2Ph)_{24}(PEt_2Ph)_3$ reaction trace after cooling and before purification. C) Absorbance traces of the two bands formed during size-exclusion chromatography. D) Absorbance of $In_{26}As_{18}(O_2CCH_2Ph)_{24}(PEt_2Ph)_3$ single crystals grown from an ether against pentane vapor diffusion and redispersed in toluene.

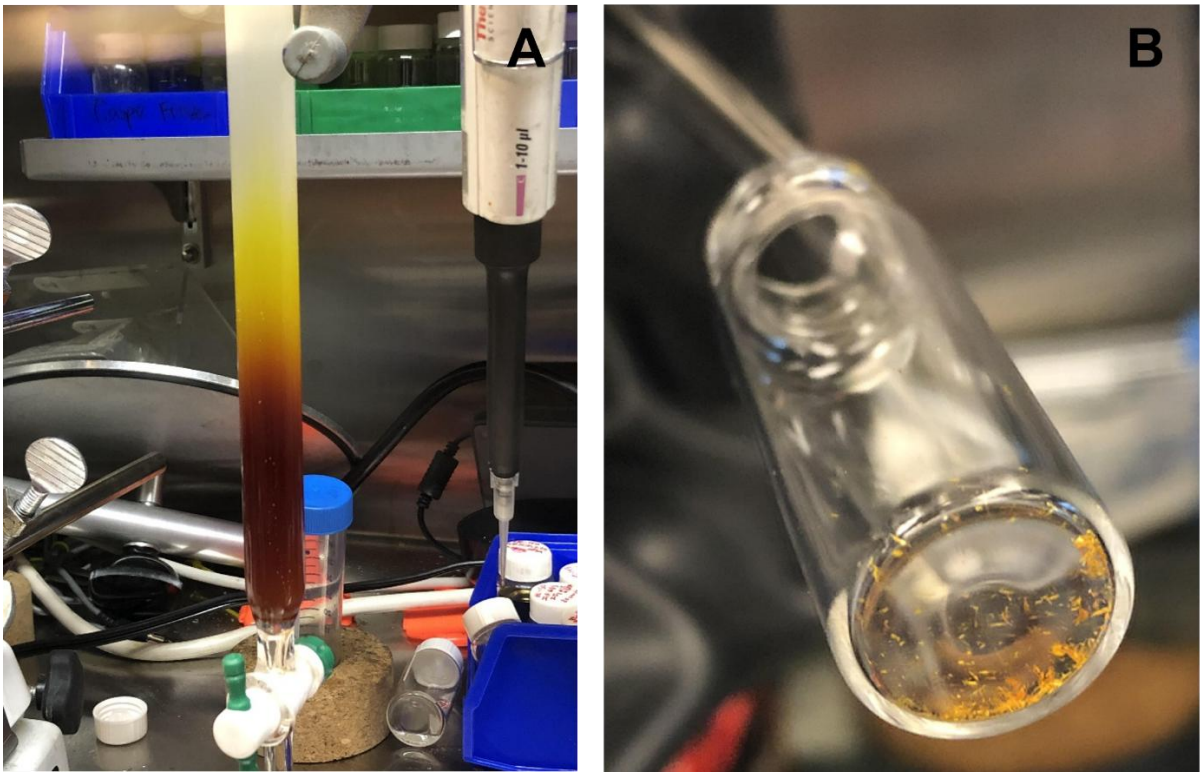

Figure 3.3.2. A) Direct purification of an InAs nanocluster reaction by size-exclusion chromatography. The yellow band is the $In_{26}As_{18}$ cluster and the dark red band is quantum dot impurity. B) Photograph of the isolated single crystals grown from an ether against pentane vapor diffusion.

The surface of this $In_{26}As_{18}$ cluster is ligated by 24 carboxylates and 3 alkylphosphines. The carboxylate ligands show a binding mode distribution of 9 chelating, 3 symmetric bridging, and 12 asymmetric bridging carboxylates. This affinity for asymmetric bridging carboxylates is consistent with other III-V cluster structures but the InAs seems to show an augmented ratio of the chelating binding mode in comparison to these other structures.[18,40] It is interesting to note that the L-type binding of water in those previously reported InP clusters forces bridging ligands into a monodentate binding mode. However, in the InAs cluster, the L-type binding of phosphines is to

otherwise 3-coordinate indium atoms, none of which are simultaneously ligated by carboxylates (**Figure 3.3.3**).

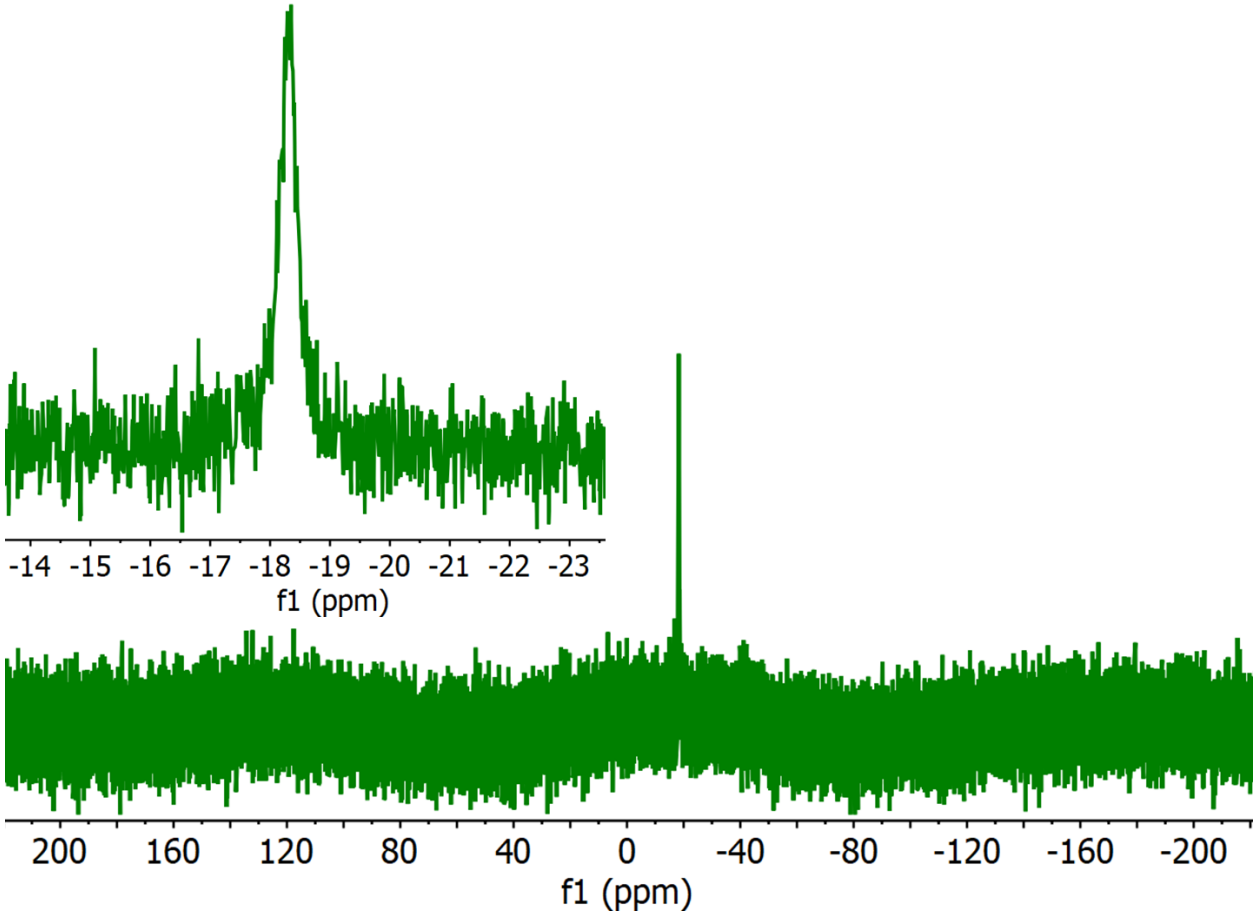

Figure 3.3.3. ^{31}P-NMR of purified $In_{26}As_{18}$ cluster with phenylacetate and tributylphosphine ligands. The inset focuses on the single feature at -18.4 ppm which is indicative of bound phosphine.

The 8:1 ratio of carboxylate to phosphine is also represented in the ^{1}H-NMR of the purified material showing that any excess alkylphosphine is efficiently removed through the purification by size-exclusion (**Figure 3.3.4**). There are only 3 surface indium atoms that form a propeller around the C_3 axis of the cluster. This symmetry is further enforced by the surface phosphines which form a similar, yet mirrored propeller around the same axis (**Figure 3.3.5B**). The C_3 symmetry axis separates the cluster into three quadrants, each of which is ligated by 4 asymmetric bridging, 1 symmetric bridging, and 3 chelating carboxylates showing that the external structure of surface ligation maintains the symmetry dictated by the core (**Figure 3.3.5C**).

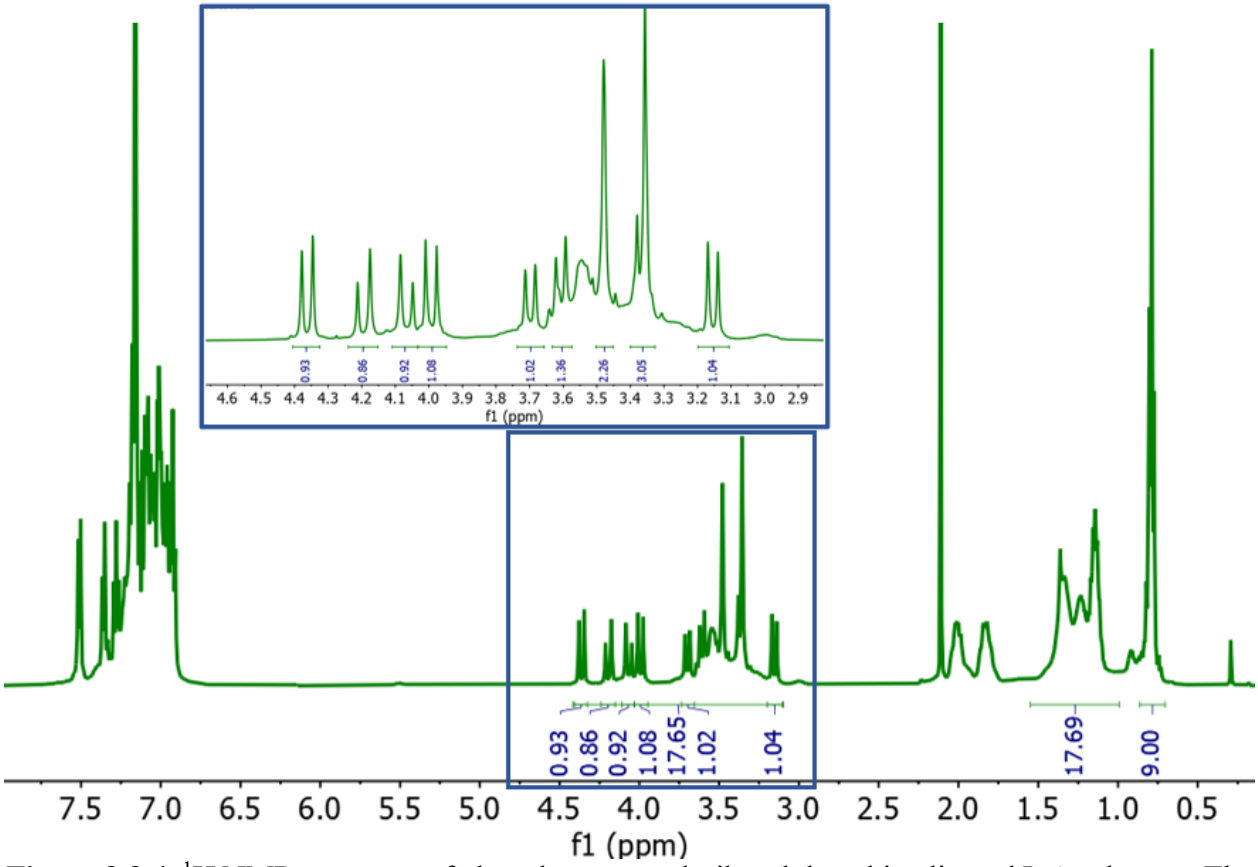

Figure 3.3.4. ^{1}H NMR spectrum of phenylacetate and tributylphosphine ligated InAs clusters. The inset shows the methylene region of the phenylacetate ligands.

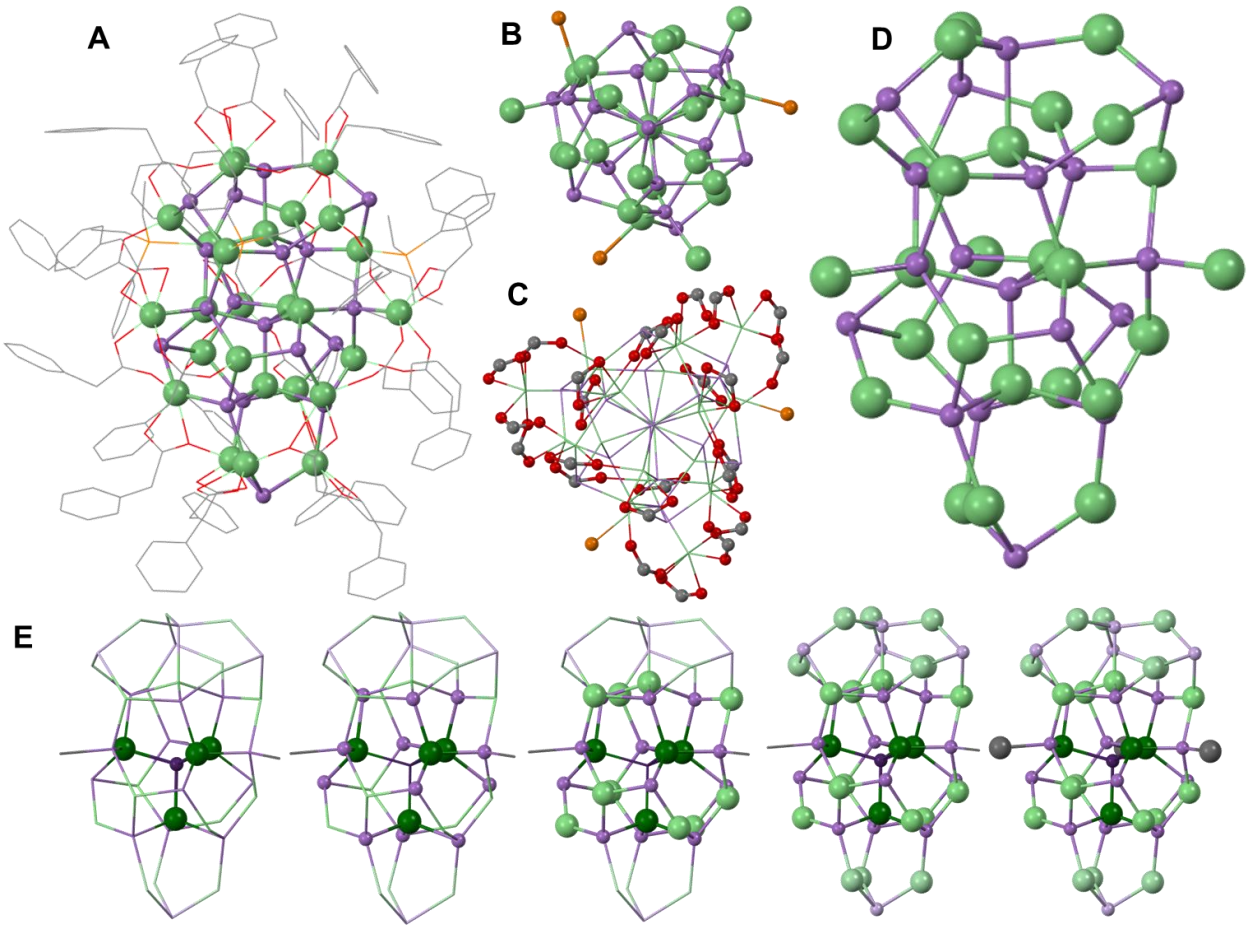

Figure 3.3.5. A) Full $In_{26}As_{18}(O_2CR)_{24}(PR_3)_3$ cluster structure with ligands shown as a wireframe. B) View of $In_{26}As_{18}$ down the C_3 axis showing the symmetry and propeller shape generated by the 3 bound P atoms. C) View of $In_{26}As_{18}$ down the C_3 axis showing the symmetry of the bound carboxylates which have been truncated at the carbonyl carbon. The core $In_{26}As_{18}$ structure is shown in wireframe. D) Inorganic core of $In_{26}As_{18}$ with ligands removed for clarity. E) Components of the $In_{26}As_{18}$ cluster that first generate the cage and then cap the cage to complete the structure. The atomic color is lightened as the structure extends to emphasize the layers of the cluster. Color legend: indium (green), arsenic (purple), phosphorus (orange), oxygen (red), carbon (grey). Hydrogen atoms have been removed for clarity.

The coordination of the surface by carboxylate can further be characterized through solution-phase FTIR in tetrachloroethylene (**Figure 3.3.6**). The individual binding modes cannot be confidently distinguished due to the likelihood of rapid exchange of carboxylates at the surface in solution.[57] However, the symmetric and asymmetric stretches of the carboxylate moiety are still clearly visible in the 1350-1650 cm^{-1} and appear much narrower than what has been reported for quantum dot materials.[58] This narrowing is a product of the molecular nature of the cluster which leads to a limited distribution of carboxylate stretches.

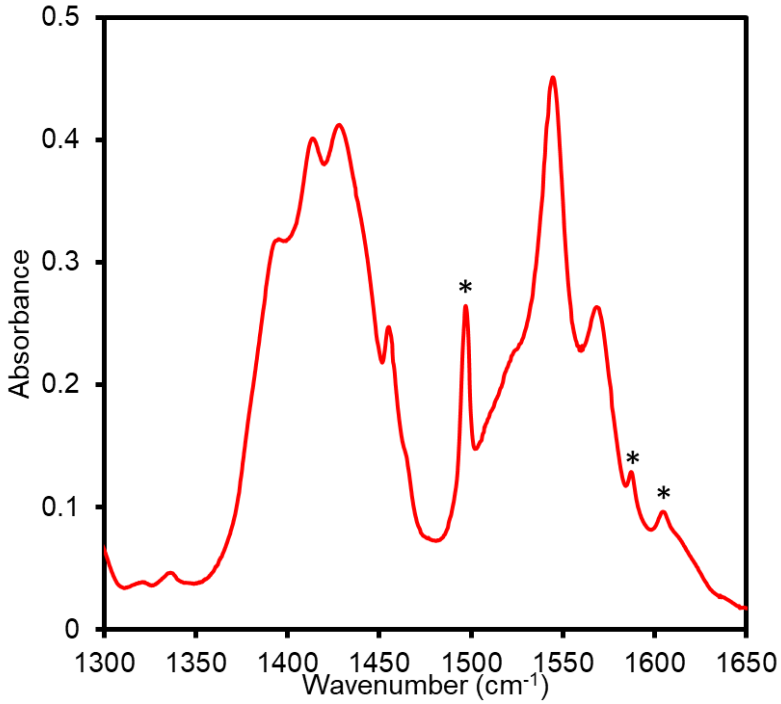

Figure 3.3.6. Solution-phase FTIR of phenylacetate and tributylphosphine ligated InAs clusters in tetrachloroethylene. The isolated ring breathing modes from phenylacetate are marked by asterisks.

Removal of the surface indium results in a nonstoichiometric core of $[In_{23}As_{18}]^{15+}$, which stands as a stark comparison to the previously reported core stoichiometries $[In_{21}P_{20}]^{3+}$ and $[In_{14}P_{13}]^{3+}$ in InP.[18,40] It becomes evident that the drastic change in core stoichiometry is driven by

the abundant 3-coordinate As atoms that make up nearly half the number of As present in the structure. We have previously concluded that in InP, there is a 4-coordinate requirement for the pnictide in cluster materials that forces a cation-rich stoichiometry through a large number of surface In atoms passivating the otherwise 3-coordinate P. We see here that this is not the case in InAs. The vast majority of In is incorporated into the core of the cluster allowing for 7 3-coordinate As atoms. This can potentially function to further explain the lack of photoluminescence in InAs materials as 3-coordinate pnictides have been linked to the formation of hole traps in tetrahedral InP QDs.[59] Therefore, 3-coordinate As on the surface may be pervasive and a strong contributing factor to the photoluminescence of this material lagging behind other III-V and II-VI materials. As mentioned above the lighter effective electron mass in InAs allows for efficient exciton coupling with surface states so the effect of underpassivated atoms, such as 3-coordinate As, is more substantial compared to other materials. While InAs is more covalent than InP with a ionicity of 0.36 compared to 0.42, this likely cannot explain the difference in pnictogen undercoordination.[60] However, it is well-documented that the basicity of arsines fall below that of their phosphine counterparts as a result of more s-character in the hybridized orbital of the lone pair.[61] This would effectively decrease the favorability for surface indium coordination. The final category that the 3-coordinate As can inform is the relative surface coverage as directed by carboxylate-ligated indium. The previously reported InP clusters that contain only 4-coordinate, fully passivated P atoms have, as a consequence, a cation-rich surface that is then completely passivated by carboxylates. This causes the ligand density at the surface to be extremely high. With the InAs cluster, the 3-coordinate As atoms drastically reduce the cation richness of the surface and thus there are significantly fewer carboxylates protecting the core of the structure (**Figure 3.3.7**). We then predict that diffusion to the cluster surface will be much faster in InAs compared to InP as the

ligand barrier preventing diffusion of reactive species is much smaller. This is important information as we seek to adapt cluster-based QD syntheses using this InAs system.

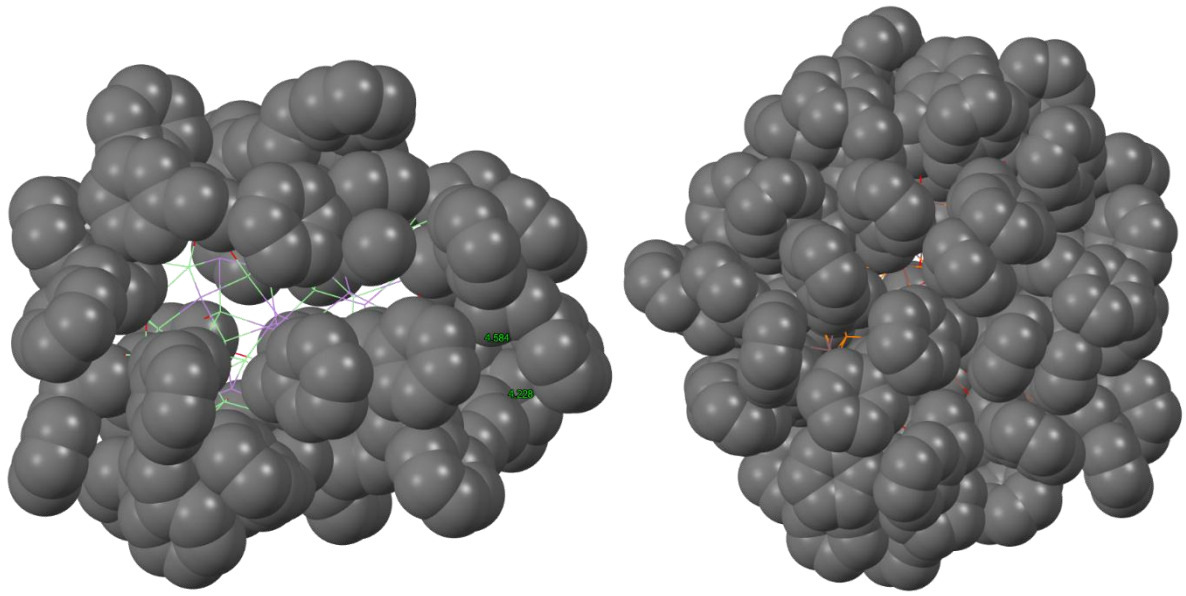

Figure 3.3.7. Fully ligated $In_{26}As_{18}(O_2CCH_2Ph)_{24}(PEt_2Ph)_3$ cluster (left). Fully ligated $In_{37}P_{20}(O_2CCH_2Ph)_{51}$ cluster (right). All carbons are presented through a space filling model and the underlying structures of the clusters are shown in wireframe. Hydrogens removed for clarity.

The structure of this $In_{26}As_{18}$ cluster appears to be related to a motif previously observed in InP, CdSe, and CdS.[18,36,39,40,43] We observe that our recently reported $In_{26}P_{13}$ structure can be superimposed onto the $In_{26}As_{18}$ structure showing that the anion sublattice has a high degree of overlap (RMS = 0.323 Å), however the indium sublattice is substantially different (**Figure 3.3.8**). The observation of the similarity in the pnictogen substructure leads us to hypothesize that the early-stage InAs-395 intermediate is likely to have an As_{13} sublattice that matches both the shape and stoichiometry of the P_{13} sublattice of $In_{26}P_{13}$. Another atomically precise InAs cluster, In_8As_8, has been synthesized and structurally characterized previously by reacting $InMe_3$ directly with

$tBuAsH_2$ but the In_8As_8 core does not bear strong structural connections with the $In_{26}As_{18}$ lattice making direct conversion unlikely (**Figure 3.3.9**).[61]

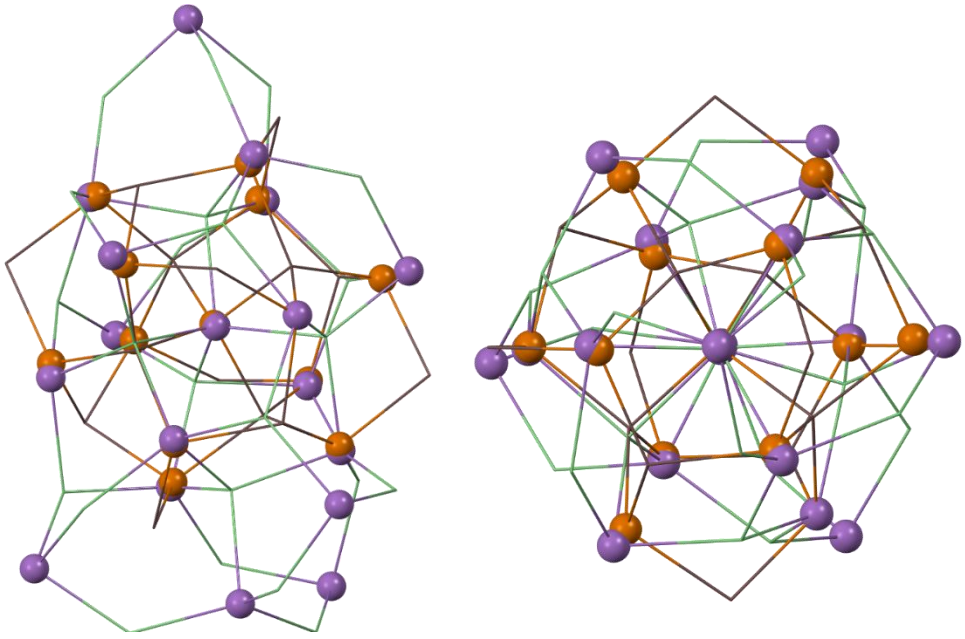

Figure 3.3.8. The overlay of the $In_{26}P_{13}$ and $In_{26}As_{18}$ anion sublattices. P (orange, ball), As (purple, ball), In from $In_{26}P_{13}$ (brown, stick), In from $In_{26}As_{18}$ (green, stick). RMS = 0.323 Å.

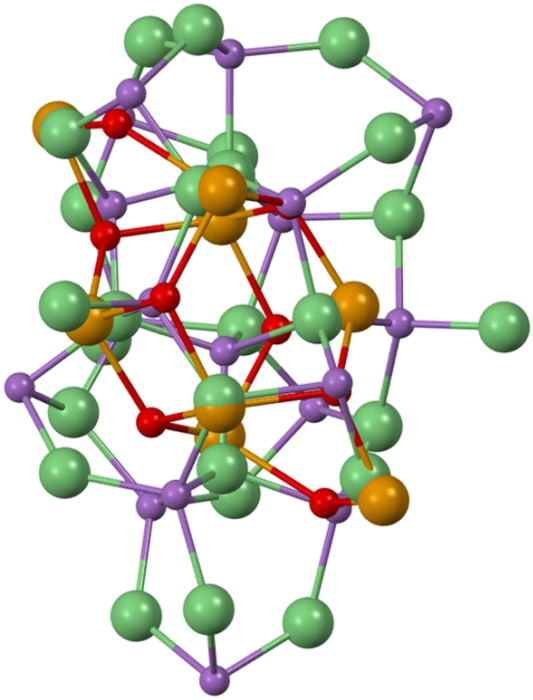

Figure 3.3.9. Structural overlay between $In_{26}As_{18}$ and In_8As_8. In from $In_{26}As_{18}$ (green), As from $In_{26}As_{18}$ (purple), In from In_8As_8 (gold), As from In_8As_8 (red).

It is interesting to note that despite the strong similarities in the anion sublattices of the $In_{26}As_{18}$ and the $In_{26}P_{13}$ and $In_{37}P_{20}$ structures, there are also significant differences (**Figure 3.3.10**). Removing the surface indium atoms, we can compare the bond angles of the $[In_{21}P_{20}]^{3+}$, $[In_{14}P_{13}]^{3+}$, and $[In_{23}As_{18}]^{15+}$ cores of the clusters to get a measure of the deviation in each cluster's structure from the bulk wurtzite crystalline phase of the III-V materials. Seeing as the E-In-E bond angle in bulk wurtzite is 109.5°, a larger divergence from this value approximates a more strained structure. Measuring the E-In-E angles in the InP and InAs cluster cores show an average and standard deviation of 109.3° ± 5.6° for $[In_{21}P_{20}]^{3+}$, 108.5° ± 6.3 for $[In_{14}P_{13}]^{3+}$, and 113.8° ± 9.8 for $[In_{23}As_{18}]^{15+}$. This shows that the core of the $In_{26}As_{18}$ cluster not only has an average that deviates the furthest from the bulk structure but also shows the widest variation in bond angles as seen from the standard deviation. Direct comparison of this structure to the bulk wurtzite phase of InAs shows that the internal stack of alternating In_4As and As_4In tetrahedra in the structure follows a similar pattern to the bulk but instead of eclipsing tetrahedra as in the bulk wurtzite phase, they are continuously offset as the structure extends down the c axis (**Figure 3.3.11**).

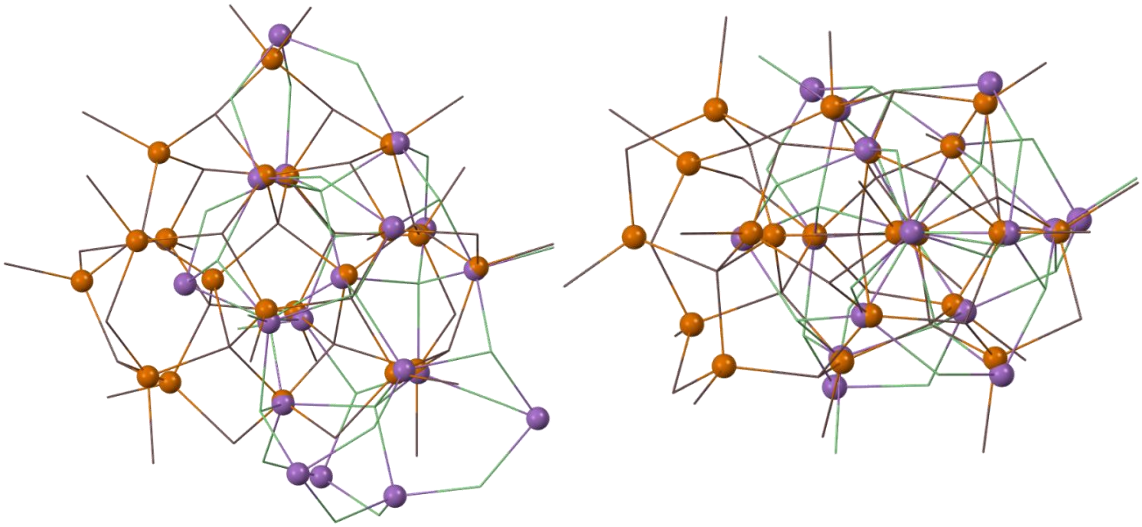

Figure 3.3.10. The overlay of $In_{37}P_{20}$ and $In_{26}As_{18}$ anion sublattices. P (orange, ball), As (purple, ball), In from $In_{37}P_{20}$ (brown, stick),.In from $In_{26}As_{18}$ (green, stick). RMS = 0.389 Å.

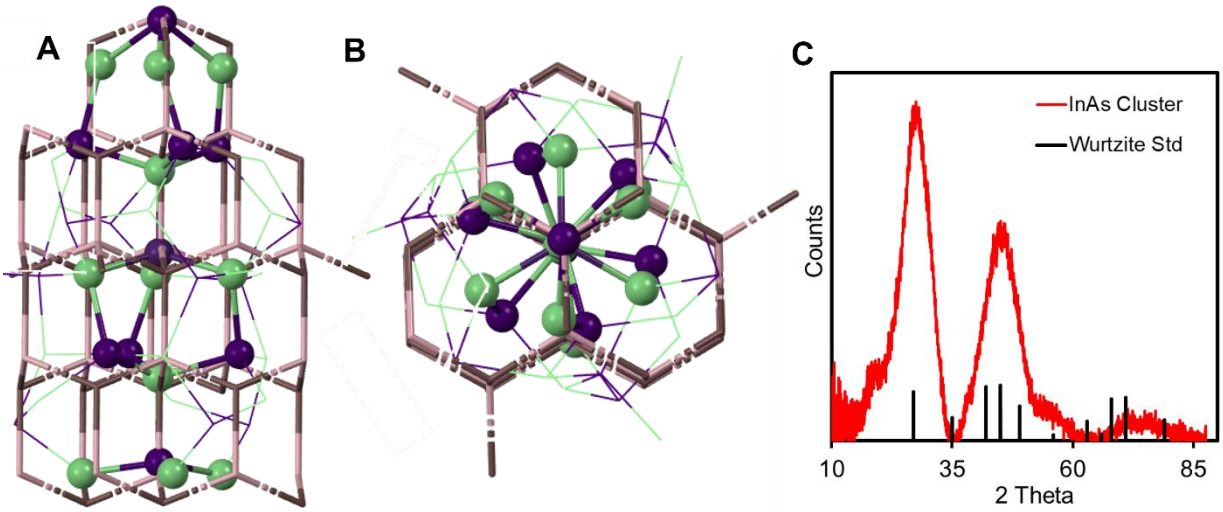

Figure 3.3.11. A, B) Structural overlap between the core $In_{26}As_{18}$ and bulk wurtzite InAs. The mirrored tetrahedra in the bulk wurtzite structure maintain an eclipsed relationship with no rotation as the lattice extends. With the pseudo-wurtzite phase of the cluster, the mirrored, alternating tetrahedra rotate slightly along the c axis misaligning the cluster phase with that of the bulk. For clarity, the core In and As-based tetrahedra of the cluster are shown in ball-and-stick whereas the atoms that extend beyond the central tower of tetrahedra are shown in wireframe. Color key: As from $In_{26}As_{18}$ (purple), In from $In_{26}As_{18}$ (green), As from bulk wurtzite InAs (pink), In from bulk wurtzite InAs (brown). C) Powder x-ray diffraction of phenylacetate and tributylphosphine ligated InAs clusters (red). The diffraction standard of bulk wurtzite InAs is shown in black.

To draw comparisons with the cage-like descriptions of previously reported clusters, there is a central, 4-coordinate As atom off of which the cluster is built. Three 4-coordinate In atoms bind the central As to generate the cage framework. The cage is then closed by the external As atoms being linked with 10 additional In atoms. The cage is extended by the addition of four $AsIn_3$ units, one of which crowns the cluster and the other three are linked by the final As atom to generate the anisotropy (**Figure 3.3.5D**). The final cluster lattice is completed by the addition of

three surface indium atoms that create the propeller. This progression is visually summarized as **Figure 3.3.5E**.

The structural description is similar to that of the $Cd_{26}Se_{17}$ structure formed through cation exchange of $Cu_{26}Se_{13}$ that was recently reported by Zeng and coworkers.[36] Comparison of the $Cd_{26}Se_{17}$ structure with $In_{26}As_{18}$ shows that the $M_{17}E_{14}$ cage structures and stoichiometries are nearly identical including the anion and cation sublattices. That being said, $Cd_{26}Se_{17}$ is nearly a tetrahedron whereas $In_{26}As_{18}$ is more anisotropic and bullet shaped. This difference can be attributed to the attachment of three M_3E units. In the case of $Cd_{26}Se_{17}$, there are three Cd_3Se units that attach to the lower half of the $[Cd_{17}Se_{14}]$ cage to form the three corners of a tetrahedron. This attachment symmetry combined with the Cd_3Se unit that forms the top of the cage creates a pseudo-tetrahedron shape. However, starting with a structurally homologous $[In_{17}As_{14}]$ cage, the three In_3As units add even lower, to the bottom of the cage being linked together by the final, extra arsenic atom that pushes the stoichiometry to $In_{26}As_{18}$. This leads $In_{26}As_{18}$ towards an anisotropic, bullet-shaped structure (**Figure 3.3.12**).

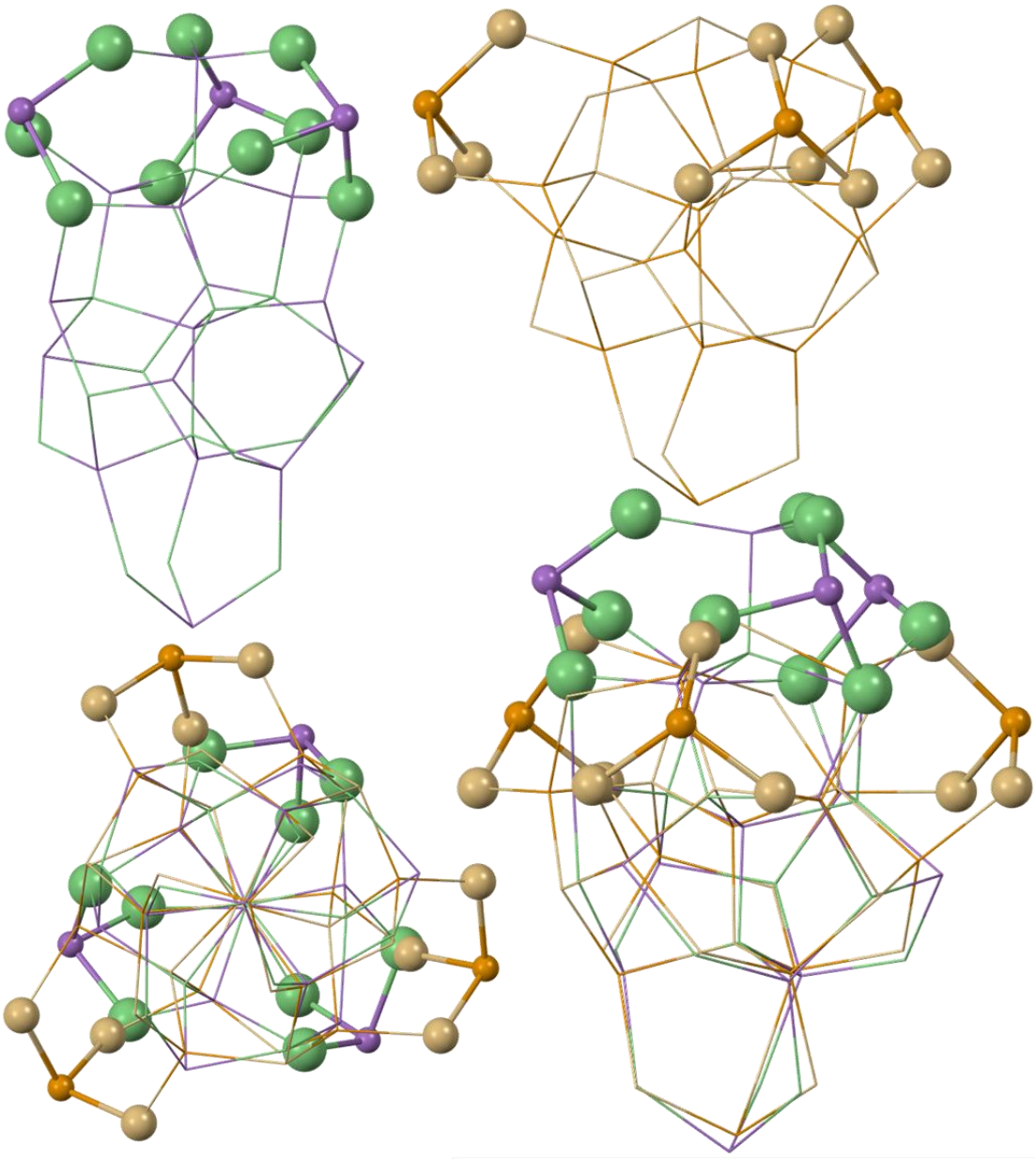

Figure 3.3.12. $In_{26}As_{18}$ structure with the surface In atoms removed shown in wireframe except for the three In_3As units that form the base of the bullet-like shape shown in ball-and-stick (top left). $Cd_{26}Se_{17}$ structure shown in wireframe except for the three Cd_3Se units that form the three corners of the base of the pseudo-tetrahedral shape shown in ball-and-stick (top right). Superimposed $Cd_{26}Se_{17}$ and $In_{26}As_{18}$ structures showing that the underlying $M_{17}E_{14}$ structure is homologous and the placement of the three M_3E units differentiate the two structures viewed from the side (bottom right) and down the C_3 axis (bottom left).

3.4 Computational Electronic Structure

As a final point of characterization, we performed TDDFT calculations using the Gaussian software package,[62] as detailed in the supporting information, to understand the orbital make-ups of the observed electronic transitions in the experimental absorption spectrum. The carboxylate ligands were truncated to acetate and the phosphine ligands were modeled with ethyl groups to reduce computational costs. As is seen experimentally, there are two distinct absorption transitions; the first of which is comprised of both the HOMO and the HOMO-1, which are essentially degenerate, and the second consisting of the HOMO-2 (**Figure 3.4.1A**). These leaving orbitals are primarily As 4p in character with the largest contributions from those that are closest to the cluster's center. We note however, that the HOMO and HOMO-1 orbitals are oriented across the width of the cluster (**Figure 3.4.1B, 3.4.1C**) as this stands in contrast to the HOMO-2 leaving orbital that participates in the second, higher energy transition, which is primarily oriented along the length of the cluster (**Figure 3.4.1D**). The arrival orbital for both transitions shows a significant degree of delocalization across the cluster structure and incorporates more In 5s character. There is, however, a qualitatively equal contribution of As character to this arrival orbital showing the high degree of covalency that is understood to occur in InAs (**Figure 3.4.1E**). Furthermore, with the isosurface contour plotted at 0.02, there is a small but noticeable contribution of P-character from the phosphine ligands to the arrival orbital distribution. This suggests that the ligand sphere, especially the phosphines, could be quite responsive to electronic excitation and may play a role in modulating the dynamics of the excited state. We note that the experimental absorption doublet is substantially red-shifted from the computationally predicted absorbance. However, the mismatch in energy is similar to that previously reported for comparable materials.[63,64] Finally, the simulated Raman modes show good agreement with those characterized experimentally, falling in

the range of 160 – 280 cm^{-1} (**Figure 3.4.2**). These energies are similar to those reported for the TO, SO, and LO modes of InAs nanowires at approximately 218, 237 and 239 cm^{-1}, respectively.[65]

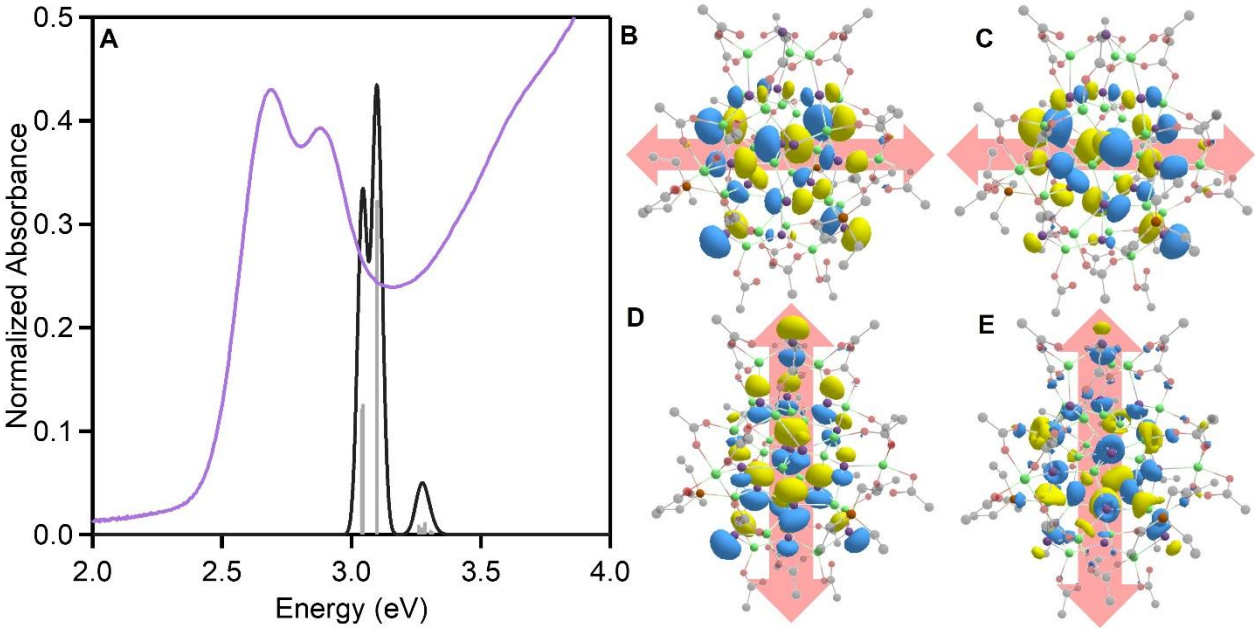

Figure 3.4.1. A) Experimental absorbance of InAs clusters with an applied correction for the Jacobian transformation (purple) compared to the calculated discrete absorbance states (grey) with a gaussian broadening of 0.02 eV (black). B) Visualization of the HOMO leaving orbital oriented along the width of the cluster. C) Visualization of the HOMO-1 leaving orbital oriented along the width of the cluster. D) Visualization of the HOMO-2 leaving orbital oriented along the length of the cluster. E) Visualization of the LUMO arrival orbital for the first three transitions.

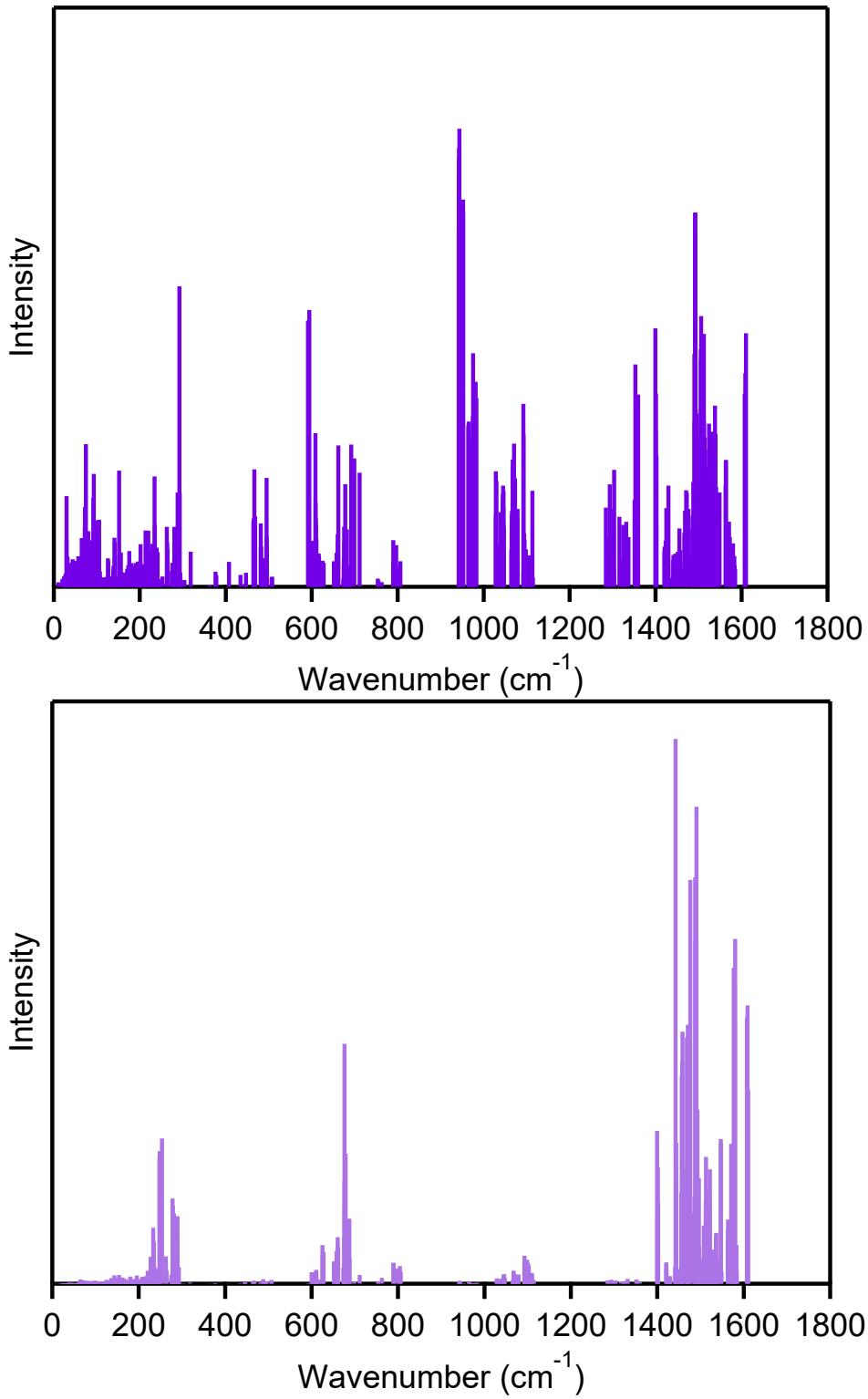

Figure 3.4.2. Computational Raman spectrum of the $In_{26}As_{18}$ cluster (top). Computational IR spectrum of the $In_{26}As_{18}$ cluster (bottom).

3.5 CONCLUSIONS

In conclusion, we have presented the synthesis, isolation, and complete structural characterization of the first molecular InAs nanocluster. This species has been extensively documented spectroscopically by its characteristic absorption doublet at 425 and 460 nm as an intermediate in the synthesis of InAs QDs using indium carboxylate, alkylphosphine, and $As(SiMe_3)_3$. We report that the concentration of phosphine is important to the overall yield and purity of InAs-460 clusters, as too much or too little results in undesirable growth of InAs QDs as side-products. With long-chain aliphatic carboxylates and phosphines, we observe the presence of a second intermediate absorbing at 395 nm that converts through an isosbestic point into the $In_{26}As_{18}$ cluster. Diffraction quality crystals were obtained using a combination of phenylacetate and diethylphenylphosphine. Single crystal X-ray diffraction of the isolated InAs-460 cluster revealed its composition as $In_{26}As_{18}(O_2CR)_{24}(PR_3)_3$. While the overall atomic arrangement does not match any previously reported structures, the anion sublattice shares important similarities with previously reported InP and CdSe clusters. Computational simulation of the absorption spectrum and associated orbitals shows a high degree of delocalization with the computed leaving orbitals being entirely composed of As p-character and the arriving orbital showing a distribution of electron density equally across In and As emphasizing the covalency of the InAs lattice. These findings stand as an important step in our understanding of the synthesis mechanisms in III-V QD systems and provide the structure of a molecular InAs cluster.

3.6 OUTLOOK

The simplest takeaway from this study was that the InAs cluster is structurally different from the InP cluster. But despite this difference, it is built out from the same $M_{14}E_{13}$ cage structure that has proven to be so prevalent in magic-sized cluster structures. As a part of the cage structure, it was exciting to see the icosahedral anion sublattice appear again but this simply emphasized the ambiguity in why the InP and InAs cluster structures were different.

The simplest and easiest answer became that the InAs cluster synthesis includes a tertiary organophosphine. The phosphine ligates the indium precursor and could also ligate surface indium during cluster formation thereby enhancing the reactivity throughout cluster nucleation and growth.[51] This, along with the difference in reactivity between $As(SiMe_3)_3$ and $P(SiMe_3)_3$, dramatically increases the reaction kinetics. This is assuming that there are no inherent differences in the behavior of InP and InAs as nanomaterials and thus the structural differences are merely a function of different precursor reaction kinetics. If this were true, using a more reactive phosphorus precursor alongside the tertiary phosphine would allow for the growth of an $In_{26}P_{18}$ and furthermore, using a less reactive arsenic source without tertiary phosphine would result in an $In_{37}As_{20}$ cluster. There may be slight differences in the In:V (V = P, As) stoichiometry of these hypothetical clusters as As doesn't seem to have the same 4-coordinate requirement as phosphorus, but the overall structure would be the same. I was hesitant to put significant effort into synthesizing different silylpnictide precursors with varying reactivities to isolate these sister clusters because it is challenging to fine tune the reactivity. There are two sites on the precursor for adjusting reactivity: 1) a trimethylgermane group can be used in place of the trimethylsilyl to decrease the reactivity, and 2) another alkyl substituent (i.e. ethyl, propyl, *t*-butyl) can be used in place of the methyl group to add steric coverage thereby decreasing the reactivity. Unfortunately, the

chlorotrimethylgermane precursor required for the synthesis is quite expensive and altering the alkyl substituent leads to very large changes in reactivity making fine tuning of the silylpnictide precursor infeasible.

Another interesting physical manifestation of the precursor reactivity was the difference in cluster growth mechanisms between InP and InAs. As discussed above, the $In_{26}As_{18}$ cluster forms from a smaller cluster absorbing at ~395 nm through direct conversion as evidenced by the isosbestic point in the absorbance aliquots (**Figure 3.6.1A**). In comparison, a consistent red-shift is seen in the absorbance aliquots for the formation of the $In_{37}P_{20}$ cluster until reaching the characteristic λ_{max} at 386 nm (**Figure 3.6.1B**). For $In_{37}P_{20}$, this growth is from unconsumed solute either in the form of indium carboxylate and $P(SiMe_3)_3$ or some partially reacted mixture of the two. A smaller cluster forms first ($In_{26}P_{13}$, the isolation and characterization of which is discussed in Chapter 2) but the unconsumed solute is still highly reactivity leading to the immediate growth of this smaller material into the kinetically stable $In_{37}P_{20}$ (**Figure 3.6.2A**). This continuous growth is evidenced by the continuous red-shift in the absorbance. In comparison, the $In_{26}As_{18}$ cluster reaction immediately shows a feature at 395 nm upon injection but instead of a continuous red-shift, this feature decreases in intensity as the two absorbance features at 425 and 460 nm, characteristic of the $In_{26}As_{18}$ cluster, grow in. This immediate smaller cluster formation followed by a slow, controlled conversion suggests that all $As(SiMe_3)_3$ is consumed at injection leaving no more highly reactive silylarsine bonds for immediate growth. This is corroborated by the enhanced reactivity of $As(SiMe_3)_3$ which should cause it to be immediately consumed whereas the $P(SiMe_3)_3$, despite still being very reactive, can exist silylated in a reaction for multiple minutes.[42]

The conversion from the $InAs_{395}$ into the $In_{26}As_{18}$ is then unlikely based in unreacted silylarsine and must then be from altering bonds between indium and arsenic.

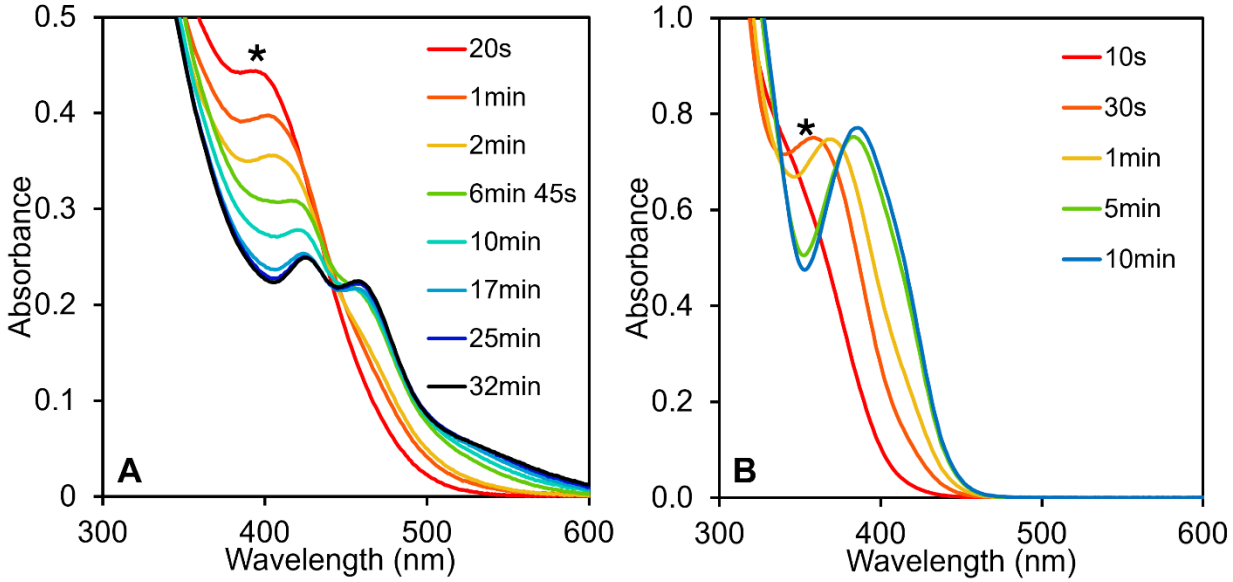

Figure 3.6.1. A) Absorbance aliquots taken over the course of a typical $In_{26}As_{18}$ cluster synthesis. B) Absorbance aliquots taken over the course of a typical $In_{37}P_{20}$ cluster synthesis. (*) Denotes where the preliminary cluster absorbs in each reaction.

If the conversion is independent of excess solute in the reaction, there are two mechanistic possibilities for conversion: 1) a structural rearrangement of the cluster (**Figure 3.6.2B**), and 2) further growth by self-consumption (**Figure 3.6.2C**). A previous study of the $In_{26}As_{18}$ cluster suggested that the conversion process is a structural rearrangement based on a difference in XRD peak intensity and breadth between $In_{26}As_{18}$ and $InAs_{395}$.[66] However, definitively proving which conversion mechanism is occurring can be done through a kinetic analysis of the reaction. A structural rearrangement requires only a single reactant, $InAs_{395}$, and therefore the conversion would be expected to be 0^{th} order with respect to cluster concentration. Conversely, the growth through self-consumption of $InAs_{395}$ would require multiple clusters (at a minimum, one to provide solute and the other to grow by consuming solute) and therefore the rate of conversion would be dependent on reaction concentration. As shown above in **Figure 3.2.4**, the conversion is indeed

dependent on cluster concentration strongly suggesting that the growth mechanism is through the dissolution and consumption of other $InAs_{395}$ clusters.

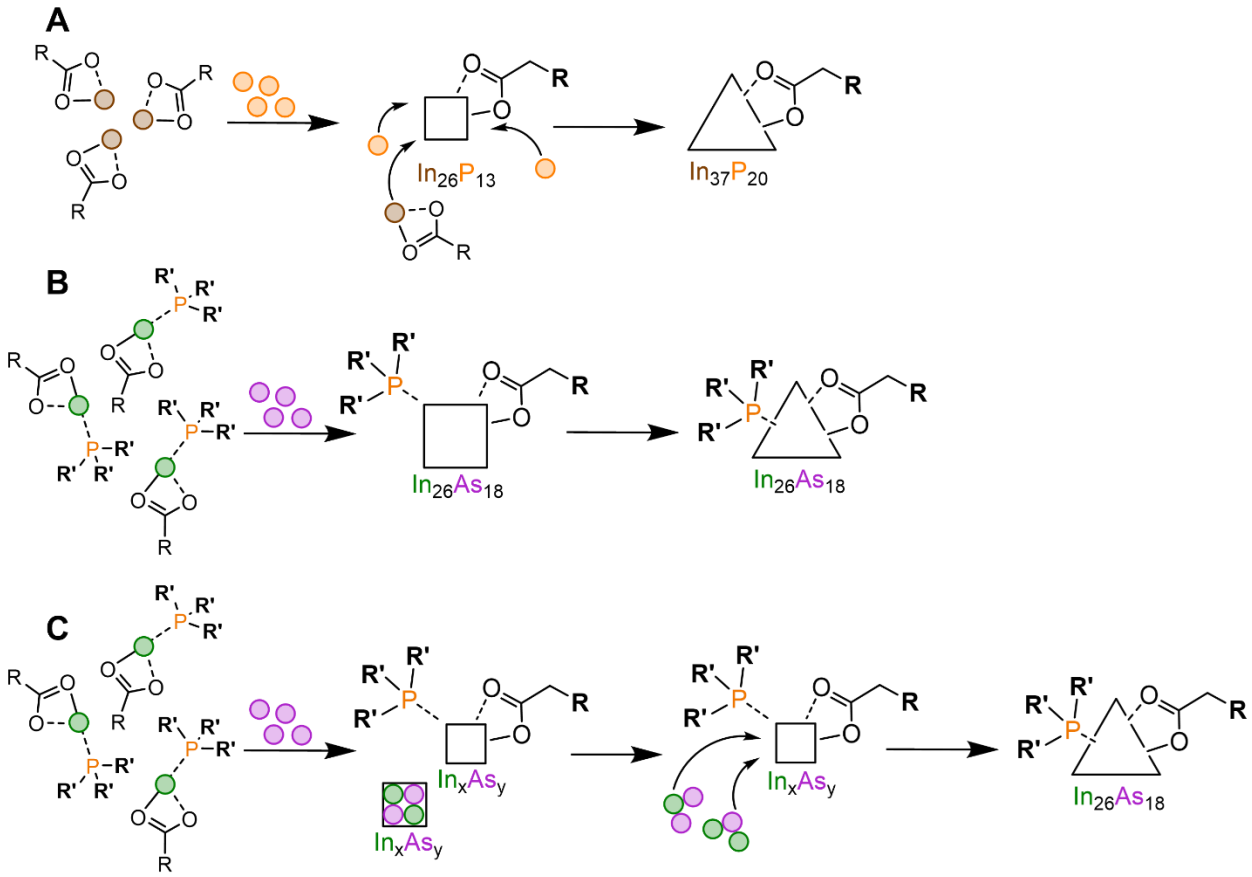

Figure 3.6.2. A) Continuous growth through unconsumed solute mechanism for $In_{37}P_{20}$. B) Structural rearrangement mechanism for $In_{26}As_{18}$ formation. C) Growth by self-consumption mechanism for $In_{26}As_{18}$ formation.

The difference in conversion mechanism can potentially be invoked to explain the difference in symmetry between the $In_{26}As_{18}$ and $In_{37}P_{20}$ clusters, as well. As described above, down the C_3 axis of $In_{26}As_{18}$ is a stack of tetrahedra that strongly resembles the wurtzite crystal phase, albeit with some degree of rotation (**Figure 3.6.3A, B**). With the $In_{37}P_{20}$ cluster, the wurtzite crystal moiety is also present as two stacks that cross through the central indium atom (**Figure 3.6.3C, D, E, F**). The biggest difference here is that in the case of $In_{26}As_{18}$, the symmetry of the cluster is built around the symmetry of the wurtzite stack. In other words, the C_3 axis of the cluster

is the same as the C_3 axis of the stack. This symmetry is even extended as far out as the ligand sphere where the arrangement of the methylene groups on the phenylacetate ligands maintain the C_3 symmetry (**Figure 3.3.4**). In contrast, for the $In_{37}P_{20}$, the wurtzite moieties independently have C_3 symmetry but their axes cannot be applied to the overall symmetry of the cluster. The $In_{37}P_{20}$ cluster as a whole only has a C_2 axis of symmetry that runs from the apical phosphorus atom down through the central indium. The fast nucleation followed by slower growth through self-consumption of the $In_{26}As_{18}$ cluster lends itself to generating a structure of higher symmetry and crystallinity. While the nucleation is faster due to the higher reactivity of $As(SiMe_3)_3$, the actual growth process is slower as the silylarsine has been consumed. This allows for the final cluster formation step to be closer towards thermodynamic control and thus the transition from the $InAs_{395}$ to $In_{26}As_{18}$ maintains high symmetry and extends the existing wurtzite moiety. In contrast, the transition from $In_{26}P_{13}$ to $In_{37}P_{20}$ continues through growth promoted by the reactive silylphosphine bonds and therefore both the nucleation and growth processes have similar kinetics. This pushes the $In_{37}P_{20}$ formation closer to kinetic control and therefore the resulting structure is not as crystalline nor as symmetric as the $In_{26}As_{18}$. For both $In_{37}P_{20}$ and $In_{26}As_{18}$, the growth outward from the smaller cluster extends the wurtzite moieties that are partially present in the $M_{14}E_{13}$ structure. But they are extended further and with higher symmetry in the case of $In_{26}As_{18}$ due to the complete consumption of the silylarsine which forces a more thermodynamically controlled cluster conversion step to form the final structure.

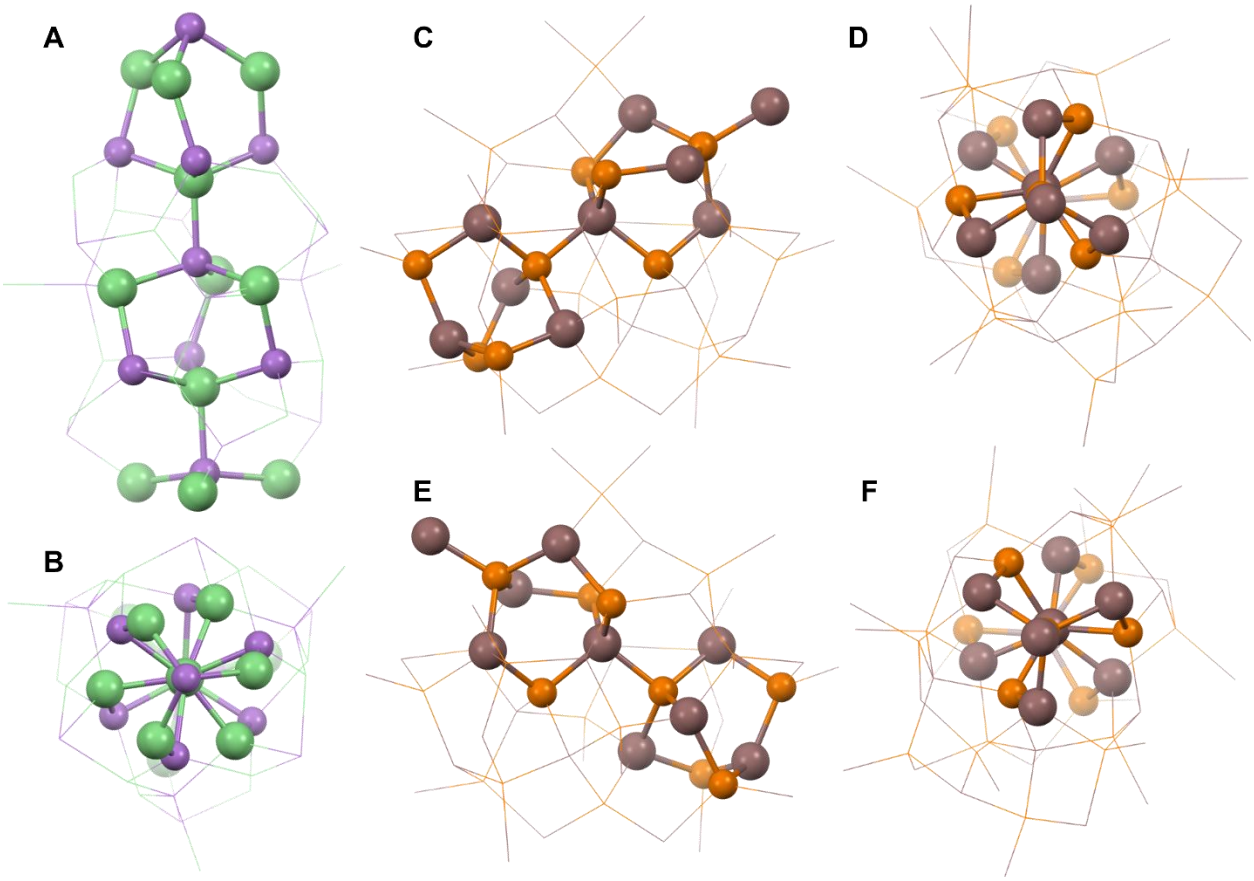

Figure 3.6.3. A) Wurtzite stack crystalline moiety in the $In_{26}As_{18}$ cluster shown as ball-and-stick with other atoms shown in wireframe. B) View down the C_3 axis of the $In_{26}As_{18}$ cluster. C) First wurtzite stack in the $In_{37}P_{20}$ cluster shown as ball-and-stick with other atoms shown in wireframe. D) View down the vertical axis of the first $In_{37}P_{20}$ wurtzite stack. E) Second wurtzite stack in the $In_{37}P_{20}$ cluster shown as ball-and-stick with other atoms shown in wireframe. F) View down the vertical axis of the second $In_{37}P_{20}$ wurtzite stack.

The difference in reaction kinetics and cluster growth mechanism between InP and InAs made it of particular interest to isolate and characterize the smaller, intermediate $InAs_{395}$ cluster. As described in Chapter 2, we were able to kinetically-trap the smaller InP cluster and identify it as $In_{26}P_{13}$. This is what allowed for the recognition of the icosahedral sublattice as a potentially

universal moiety in cluster systems with tetrahedral coordination. We note that again, this sublattice clearly appears at the center of the $In_{26}As_{18}$ cluster (**Figure 3.6.4**)

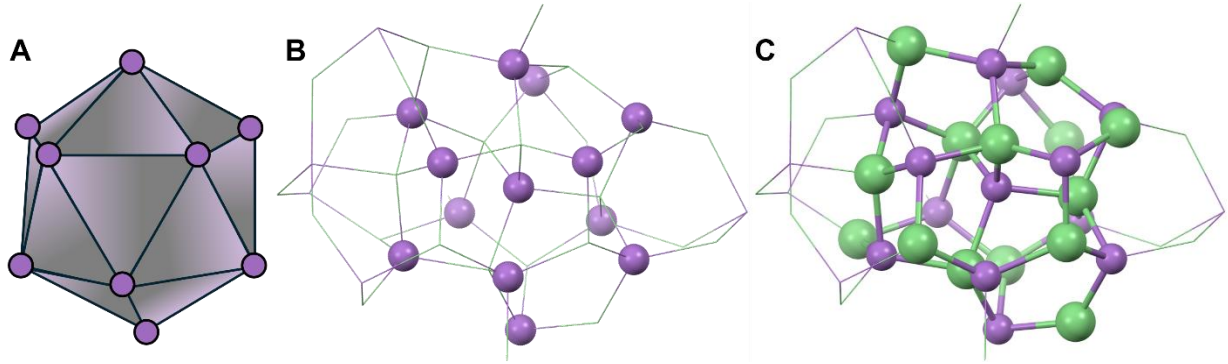

Figure 3.6.4. A) Platonic icosahedron with purple circles at each vertex. B) Arsenic sublattice in the $In_{26}As_{18}$ cluster that forms the icosahedron. C) $In_{14}As_{13}$ cage structure highlighted that forms as a result of the icosahedral anion sublattice.

Seeing as both CdSe and InP have preliminary clusters based on the $M_{14}E_{13}$ cage structure ($Cd_{14}Se_{13}$ and $In_{26}P_{13}$) which then convert into larger structures that contain the $M_{14}E_{13}$ cage as a subunit, it is highly likely that the $InAs_{395}$ preliminary cluster is some perturbation on the $M_{14}E_{13}$ cage. The only way to prove this would be through isolation and SCXRD characterization of the $InAs_{395}$ so I sought to trap this smaller cluster and attempt crystal growth.

If the InAs cluster conversion mechanism is truly based in fast nucleation followed by self-consumption, this makes isolation very challenging. The route of controlling diffusion using a sterically hindered carboxylate that worked to isolate $In_{26}P_{13}$ will not have an effect on the InAs system because the conversion is not based in precursor migrating to the cluster surface and instead depends upon an inherent thermal instability of the preliminary $InAs_{395}$. Furthermore, altering precursor reactivity will only influence the formation of $InAs_{395}$, preventing its formation entirely if changed too drastically, and will not impact the cluster-to-cluster conversion which is the process

that needs modulating. From my perspective, this left one potential route towards isolating the smaller cluster – a brute force route: quenching. If the conversion is from thermal instability, then once the cluster forms, if all thermal energy is immediately removed, potentially the cluster's metastability can be maintained.

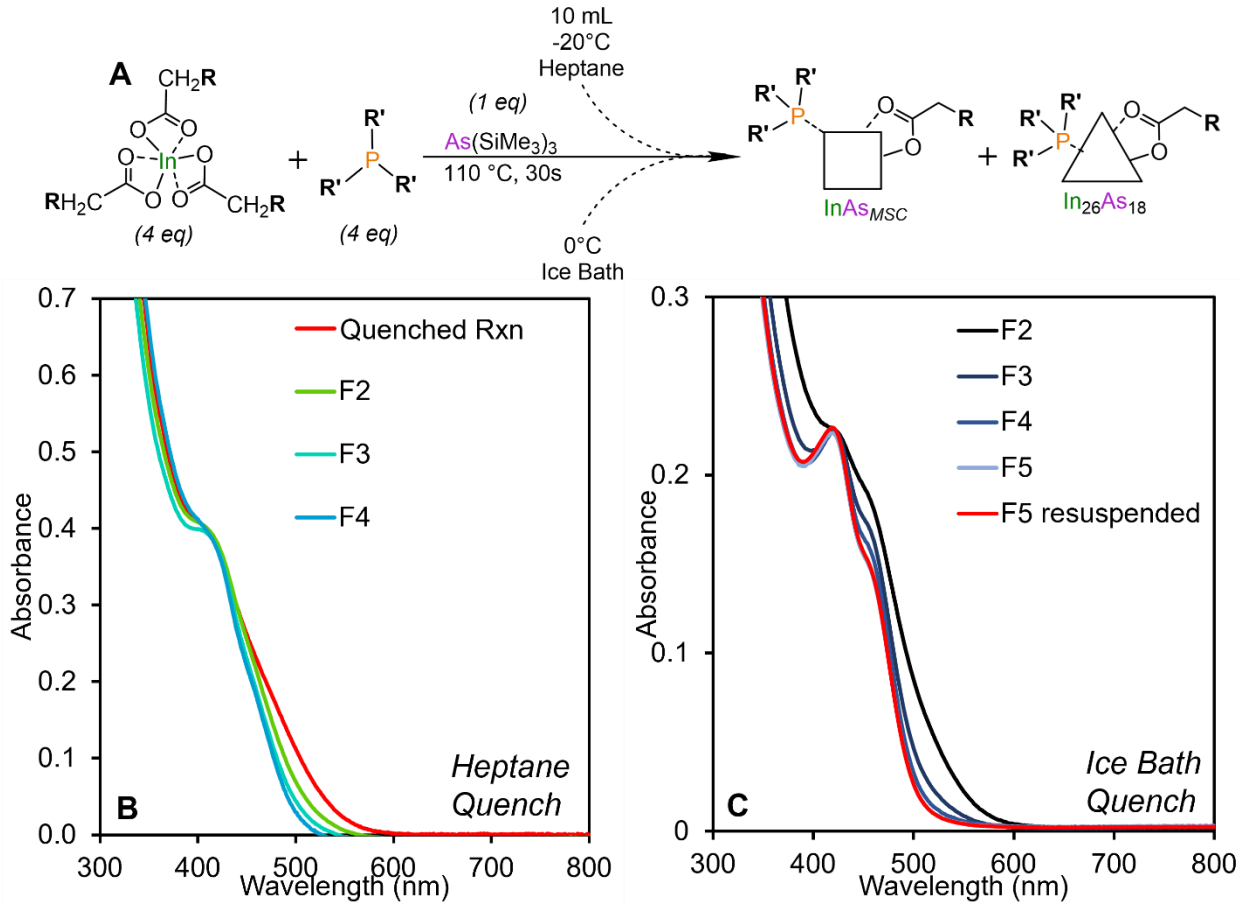

Figure 3.6.5. A) Reaction scheme for quenching a typical $In_{26}As_{18}$ cluster reaction to isolate $InAs_{395}$. B) Absorbance of fractions after column purification of a crude reaction quenched by 10 mL of -20 °C heptane. C) Absorbance of fractions after column purification of a crude reaction quenched in a 0 °C ice bath.

I took two approaches to quenching: 30 seconds after injecting the $As(SiMe_3)_3$ at 110 °C, either 1) injecting 10 mL of -20 °C heptane, or 2) placing the flask in a 0 °C ice bath (**Figure 3.6.5A**). The benefit of the heptane injection is that heptane can function as an antisolvent for the

clusters when they are ligated with phenylacetate and diethylphenylphosphine. This means it could remove them from solution and, in the process, stop any solute diffusion that might occur in solution and lead to growth. That being said, hot-injecting an antisolvent could also lead to severe changes in the ligand chemistry at the surface and could destabilize the cluster. While the ice bath does not chemically perturb the reaction, it results in a slower quench and all species remain in solution which would potentially allow for solute diffusion and growth. After quenching, similar to the $In_{26}As_{18}$ purification, the reaction must be run through a size-exclusion column to isolate the clusters. The results from these column purifications are shown in **Figure 3.6.5B, C**. The ice bath quench leads to much more well-defined absorbance feature which suggests better purity and indicates that the heptane is indeed altering the surface chemistry. While the feature is well-pronounced, it is obvious there is some amount of $In_{26}As_{18}$ impurity evidenced by the shoulder around 460 nm in all the spectra. Allowing these column fractions to sit in solution for multiple hours led to a loss in peak definition, thereby suggesting some degradation process. While this showed the $InAs_{395}$ could be isolated, its stability was not consistent which did not bode well for attempts at single crystal growth. I therefore moved beyond these experiments to target projects that were more impactful and less risky.

While this leaves the identity of the $InAs_{395}$ cluster in ambiguity, it is still interesting to posit as to why InP and InAs, two materials with such similar structural properties grow so differently (**Figure 3.6.6**). While it is likely due to the large difference in reactivity as described above, potentially the phosphine also contributes to the ligation of $InAs_{395}$ leading to a different growth pathway. Furthermore, the lack of a 4-coordinate requirement for arsenic could also push the growth in a different direction thereby allowing for a more anisotropic structure. These questions were left unanswered as the pursuit of other cluster materials became of interest.

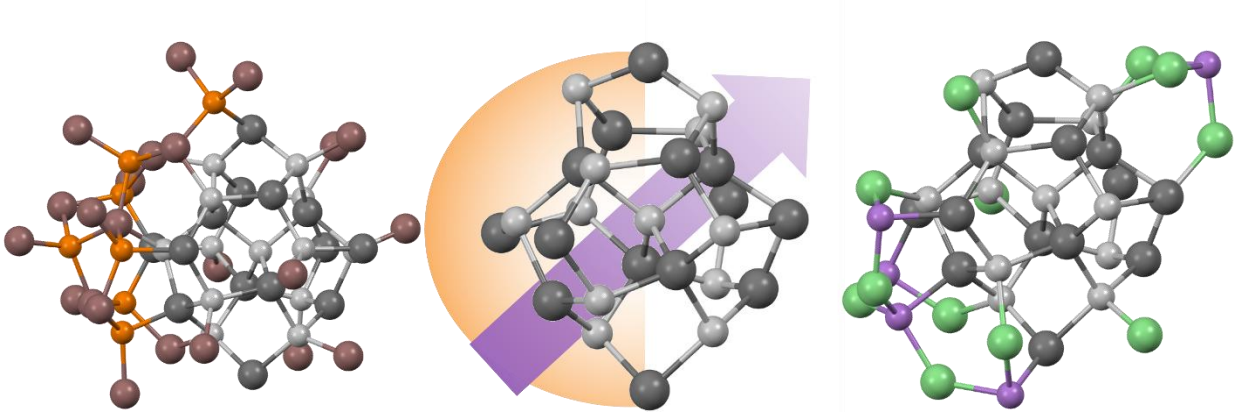

Figure 3.6.6. Comparison between how $In_{37}P_{20}$ and $In_{26}As_{18}$ growth from the underlying $M_{14}E_{13}$ cage motif.

3.7 Experimental Methods.

3.7.1 *General Considerations.*

Trioctylphosphine (97%), myristic acid (≥99%%), chlorotrimethylsilane (≥99%), phenylacetic acid (99%), tri-n-butylphosphine (≥93.5%), sodium metal (ACS reagent, dry), and naphthalene (99%) were obtained from Sigma Aldrich. Trioctylphosphine and tributylphosphine were vacuum distilled and naphthalene was sublimated prior to use. Dimethoxyethane (≥99%) obtained from TCI and distilled from sodium prior to use. Trimethyl indium (98%) and arsenic powder (99%) were obtained from Strem Chemicals and used as received. Diethylphenylphosphine (98%) was obtained from 1st Scientific and used without further purification. Deuterated benzene (C_6D_6) was obtained from Cambridge Isotope Laboratories, dried over CaH_2 and distilled prior to use. Tris(trimethylsilyl)arsine ($As(SiMe_3)_3$) was prepared according to a literature procedure for tris(trimethylsilyl)phosphine using metallic arsenic in the place of red phosphorus.[67] All manipulations were performed under an inert atmosphere of dry N_2 using standard Schlenk line or glovebox techniques unless otherwise indicated. Optical spectra

were acquired on Cary 5000 and Cary 60 UV-Vis spectrophotometers from Agilent Technologies. NMR spectra were acquired on 300 and 500 MHz Bruker Avance spectrometers in C_6D_6. Diffractograms were collected on a Bruker D8 powder x-ray diffractometer with a Pilatus 100K large-area 2D detector using a 1 mm collimator. All solution phase FT-IR measurements were acquired on a PerkinElmer Frontier FT-IR spectrometer using a CaF_2 window liquid cell with the sample dissolved in tetrachloroethylene. The solvent signal was subtracted as a background before plotting. ICP-OES was conducted on a Perkin Elmer Optima 8300 inductively couple plasma – optical emission spectrophotometer after sample digestion overnight in 1:1 70% nitric acid/hydrogen peroxide and dilution to 2% nitric acid.

3.7.2 *Synthesis of $In_{26}As_{18}(O_2C(CH_2)_{12}CH_3)_{24}(TOP)_3$.*

In a typical synthesis, myristic acid (0.548 g, 2.4 mmol) is added to an oven-dried 15 mL 3-neck round-bottom flask fitted with a thermowell, T-adapter, and septum. The flask is placed under vacuum at 50 mtorr for 30 minutes after which the system is placed under positive nitrogen flow and anhydrous toluene (2 mL) is injected into the flask. Trimethylindium (128 mg, 0.8 mmol) is dissolved in 1 mL of toluene and added dropwise to the flask with 800 rpm stirring at 2 drops per second. The solution is left to stir for 30 minutes after which trioctylphosphine (1.0 mL, 0.831 g, 2.24 mmol) is injected followed by stirring at 1200 rpm for an additional 15 minutes. The temperature is raised to 110 °C and within 5 minutes of reaching this temperature a solution of $As(SiMe_3)_3$ (60 uL, 0.2 mmol) in anhydrous toluene (0.5 mL) is then promptly injected into the flask. After 40 minutes at 110 °C, the reaction is allowed to cool to room temperature. Once cool, the crude reaction is purified directly by size-exclusion chromatography in toluene in 0.75 mL

increments. The toluene is removed under vacuum after purification to yield a dark orange, waxy solid.

3.7.3 *Synthesis of $In_{26}As_{18}(O_2CCH_2Ph)_{24}(PEt_2Ph)_3$.*

Phenylacetic acid (0.654 g, 4.8 mmol) is added to an oven-dried 15 mL 3-neck round-bottom flask fitted with a thermowell, t-adapter, and septum. The flask is placed under vacuum at 50 mtorr for 30 minutes after which the system is placed under positive nitrogen flow and anhydrous toluene (2 mL) is injected into the flask. Trimethylindium (256 mg, 1.6 mmol) is dissolved in 1 mL of toluene and added dropwise to the flask with 800 rpm stirring at 2 drops per second. The solution is left to stir for 30 minutes after which diethylphenylphosphine (0.226 g, 279 uL, 1.6 mmol) is injected followed by stirring at 1200 rpm for an additional 15 minutes. The temperature is raised to 110 °C and within 5 minutes of reaching this temperature a solution of $As(SiMe_3)_3$ (120 uL, 0.4 mmol) in anhydrous toluene (0.5 mL) is then promptly injected into the flask. After 20 minutes at 110 °C, the reaction is allowed to cool to room temperature. Once cool, the crude reaction is purified directly by size-exclusion chromatography in toluene in 0.75 mL increments. The toluene is removed under vacuum after purification to yield a dark orange, crystalline solid. ICP-OES of the purified material showed an In:As ratio of 1.42:1. Elemental analysis $In_{26}As_{18}P_3O_{48}C_{222}H_{213}$: calculated C 33.0%, H 2.60%, N 0.00%; actual C 40.55%, H 3.64%, N 0.00%.

For crystallization, under a nitrogen atmosphere, 4 mg of isolated cluster is dissolved in 500 µL of toluene in a 2 mL screw top scintillation vial and the opening of the vial is completely covered with aluminum foil. This vessel is then sealed in a 20 mL scintillation vial with 3 mL of

pentane. After 6 days of pentane diffusion into the toluene, bright orange crystals grew at the bottom of the inner vial. Single crystals of this material could also be grown using an identical method with diethyl ether in place of toluene.

3.7.4 *Synthesis of $In_{26}As_{18}(O_2CCH_2Ph)_{24}(PBu_3)_3$.*

The procedure is the same as reported above for $In_{26}As_{18}(O_2CCH_2Ph)_{24}(PEt_2Ph)_3$ replacing diethylphenylphosphine with tri-n-butylphosphine (0.324 g, 395 uL, 1.6 mmol).

3.7.5 *Computational Methods.*

Computational studies were performed using the Gaussian[62] electronic structure package. The HSE06[68–70] range-separated hybrid DFT functional was used to perform the linear-response TDDFT absorption spectra with the LANL2DZ basis set. This method has been used previously by our group to characterize the electronic structure of the $In_{37}P_{20}$ cluster.[71–73] Initial structures were taken from XRD, optimized until the total and root mean squared displacement and force were under $1.80*10^{-3}$ and $1.20*10^{-3}$ Bohr, and $4.50*10^{-4}$ and $3.00*10^{-4}$ Har/Bohr, respectively. Linear Response TDDFT[74–76] was used to compute both the excitation energies and corresponding oscillator strengths of the first 25 electronic transitions.

3.7.6 *Single Crystal X-ray Diffraction Methods.*

An orange block from a toluene/pentane vapor diffusion, measuring 0.07 x 0.06 x 0.05 mm^3 was mounted on a loop with oil. Data was collected at -173°C on a Bruker APEX II single crystal X-ray diffractometer, Mo-radiation, equipped with a Miracol X-ray optical collimator.

Crystal-to-detector distance was 40 mm and exposure time was 120 seconds per frame for all sets. The scan width was 0.7°. Data collection was 99.9% complete to 24.407° in Θ. A total of 176486 reflections were collected covering the indices, -44<=h<=44, -24<=k<=24, -43<=l<=43. 43904 reflections were symmetry independent and the elevated R_{int} = 0.2442 relates to the small sample size. Indexing and unit cell refinement indicated a monoclinic lattice. The space group was found to be P $2_1/c$ (No.14). The data was integrated and scaled using SAINT, SADABS within the APEX2 software package by Bruker.[77] Solution by direct methods (SHELXT[78]) produced a complete heavy atom phasing model consistent with the proposed structure. The structure was completed by difference Fourier synthesis with SHELXL.[79,80] Scattering factors are from Waasmair and Kirfel.[81] Hydrogen atoms were placed in geometrically idealized positions and constrained to ride on their parent atoms with C---H distances in the range 0.95-1.00 Angstrom. Isotropic thermal parameters U_{eq} were fixed such that they were 1.2Ueq of their parent atom U_{eq} for CH's and 1.5Ueq of their parent atom U_{eq} in case of methyl groups. All non-hydrogen atoms were refined anisotropically by full-matrix least-squares. The contribution of disordered toluene and possibly pentane solvent to the diffraction pattern was removed with SQUEEZE,[82–84] and some disorder of the bound ligands was modeled. The crystallographic data for the structure has been deposited in the Cambridge Crystallographic Database under deposition number 2308638.

3.8 REFERENCES

(1) Viswanatha, R.; Amenitsch, H.; Santra, S.; Sapra, S.; Datar, S. S.; Zhou, Y.; Nayak, S. K.; Kumar, S. K.; Sarma, D. D. Growth Mechanism of Cadmium Sulfide Nanocrystals. *J Phys Chem Lett* **2010**, *1* (1), 304–308. https://doi.org/10.1021/jz9001339.

(2) Sowers, K. L.; Swartz, B.; Krauss, T. D. Chemical Mechanisms of Semiconductor Nanocrystal Synthesis. *Chem Mater* **2013**, *25* (8), 1351–1362. https://doi.org/10.1021/cm400005c.

(3) Wang, F.; Richards, V. N.; Shields, S. P.; Buhro, W. E. Kinetics and Mechanisms of Aggregative Nanocrystal Growth. *Chem. Mater.* **2014**, *26* (1), 5–21. https://doi.org/10.1021/cm402139r.

(4) Mule, A. S.; Mazzotti, S.; Rossinelli, A. A.; Aellen, M.; Prins, P. T.; Bok, J. C.; Solari, S. F.; Glauser, Y. M.; Kumar, P. V.; Riedinger, A.; Norris, D. J. Unraveling the Growth Mechanism of Magic-Sized Semiconductor Nanocrystals. *J Am Chem Soc* **2021**, *143* (4), 2037–2048. https://doi.org/10.1021/jacs.0c12185.

(5) Cossairt, B. M. Shining Light on Indium Phosphide Quantum Dots: Understanding the Interplay among Precursor Conversion, Nucleation, and Growth. *Chem Mater* **2016**, *28* (20), 7181–7189. https://doi.org/10.1021/acs.chemmater.6b03408.

(6) Liu, M.; Wang, K.; Wang, L.; Han, S.; Fan, H.; Rowell, N.; Ripmeester, J. A.; Renoud, R.; Bian, F.; Zeng, J.; Yu, K. Probing Intermediates of the Induction Period Prior to Nucleation and Growth of Semiconductor Quantum Dots. *Nat Commun* **2017**, *8* (1), 15467. https://doi.org/10.1038/ncomms15467.

(7) Owen, J. S.; Chan, E. M.; Liu, H.; Alivisatos, A. P. Precursor Conversion Kinetics and the Nucleation of Cadmium Selenide Nanocrystals. *J Am Chem Soc* **2010**, *132* (51), 18206–18213. https://doi.org/10.1021/ja106777j.

(8) Thanh, N. T. K.; Maclean, N.; Mahiddine, S. Mechanisms of Nucleation and Growth of Nanoparticles in Solution. *Chem Rev* **2014**, *114* (15), 7610–7630. https://doi.org/10.1021/cr400544s.

(9) Li, Y.; Rowell, N.; Luan, C.; Zhang, M.; Chen, X.; Yu, K. A Two-Pathway Model for the Evolution of Colloidal Compound Semiconductor Quantum Dots and Magic-Size Clusters. *Adv. Mater.* **2022**, *34* (46), 2107940. https://doi.org/10.1002/adma.202107940.

(10) Murray, C. B.; Norris, D. J.; Bawendi, M. G. Synthesis and Characterization of Nearly Monodisperse CdE (E = Sulfur, Selenium, Tellurium) Semiconductor Nanocrystallites. *J. Am. Chem. Soc.* **1993**, *115* (19), 8706–8715. https://doi.org/10.1021/ja00072a025.

(11) Hendricks, M. P.; Campos, M. P.; Cleveland, G. T.; Plante, I. J.-L.; Owen, J. S. A Tunable Library of Substituted Thiourea Precursors to Metal Sulfide Nanocrystals. *Science* **2015**, *348* (6240), 1226–1230. https://doi.org/10.1126/science.aaa2951.

(12) Gary, D. C.; Terban, M. W.; Billinge, S. J. L.; Cossairt, B. M. Two-Step Nucleation and Growth of InP Quantum Dots via Magic-Sized Cluster Intermediates. *Chem Mater* **2015**, *27* (4), 1432–1441. https://doi.org/10.1021/acs.chemmater.5b00286.

(13) Zhu, T.; Zhang, B.; Zhang, J.; Lu, J.; Fan, H.; Rowell, N.; Ripmeester, J. A.; Han, S.; Yu, K. Two-Step Nucleation of CdS Magic-Size Nanocluster MSC–311. *Chem. Mater.* **2017**, *29* (13), 5727–5735. https://doi.org/10.1021/acs.chemmater.7b02014.

(14) McMurtry, B. M.; Qian, K.; Teglasi, J. K.; Swarnakar, A. K.; Roo, J.; Owen, J. S. Continuous Nucleation and Size Dependent Growth Kinetics of Indium Phosphide Nanocrystals. *Chem Mater* **2020**, *32* (10), 4358–4368. https://doi.org/10.1021/acs.chemmater.0c01561.

(15) Yu, K. CdSe Magic-Sized Nuclei, Magic-Sized Nanoclusters and Regular Nanocrystals: Monomer Effects on Nucleation and Growth. *Adv. Mater.* **2012**, *24* (8), 1123–1132. https://doi.org/10.1002/adma.201104081.

(16) Evans, C. M.; Guo, L.; Peterson, J. J.; Maccagnano-Zacher, S.; Krauss, T. D. Ultrabright PbSe Magic-Sized Clusters. *Nano Lett* **2008**, *8* (9), 2896–2899. https://doi.org/10.1021/nl801685a.

(17) Zhang, J.; Hao, X.; Rowell, N.; Kreouzis, T.; Han, S.; Fan, H.; Zhang, C.; Hu, C.; Zhang, M.; Yu, K. Individual Pathways in the Formation of Magic-Size Clusters and Conventional Quantum Dots. *J Phys Chem Lett* **2018**, *9* (13), 3660–3666. https://doi.org/10.1021/acs.jpclett.8b01520.

(18) Gary, D. C.; Flowers, S. E.; Kaminsky, W.; Petrone, A.; Li, X.; Cossairt, B. M. Single-Crystal and Electronic Structure of a 1.3 Nm Indium Phosphide Nanocluster. *J Am Chem Soc* **2016**, *138* (5), 1510–1513. https://doi.org/10.1021/jacs.5b13214.

(19) Ning, J.; Banin, U. Magic Size InP and InAs Clusters: Synthesis, Characterization and Shell Growth. *Chem. Commun.* **2017**, *53* (17), 2626–2629. https://doi.org/10.1039/C6CC09778B.

(20) Xie, R.; Peng, X. Synthetic Scheme for High-Quality InAs Nanocrystals Based on Self-Focusing and One-Pot Synthesis of InAs-Based Core–Shell Nanocrystals. *Angew. Chem. Int. Ed.* **2008**, *47* (40), 7677–7680. https://doi.org/10.1002/anie.200802867.

(21) Dagtepe, P.; Chikan, V.; Jasinski, J.; Leppert, V. J. Quantized Growth of CdTe Quantum Dots; Observation of Magic-Sized CdTe Quantum Dots. *J Phys Chem C* **2007**, *111* (41), 14977–14983. https://doi.org/10.1021/jp072516b.

(22) Beecher, A. N.; Yang, X.; Palmer, J. H.; LaGrassa, A. L.; Juhas, P.; Billinge, S. J. L.; Owen, J. S. Atomic Structures and Gram Scale Synthesis of Three Tetrahedral Quantum Dots. *J. Am. Chem. Soc.* **2014**, *136* (30), 10645–10653. https://doi.org/10.1021/ja503590h.

(23) Lee, K.; Deng, G.; Bootharaju, M. S.; Hyeon, T. Synthesis, Assembly, and Applications of Magic-Sized Semiconductor (CdSe)13 Cluster. *Acc. Chem. Res.* **2023**, *56* (9), 1118–1127. https://doi.org/10.1021/acs.accounts.3c00061.

(24) Won, Y.-H.; Cho, O.; Kim, T.; Chung, D.-Y.; Kim, T.; Chung, H.; Jang, H.; Lee, J.; Kim, D.; Jang, E. Highly Efficient and Stable InP/ZnSe/ZnS Quantum Dot Light-Emitting Diodes. *Nature* **2019**, *575* (7784), 634–638. https://doi.org/10.1038/s41586-019-1771-5.

(25) Kim, Y.; Ham, S.; Jang, H.; Min, J. H.; Chung, H.; Lee, J.; Kim, D.; Jang, E. Bright and Uniform Green Light Emitting InP/ZnSe/ZnS Quantum Dots for Wide Color Gamut Displays. *ACS Appl Nano Mater* **2019**, *2* (3), 1496–1504. https://doi.org/10.1021/acsanm.8b02063.

(26) Battaglia, D.; Peng, X. Formation of High Quality InP and InAs Nanocrystals in a Noncoordinating Solvent. *Nano Lett.* **2002**, *2* (9), 1027–1030. https://doi.org/10.1021/nl025687v.

(27) Wang, R.; Ratcliffe, C. I.; Wu, X.; Voznyy, O.; Tao, Y.; Yu, K. Magic-Sized Cd3P2 II−V Nanoparticles Exhibiting Bandgap Photoemission. *J. Phys. Chem. C* **2009**, *113* (42), 17979–17982. https://doi.org/10.1021/jp907642b.

(28) Stein, J. L.; Steimle, M. I.; Terban, M. W.; Petrone, A.; Billinge, S. J. L.; Li, X.; Cossairt, B. M. Cation Exchange Induced Transformation of InP Magic-Sized Clusters. *Chem. Mater.* **2017**, *29* (18), 7984–7992. https://doi.org/10.1021/acs.chemmater.7b03075.

(29) Ritchhart, A.; Cossairt, B. M. Quantifying Ligand Exchange on InP Using an Atomically Precise Cluster Platform. *Inorg Chem* **2019**, *58* (4), 2840–2847. https://doi.org/10.1021/acs.inorgchem.8b03524.

(30) Friedfeld, M. R.; Stein, J. L.; Johnson, D. A.; Park, N.; Henry, N. A.; Enright, M. J.; Mocatta, D.; Cossairt, B. M. Effects of Zn2+ and Ga3+ Doping on the Quantum Yield of Cluster-Derived InP Quantum Dots. *J Chem Phys* **2019**, *151* (19). https://doi.org/10.1063/1.5126971.

(31) Ripberger, H. H.; Schnitzenbaumer, K. J.; Nguyen, L. K.; Ladd, D. M.; Levine, K. R.; Dayton, D. G.; Toney, M. F.; Cossairt, B. M. Navigating the Potential Energy Surface of CdSe Magic-Sized Clusters: Synthesis and Interconversion of Atomically Precise Nanocrystal Polymorphs. *J. Am. Chem. Soc.* **2023**, *145* (50), 27480–27492. https://doi.org/10.1021/jacs.3c08897.

(32) Jo, J. H.; Heo, H. S.; Yun, C.; Baek, S.; Lee, K. Destabilizing Magic-Sized Clusters for Synthesis of Monodisperse and Highly Luminescent In(Zn)P/ZnSe/ZnS Quantum Dots. *Chem Mater* **2023**, *35* (15), 6161–6167. https://doi.org/10.1021/acs.chemmater.3c01359.

(33) Kwon, Y.; Oh, J.; Lee, E.; Lee, S. H.; Agnes, A.; Bang, G.; Kim, J.; Kim, D.; Kim, S. Evolution from Unimolecular to Colloidal-Quantum-Dot-like Character in Chlorine or Zinc Incorporated InP Magic Size Clusters. *Nat Commun* **2020**, *11* (1), 3127. https://doi.org/10.1038/s41467-020-16855-9.

(34) Yang, J.; Fainblat, R.; Kwon, S. G.; Münzer, F.; Yu, J. H.; Terlinden, H.; Kim, B. H.; Iavarone, D.; Choi, M. K.; Kim, I. Y.; Park, I.; Hong, H.-K.; Lee, J.; Son, J. S.; Lee, Z.; Kang, K.; Hwang, S.-J.; Bacher, G.; Hyeon, T. Route to the Smallest Doped Semiconductor: Mn2+-Doped (CdSe)13 Clusters. *J. Am. Chem. Soc.* **2015**, *137* (40), 12776–12779. https://doi.org/10.1021/jacs.5b07888.

(35) Yang, J.; Muckel, F.; Choi, B. K.; Lorenz, S.; Kim, I. Y.; Ackermann, J.; Chang, H.; Czerney, T.; Kale, V. S.; Hwang, S.-J.; Bacher, G.; Hyeon, T. Co2+-Doping of Magic-

Sized CdSe Clusters: Structural Insights via Ligand Field Transitions. *Nano Lett* **2018**, *18* (11), 7350–7357. https://doi.org/10.1021/acs.nanolett.8b03627.

(36) Ma, F.; Abboud, K. A.; Zeng, C. Precision Synthesis of a CdSe Semiconductor Nanocluster via Cation Exchange. *Nat. Synth.* **2023**, 1–11. https://doi.org/10.1038/s44160-023-00330-6.

(37) Baek, W.; Bootharaju, M. S.; Walsh, K. M.; Lee, S.; Gamelin, D. R.; Hyeon, T. Highly Luminescent and Catalytically Active Suprastructures of Magic-Sized Semiconductor Nanoclusters. *Nat Mater* **2021**, *20* (5), 650–657. https://doi.org/10.1038/s41563-020-00880-6.

(38) Du, Y.; Sheng, H.; Astruc, D.; Zhu, M. Atomically Precise Noble Metal Nanoclusters as Efficient Catalysts: A Bridge between Structure and Properties. *Chem Rev* **2020**, *120* (2), 526–622. https://doi.org/10.1021/acs.chemrev.8b00726.

(39) Bootharaju, M. S.; Baek, W.; Deng, G.; Singh, K.; Voznyy, O.; Zheng, N.; Hyeon, T. Structure of a Subnanometer-Sized Semiconductor Cd14Se13 Cluster. *Chem* **2022**, *8* (11), 2978–2989. https://doi.org/10.1016/j.chempr.2022.06.025.

(40) Sandeno, S. F.; Schnitzenbaumer, K. J.; Krajewski, S. M.; Beck, R. A.; Ladd, D. M.; Levine, K. R.; Dayton, D.; Toney, M. F.; Kaminsky, W.; Li, X.; Cossairt, B. M. Ligand Steric Profile Tunes the Reactivity of Indium Phosphide Clusters. *J. Am. Chem. Soc.* **2024**, *146* (5), 3102–3113. https://doi.org/10.1021/jacs.3c10203.

(41) Franke, D.; Harris, D. K.; Xie, L.; Jensen, K. F.; Bawendi, M. G. The Unexpected Influence of Precursor Conversion Rate in the Synthesis of III–V Quantum Dots. *Angew. Chem. Int. Ed.* **2015**, *54* (48), 14299–14303. https://doi.org/10.1002/anie.201505972.

(42) Harris, D. K.; Bawendi, M. G. Improved Precursor Chemistry for the Synthesis of III–V Quantum Dots. *J. Am. Chem. Soc.* **2012**, *134* (50), 20211–20213. https://doi.org/10.1021/ja309863n.

(43) Williamson, C. B.; Nevers, D. R.; Nelson, A.; Hadar, I.; Banin, U.; Hanrath, T.; Robinson, R. D. Chemically Reversible Isomerization of Inorganic Clusters. *Science* **2019**, *363* (6428), 731–735. https://doi.org/10.1126/science.aau9464.

(44) Cunningham, P. D.; Coropceanu, I.; Mulloy, K.; Cho, W.; Talapin, D. V. Quantized Reaction Pathways for Solution Synthesis of Colloidal ZnSe Nanostructures: A Connection between Clusters, Nanowires, and Two-Dimensional Nanoplatelets. *ACS Nano* **2020**, *14* (4), 3847–3857. https://doi.org/10.1021/acsnano.9b09051.

(45) Wang, Y.; Liu, Y.-H.; Zhang, Y.; Wang, F.; Kowalski, P. J.; Rohrs, H. W.; Loomis, R. A.; Gross, M. L.; Buhro, W. E. Isolation of the Magic-Size CdSe Nanoclusters [(CdSe)13(n-Octylamine)13] and [(CdSe)13(Oleylamine)13]. *Angew. Chem. Int. Ed.* **2012**, *51* (25), 6154–6157. https://doi.org/10.1002/anie.201202380.

(46) Kim, T.; Park, S.; Jeong, S. Diffusion Dynamics Controlled Colloidal Synthesis of Highly Monodisperse InAs Nanocrystals. *Nat Commun* **2021**, *12* (1), 3013. https://doi.org/10.1038/s41467-021-23259-w.

(47) Tamang, S.; Lee, S.; Choi, H.; Jeong, S. Tuning Size and Size Distribution of Colloidal InAs Nanocrystals via Continuous Supply of Prenucleation Clusters on Nanocrystal Seeds. *Chem Mater* **2016**, *28* (22), 8119–8122. https://doi.org/10.1021/acs.chemmater.6b03585.

(48) Srivastava, V.; Dunietz, E.; Kamysbayev, V.; Anderson, J. S.; Talapin, D. V. Monodisperse InAs Quantum Dots from Aminoarsine Precursors: Understanding the Role of Reducing

Agent. *Chem Mater* **2018**, *30* (11), 3623–3627. https://doi.org/10.1021/acs.chemmater.8b01137.

(49) Zhu, D.; Bahmani Jalali, H.; Saleh, G.; Stasio, F.; Prato, M.; Polykarpou, N.; Othonos, A.; Christodoulou, S.; Ivanov, Y. P.; Divitini, G.; Infante, I.; Trizio, L.; Manna, L. Boosting the Photoluminescence Efficiency of InAs Nanocrystals Synthesized with Aminoarsine via a ZnSe Thick-Shell Overgrowth. *Adv. Mater.* **2023**, *35* (38), 2303621. https://doi.org/10.1002/adma.202303621.

(50) Liu, Z.; Pascazio, R.; Goldoni, L.; Maggioni, D.; Zhu, D.; Ivanov, Y. P.; Divitini, G.; Camarelles, J. L.; Jalali, H. B.; Infante, I.; Trizio, L.; Manna, L. Colloidal InAs Tetrapods: Impact of Surfactants on the Shape Control. *J Am Chem Soc* **2023**, *145* (33), 18329–18339. https://doi.org/10.1021/jacs.3c03906.

(51) Li, Y.; Hou, X.; Shen, Y.; Dai, N.; Peng, X. Tuning the Reactivity of Indium Alkanoates by Tertiary Organophosphines for the Synthesis of Indium-Based Quantum Dots. *Chem. Mater.* **2021**, *33* (23), 9348–9356. https://doi.org/10.1021/acs.chemmater.1c03219.

(52) Allen, P. M.; Walker, B. J.; Bawendi, M. G. Mechanistic Insights into the Formation of InP Quantum Dots. *Angew. Chem.* **2010**, *122* (4), 772–774. https://doi.org/10.1002/ange.200905632.

(53) Hu, R.; He, F.; Hou, R.; Wu, Z.; Zhang, X.; Shen, H. The Narrow Synthetic Window for Highly Homogenous InP Quantum Dots toward Narrow Red Emission. *Inorg Chem* **2024**. https://doi.org/10.1021/acs.inorgchem.3c04358.

(54) Tolman, C. A. Steric Effects of Phosphorus Ligands in Organometallic Chemistry and Homogeneous Catalysis. *Chem Rev* **1977**, *77* (3), 313–348. https://doi.org/10.1021/cr60307a002.

(55) Savchenko, S. S.; Vokhmintsev, A. S.; Weinstein, I. A. Temperature Dependence of the Optical Absorption Spectra of InP/ZnS Quantum Dots. *Tech Phys Lett* **2017**, *43* (3), 297–300. https://doi.org/10.1134/S1063785017030221.

(56) Bouarissa, N.; Aourag, H. Effective Masses of Electrons and Heavy Holes in InAs, InSb, GaSb, GaAs and Some of Their Ternary Compounds. *Infrared Phys. Technol.* **1999**, *40* (4), 343–349. https://doi.org/10.1016/S1350-4495(99)00020-1.

(57) Klein, M. D.; Bisted, C. H.; Dou, F. Y.; Sandwisch, J. W.; Cossairt, B. M.; Khalil, M. Measuring Relative Energies of Ligand Binding Conformations on Nanocluster Surfaces with Temperature-Dependent FTIR Spectroscopy. *J Phys Chem C* **2023**. https://doi.org/10.1021/acs.jpcc.3c03951.

(58) Cros-Gagneux, A.; Delpech, F.; Nayral, C.; Cornejo, A.; Coppel, Y.; Chaudret, B. Surface Chemistry of InP Quantum Dots: A Comprehensive Study. *J. Am. Chem. Soc.* **2010**, *132* (51), 18147–18157. https://doi.org/10.1021/ja104673y.

(59) Dümbgen, K. C.; Zito, J.; Infante, I.; Hens, Z. Shape, Electronic Structure, and Trap States in Indium Phosphide Quantum Dots. *Chem. Mater.* **2021**, *33* (17), 6885–6896. https://doi.org/10.1021/acs.chemmater.1c01795.

(60) Christensen, N. E.; Satpathy, S.; Pawlowska, Z. Bonding and Ionicity in Semiconductors. *Phys. Rev. B* **1987**, *36* (2), 1032–1050. https://doi.org/10.1103/PhysRevB.36.1032.

(61) Marchand, P.; Sathasivam, S.; Williamson, B. A. D.; Pugh, D.; Bawaked, S. M.; Basahel, S. N.; Obaid, A. Y.; Scanlon, D. O.; Parkin, I. P.; Carmalt, C. J. A Single-Source Precursor Approach to Solution Processed Indium Arsenide Thin Films. *J. Mater. Chem. C* **2016**, *4* (28), 6761–6768. https://doi.org/10.1039/C6TC02293F.

(62) Gaussian 16, Revision C.01, Frisch, M. J.; Trucks, G. W.; Schlegel, H. B.; Scuseria, G. E.; Robb, M. A.; Cheeseman, J. R.; Scalmani, G.; Barone, V.; Petersson, G. A.; Nakatsuji, H.; Li, X.; Caricato, M.; Marenich, A. V.; Bloino, J.; Janesko, B. G.; Gomperts, R.; Mennucci, B.; Hratchian, H. P.; Ortiz, J. V.; Izmaylov, A. F.; Sonnenberg, J. L.; Williams-Young, D.; Ding, F.; Lipparini, F.; Egidi, F.; Goings, J.; Peng, B.; Petrone, A.; Henderson, T.; Ranasinghe, D.; Zakrzewski, V. G.; Gao, J.; Rega, N.; Zheng, G.; Liang, W.; Hada, M.; Ehara, M.; Toyota, K.; Fukuda, R.; Hasegawa, J.; Ishida, M.; Nakajima, T.; Honda, Y.; Kitao, O.; Nakai, H.; Vreven, T.; Throssell, K.; Montgomery, J. A., Jr.; Peralta, J. E.; Ogliaro, F.; Bearpark, M. J.; Heyd, J. J.; Brothers, E. N.; Kudin, K. N.; Staroverov, V. N.; Keith, T. A.; Kobayashi, R.; Normand, J.; Raghavachari, K.; Rendell, A. P.; Burant, J. C.; Iyengar, S. S.; Tomasi, J.; Cossi, M.; Millam, J. M.; Klene, M.; Adamo, C.; Cammi, R.; Ochterski, J. W.; Martin, R. L.; Morokuma, K.; Farkas, O.; Foresman, J. B.; Fox, D. J. Gaussian, Inc., Wallingford CT, 2016.

(63) Gary, D. C.; Flowers, S. E.; Kaminsky, W.; Petrone, A.; Li, X.; Cossairt, B. M. Single-Crystal and Electronic Structure of a 1.3 Nm Indium Phosphide Nanocluster. *J. Am. Chem. Soc.* **2016**, *138* (5), 1510–1513. https://doi.org/10.1021/jacs.5b13214.

(64) Sandeno, S.; Schnitzenbaumer, K.; Krajewski, S.; Beck, R.; Ladd, D.; Levine, K.; Dayton, D.; Toney, M.; Li, X.; Kaminsky, W.; Cossairt, B. Ligand Steric Profile Tunes the Reactivity of Indium Phosphide Clusters. ChemRxiv September 18, 2023. https://doi.org/10.26434/chemrxiv-2023-555vg.

(65) Möller, M.; Lima, M. M.; Cantarero, A.; Dacal, L. C. O.; Madureira, J. R.; Iikawa, F.; Chiaramonte, T.; Cotta, M. A. Polarized and Resonant Raman Spectroscopy on Single InAs

Nanowires. *Phys Rev B* **2011**, *84* (8), 085318. https://doi.org/10.1103/PhysRevB.84.085318.

(66) Shin, J.; Choi, M.; Shim, D.; Ziehl, T. J.; Park, S.; Cho, E.; Zhang, P.; Lee, H.; Kang, J.; Jeong, S. Unveiling the Nanocluster Conversion Pathway for Highly Monodisperse InAs Colloidal Quantum Dots. *JACS Au* **2024**, *4* (3), 1097–1106. https://doi.org/10.1021/jacsau.3c00809.

(67) Gary, D. C.; Cossairt, B. M. Role of Acid in Precursor Conversion During InP Quantum Dot Synthesis. *Chem. Mater.* **2013**, *25* (12), 2463–2469. https://doi.org/10.1021/cm401289j.

(68) Heyd, J.; Scuseria, G. E. Efficient Hybrid Density Functional Calculations in Solids: Assessment of the Heyd–Scuseria–Ernzerhof Screened Coulomb Hybrid Functional. *J. Chem. Phys.* **2004**, *121* (3), 1187–1192. https://doi.org/10.1063/1.1760074.

(69) Heyd, J.; Scuseria, G. E.; Ernzerhof, M. Hybrid Functionals Based on a Screened Coulomb Potential. *J. Chem. Phys.* **2003**, *118* (18), 8207–8215. https://doi.org/10.1063/1.1564060.

(70) Vydrov, O. A.; Heyd, J.; Krukau, A. V.; Scuseria, G. E. Importance of Short-Range versus Long-Range Hartree-Fock Exchange for the Performance of Hybrid Density Functionals. *J. Chem. Phys.* **2006**, *125* (7), 074106. https://doi.org/10.1063/1.2244560.

(71) Gary, D. C.; Flowers, S. E.; Kaminsky, W.; Petrone, A.; Li, X.; Cossairt, B. M. Single-Crystal and Electronic Structure of a 1.3 Nm Indium Phosphide Nanocluster. *J. Am. Chem. Soc.* **2016**, *138* (5), 1510–1513. https://doi.org/10.1021/jacs.5b13214.

(72) Cho, E.; Jang, H.; Lee, J.; Jang, E. Modeling on the Size Dependent Properties of InP Quantum Dots: A Hybrid Functional Study. *Nanotechnology* **2013**, *24* (21), 215201. https://doi.org/10.1088/0957-4484/24/21/215201.

(73) Leger, J. D.; Friedfeld, M. R.; Beck, R. A.; Gaynor, J. D.; Petrone, A.; Li, X.; Cossairt, B. M.; Khalil, M. Carboxylate Anchors Act as Exciton Reporters in 1.3 Nm Indium Phosphide Nanoclusters. *J. Phys. Chem. Lett.* **2019**, *10* (8), 1833–1839. https://doi.org/10.1021/acs.jpclett.9b00602.

(74) Casida, M. E.; Jamorski, C.; Casida, K. C.; Salahub, D. R. Molecular Excitation Energies to High-Lying Bound States from Time-Dependent Density-Functional Response Theory: Characterization and Correction of the Time-Dependent Local Density Approximation Ionization Threshold. *J. Chem. Phys.* **1998**, *108* (11), 4439–4449. https://doi.org/10.1063/1.475855.

(75) Furche, F.; Ahlrichs, R. Adiabatic Time-Dependent Density Functional Methods for Excited State Properties. *J. Chem. Phys.* **2002**, *117* (16), 7433–7447. https://doi.org/10.1063/1.1508368.

(76) Stratmann, R. E.; Scuseria, G. E.; Frisch, M. J. An Efficient Implementation of Time-Dependent Density-Functional Theory for the Calculation of Excitation Energies of Large Molecules. *J. Chem. Phys.* **1998**, *109* (19), 8218–8224. https://doi.org/10.1063/1.477483.

(77) Bruker. APEX2, 2007.

(78) Sheldrick, G. M. SHELXT - Integrated Space-Group and Crystal-Structure Determination. *Acta* **2015**.

(79) Sheldrick, G. M. A Short History of SHELX. *Acta Crystallogr. A* **2008**, *64* (1), 112–122. https://doi.org/10.1107/S0108767307043930.

(80) MaXus: A Computer Program for the Solution and Refinement of Crystal Structures from Diffraction Data.

(81) Waasmaier, D.; Kirfel, A. New Analytical Scattering Factor Functions for Free Atoms and Ions, 1995.

(82) Spek A. *J Appl Cryst* **2003**, *36*, 7–13.

(83) Spek, A. L. Acta. *Cryst* **2009**, *D65*, 148–155.

(84) Sluis; Spek, A. L. Acta Cryst, 1990, *A46*, 194–201.

Chapter 4. NARROW BLUE EMISSION FROM CADMIUM PHOSPHIDE CLUSTERS ENHANCED THROUGH PHOSPHINATE LIGATION

Components of this chapter were republished with permission of the American Chemical Society, from "Narrow Blue Emission from Cadmium Phosphide Clusters Enhanced through Phosphinate Ligation", Soren F. Sandeno, Samantha M. Harvey, Vijay N. Lin, and Brandi M. Cossairt; *Nano Letters.* **2025**, *25* (23), 9410–9416; Copyright 2025 American Chemical Society.

4.1 INTRODUCTION

Advanced optoelectronic technologies form the basis of today's information age and will be paramount in tomorrow's quantum information age. Given this, semiconductor nanocrystals, or quantum dots (QDs), have emerged as a proven active medium for generating color-pure light.[1–3] They offer colloidal processability, highly tunable emission wavelengths, large absorption cross-sections, and high stability, all of which contribute to current efforts to control their emissive properties for advanced classical and quantum light technologies.[4,5] Many of these efforts have focused on eliminating nonradiative recombination through molecular passivation of surface defects and inorganic shelling procedures.[6–11] However, challenges beyond maximizing the photoluminescence quantum yield (PLQY) still hinder progress toward QD adoption on a larger scale. One such challenge is the ensemble heterogeneity of a QD sample both within a singular batch and between batches made through identical procedures.[12] Intra-batch heterogeneity can broaden emission line widths, which minimizes color purity, and inter-batch heterogeneity

challenges the reproducibility of lab-scale QD synthesis and scale-up for commercialization. Minimizing heterogeneity across the board is essential for further development of QDs.

The optimal synthetic candidate for addressing these challenges would be a perfect molecular QD. A singular QD batch would contain particles of identical sizes, leading to extremely high color purity and zero batch-to-batch variability. All the while, colloidal processability, large absorption cross-sections, and stability would be maintained. The discovery of magic-sized clusters has pushed the field closer to this goal.[13,14] These molecular semiconductor clusters exist as metastable intermediates that form during QD syntheses. Despite their prevalence across many different materials that are heralded for their optical properties, the majority of clusters are not high-quality emitters. Due to their small size, an array of vibrational modes is available, resulting in predominately non-radiative recombination.[15] Even when these materials emit, strong vibrational coupling in the excited state leads to very large apparent Stokes shifts and extremely broad emission, both characteristic features of self-trapped exciton behavior.[16–18] Additionally, many of these precise structures have a cluster-ligand interface passivated by relatively weakly bound carboxylate or L-type ligands such as amines. The ligand population is thus dynamic, leading to a lack of complete passivation at equilibrium, which can transiently influence the emissive behavior.[19,20] While these atomically precise clusters could address challenges in ensemble heterogeneity and batch-to-batch reproducibility, their poor emission characteristics hinder their applicability.

The array of treatments that may be used to address the challenges of nonradiative recombination is limited for magic-sized clusters due to their inherent metastability. Any perturbations in the material's internal structure can lead to destabilization and loss of precision.[21] However, this still leaves the cluster-ligand interface as a focal point for controlling emissive

behavior. Due to the prevalence of carboxylic acids in QD synthesis, many clusters that have been isolated and characterized as pure substances are either primarily or entirely ligated by carboxylates, including InP, InAs, CdSe, CdS, Cd_3P_2, and Cd_3As_2.[22–27] These clusters show a distribution of binding motifs, including chelating, bridging syn-anti, bridging syn-syn, and monodentate.[22,23,28–30] This distribution of coordination environments is essential for stabilizing the cluster structure, and deviation from the denticity preset by the carboxylate would likely lead to structural destabilization. With this in mind, we focused our efforts on controlling surface chemistry towards ligands that bind stronger than carboxylates but maintain the bidentate chelation.

Recently, phosphinic acids have been reported as a new class of ligands for controlling the reactivity of the metal precursor in QD synthesis.[31,32] The phosphinic acid ligand closely simulates the binding strength of a phosphonic acid but only provides two available binding sites, thereby mimicking the coordination of a carboxylic acid. Furthermore, the similarity in coordination has been previously explored with zirconium and hafnium metal oxo clusters.[33] We hypothesized that phosphinate coordination to a magic-sized cluster would allow for structural retention, as seen with the metal oxo clusters, while enhancing emission in semiconductor materials due to the significantly higher binding affinity of the phosphinate compared to the carboxylate. Phosphinate-ligated CdSe and CdTe magic-sized clusters have been reported previously but required 310 °C synthesis temperatures, likely due to decreased cadmium precursor reactivity from the greater phosphinate binding strength.[34] Because of this, we believed a ligand exchange procedure could mitigate this high-temperature requirement.

We chose the Cd_3P_2 cluster originally reported by Wang et al. to test our hypothesis that substitution of carboxylates with phosphinates would boost PLQY.[26,35] It is synthesized with oleic acid, and while it has highly narrow emission in the blue region (PL λ_{max} = 457 nm), the PLQY of ~7% was evidence of fast nonradiative recombination rates (**Figure 4.1.1**). Furthermore, the closely related Cd_3As_2 cluster has been documented with similarly narrow emission in the green (PL λ_{max} = 534 nm) and could benefit from the same surface treatment.[27,36]

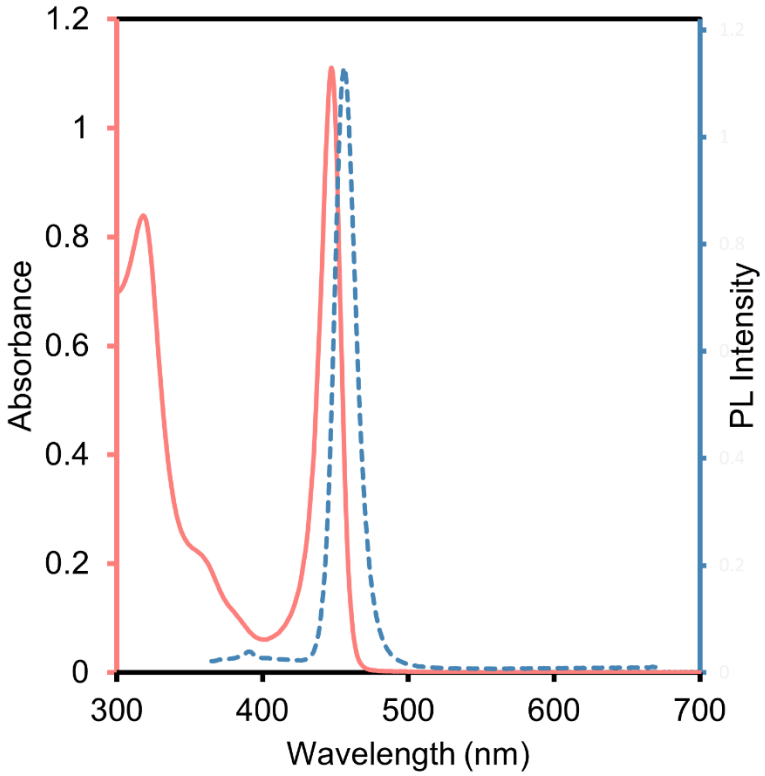

Figure 4.1.1. Absorbance (red) and photoluminescence (blue) spectra of as-synthesized, oleate-ligated Cd_3P_2 clusters.

Herein, we report ligand exchange of oleate-capped II-V clusters with alkylphosphinic acids. Using a combination of steady-state and time-resolved optical spectroscopy, we observed that alkylphosphinates do not perturb the metastability of these atomically-precise clusters but strongly enhance their emissive characteristics. We find that phosphinate ligation reduces

nonradiative recombination, thereby extending the radiative lifetime, as well as alters the surface dipole, leading to a bathochromic shift in both the absorbance and emission profiles. This ultimately results in an atomically-precise Cd_3P_2 cluster that emits at 467 nm with a 26% PLQY and an ultra-narrow, 96 meV full width at half maximum (FWHM). This strategy was also applied to the related Cd_3As_2 clusters, increasing the PLQY from 0.5% to 9% with emission at 550 nm and a 96 meV FWHM.

4.2 Ligand Exchange with Phosphinic Acids

To investigate the influence of phosphinate ligation, a suite of phosphinic acids was synthesized with varying chain lengths and degrees of rigidity. Octadecyl-, dodecyl-, and hexylphosphinic acid were used to assess chain length influence, whereas oleyl- and benzylphosphinic acid served to disrupt the ligand ordering on the surface of the cluster to understand its impact (**Figure 4.2.1A**). The ligand exchanges were performed on oleate-capped Cd_3P_2 clusters (**Figure 4.2.2**) by successive injection of a solution containing 0.58 eq phosphinic acid with respect to oleate (as determined by ^{1}H NMR) in tetrachloroethylene.

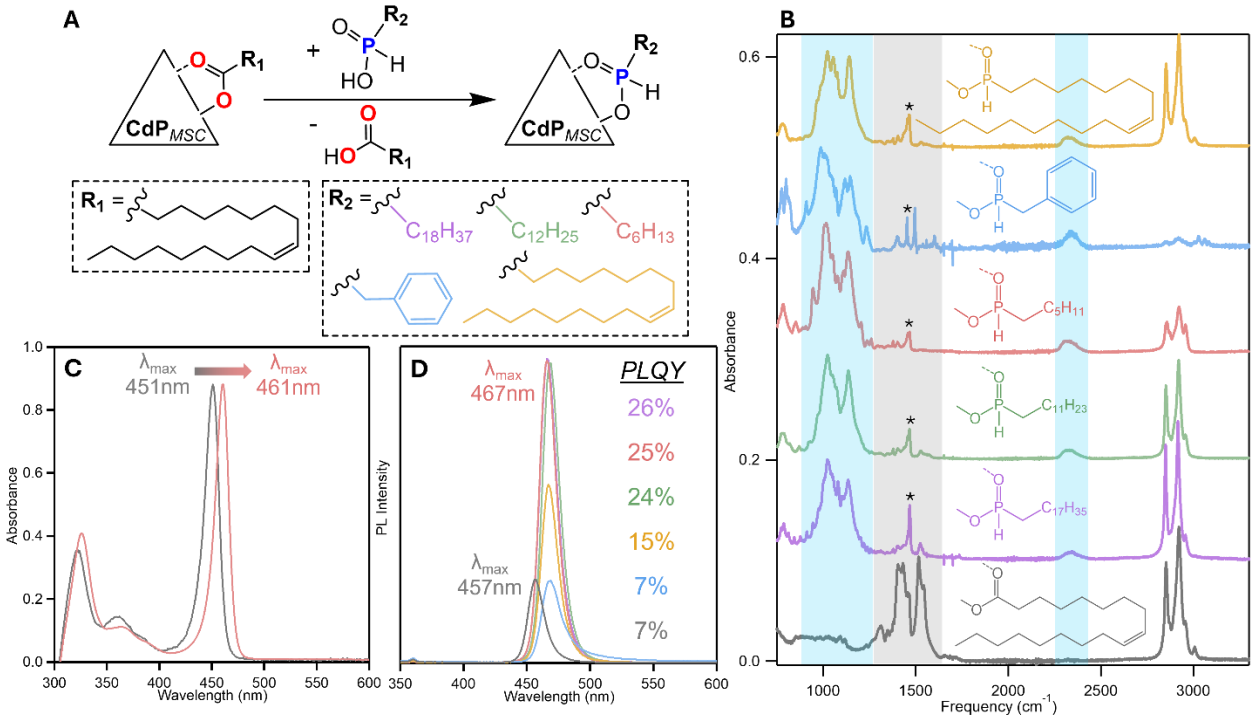

Figure 4.2.1. A) Ligand exchange schematic showing the native oleate ligands and the suite of phosphinic acid ligand tails. B) Full FTIR spectrum of all phosphinate-ligated Cd_3P_2 clusters after exchange compared to oleate-ligated Cd_3P_2 before exchange (grey). (*) marks the residual solvent signal from toluene. C) UV-Vis absorbance of Cd_3P_2 clusters with oleate ligands (grey) before exchange and hexylphosphinate ligands (red) after exchange. D) Photoluminescence of Cd_3P_2 clusters before and after ligand exchange with varying phosphinic acids.

Successful phosphinate exchange was confirmed by Fourier transform infrared spectroscopy (FTIR), showing that for each new ligand, the asymmetric and symmetric carboxylate stretches (~1400-1600 cm^{-1}) were replaced by the P=O and P-O(M) phosphinate stretching frequencies around 1100 cm^{-1} (**Figure 4.2.1B**). Specifically, we note the P-O(H) stretch of the free phosphinic acid at 975 cm^{-1} shifts to 1020 cm^{-1} which is characteristic of the P-O(M) stretch in metal phosphinate complexes and further confirms binding.[37] While specific coordination motifs cannot be determined, it has been found previously that phosphinates strongly prefer a bridging geometry over chelating coordination.[33] Furthermore, the characteristic P-H stretch centered at 2330 cm^{-1} is visible upon exchange. The presence of bound alkylphosphinate is also evidenced by ^{31}P-NMR spectroscopy (**Figure 4.2.2**).

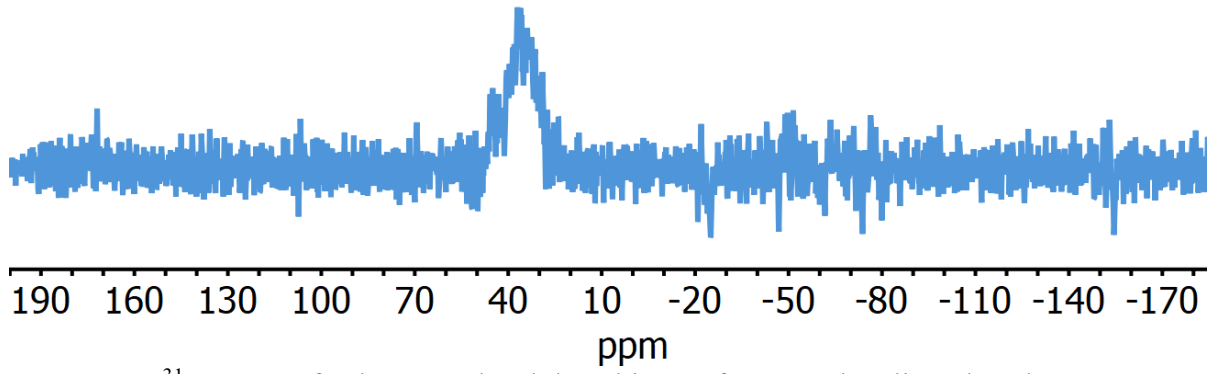

Figure 4.2.2. ^{31}P-NMR of Cd_3P_2-octadecylphosphinate after complete ligand exchange.

We note that ^{1}H-NMR spectroscopy of the exchanged Cd_3P_2-phosphinate clusters shows 3.3% residual oleate still bound to the cluster surface as well as a similar amount of free oleic acid left over after purification (**Figure 4.2.3**).

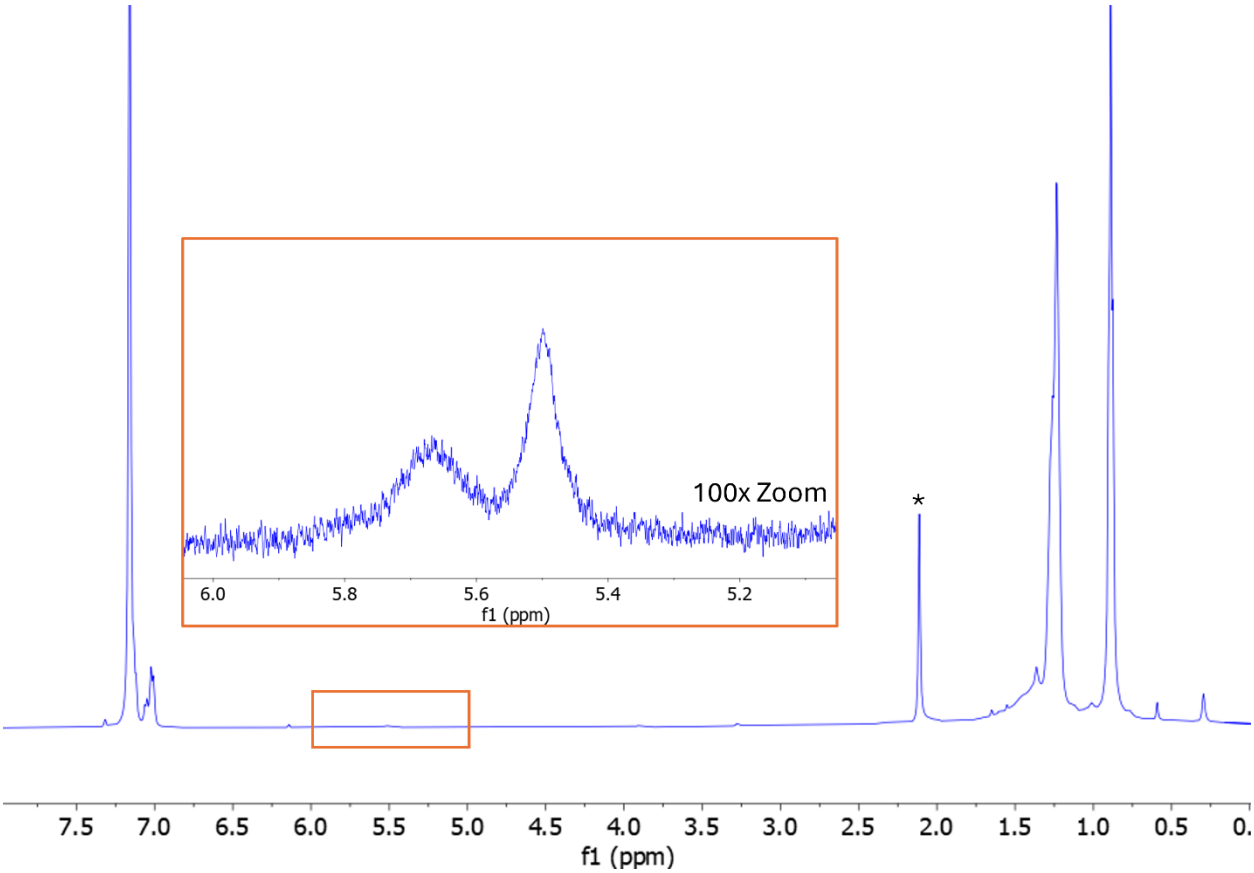

Figure 4.2.3. ^{1}H-NMR of purified Cd_3P_2-octadecylphosphinate clusters showing oleate and oleic acid that are still present after purification.(*) Designates the residual solvent signal from toluene.

Any attempts at further exchange on the Cd_3P_2-phosphinate clusters to completely remove residual oleate resulted in dissolution of the clusters. This emphasizes the metastability of these clusters, especially as it relates to the cluster-ligand interface.

Further characterization of the Cd_3P_2 clusters before and after exchange with phosphinic acid shows that ligation with phosphinate induces a 10 nm red shift in the λ_{max} of the cluster absorbance (**Figure 4.2.1C**). Despite the shift in the lowest energy excitonic transition, the overall absorbance profile remains the same. We find that this induced red shift occurs continuously as more phosphinate is substituted onto the cluster surface during the exchange. We hypothesize this

red shift is induced by a difference in the surface dipole established by oleate versus phosphinate. Surface dipoles alter the stability of the conduction band and valence band edges in QDs.[38,39] If this effect is more pronounced in one band edge over the other, this can induce a change in the energy of the bandgap and, therefore, shift the λ_{max} of the sample. To confirm a difference in the induced dipole between carboxylate and phosphinate, first principles calculations of the dipole in potassium ethanoate is compared to that of potassium ethylphosphinate. In both instances, the overall dipole is oriented directly from the head group toward the coordinated metal (**Figure 4.2.4**). The magnitude of this dipole is 7.80 Debye and 5.95 Debye in the case of the carboxylate and phosphinate, respectively. This 1.85 Debye difference induces an 80 meV red shift, which is similar to what has been previously reported for thiophenol ligands on PbS QDs.[40]

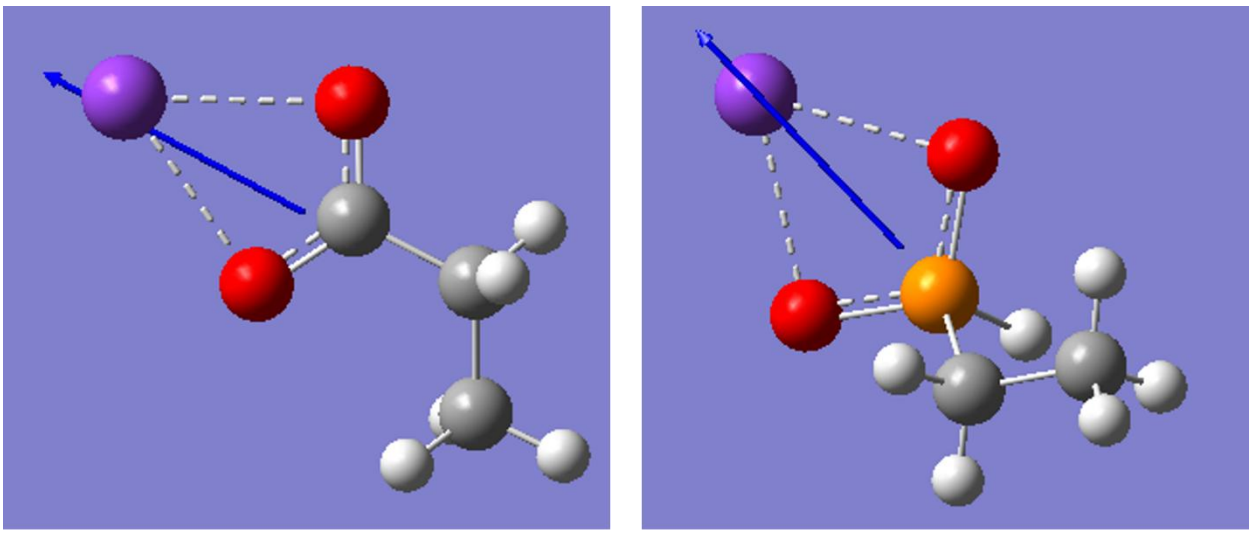

Figure 4.2.4. Visualization of the overall dipole (blue) in potassium ethanoate (left, 7.80 Debye) versus potassium ethylphosphinate (right, 5.95 Debye). The length of the dipole is arbitrary and does not reflect the magnitude.

We find that the red shift also applies to the photoluminescence after exchange. With the original Cd_3P_2-oleate cluster emitting at 457 nm, exchange for phosphinate ligands results in

emission at 467 nm (**Figure 4.2.1D**). We observe no change in the FWHM (96 meV) of the emission profile after the ligand exchange. Finally, we see that, especially in the case of the alkylphosphinates, the PLQY is substantially enhanced, reaching as high as 26% (**Figure 4.2.1D**). This is more than triple the PLQY of the Cd_3P_2 with native oleate ligands. These three characteristics: the 467 nm $\lambda_{max,}$ which is desirable for blue emission, the 96 meV FWHM showing very high color purity, and the 26% PLQY, all from an atomically precise material, is an exciting result. While the PLQY after exchange is similar for other unsaturated linear phosphinic acids, the emission is substantially lower for benzyl (7%) and oleyl (15%) phosphinic acid. This is a surprising result as the cluster-ligand inner-coordination sphere is identical, but the ligand tail identity changes, implicating the importance of ligand ordering on PLQY.

Seeing as the stronger binding of the monoalkylphosphinate led to enhanced optical properties and the structure of the tail was also influencing the emission, we further investigated the effects of ligand exchange by diisooctylphosphinic acid, hexylphosphonic acid, and hexylsulfonic acid. In the case of the dialkylphosphinic acid, we were able to confirm successful exchange by FTIR (**Figure 4.2.5A**). However, it was more difficult to exchange and required much higher equivalents to obtain similar degrees of oleate displacement when compared to the monoalkylphosphinic acids. We also note that pushing the exchange led to destabilization of the cluster, evidenced by a loss of peak definition in the absorbance spectrum and almost complete loss of PL intensity (**Figure 4.2.5B**).

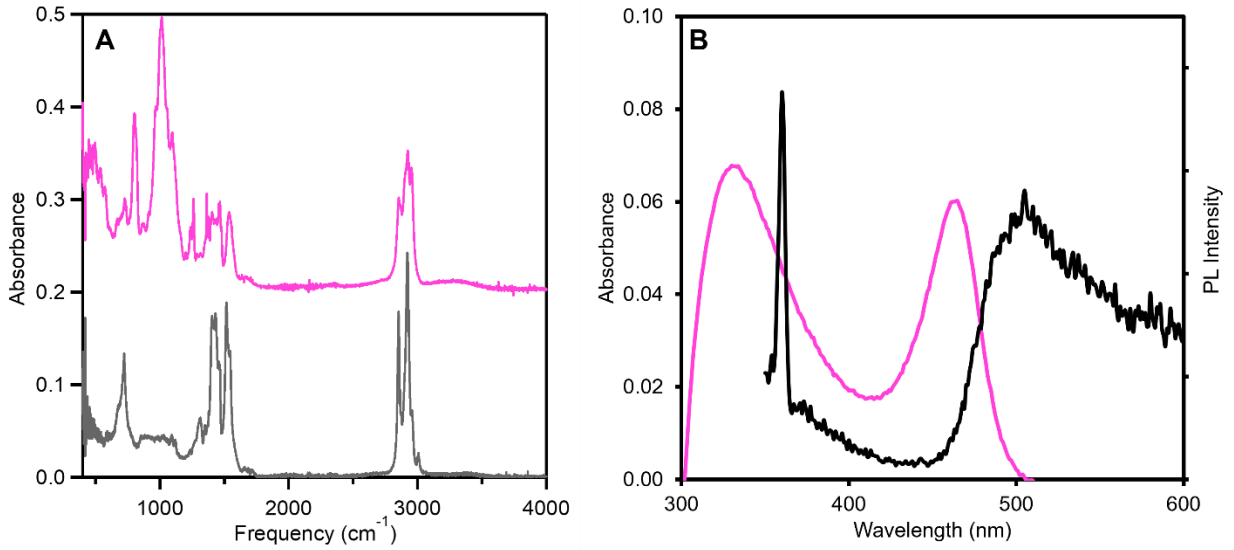

Figure 4.2.5. A) FTIR of Cd_3P_2-oleate (grey) and Cd_3P_2 after exchange with diisooctylphosphinic acid (pink). B) Absorbance (pink) and emission (black) of Cd_3P_2 clusters after ligand exchange with diisooctylphosphinic acid. The sharp feature at 360 nm in the photoluminescence spectrum (black) originates from the solvent and is not related to Cd_3P_2 emission.

We believe this degradation is based on the larger steric profile of the dialkyl substituents, which cannot comfortably passivate all open cadmium sites without significant steric pressure between ligand tails. Similar results have been reported with dialkylphosphinate at the surface of metal oxo clusters.[33] Increasing the binding affinity of the head group by using hexylphosphonic acid led to similar results (**Figure 4.2.6**). It is likely that in the case of phosphonic acid, switching to a tridentate ligand disturbs the balance of stability at the surface, leading to an imprecise material. Finally, we investigated hexylsulfonic acid, which, upon treating Cd_3P_2-oleate, maintains the absorbance profile of the cluster but leads to a decrease in the overall PL intensity (**Figure 4.2.6**). These investigations confirm that the bidentate monoalkylphosphinic acids are uniquely poised to passivate cluster surfaces, thereby enhancing the PL without structural degradation. We therefore focused our efforts on the monoalkylphosphinate passivation and sought to understand

the differences in the PLQY caused by the substituent on the phosphinate through time-resolved spectroscopy.

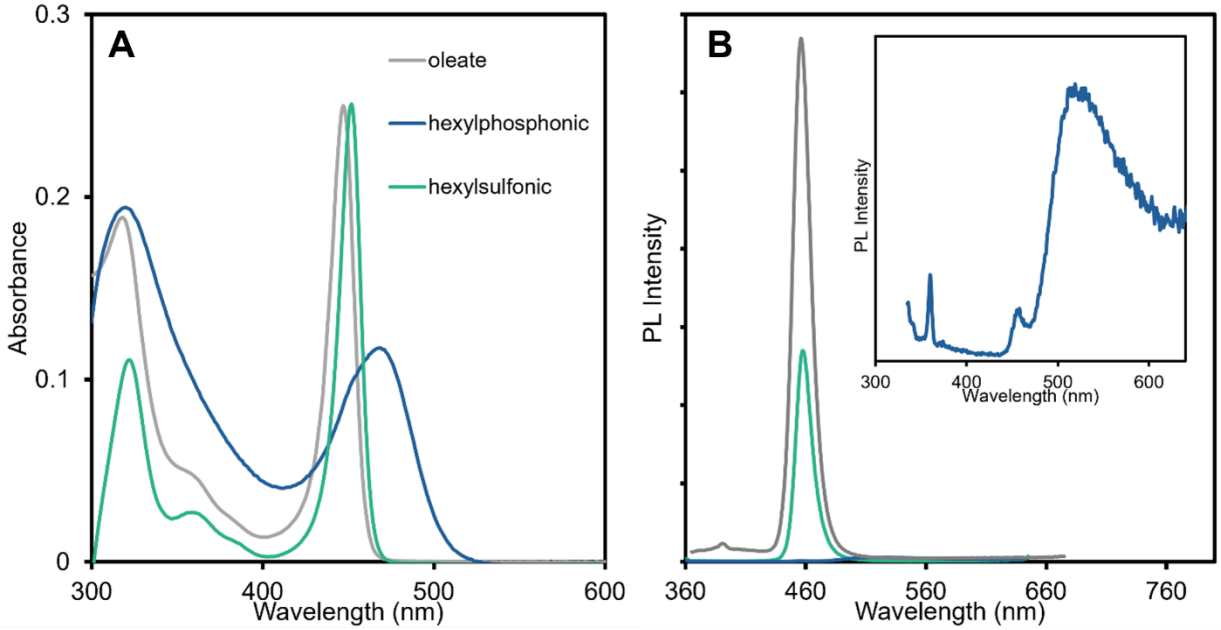

Figure 4.2.6. A) Absorbance profiles of Cd_3P_2-oleate clusters (grey) after attempted exchange with hexylphosphonic (blue) and hexylsulfonic (cyan) acid. B) Emission profiles (right) after attempted exchange with hexylphosphonic (blue) and hexylsulfonic (cyan) acid.

4.3 Transient Spectroscopy of Phosphinate-Ligated Cd_3P_2

To further investigate the PLQY differences we observed across the suite of phosphinate ligands, time-resolved photoluminescence spectroscopy (TRPL) was performed to assess radiative lifetimes. Firstly, the TRPL decay rate for the oleate-ligated Cd_3P_2 clusters could not be confidently measured on our instrument as the lifetime was faster than the instrument response time. We, therefore, approximate the decay rate as that previously measured for oleate-ligated Cd_3P_2 clusters, $\langle\tau\rangle = 0.41$ ns.[41] It is qualitatively apparent, however, that the radiative lifetime is extended significantly upon ligation with phosphinate (**Figure 4.3.1A**). The extension in the

radiative lifetime, when considered alongside the increase in PLQY, suggests that the phosphinate ligands are suppressing non-radiative processes that would otherwise compete with radiative recombination.

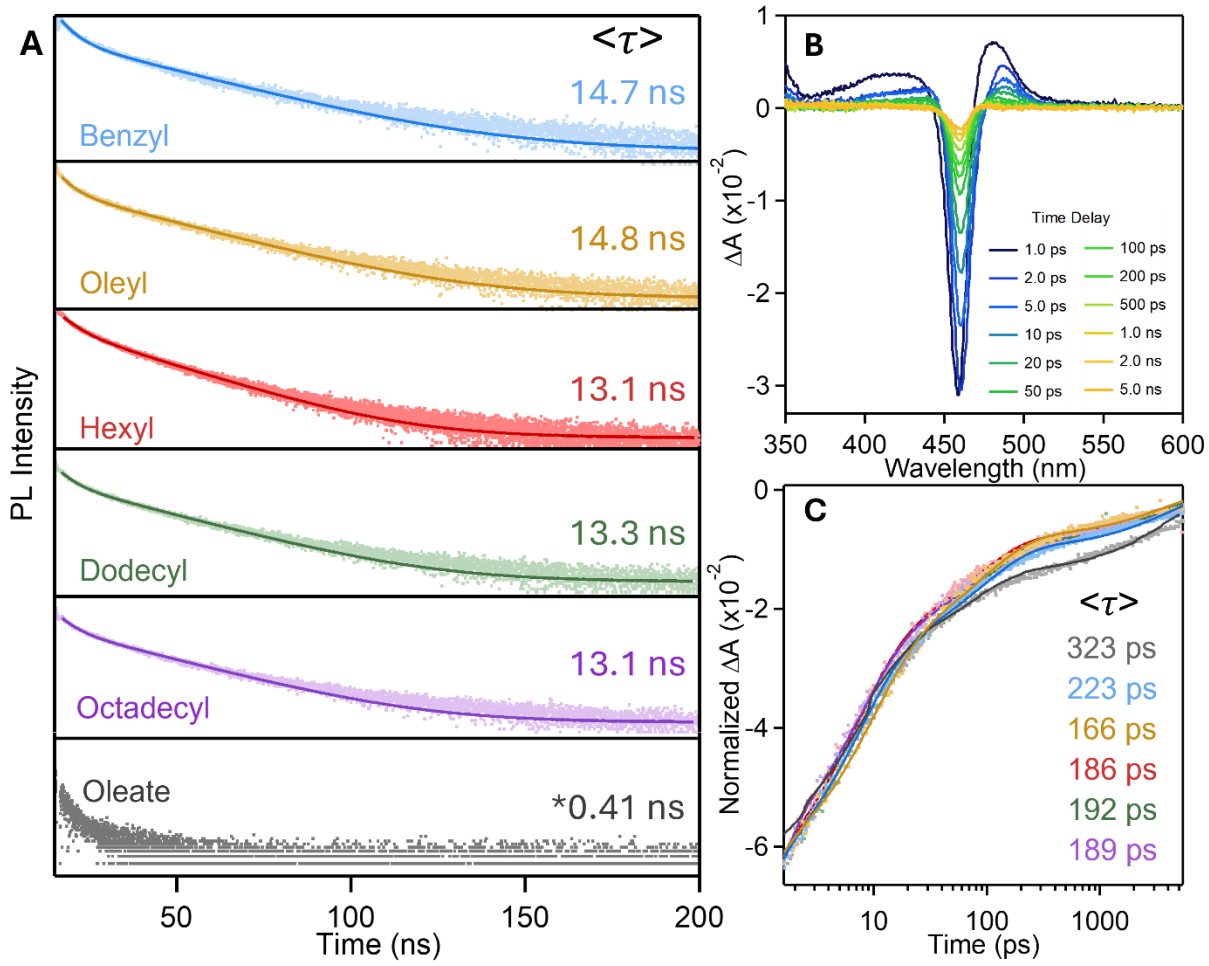

Figure 4.3.1. A) Time-resolved photoluminescence spectroscopy of all phosphinate-ligated Cd_3P_2 clusters monitored at 467 nm and oleate-ligated Cd_3P_2 clusters monitored at 457 nm (λ_{ex} = 405 nm). B) Transient absorption spectra of octadecylphosphinate-ligated Cd_3P_2 clusters up to five nanosecond time delay. C) Comparison of the ground state bleach recovery dynamics from transient absorption.

We note, though, that the trend in the TRPL radiative decay rates does not coincide with PLQY. In fact, the two phosphinate ligands with the lowest PLQY, benzyl- (<τ> = 14.7 ns) and oleylphosphinate (<τ> = 14.8 ns), have negligibly longer radiative lifetimes compared to hexyl- (<τ> = 13.1 ns), dodecyl- (<τ> = 13.3 ns), and octadecylphosphinate (<τ> = 13.1 ns) (**Figure 4.3.1A, 4.3.2**).

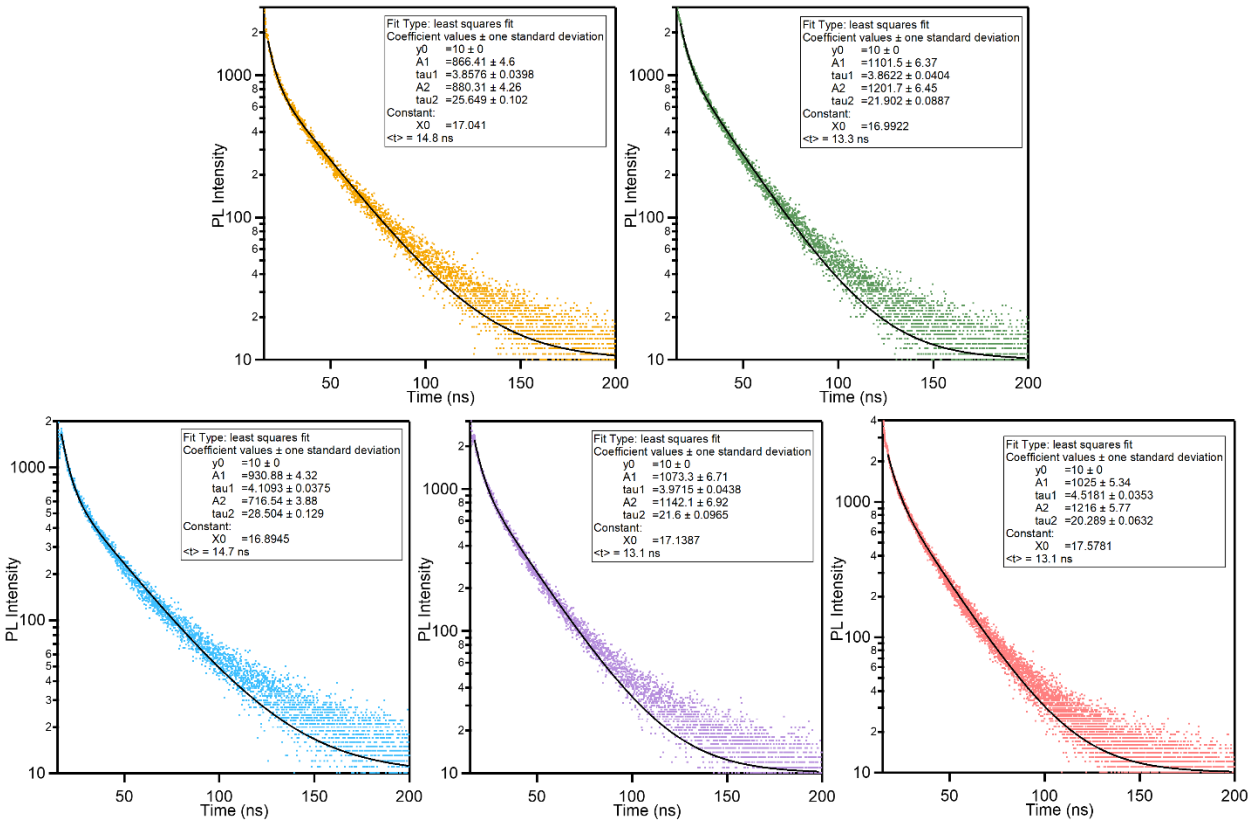

Figure 4.3.2. All Cd_3P_2 TRPL decays fit to a double exponential with an x-offset. Oleylphosphinate (yellow, top left), dodecylphosphinate (green, top right), benzylphosphinate (blue, bottom left), octadecylphosphinate (purple, bottom middle), hexylphosphinate (red, bottom right).

To look at this apparent discrepancy further, we turned to transient absorption (TA) spectroscopy, which provides information on the carrier dynamics that occur at timescales too fast

for TRPL. TA spectra for the octadecylphosphinate-ligated cluster up to ~5 ns is presented in **Figure 4.3.1B**. The phosphinate-capped clusters show similar spectral lineshapes except for a redshift in the ground state bleach from 450 nm to 460 nm that mirrors the redshift in the absorption spectra (**Figure 4.3.3**). We examined differences in lifetimes for all samples by monitoring the recovery at the minimum of the ground state bleach. These kinetics, along with the exponential fits, are provided in **Figure 4.3.1C and 4.3.4** (individual lifetimes are reported in T**able 4.3.1**).

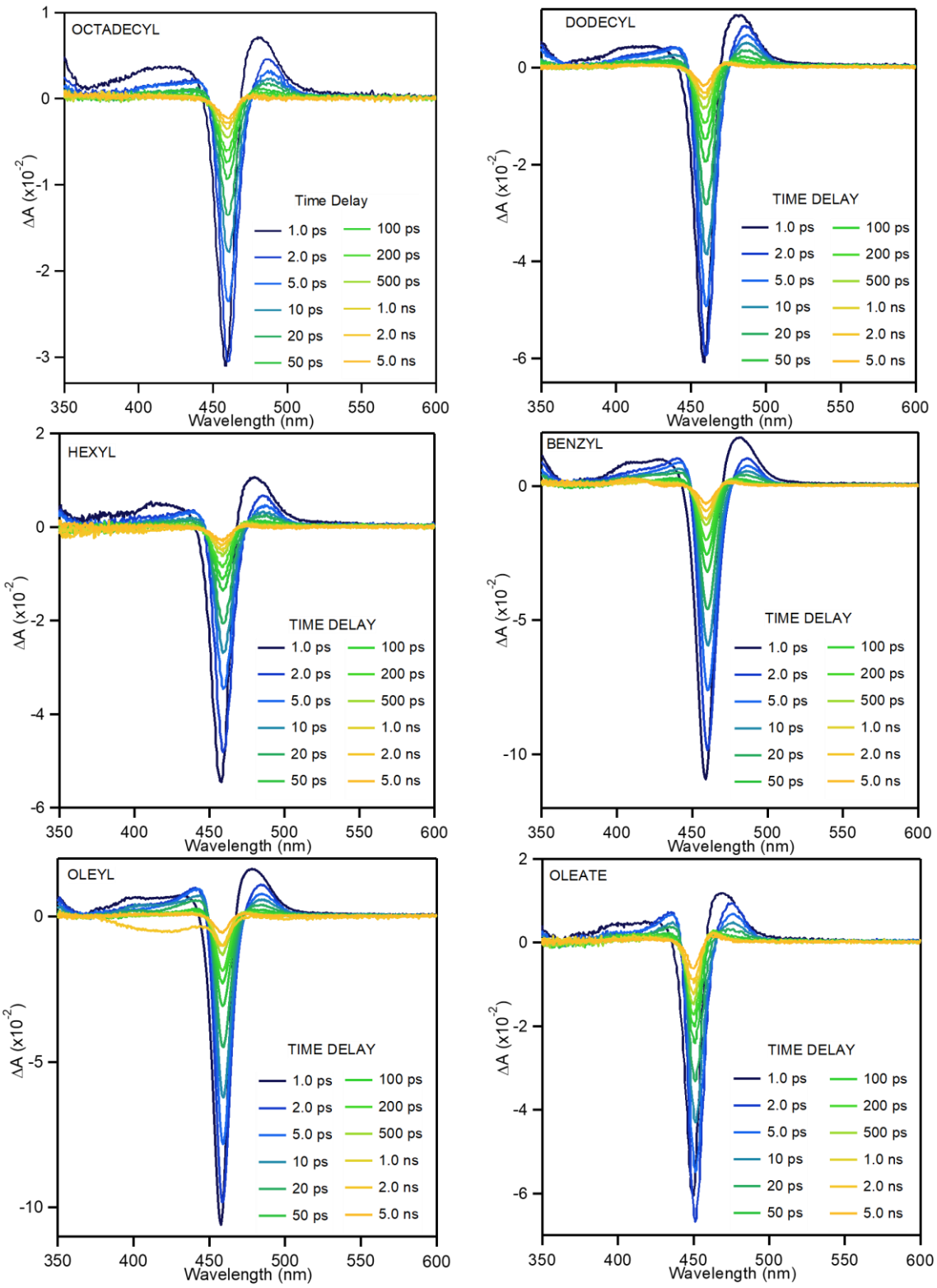

Figure 4.3.3. Bleach decays for Cd_3P_2 clusters for phosphinate-ligated clusters (octadecyl, dodecyl, hexyl, benzyl, oleyl) and the oleate-ligated cluster (oleate).

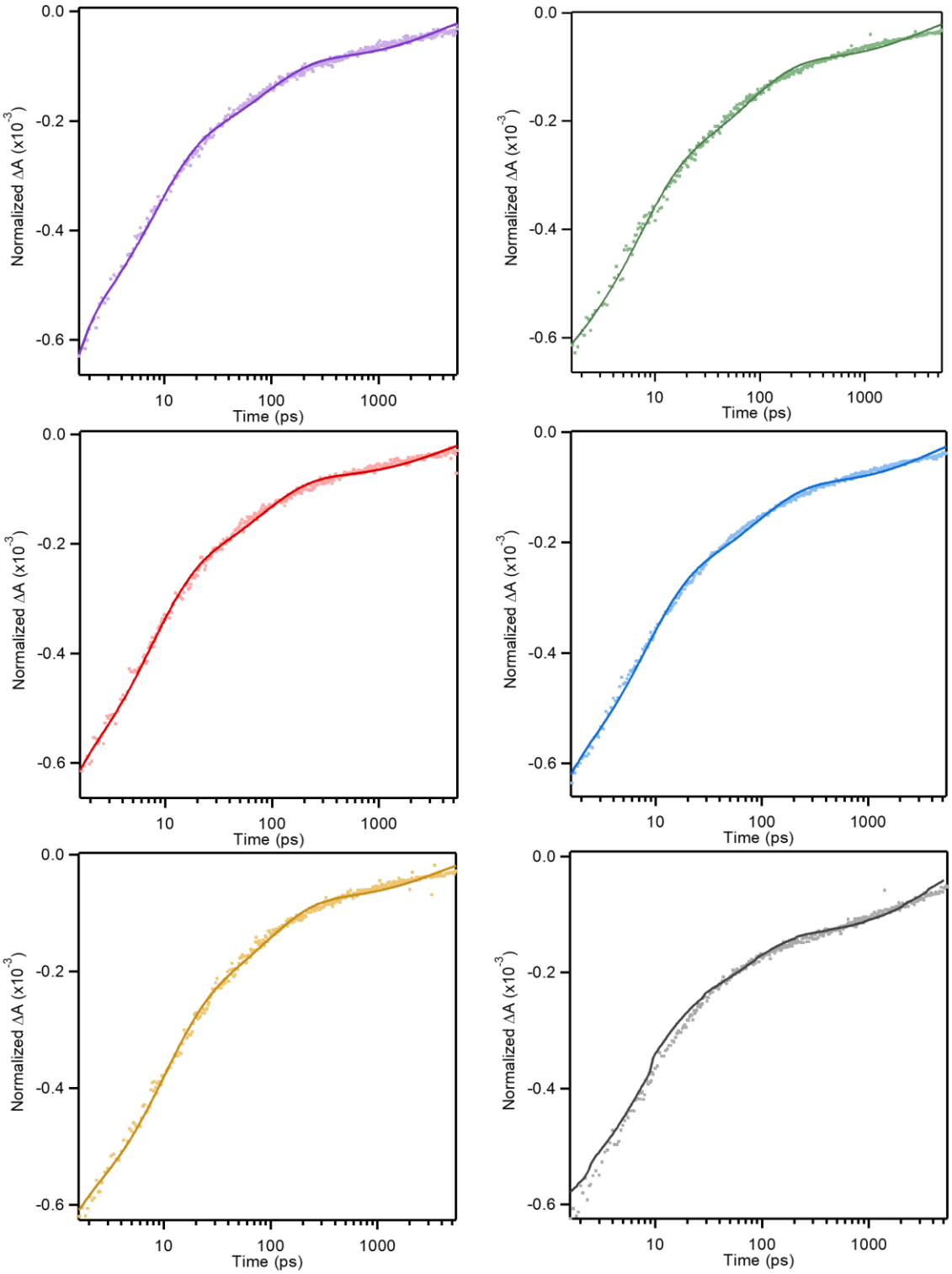

Figure 4.3.4. Bleach decay kinetics of all Cd_3P_2 clusters monitored at 460 nm for phosphinate-ligated clusters (octadecyl (purple), dodecyl (green), hexyl (red), benzyl (blue), and oleyl (yellow)) and monitored at 450 nm for the oleate-ligated cluster (grey).

Ligand	τ_1 (ps)	τ_2 (ps)	τ_3 (ps)	τ_4 (ps)	$\langle\tau\rangle$ (ps)
Octadecyl	0.47	7.3	86	3800	189
Dodecyl	0.46	6.5	79	3700	192
Hexyl	0.42	6.8	81	3900	186
Benzyl	0.49	7.4	91	4100	223
Oleyl	0.44	9.4	93	3700	166
Oleate	0.31	7.4	72	4400	323

Table 4.3.1. Individual fit parameters for the transient absorbance bleach decay monitored at 460 nm for all phosphinate ligands (octadecyl, dodecyl, hexyl, benzyl, and oleyl) and 450 nm for oleate.

We note that the decay lifetimes are quite similar despite the difference in the ligation, except in the case of oleate, where the lifetime is slightly longer at longer time scales. It is noteworthy then that the non-radiative process that is causing the differences in PLQY across the phosphinate ligand suite is not observable on the nanosecond timescale as evidenced by TRPL or on the picosecond timescale as seen in the TA lifetimes. Thus, we believe that the non-radiative process must occur around or below the femtosecond time scale. Carrier trapping has been observed in CdSe QDs at this time scale and shows a trapping rate that is size-dependent.[42,43] As our clusters are even smaller in diameter, the trapping rate is expected to be even more rapid. The oleyl- and benzyl- substituents seem to promote this nonradiative process likely as a result of their steric profile. The oleyl group includes a double bond, which precludes aliphatic packing at the surface, thereby increasing steric pressure in the ligand sphere. The benzyl group is expected to have an even more detrimental impact on steric pressure due to its larger physical profile at the

cluster interface.[44] Seeing as the extent of nonradiative recombination trends with the degree of unsaturation in the ligand tail and the clusters are particularly strongly confined, it has been considered that there may be some degree of delocalization into orbitals with ligand character. This could feasibly allow for new recombination pathways that would influence the overall PLQY and could occur on subpicosecond timescales.[45] However, studies that report these electronic behaviors use anchoring atoms that share orbital symmetry and electronic alignment with either the cation or anion sublattice.[39,46–49] Furthermore, the unsaturated ligand moieties must then be directly physically coupled to the anchoring head group for delocalization to occur. Seeing as the anchoring oxygen atoms of the phosphinate do not satisfy the electronic requirements for coupling and the unsaturated portions of the benzyl and oleyl substituents are decoupled from the head group by methylene units, it is unlikely that the ligand tails are electronically participating.

4.4 Ligand Exchange on Cd_3As_2

Seeing the impressive enhancement in the emissive characteristics from the Cd_3P_2 clusters, we sought to implement the phosphinate ligation elsewhere. The related Cd_3As_2 cluster has also been isolated and shows a similar absorbance profile to the Cd_3P_2 cluster with a very narrow lowest energy transition with a λ_{max} at 525 nm (**Figure 4.4.1**).

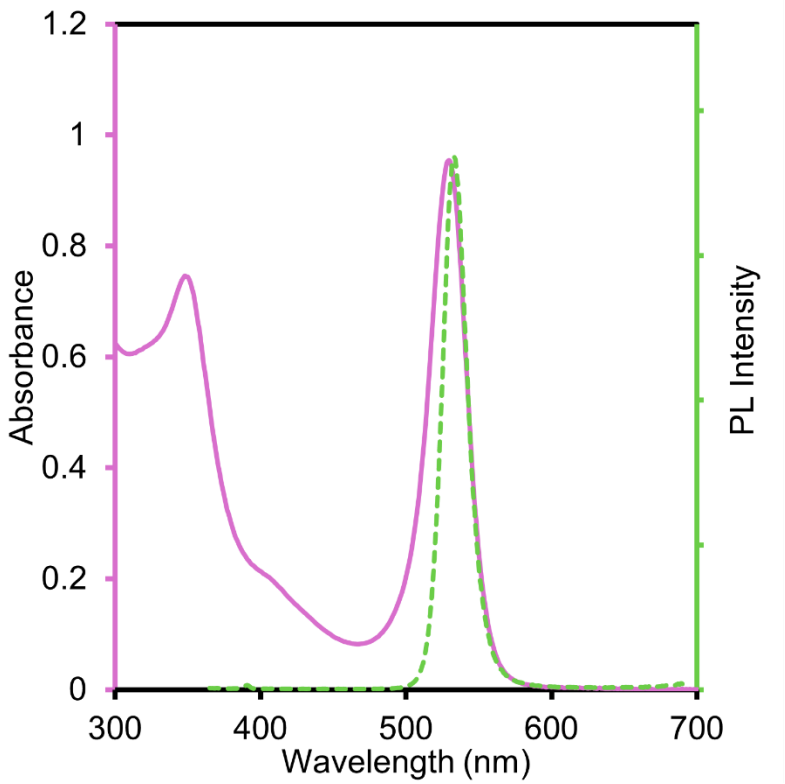

Figure 4.4.1. Absorbance (purple) and photoluminescence (green) spectra of as-synthesized, oleate-ligated Cd_3P_2 clusters.

We followed the same ligand exchange protocol developed for the Cd_3P_2 clusters and found that fewer additions of phosphinic acid were required for complete ligation. Similar to Cd_3P_2, the addition of phosphinic acid results in a consistent red shift in the electronic transitions of the absorbance (**Figure 4.4.2A**). After the first addition of octadecylphosphinic acid (0.56 eq with respect to oleate), the lowest energy electronic transition is shifted to 542 nm. After purification and a second addition of 0.56 eq phosphinic acid, oleate is no longer visible by FTIR, and the λ_{max} shifts to 545 nm.

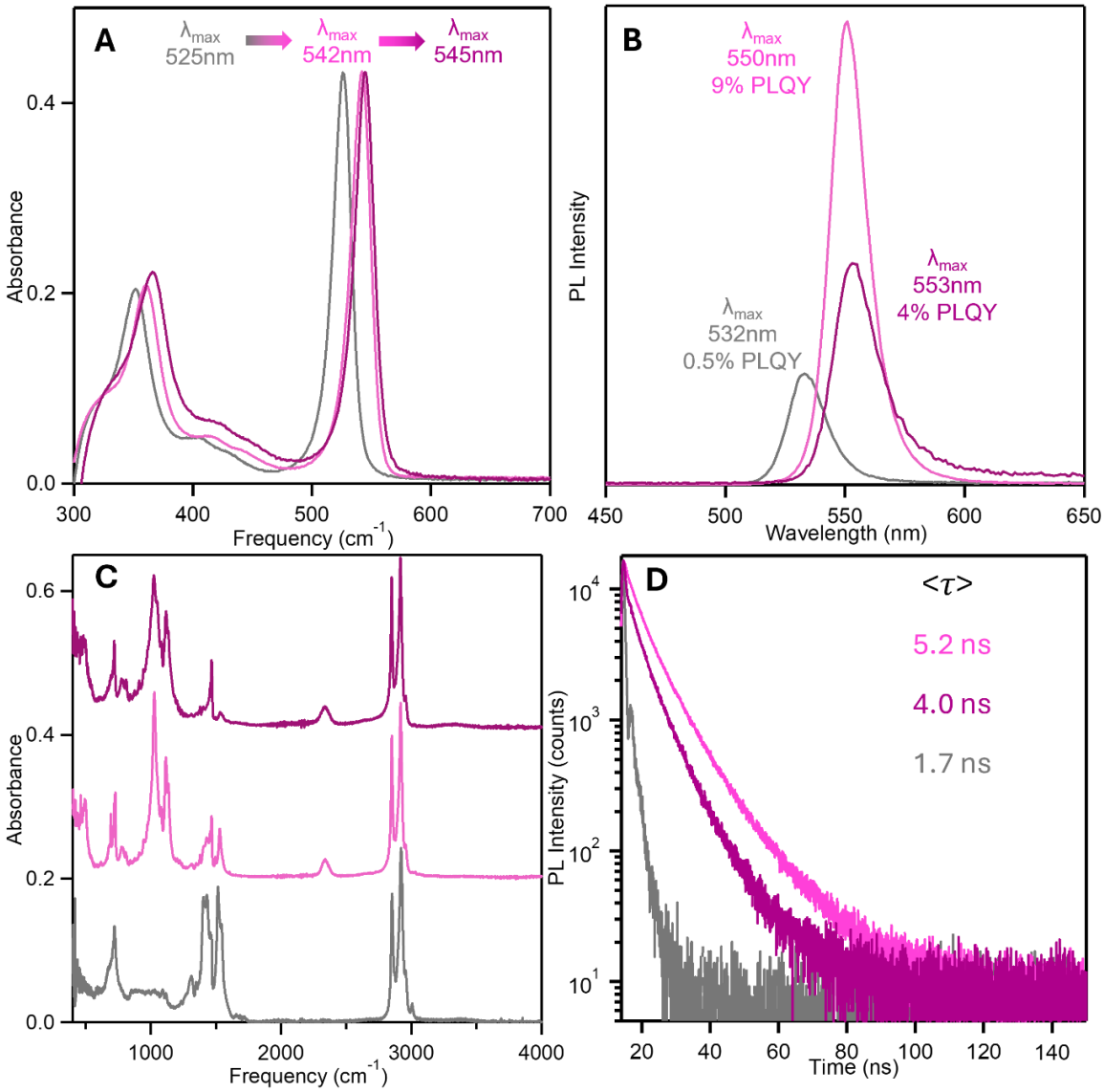

Figure 4.4.2. A) The absorbance profile of the oleate-ligated Cd_3As_2 cluster (grey, λ_{max} = 525 nm) red shifts upon the 1st addition (pink, λ_{max} = 542 nm) and 2nd addition (purple, λ_{max} = 545 nm) of octadecylphosphinic acid. B) Cd_3As_2 cluster PL and PLQY with oleate ligands (grey), 1st addition (pink), and 2nd addition of octadecylphosphinic acid (purple). C) Time-resolved photoluminescence spectroscopy of Cd_3As_2 cluster with oleate ligands (grey), first addition (pink), and second addition (purple) of octadecylphosphinic acid. D) FTIR of CdAs-oleate (grey), after 1 addition (pink) and 2 additions (purple) of octadecylphosphinic acid. (*) Marks residual solvent signal from toluene.

The response in the photoluminescence of these clusters is similar to Cd_3P_2, if not more dramatic. The first addition of octadecylphosphinic acid improves the PLQY from <1% up to 9% while maintaining the highly narrow emission profile (**Figure 4.4.2B**). However, unlike Cd_3P_2, we find that further addition of octadecylphosphinic acid does not necessarily benefit the emission. Upon complete ligation with octadecylphosphinate, the PLQY is initially measured at 4%.

However, over the course of 72 hours, this emission intensity decreases substantially down to <1% PLQY. Further investigation of the emission profiles shows that the further exchanged Cd_3As_2 develops a tail on the red side of the emission. This observation, in conjunction with the loss of emission intensity over time, suggests that complete phosphinate ligation of the Cd_3As_2 clusters does not result in a stable product. The difference in emissive behavior and stability between the II-V clusters with respect to their phosphinate ligation is likely due to a potential difference in the density of the ligand sphere. The results from ICP-OES show that the Cd_3P_2 clusters are indeed more cadmium rich, which suggests a difference in the cadmium coverage at the cluster surface and corroborates our findings that fewer octadecylphosphinic acid ligands are required to passivate Cd_3As_2 **(Table 4.4.1).**

Results of Inductively Coupled Plasma Optical Emission Spectroscopy	
Sample	**Cd:E ratio (E = P, As)**
Cd_3P_2	3.4:1
Cd_3As_2	3.1:1

Table 4.4.1. Results of Inductively Coupled Plasma Optical Emission Spectroscopy indicating a higher Cd:E ratio in Cd_3P_2 compared to Cd_3As_2.

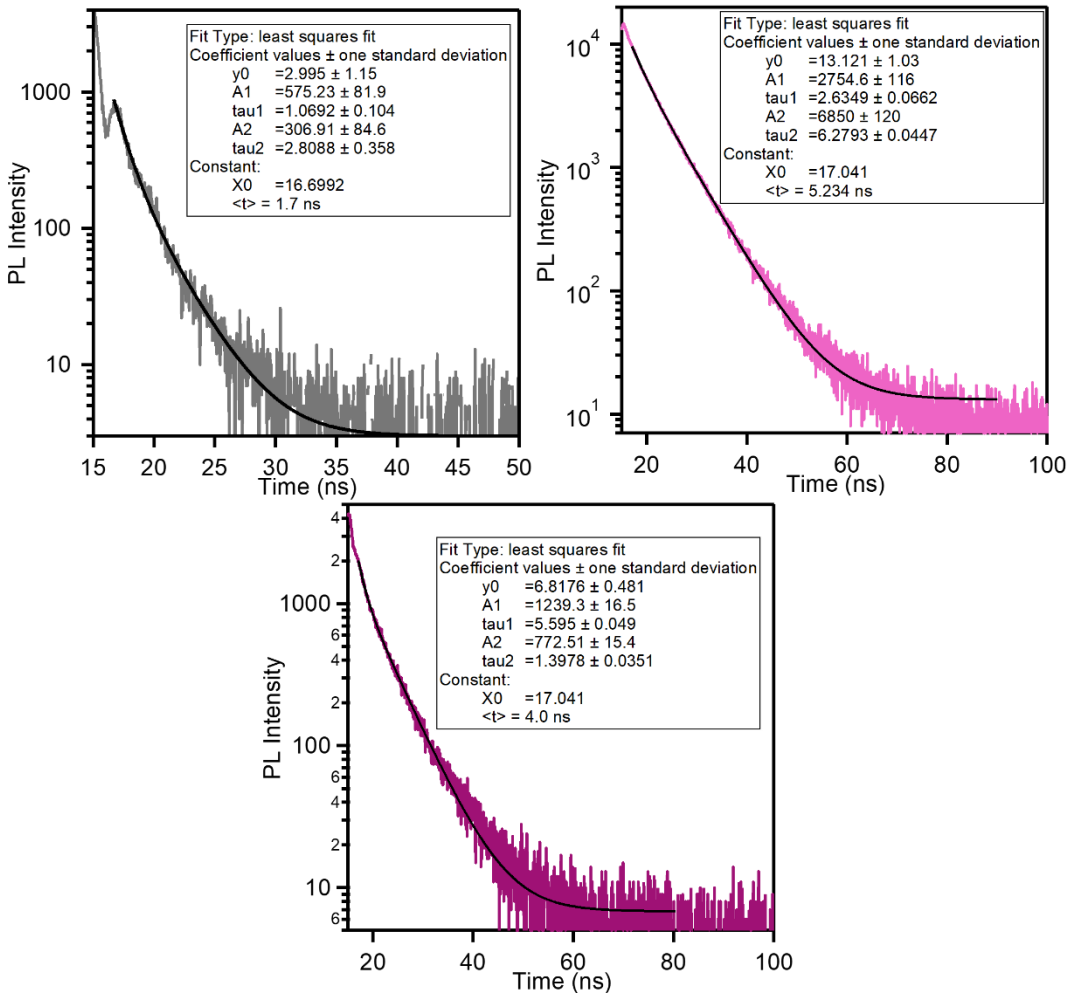

Figure 4.4.3. All Cd_3As_2 TRPL decays fit to a double exponential with an x-offset. Oleate (top left, grey), partially exchanged octadecylphosphinate (top right, pink), fully exchanged octadecylphosphinate (bottom, purple).

It is interesting to note that we have seen similar patterns in the relative cation richness of InP and InAs clusters.[23,30] To further investigate the Cd_3As_2 stability, we measured TRPL before and after exchange with phosphinic acid (**Figure 4.4.2C**). The oleate-Cd_3As_2 shows the fastest decay ($<\tau>$ = 1.7 ns), followed by the further exchanged octadecylphosphinate-Cd_3As_2 ($<\tau>$ = 4.0 ns), and finally, the partially exchanged octadecylphosphinate-Cd_3As_2 ($<\tau>$ = 5.2 ns) (**Figure 4.4.2D, 4.4.3**). In this instance, the TRPL and PLQY follow similar trends, suggesting a simpler mechanism for nonradiative decay differences where the lack of stability of the further exchanged Cd_3As_2 leads to cluster degradation and the development of obvious trap states that cause nonradiative recombination. Despite the lack of stability of the further exchanged product, we are still able to significantly enhance the emission intensity of the Cd_3As_2 cluster through partial phosphinate ligation.

4.5 CONCLUSIONS

In this study, we have developed a ligand exchange protocol for ligating the surface of II-V clusters with phosphinate. We find that with these new ligands, a change in surface dipole induces a red-shift of the λ_{max} in both the absorbance and the photoluminescence of these materials. In the case of Cd_3P_2, the absorbance maximum is shifted from 451 nm to 461 nm, and the PL maximum is shifted from 457 nm to 467 nm. This shift is accompanied by an impressive increase in the PLQY from 7% to 26% in the case of the saturated, straight-chain alkylphosphinates. We find, however, that the ligand tail has a dramatic influence on PLQY, where benzyl and oleyl substituents result in 7% and 15% PLQY, respectively. The difference in radiative efficiency across phosphinate ligands is likely a result of ultrafast carrier trapping as evidenced by very similar decay rates in both TRPL on the nanosecond time scale and TA on the picosecond time

scale. We believe the trapping to be exacerbated by constrained ligand geometry as the oleyl and benzyl substituents have negative effects on the PLQY. Thus, the emission is maximized by strong ligand binding and small steric profile. Along with an increase in the brightness, the phosphinate ligands maintain the exceptionally narrow 96 meV emission line width, resulting in a very pure blue emitter. We find that a similar protocol can be applied to related Cd_3As_2 clusters with similar outcomes, leading to ultra-narrow green emission at 550 nm.

4.6 OUTLOOK

One of the main conclusions that was unable to be elucidated from the above work was the actual photophysical mechanism by which phosphinates were shutting down nonradiative recombination and extending the photoluminescence lifetime. This was especially challenging because the TA data looked qualitatively identical across the entire phosphinate ligand suite. This similarity suggested that whatever nonradiative processes were occurring to lead to differences in the PLQY, they must be occurring on a timescale that cannot be measured by our TA set-up (i.e. femtosecond or faster). While at face value, this initially might seem to be completely unreasonable, the Bohr radii of bulk Cd_3P_2 and Cd_3As_2 are 36 nm and 47 nm, respectively. Assuming these clusters are approximately 2 nm, the degree of confinement is therefore extremely strong which would lead to extremely fast recombination rates (whether they be radiative or nonradiative). So, upon further consideration, the femtosecond timescale could in fact be reasonable for these systems. However, the hypothesis that these processes are indeed that fast runs into a secondary problem. If the nonradiative rate is indeed on the femtosecond timescale, we have just measured the photoluminescence lifetime to be ~14 nanoseconds and with a nonradiative rate that is six orders of magnitude faster than the radiative rate, there would be negligible

emission. Therefore, there must be a more complex rationalization for the difference in PLQY that can take into account the possibility of femtosecond nonradiative recombination. Furthermore, the PLQY measurements taken on these clusters used an excitation energy that was resonant with the second absorbance transition. The proposed mechanisms must then start from the second singlet state (S_2).

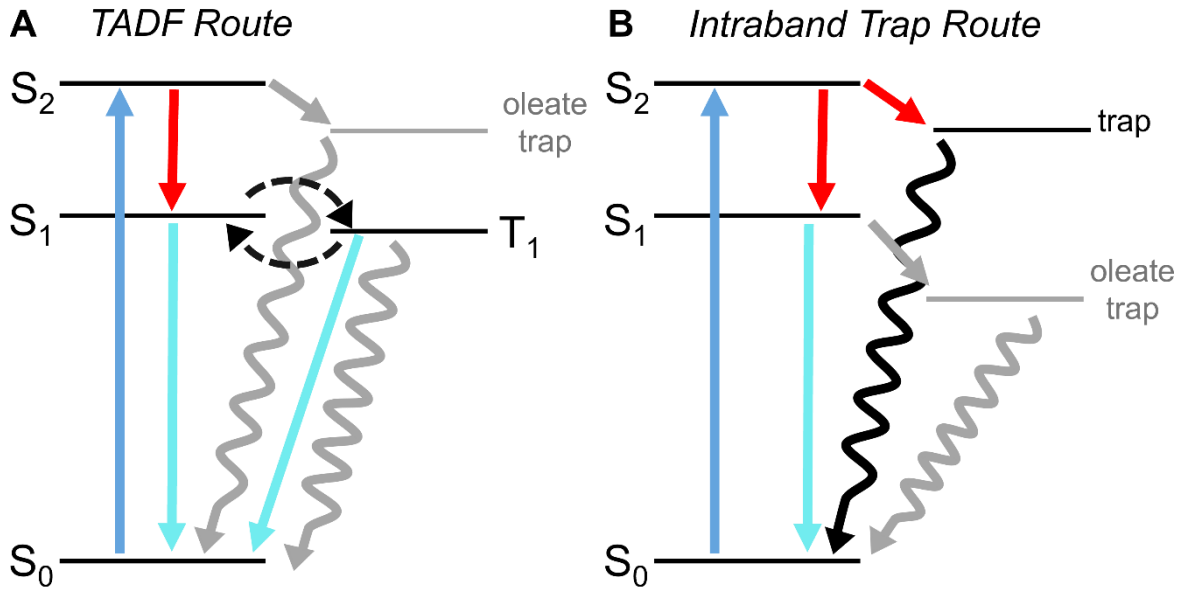

Figure 4.6.1. A) Photophysical mechanism for TADF resulting in delayed fluorescence from the T_1 state. B) Photophysical mechanism for intraband relaxation outcompeting nonradiative recombination.

There are two possible hypotheses to consider here shown in **Figure 4.6.1**. The first of which suggests that these clusters could be undergoing thermally activated delayed fluorescence (TADF) where the emissive singlet state and a triplet state (also potentially emissive) are close enough in energy that any available thermal energy can repopulate the singlet state from carriers that have fallen into the triplet state. For this to be the case, the oleate-ligated clusters would have a trap state that lies somewhere between S_1 and S_2 and phosphinate ligation would decrease the affinity for this trap state in some way either by passivating the trap, dampening vibrational

coupling, or increasing the intraband relaxation rate. With the oleate-derived nonradiative recombination pathway mitigated, the majority of carriers in the phosphinate-ligated clusters would quickly relax to the S_1 state and radiatively recombine. However, a portion would undergo ISC into the T_1 and either radiatively recombine by relaxing into the S_0 ground state, nonradiatively recombine through vibrational losses or be thermally converted back into the S_1 through TADF. This would mean that the fluorescence lifetime from the S_1->S_0 could potentially be on the femtosecond timescale and thus compete with the ultrafast nonradiative recombination rate. The TRPL signal with the 14 ns lifetime is thus coming from the T_1->S_0 transition and is giving the appearance of a longer radiative rate. The TA spectra show a photoinduced absorption feature around 480 nm which could be the S_1->T_1 ISC. The different substituents on the phosphinate head group would then cause surface distortions that influence the allowedness of the ISC and RISC and the difference in PQLY would be derived from the T_1 lifetime. While this is possible, the strongest argument against this hypothesis comes from the two emitting states. These clusters have exceptionally narrow photoluminescence linewidths and therefore it would be highly unlikely for there to be two, indistinguishable emitting states (S_1 and T_1). Furthermore, monitoring the photoluminescence lifetime at different wavelengths leads to identical lifetimes which further suggests a single emitting state. For this to be possible, the S_1 and T_1 would need to be essentially degenerate and have almost identical degrees of coupling to the surface vibrations that intrinsically broaden the PL.

The other possibility is two intraband trap states, one that is derived from the oleate-ligation and one that is modulated by the phosphinate ligand tail. In this instance, the radiative rate wouldn't be directly competing with the ultrafast nonradiative rate as the trap state is above S_1. Instead, the intraband relaxation rate, which would be significantly faster than the radiative rate, would

compete with nonradiative recombination. The difference in PLQY between phosphinates is then derived from the rate of hot trapping and strained ligand conformations from steric pressure promotes the hot trapping. Due to the infeasibility of perfectly overlapping S_1 and T_1 emission, the intraband trap route is more likely.

Along with the ambiguity of the radiative mechanism, the degradation pathway of the Cd_3As_2 cluster is also unclear. This is a difficult process to directly experimentally probe but seeing as the degradation is promoted upon full ligand exchange, the pathway is most likely surface-derived. Taking into account the slight difference in the Cd:E (E = P, As) ratio as found from ICP-OES (3.1:1 for Cd_3As_2 and 3.4:1 for Cd_3P_2), the Cd_3As_2 clusters could be less cation rich on the surface. Sparser surface cadmium would then result in unfavorable binding angles and conformations eventually leading to the full removal of cadmium phosphinate units from the surface (**Figure 4.6.2**). This would quickly lead to trap state generation and the PL would suffer.

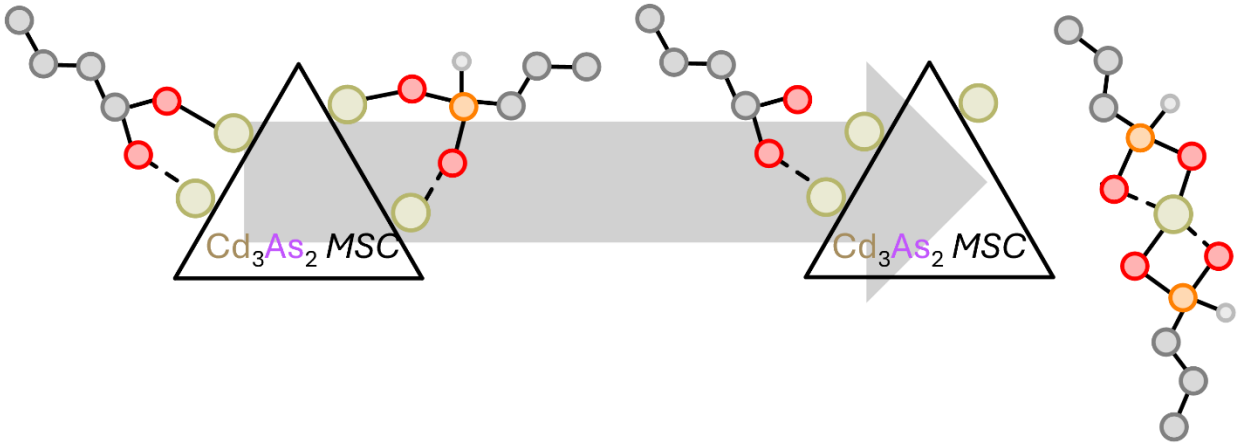

Figure 4.6.2. Degradation pathway of Cd_3As_2 clusters as promoted by phosphinate ligand binding.

While this project as a whole substantially improved the brightness of these cluster materials, on the grounds of applicability, clusters still don't have the functionality to compete with QDs. The main two reasons for this are the brightness (still) and the stability. While achieving up to 25% PLQY from a cluster, especially emitting such high energy light in the blue, is exciting,

the small size continues to be a challenge as the extremely strong confinement leads to so much vibrational coupling and nonradiative recombination. Pushing surface treatment routes further to dampen and mitigate this coupling, maybe even pushing as far as trapping clusters in some sort of matrix, would be the only way to increase the PLQY high enough to make the emission efficiency applicable. Regarding the stability, the surface energy that allows these materials to be atomically-precise also causes their metastability. This means that taking advantage of their molecular nature will always be accompanied by the baggage of instability. This is a challenge that extends beyond just the surface as many of these materials have internal atomic arrangements that do not match a bulk crystalline phase. With enough energy, the entire cluster will be pushed towards a full rearrangement to achieve the thermodynamically stable crystalline phase. As there seem to be no feasible ways around this, it could be that devices that incorporate clusters must be run at low temperatures to avoid this instability.

The final challenge that causes clusters to lag behind the applicability of QDs (and potentially the most addressable) is their tunability. The structures and therefore the properties of these atomically-precise materials have been predetermined as dictated by the strict balance between the surface energy and internal crystalline arrangement. Any perturbations in this structure leads to complete destabilization so only the preconceived, discrete sizes of clusters exist. If they grow, they will only grow to the next discrete size and therefore, many wavelengths of absorption and emission are left inaccessible. After completing this project and enhancing the emission from clusters, the next goal became finding a route towards maintaining atomic-precision of the system while introducing continuous tunability in the emission.

4.7 Experimental Methods.

4.7.1 *General Considerations.*

Oleic Acid (90%), trifluoroacetic acid (>99%), octadecene (90%), dodecane (95%), hexene (97%), triethylborane (1.0 M in THF), diisooctylphosphinic acid (90%), hexylphosphonic acid (95%), sodium hexanesulfonate (98%), sodium hypophosphite monohydrate (≥99%), tetrabromomethane (99%), triphenylphosphine (99%), diethylchlorophosphite (95%), benzyl bromide (98%), red phosphorus (≥99.99%), calcium hydride (95%), chlorotrimethylsilane (≥99%), naphthalene (99%), sodium metal (ACS reagent, dry), deuterated benzene (C_6D_6, 99.6% D), and magnesium were obtained from Sigma Aldrich. Naphthalene was sublimated and C_6D_6 was dried over CaH_2 and distilled prior to use. Dimethoxyethane (≥99%) and trifluoroacetic anhydride (>98%) were obtained from TCI. Dimethoxyethane was distilled from sodium prior to use. Arsenic powder (99%) was obtained from Strem Chemicals and used as received. Cadmium oxide (99.95%) was obtained from Alfa Aesar. Potassium hydrogen sulfate was obtained from VWR international. Oleyl alcohol (80-85%) was obtained from ThermoScientific. Deuterated chloroform ($CDCl_3$, 99.8% D) was obtained from Cambridge Isotope Laboratories. Tris(trimethylsilyl)arsine ($As(SiMe_3)_3$) and tris(trimethylsilyl)phosphine ($P(SiMe_3)_3$) were prepared according to a literature procedure using either metallic arsenic or red phosphorus.[50] All manipulations were performed under an inert atmosphere of dry N_2 using standard Schlenk line or glovebox techniques unless otherwise indicated. UV-Vis absorbance spectroscopy was carried out using Cary 5000 and Cary 60 spectrophotometers from Agilent Technologies. Steady-state and time-resolved photoluminescence spectroscopy as well as PLQY by integrating sphere were performed using an Edinburgh PLS 1000 Fluorimeter located in the University of Washington's MEM-C shared user facility. NMR spectra were acquired on 300 and 500 MHz Bruker Avance

spectrometers in $CDCl_3$ and C_6D_6. All FT-IR measurements were acquired in the solid-state on a PerkinElmer Frontier FT-IR spectrometer.

4.7.2 *Transient Absorption Measurements.*

Transient absorption measurements were done at the University of Washington's Molecular Analysis Facility and has been described elsewhere.[51] The pump wavelength of 325 nm was chosen to coincide with PLQY measurements and reduce scattering. The pump power was maintained at 50 μW for each sample to ensure that only single excitons were formed in order to eliminate effects from Auger recombination. White light was generated using CaF_2.

4.7.3 *Quantitative H-NMR and Determination of Equivalents.*

To determine the amount of oleate present in Cd_3P_2 and Cd_3As_2 samples, quantitative H-NMR was performed using a mesitylene internal standard. The appropriate regions (^{1}H NMR (300 MHz, $CDCl_3$): mesitylene δ 6.81 (s, 3H) and oleate δ 5.34 (br, 2H)) were normalized by the number of protons before being converted to a total mass of oleate. This analysis determined 7.7 mg of oleate in a 10.0 mg sample of Cd_3P_2 clusters and 7.9 mg of oleate in a 10.0 mg sample of Cd_3As_2 clusters. This analysis also allows for the expression of phosphinic acid added in terms of equivalents with respect to oleate as described in the ligand exchange protocols below.

4.7.4 *Computational Methods.*

Computational studies were performed using the Gaussian electronic structure package.[52] The B3LYP hybrid DFT functional was used alongside the 6-311g basis set to perform a geometry optimization before calculating the dipole direction and magnitude of the molecule.

4.7.5 *Synthesis of Cadmium Oleate.*

Cadmium oleate was synthesized according to a previous literature procedure.[53] In short, with cadmium oxide (9.5 g, 74 mmol) and acetonitrile (95 mL) stirring at room temperature, trifluoroacetic acid (1.6 mL, 20.9 mmol) and trifluoroacetic anhydride (11 mL, 79 mmol) are added. Once the solution has become clear and colorless, a solution of oleic acid (46.7 mL, 148 mmol) and triethylamine (26.3 mL, 188.7 mmol) in dichloromethane (740 mL) is added dropwise. Upon complete addition, acetonitrile (600 mL) is added to the reaction to precipitate the product followed by storing in the fridge overnight. The product is then vacuum filtered and washed with 1 L of acetonitrile before being dried under vacuum to yield a white powder.

4.7.6 *Synthesis of CdP-oleate Nanoclusters.*

In a nitrogen-filled glovebox, cadmium oleate (540 mg, 0.8 mmol, 1 eq) is combined with oleic acid (372 μL, 1.2 mmol, 1.5 eq) and 24 mL of toluene. This mixture is vigorously vortexed until complete dissolution of the cadmium oleate. The solution is then injected into an oven-dried 3-neck round bottom flask under nitrogen and stirring is set at 1200 rpm. The flask is heated to 50 °C after which a solution of $P(SiMe_3)_3$ (100 μL, 0.3445 mmol, 0.43 eq) in 2 mL of toluene is promptly injected into the flask. Immediately after injection the temperature is set to 110 °C. The

reaction is removed from the heat 35 minutes after injection when consecutive aliquots have identical absorbance spectra. The resulting clusters are precipitated with 7.5 mL of acetonitrile followed by centrifugation at 7830 rpm for 6 minutes. The supernatant is discarded, and the bright yellow pellet is dried under vacuum and stored as a solid (final mass: 310 mg).

4.7.7 *Synthesis of CdAs-oleate Nanoclusters.*

Cadmium acetate dihydrate (53.3 mg, 0.2 mmol, 1 eq) is added to an oven-dried 3-neck round bottom flask under positive nitrogen after which it is heated to 40 °C under vacuum to remove water. Oleic acid (107 mg, 0.38 mmol, 1.9 eq) in 1-octadecene (5 mL) is then injected into the flask under positive nitrogen. With stirring at 350 rpm, the temperature is increased to 90 °C under full vacuum to form the cadmium oleate precursor. *Note: During this formation step, it is important to ensure that the cadmium acetate does not agglomerate on the side of the flask thereby hindering its reactivity.* After reacting at 90 °C for 2 hours, the reaction is cooled to 50 °C and placed under positive nitrogen. After the temperature has stabilized, a solution of $As(SiMe_3)_3$ (15 µL, 0.05 mmol, 0.25 eq) in 1 mL of toluene is promptly injected into the flask. Immediately after injection the temperature is set to 90 °C. The reaction is removed from the heat 7 minutes after injection when consecutive aliquots have identical absorbance spectra. The resulting clusters are precipitated with 12 mL methyl acetate followed by centrifugation at 7830 rpm for 6 minutes. The supernatant is discarded, and the pellet is resuspended in 10 mL of toluene before a second precipitation with methyl acetate. The bright red pellet is dried under vacuum and stored as a solid (final mass: 75 mg).

4.7.8 *Synthesis of Monosubstituted Phosphinic Acids.*

All phosphinic acids were synthesized according to previous literature reports.[31,54]

4.7.9 *Ligand Exchange of CdP-oleate for Monosubstituted phosphinate.*

Purified CdP-oleate cluster (10 mg) is dissolved in 10 mL of toluene and placed under stirring at 800 rpm. In the case of octadecyl-, dodecyl-, hexyl-, and oleylphosphinic acid, a 15.8 μmol/mL solution of phosphinic acid in tetrachloroethylene is prepared. In the case of benzylphosphinic acid, the 15.8 μmol/mL solution is prepared in a 2:1 ratio of tetrachloroethylene to dichloromethane due to poor solubility. A 1 mL portion of the phosphinic acid solution (0.58 eq, see *Quantitative H-NMR* section above) is injected into the CdP-oleate cluster followed by 60 minutes of stirring at room temperature. The partially exchanged clusters are precipitated with 7.5 mL of acetonitrile followed by centrifugation at 7830 rpm for 6 minutes. The clear supernatant is discarded, and the resulting bright yellow pellet is resuspended in 10 mL of toluene. This process of phosphinic acid addition, precipitation and resuspension is repeated twice more to yield CdP-phosphinate clusters (final mass: 11 mg).

4.7.10 *Ligand Exchange of CdAs-oleate for Octadecylphosphinate.*

Purified CdAs-oleate cluster (10 mg) is dissolved in 10 mL of toluene and placed under stirring at 800 rpm. A 15.8 μmol/mL solution of octadecylphosphinic acid (15 mg, 50 μmol) in 3 mL of tetrachloroethylene is prepared. A 1 mL portion of the phosphinic acid solution (0.56 eq, see *Quantitative H-NMR* section above) is injected into the CdAs-oleate cluster followed by 60 minutes of stirring at room temperature. The partially exchanged clusters are precipitated with 7.5

mL of acetonitrile followed by centrifugation at 7830 rpm for 6 minutes. The clear supernatant is discarded, and the resulting bright red pellet is resuspended in 10 mL of toluene. This process of phosphinic acid addition, precipitation and resuspension is repeated once more to yield CdAs-octadecylphosphinate clusters (final mass: 11 mg).

4.8 REFERENCES

(1) Jang, E.; Jang, H. Review: Quantum Dot Light-Emitting Diodes. *Chem. Rev.* **2023**, *123* (8), 4663–4692. https://doi.org/10.1021/acs.chemrev.2c00695.

(2) Tian, D.; Ma, H.; Huang, G.; Gao, M.; Cai, F.; Fang, Y.; Li, C.; Jiang, X.; Wang, A.; Wang, S.; Du, Z. A Review on Quantum Dot Light-Emitting Diodes: From Materials to Applications. *Adv. Opt. Mater.* **2023**, *11* (2), 2201965. https://doi.org/10.1002/adom.202201965.

(3) Shu, Y.; Lin, X.; Qin, H.; Hu, Z.; Jin, Y.; Peng, X. Quantum Dots for Display Applications. *Angew. Chem.* **2020**, *132* (50), 22496–22507. https://doi.org/10.1002/ange.202004857.

(4) Cotta, M. A. Quantum Dots and Their Applications: What Lies Ahead? *ACS Appl. Nano Mater.* **2020**, *3* (6), 4920–4924. https://doi.org/10.1021/acsanm.0c01386.

(5) Nguyen, H. A.; Dixon, G.; Dou, F. Y.; Gallagher, S.; Gibbs, S.; Ladd, D. M.; Marino, E.; Ondry, J. C.; Shanahan, J. P.; Vasileiadou, E. S.; Barlow, S.; Gamelin, D. R.; Ginger, D. S.; Jonas, D. M.; Kanatzidis, M. G.; Marder, S. R.; Morton, D.; Murray, C. B.; Owen, J. S.; Talapin, D. V.; Toney, M. F.; Cossairt, B. M. Design Rules for Obtaining Narrow Luminescence from Semiconductors Made in Solution. *Chem. Rev.* **2023**, *123* (12), 7890–7952. https://doi.org/10.1021/acs.chemrev.3c00097.

(6) Kim, K.; Yoo, D.; Choi, H.; Tamang, S.; Ko, J.-H.; Kim, S.; Kim, Y.-H.; Jeong, S. Halide–Amine Co-Passivated Indium Phosphide Colloidal Quantum Dots in Tetrahedral Shape. *Angew. Chem.* **2016**, *128* (11), 3778–3782. https://doi.org/10.1002/ange.201600289.

(7) Sun, Z.; Hou, Q.; Kong, J.; Wang, K.; Zhang, R.; Liu, F.; Ning, J.; Tang, J.; Du, Z. Surface Passivation toward Multiple Inherent Dangling Bonds in Indium Phosphide Quantum Dots. *Inorg. Chem.* **2024**, *63* (14), 6396–6407. https://doi.org/10.1021/acs.inorgchem.4c00168.

(8) Majetich, S. A.; Carter, A. C. Surface Effects on the Optical Properties of Cadmium Selenide Quantum Dots. *J. Phys. Chem.* **1993**, *97* (34), 8727–8731. https://doi.org/10.1021/j100136a013.

(9) Kim, T.-G.; Zherebetskyy, D.; Bekenstein, Y.; Oh, M. H.; Wang, L.-W.; Jang, E.; Alivisatos, A. P. Trap Passivation in Indium-Based Quantum Dots through Surface Fluorination: Mechanism and Applications. *ACS Nano* **2018**, *12* (11), 11529–11540. https://doi.org/10.1021/acsnano.8b06692.

(10) Chen, H.-S.; Chen, C.-Y.; Wu, Y.-C. High-Performance Giant InP Quantum Dots with Stress-Released Morphological ZnSe-ZnSeS-ZnS Shell. *Adv. Mater. n/a* (n/a), 2407026. https://doi.org/10.1002/adma.202407026.

(11) Neo, D. C. J.; Cheng, C.; Stranks, S. D.; Fairclough, S. M.; Kim, J. S.; Kirkland, A. I.; Smith, J. M.; Snaith, H. J.; Assender, H. E.; Watt, A. A. R. Influence of Shell Thickness and Surface Passivation on PbS/CdS Core/Shell Colloidal Quantum Dot Solar Cells. *Chem. Mater.* **2014**, *26* (13), 4004–4013. https://doi.org/10.1021/cm501595u.

(12) Pu, Y.; Cai, F.; Wang, D.; Wang, J.-X.; Chen, J.-F. Colloidal Synthesis of Semiconductor Quantum Dots toward Large-Scale Production: A Review. *Ind. Eng. Chem. Res.* **2018**, *57* (6), 1790–1802. https://doi.org/10.1021/acs.iecr.7b04836.

(13) Singh, V.; Priyanka; Vilas More, P.; Hemmer, E.; Kumar Mishra, Y.; K. Khanna, P. Magic-Sized CdSe Nanoclusters: A Review on Synthesis, Properties and White Light Potential. *Mater. Adv.* **2021**, *2* (4), 1204–1228. https://doi.org/10.1039/D0MA00921K.

(14) Kwon, Y.; Kim, S. Indium Phosphide Magic-Sized Clusters: Chemistry and Applications. *NPG Asia Mater.* **2021**, *13* (1), 1–16. https://doi.org/10.1038/s41427-021-00300-4.

(15) Beecher, A. N.; Dziatko, R. A.; Steigerwald, M. L.; Owen, J. S.; Crowther, A. C. Transition from Molecular Vibrations to Phonons in Atomically Precise Cadmium Selenide Quantum Dots. *J. Am. Chem. Soc.* **2016**, *138* (51), 16754–16763. https://doi.org/10.1021/jacs.6b10705.

(16) Beecher, A. N.; Yang, X.; Palmer, J. H.; LaGrassa, A. L.; Juhas, P.; Billinge, S. J. L.; Owen, J. S. Atomic Structures and Gram Scale Synthesis of Three Tetrahedral Quantum Dots. *J. Am. Chem. Soc.* **2014**, *136* (30), 10645–10653. https://doi.org/10.1021/ja503590h.

(17) Bootharaju, M. S.; Baek, W.; Deng, G.; Singh, K.; Voznyy, O.; Zheng, N.; Hyeon, T. Structure of a Subnanometer-Sized Semiconductor Cd14Se13 Cluster. *Chem* **2022**, *8* (11), 2978–2989. https://doi.org/10.1016/j.chempr.2022.06.025.

(18) Bowers, M. J.; McBride, J. R.; Rosenthal, S. J. White-Light Emission from Magic-Sized Cadmium Selenide Nanocrystals. *J. Am. Chem. Soc.* **2005**, *127* (44), 15378–15379. https://doi.org/10.1021/ja055470d.

(19) Calvin, J. J.; Ben-Moshe, A.; Curling, E. B.; Brewer, A. S.; Sedlak, A. B.; Kaufman, T. M.; Alivisatos, A. P. Thermodynamics of the Adsorption of Cadmium Oleate to Cadmium Sulfide Quantum Dots and Implications of a Dynamic Ligand Shell. *J. Phys. Chem. C* **2022**, *126* (30), 12958–12971. https://doi.org/10.1021/acs.jpcc.2c04223.

(20) Klein, M. D.; Bisted, C. H.; Dou, F. Y.; Sandwisch, J. W.; Cossairt, B. M.; Khalil, M. Measuring Relative Energies of Ligand Binding Conformations on Nanocluster Surfaces

with Temperature-Dependent FTIR Spectroscopy. *J. Phys. Chem. C* **2023**, *127* (34), 16970–16978. https://doi.org/10.1021/acs.jpcc.3c03951.

(21) Busatto, S.; de Mello Donega, C. Magic-Size Semiconductor Nanostructures: Where Does the Magic Come From? *ACS Mater. Au* **2022**, *2* (3), 237–249. https://doi.org/10.1021/acsmaterialsau.1c00075.

(22) Gary, D. C.; Flowers, S. E.; Kaminsky, W.; Petrone, A.; Li, X.; Cossairt, B. M. Single-Crystal and Electronic Structure of a 1.3 Nm Indium Phosphide Nanocluster. *J. Am. Chem. Soc.* **2016**, *138* (5), 1510–1513. https://doi.org/10.1021/jacs.5b13214.

(23) Sandeno, S.; Krajewski, S.; Beck, R.; Kaminsky, W.; Li, X.; Cossairt, B. Synthesis and Single Crystal X-Ray Diffraction Structure of an Indium Arsenide Nanocluster. ChemRxiv December 7, 2023. https://doi.org/10.26434/chemrxiv-2023-21scg.

(24) Ripberger, H.; Schnitzenbaumer, K.; Nguyen, L.; Ladd, D.; Levine, K.; Dayton, D.; Toney, M.; Cossairt, B. Navigating the Potential Energy Surface of CdSe Magic-Sized Clusters: Synthesis and Interconversion of Atomically Precise Nanocrystal Polymorphs. ChemRxiv August 16, 2023. https://doi.org/10.26434/chemrxiv-2023-jzwm3.

(25) Williamson, C. B.; Nevers, D. R.; Nelson, A.; Hadar, I.; Banin, U.; Hanrath, T.; Robinson, R. D. Chemically Reversible Isomerization of Inorganic Clusters. *Science* **2019**, *363* (6428), 731–735. https://doi.org/10.1126/science.aau9464.

(26) Wang, R.; Ratcliffe, C. I.; Wu, X.; Voznyy, O.; Tao, Y.; Yu, K. Magic-Sized Cd3P2 II−V Nanoparticles Exhibiting Bandgap Photoemission. *J. Phys. Chem. C* **2009**, *113* (42), 17979–17982. https://doi.org/10.1021/jp907642b.

(27) Harris, D. K.; Allen, P. M.; Han, H.-S.; Walker, B. J.; Lee, J.; Bawendi, M. G. Synthesis of Cadmium Arsenide Quantum Dots Luminescent in the Infrared. *J. Am. Chem. Soc.* **2011**, *133* (13), 4676–4679. https://doi.org/10.1021/ja1101932.

(28) Klein, M. D.; Bisted, C. H.; Dou, F. Y.; Sandwisch, J. W.; Cossairt, B. M.; Khalil, M. Measuring Relative Energies of Ligand Binding Conformations on Nanocluster Surfaces with Temperature-Dependent FTIR Spectroscopy. *J. Phys. Chem. C* **2023**. https://doi.org/10.1021/acs.jpcc.3c03951.

(29) Leger, J. D.; Friedfeld, M. R.; Beck, R. A.; Gaynor, J. D.; Petrone, A.; Li, X.; Cossairt, B. M.; Khalil, M. Carboxylate Anchors Act as Exciton Reporters in 1.3 Nm Indium Phosphide Nanoclusters. *J. Phys. Chem. Lett.* **2019**, *10* (8), 1833–1839. https://doi.org/10.1021/acs.jpclett.9b00602.

(30) Sandeno, S. F.; Schnitzenbaumer, K. J.; Krajewski, S. M.; Beck, R. A.; Ladd, D. M.; Levine, K. R.; Dayton, D.; Toney, M. F.; Kaminsky, W.; Li, X.; Cossairt, B. M. Ligand Steric Profile Tunes the Reactivity of Indium Phosphide Clusters. *J. Am. Chem. Soc.* **2024**, *146* (5), 3102–3113. https://doi.org/10.1021/jacs.3c10203.

(31) Dhaene, E.; Pokratath, R.; Aalling-Frederiksen, O.; Jensen, K. M. Ø.; Smet, P. F.; De Buysser, K.; De Roo, J. Monoalkyl Phosphinic Acids as Ligands in Nanocrystal Synthesis. *ACS Nano* **2022**, *16* (5), 7361–7372. https://doi.org/10.1021/acsnano.1c08966.

(32) Dhaene, E.; Coppenolle, S.; Deblock, L.; De Buysser, K.; De Roo, J. Binding Affinity of Monoalkyl Phosphinic Acid Ligands toward Nanocrystal Surfaces. *Chem. Mater.* **2023**, *35* (2), 558–569. https://doi.org/10.1021/acs.chemmater.2c02989.

(33) Parambil, A. R. U.; Pokratath, R.; Parammal, M. J.; Dhaene, E.; Eynden, D. V. den; Balog, S.; Prescimone, A.; Infante, I.; Shahgaldian, P.; Roo, J. D. Atomically Precise Surface

Chemistry of Zirconium and Hafnium Metal Oxo Clusters beyond Carboxylate Ligands. *Chem. Sci.* **2024**, *15* (42), 17380–17396. https://doi.org/10.1039/D4SC03859B.

(34) Dukes, A. D. I.; McBride, J. R.; Rosenthal, S. J. Synthesis of Magic-Sized CdSe and CdTe Nanocrystals with Diisooctylphosphinic Acid. *Chem. Mater.* **2010**, *22* (23), 6402–6408. https://doi.org/10.1021/cm102370a.

(35) Tiwari, N.; Liang, Q.; Fedin, I. Cd3P2 QDs Emitting in the SWIR through Overgrowth of Cadmium Phosphide Clusters. *Nanoscale* **2025**. https://doi.org/10.1039/D5NR00002E.

(36) Huang, M.; Hickey, S. G.; Höfer, B.; Ding, F.; He, S.; Schmidt, O. G.; Eychmüller, A.; Miao, S. Band-Emission Evolutions from Magic-Sized Clusters to Nanosized Quantum Dots of Cd3As2 in the Hot-Bubbling Synthesis. *J. Phys. Chem. C* **2015**, *119* (28), 16390–16395. https://doi.org/10.1021/acs.jpcc.5b04437.

(37) Alexandratos, S. D.; Zhu, X. ATR-FTIR Spectroscopy as a Probe for Metal Ion Binding onto Immobilized Ligands. *Mater. Chem. Phys.* **2018**, *218*, 196–203. https://doi.org/10.1016/j.matchemphys.2018.07.026.

(38) Teunis, M. B.; Dolai, S.; Sardar, R. Effects of Surface-Passivating Ligands and Ultrasmall CdSe Nanocrystal Size on the Delocalization of Exciton Confinement. *Langmuir* **2014**, *30* (26), 7851–7858. https://doi.org/10.1021/la501533t.

(39) Harris, R. D.; Bettis Homan, S.; Kodaimati, M.; He, C.; Nepomnyashchii, A. B.; Swenson, N. K.; Lian, S.; Calzada, R.; Weiss, E. A. Electronic Processes within Quantum Dot-Molecule Complexes. *Chem. Rev.* **2016**, *116* (21), 12865–12919. https://doi.org/10.1021/acs.chemrev.6b00102.

(40) Santra, P. K.; Palmstrom, A. F.; Tanskanen, J. T.; Yang, N.; Bent, S. F. Improving Performance in Colloidal Quantum Dot Solar Cells by Tuning Band Alignment through

Surface Dipole Moments. *J. Phys. Chem. C* **2015**, *119* (6), 2996–3005. https://doi.org/10.1021/acs.jpcc.5b00341.

(41) Liu, Y.; Li, Y.; Yang, Y.; Zhu, J.; Wu, K. Transient Spectral and Dynamic Properties of Magic-Size Cd3P2 Nanoclusters in the Limit of Strong Confinement. *Sci. China Chem.* **2023**, *66* (12), 3628–3635. https://doi.org/10.1007/s11426-023-1870-1.

(42) Klimov, V. I.; McBranch, D. W. Femtosecond 1 P -to- 1 S Electron Relaxation in Strongly Confined Semiconductor Nanocrystals. *Phys. Rev. Lett.* **1998**, *80* (18), 4028–4031. https://doi.org/10.1103/PhysRevLett.80.4028.

(43) Underwood, D. F.; Kippeny, T.; Rosenthal, S. J. Ultrafast Carrier Dynamics in CdSe Nanocrystals Determined by Femtosecond Fluorescence Upconversion Spectroscopy. *J. Phys. Chem. B* **2001**, *105* (2), 436–443. https://doi.org/10.1021/jp003088b.

(44) Giansante, C. Library Design of Ligands at the Surface of Colloidal Nanocrystals. *Acc. Chem. Res.* **2020**, *53* (8), 1458–1467. https://doi.org/10.1021/acs.accounts.0c00204.

(45) Lian, S.; Weinberg, D. J.; Harris, R. D.; Kodaimati, M. S.; Weiss, E. A. Subpicosecond Photoinduced Hole Transfer from a CdS Quantum Dot to a Molecular Acceptor Bound Through an Exciton-Delocalizing Ligand. *ACS Nano* **2016**, *10* (6), 6372–6382. https://doi.org/10.1021/acsnano.6b02814.

(46) Giansante, C.; Infante, I.; Fabiano, E.; Grisorio, R.; Suranna, G. P.; Gigli, G. "Darker-than-Black" PbS Quantum Dots: Enhancing Optical Absorption of Colloidal Semiconductor Nanocrystals via Short Conjugated Ligands. *J. Am. Chem. Soc.* **2015**, *137* (5), 1875–1886. https://doi.org/10.1021/ja510739q.

(47) Buckley, J. J.; Couderc, E.; Greaney, M. J.; Munteanu, J.; Riche, C. T.; Bradforth, S. E.; Brutchey, R. L. Chalcogenol Ligand Toolbox for CdSe Nanocrystals and Their Influence on

Exciton Relaxation Pathways. *ACS Nano* **2014**, *8* (3), 2512–2521. https://doi.org/10.1021/nn406109v.

(48) Westmoreland, D. E.; López-Arteaga, R.; Kantt, L. P.; Wasielewski, M. R.; Weiss, E. A. Dynamic Tuning of the Bandgap of CdSe Quantum Dots through Redox-Active Exciton-Delocalizing N-Heterocyclic Carbene Ligands. *J. Am. Chem. Soc.* **2022**, *144* (10), 4300–4304. https://doi.org/10.1021/jacs.1c12842.

(49) Baldwin, M. T.; Lee, C.; López-Arteaga, R.; Weiss, E. A.; Chen, L. X. Slowing Hot Electron Cooling in CdSe Quantum Dots Using Electron-Rich Exciton-Delocalizing Ligands. *ChemPhotoChem* **2024**, *8* (5), e202300234. https://doi.org/10.1002/cptc.202300234.

(50) Gary, D. C.; Cossairt, B. M. Role of Acid in Precursor Conversion During InP Quantum Dot Synthesis. *Chem. Mater.* **2013**, *25* (12), 2463–2469. https://doi.org/10.1021/cm401289j.

(51) Eagle, F. W.; Harvey, S.; Beck, R.; Li, X.; Gamelin, D. R.; Cossairt, B. M. Enhanced Charge Transfer from Coinage Metal Doped InP Quantum Dots. *ACS Nanosci. Au* **2023**, *3* (6), 451–461. https://doi.org/10.1021/acsnanoscienceau.3c00029.

(52) Gaussian 16, Revision C.01, Frisch, M. J.; Trucks, G. W.; Schlegel, H. B.; Scuseria, G. E.; Robb, M. A.; Cheeseman, J. R.; Scalmani, G.; Barone, V.; Petersson, G. A.; Nakatsuji, H.; Li, X.; Caricato, M.; Marenich, A. V.; Bloino, J.; Janesko, B. G.; Gomperts, R.; Mennucci, B.; Hratchian, H. P.; Ortiz, J. V.; Izmaylov, A. F.; Sonnenberg, J. L.; Williams-Young, D.; Ding, F.; Lipparini, F.; Egidi, F.; Goings, J.; Peng, B.; Petrone, A.; Henderson, T.; Ranasinghe, D.; Zakrzewski, V. G.; Gao, J.; Rega, N.; Zheng, G.; Liang, W.; Hada, M.; Ehara, M.; Toyota, K.; Fukuda, R.; Hasegawa, J.; Ishida, M.; Nakajima, T.; Honda, Y.; Kitao, O.; Nakai, H.; Vreven, T.; Throssell, K.; Montgomery, J. A., Jr.; Peralta, J. E.; Ogliaro, F.; Bearpark, M. J.; Heyd, J. J.; Brothers, E. N.; Kudin, K. N.; Staroverov, V. N.; Keith, T. A.;

Kobayashi, R.; Normand, J.; Raghavachari, K.; Rendell, A. P.; Burant, J. C.; Iyengar, S. S.; Tomasi, J.; Cossi, M.; Millam, J. M.; Klene, M.; Adamo, C.; Cammi, R.; Ochterski, J. W.; Martin, R. L.; Morokuma, K.; Farkas, O.; Foresman, J. B.; Fox, D. J. Gaussian, Inc., Wallingford CT, 2016.

(53) Hamachi, L. S.; Yang, H.; Jen-La Plante, I.; Saenz, N.; Qian, K.; Campos, M. P.; Cleveland, G. T.; Rreza, I.; Oza, A.; Walravens, W.; Chan, E. M.; Hens, Z.; Crowther, A. C.; Owen, J. S. Precursor Reaction Kinetics Control Compositional Grading and Size of $CdSe_{1-x}S_x$ Nanocrystal Heterostructures. *Chem. Sci.* **2019**, *10* (26), 6539–6552. https://doi.org/10.1039/C9SC00989B.

(54) Montchamp, J.-L. Phosphinate Chemistry in the 21st Century: A Viable Alternative to the Use of Phosphorus Trichloride in Organophosphorus Synthesis. *Acc. Chem. Res.* **2014**, *47* (1), 77–87. https://doi.org/10.1021/ar400071v.

Chapter 5. STRUCTURAL HOMOLOGY ALLOWS ALLOYED II-V MAGIC-SIZED CLUSTERS WITH CONTINUOUSLY TUNABLE EMISSION

5.1 INTRODUCTION

Semiconductor nanocrystals have garnered recent interest due to their tunable emission, thermal- and photostability, and solution processibility.[1–4] For applications in solid-state lighting and quantum information science, it has become imperative to reproducibly synthesize highly homogeneous nanocrystal samples.[5–8] Any heterogeneity in the core or surface of these materials leads to variation in absorption and emission energies, which will reduce color purity for displays and challenge indistinguishability of single photons for quantum computing and communication.[2,9] While nanocrystal syntheses have evolved to achieve narrow size distributions,[10–12] the continuous growth of these materials disallows atomistic precision. This lack of precision can manifest from overlapping nucleation and growth regimes,[13–15] surface-dependent growth,[16,17] unbalanced precursor conversion rates,[18–20] and late-stage ripening[21,22]. Any imperfections are compounded throughout the course of the synthesis causing broader size distributions and detrimental defects.[23–25] With these processes happening on unpredictable timescales and without atomistic control,[26] the development of other synthesis pathways is warranted.

In pursuit of precise nanocrystals, researchers have discovered the existence of magic-sized clusters – molecular quantum dots that form on small size scales where the high surface energy dominates stability.[27–29] The unique thermodynamic balance between core and surface energies in these materials create such a strong bias for structure and size that the resulting materials are atomically precise.[30–37] The expectation would be that these molecular nanocrystals would

immediately provide unprecedented emission linewidths due to the perfect homogeneous ensemble. However, narrow, bright emission is not normally documented in these cluster materials. The high surface energy driving the atomic-precision means the majority of these clusters exist at small size scales and the resulting reduced lattice dimensions allow for strong vibrational coupling and nonradiative recombination.[38–41] Furthermore, the extreme confinement directs a higher degree of wavefunction interaction at the surface which can broaden linewidths and further promote nonradiative decay.[42–44] Finally, many of these materials are kinetically-trapped and require reactive reagents and thus the coordination of the metal precursor and the resulting cluster are with relatively labile ligands such as carboxylate or amine. The optical properties can then suffer in response to the dynamic ligand population.[45–48] We recently sought to improve the emission of some of these clusters by targeting the lability of surface ligands on II-V clusters and found that exchanging carboxylates for phosphinates dramatically enhanced the photoluminescence quantum yield.[49] While this improved the brightness, the functionality of clusters still lags behind larger nanocrystals due to a lack of continuous tunability.

The discrete stability of magic-sized clusters inherently disallows for the continuous growth that is possible with nanocrystals. If certain structures are more stable than others, the reaction is biased to the formation of those particular structures. The growth of these magic-sized clusters then proceeds through discrete steps in size as the system continues to traverse local thermodynamic minima in the potential energy landscape of the growing crystal.[50–52] At a certain size or temperature, the high surface energy is overwhelmed by the internal energy of the particles and atomic precision is lost.[53–56] A wide wavelength range is accessible before the size precludes precision using the discrete growth of magic-sized CdSe tetrahedra, but certain wavelengths of absorption and emission are left inaccessible as there are no intermediate sizes.[50] Introducing

continuous tunability to magic-sized clusters would combine the benefits of atomic precision (i.e., batch-to-batch reproducibility and narrow linewidths) with the broad range of accessible optical wavelengths possible with heterogeneous nanocrystals. To achieve this, the structure must not be altered but the band gap of the material must be changed. The addition of an isovalent anion can leave a structure generally unperturbed but the electronic contribution from the alloyed atom provides continuous tunability through the composition to access desirable properties.

Alloying of the anion sublattice to influence optoelectronic properties has been successful in many nanocrystal systems including $InP_{1-x}As_x$,[57,58] $InAs_{1-x}Sb_x$,[59,60] $CdS_{1-x}Se_x$,[61–65] and $CdSe_{1-x}Te_x$[66–68]. However, for magic-sized clusters, examples are rare. As many magic-sized clusters are not known for impressive emissive properties, these studies have focused on the fundamentals of alloy formation as opposed to the modulation of optoelectronic behavior and oftentimes only include a single alloyed example.[69–73] The application of these alloyed clusters has then been as single-source precursors to larger alloyed nanomaterials.[72] However, if a cluster framework is used that has band edge emission and can structurally withstand anion alloying, the optoelectronics of the atomically-precise material could be tuned with varying degrees of incorporation. We thus sought to introduce continuously tunable emission to atomically precise clusters using Cd_3P_2[74] and Cd_3As_2[75,76]. Both of these materials have independent, atomically-precise clusters with narrow emission linewidths and highly similar absorbance profiles suggesting structural homology. Assuming the structures are the same, different ratios of P and As precursors could lead to magic-sized $Cd_3P_{2-x}As_x$ with tunable properties.

5.2 Synthesis and Structure of CdP and CdAs Clusters

Studies that have characterized the Cd_3P_2 and Cd_3As_2 clusters document an absorbance profile with two clearly defined exitonic transitions both with impressive peak-to-trough ratios (**Figure 5.2.1B, C**).[74–76] Furthermore, we have recently reported that both clusters can be synthesized following identical synthetic procedures using $E(SiMe_3)_3$ (E= P, As) as the pnictide precursor (**Figure 5.2.1A**).[49] These two observations in tandem strongly suggested structural homology, but there are few studies that have investigated the atomic arrangement of these two materials. Furthermore, while many magic-sized clusters emit with broad photoluminescence and low PLQYs, these clusters show strong, narrow emission. We therefore also sought to develop a link between these shared structural motifs and impressive optical properties.

Efforts to passivate these materials with conformationally rigid ligands led to severe aggregation and insolubility. Thus, the growth of single crystals was unfeasible. In the absence of complete structural refinement, pair distribution function (PDF) analysis can be performed to investigate the structure of both clusters.

We also attempted the cluster synthesis using $Sb(SiMe_3)_3$ to generate the Cd_3Sb_2 analog but found that under identical conditions, a magic-sized cluster does not form. This could potentially be due to an increase in reactivity of the $E(SiMe_3)_3$, as $As(SiMe_3)_3$ has been documented to be significantly more reactive than $P(SiMe_3)_3$, we would expect the trend to continue to $Sb(SiMe_3)_3$.[77] However, it is equally notable that the bulk crystal system of Cd_3P_2 and Cd_3As_2 is tetragonal whereas Cd_3Sb_2 is orthorhombic.[78–80] This intrinsic difference in preferred atomic arrangement could lead to deviations in structurally stability at the nanoscale.

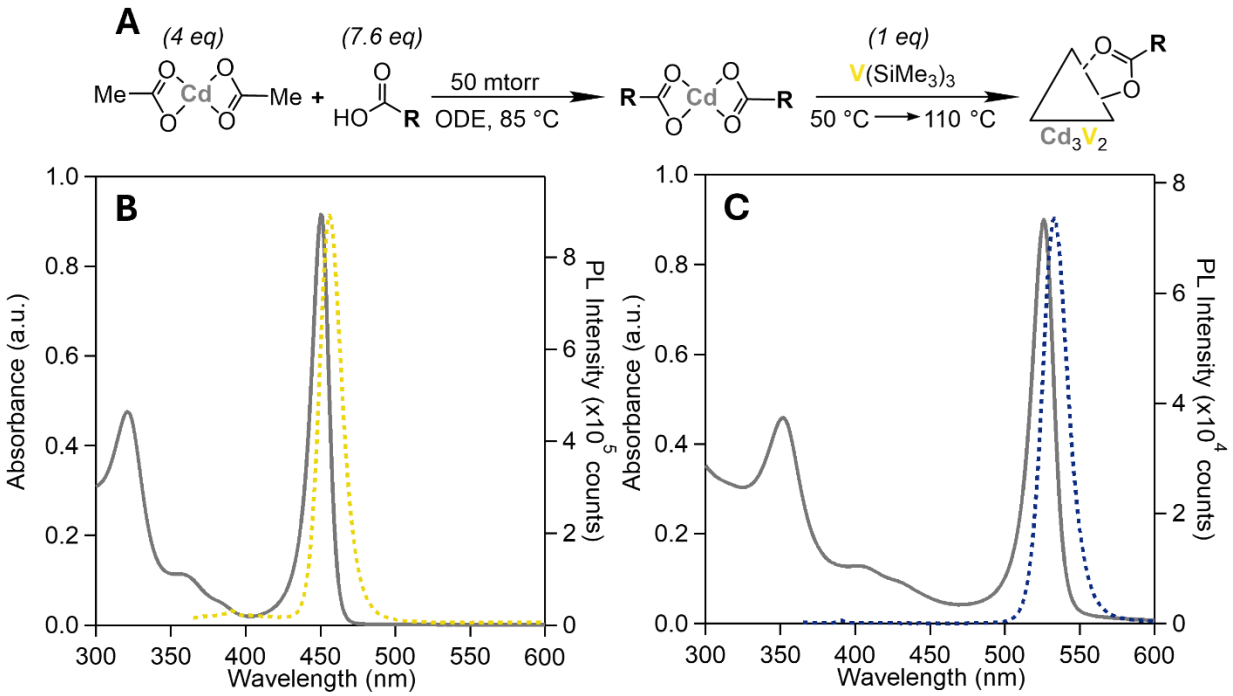

Figure 5.2.1. A) Scheme for the synthesis of oleate-ligated II-V clusters, Cd_3P_2-450 and Cd_3As_2-525. B) Absorbance (grey, solid) and photoluminescence (yellow, dotted) of Cd_3P_2-450 clusters. C) Absorbance (grey, solid) and photoluminescence (blue, dotted) of Cd_3As_2-525 clusters.

5.3 Synthesis of CdP-390 Baby Cluster

During efforts to passivate the II-V clusters with rigid ligands that would allow for single-crystal growth, 4-tert-butylphenylacetate was used for the cadmium carboxylate precursor alongside $P(SiMe_3)_3$ (**Figure 5.3.2A**). If the temperature is raised and maintained at 70 °C instead of increasing to 110 °C, a single well-defined feature at 390 nm forms in place of the strong feature at 450 nm characteristic of the Cd_3P_2-450 (**Figure 5.3.2B**). A similarly high peak-to-trough ratio is present that seems to be characteristic for II-V magic-sized clusters. While Cd_3P_2-390 also shows band-edge emission at 406 nm, the intensity of the photoluminescence is very low when compared

to the Cd_3P_2-450 (**Figure 5.3.1**). A relative comparison of the PL intensities normalized to the absorbance at the excitation wavelength would suggest that the PLQY of the Cd_3P_2-390 is <0.1%.

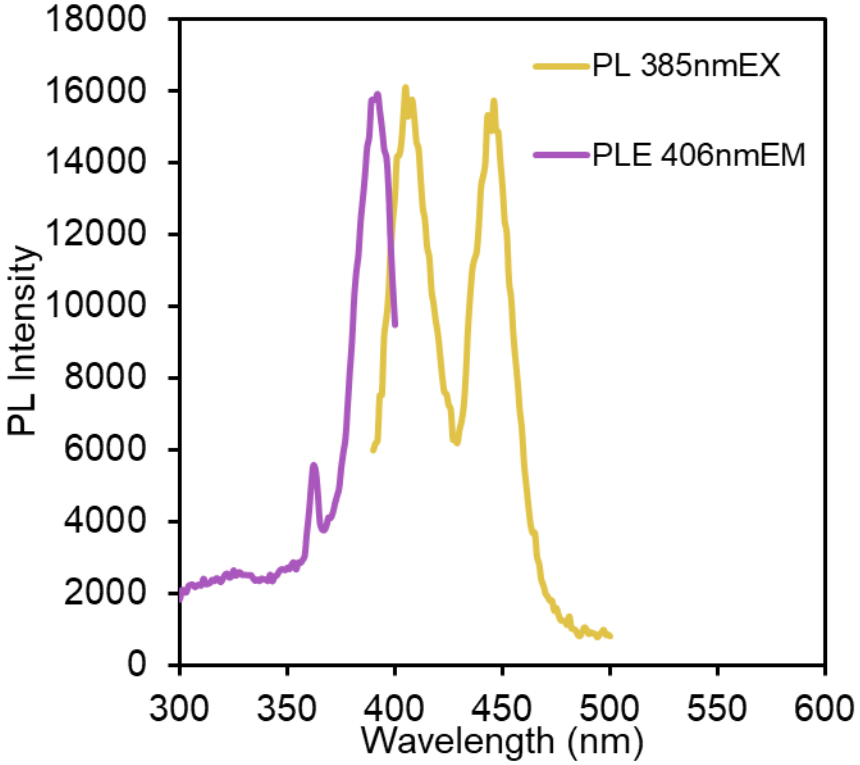

Figure 5.3.1. Photoluminescence spectrum of Cd_3P_2-390 clusters (gold, λ_{ex} = 386 nm). Photoluminescence excitation spectrum of Cd_3P_2-390 clusters (purple, λ_{em} = 406 nm). (*) Denotes emission from the Cd_3P_2-450 impurity in the sample.

Seeing the synthetic similarities, we hypothesized that this Cd_3P_2-390 cluster is an intermediate in the formation of the Cd_3P_2-450 cluster and thus sought to experimentally document direct conversion. After synthesizing the Cd_3P_2-390 cluster at 70 °C, increasing the temperature to 100 °C, led to a decrease in the absorbance feature at 390 nm, giving way to a new feature at 450 nm (**Figure 5.3.2C**). As mentioned previously, Cd_3P_2-450 aggregates severely with rigid ligands and so the product of the conversion has less well-defined absorbance features compared to those of the oleate-ligated cluster. We previously demonstrated the use of 4-tert-butylphenylacetate to

promote the isolation of a smaller magic-sized cluster in the case of $In_{26}P_{13}(O_2CR)_{39}$.[54] While the solubility of the Cd_3P_2-390 cluster is better than that of Cd_3P_2-450 with the same ligand sphere, there is still visible aggregation in solution. Recent characterization of the Cd_3P_2-450 cluster by MALDI-TOF has suggested a very low ligand surface coverage, which could explain the aggregative behavior of these materials.[81]

Further characterization of Cd_3P_2-390 by ^{31}P NMR revealed two peaks at -383 ppm and -392 ppm (**Figure 5.3.2D**). This is can be compared to previous characterization of the Cd_3P_2-450 cluster by ^{31}P NMR, showing a single resonance at -364 ppm.[82] This shows that there are two separate P environments in the smaller cluster that coalescence into a single environment upon growth into the larger cluster. While the bulk structure of Cd_3P_2 incorporates three inequivalent P sites, it would be unusual to see only slight changes in bond angle give rise to a shift as large as 9 ppm. This would suggest the two signals arise from two sets of P atoms that are at different distances from the surface of the cluster. Further growth into Cd_3P_2-450 would introduce more P signals and cause the coalescence into the peak at -364. The relatively large shift upon growth could indicate that there are a significant portion of underpassivated P atoms in the Cd_3P_2-390 structure. Fewer atoms in the smaller cluster with varying degrees of passivation could lead to the resolution of independent, discrete signals in the spectrum. Upon growth, these atoms are passivated and more P environments are introduced leading to the averaging into a single feature.

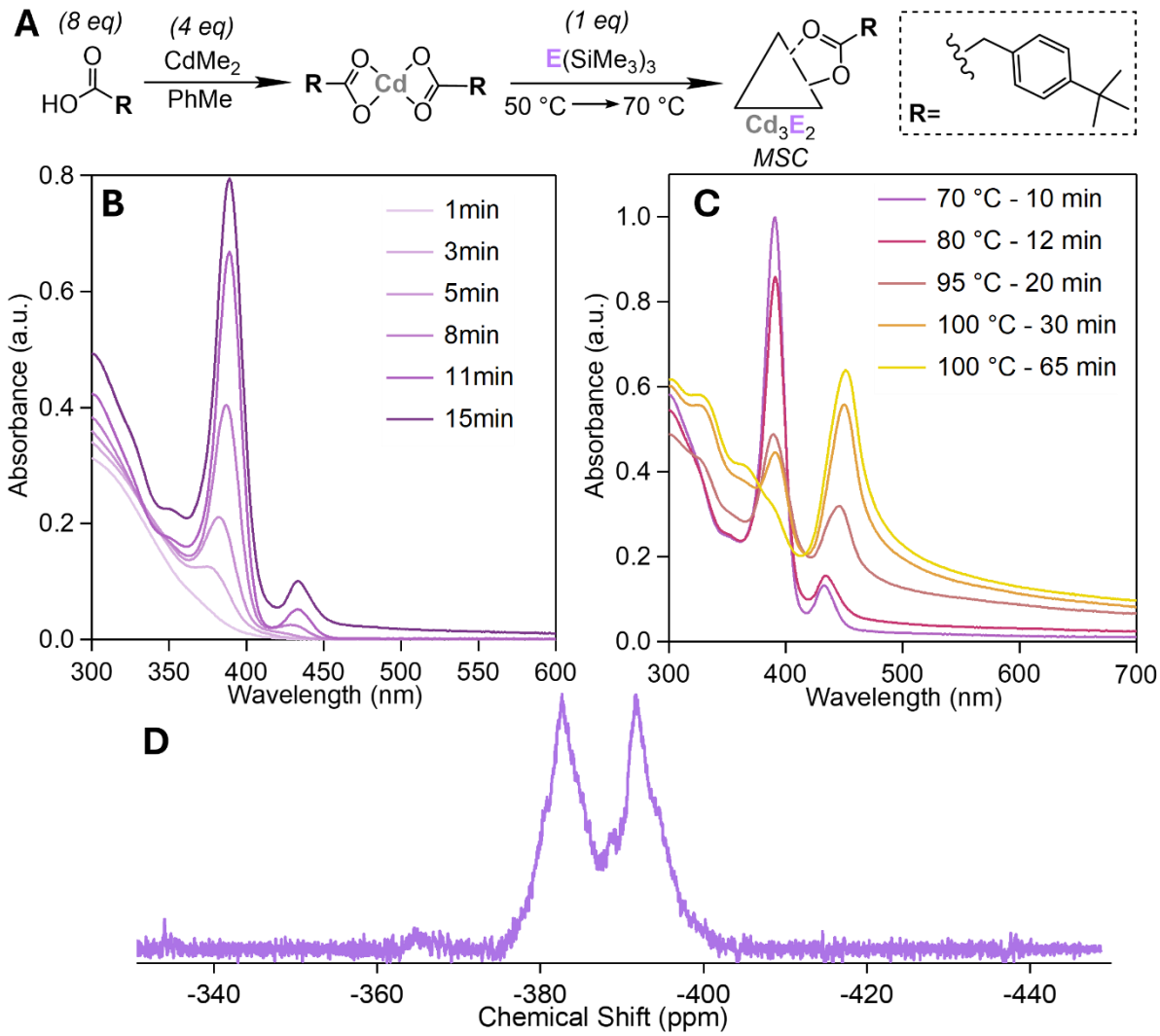

Figure 5.3.2. A) Scheme for the synthesis of Cd_3P_2-390 clusters. B) Absorbance aliquots from a typical synthesis of Cd_3P_2-390 showing the development of the main absorbance feature with λ_{max} = 390 nm. A small impurity of Cd_3P_2-450 becomes visible as the synthesis progresses. C) Absorbance aliquots from the conversion of Cd_3P_2-390 to Cd_3P_2-450 showing that at 100 °C, the 390 nm feature decreases in intensity giving rise to the characteristic 450 nm feature along with significant aggregation. D) ^{31}P NMR of purified Cd_3P_2-390 in $CDCl_3$.

5.4 Synthesis of Alloyed CdPAs Clusters

After the structural investigation of the II-V clusters and confirming the similarity in structure between the Cd_3P_2-450 and Cd_3As_2-525 by PDF, we turned to synthetic strategies to achieve cluster alloys. Seeing as both clusters are synthesized with identical protocols, alloying was targeted by the simultaneous injection of a predetermined ratio of $P(SiMe_3)_3$ and $As(SiMe_3)_3$ into the cadmium oleate precursor (**Figure 5.4.1A**). By altering the ratio of $P(SiMe_3)_3$ and $As(SiMe_3)_3$ at injection, the λ_{max} of the first absorbance transition is continuously tunable from 450 nm to 525 nm (**Figure 5.4.1B**). Most importantly, the two characteristic transitions in the absorbance are maintained for all percentages of alloying with no detrimental changes in the peak-to-trough ratio or peak definition. This serves as strong evidence for retention of the magic-sized cluster structure despite varying differences in the P:As ratio. Furthermore, the narrow emission is also retained upon alloying and follows the tunability of the absorbance, showing a continuous change from 457 nm to 532 nm depending on the extent of As incorporation (**Figure 5.4.1C**).

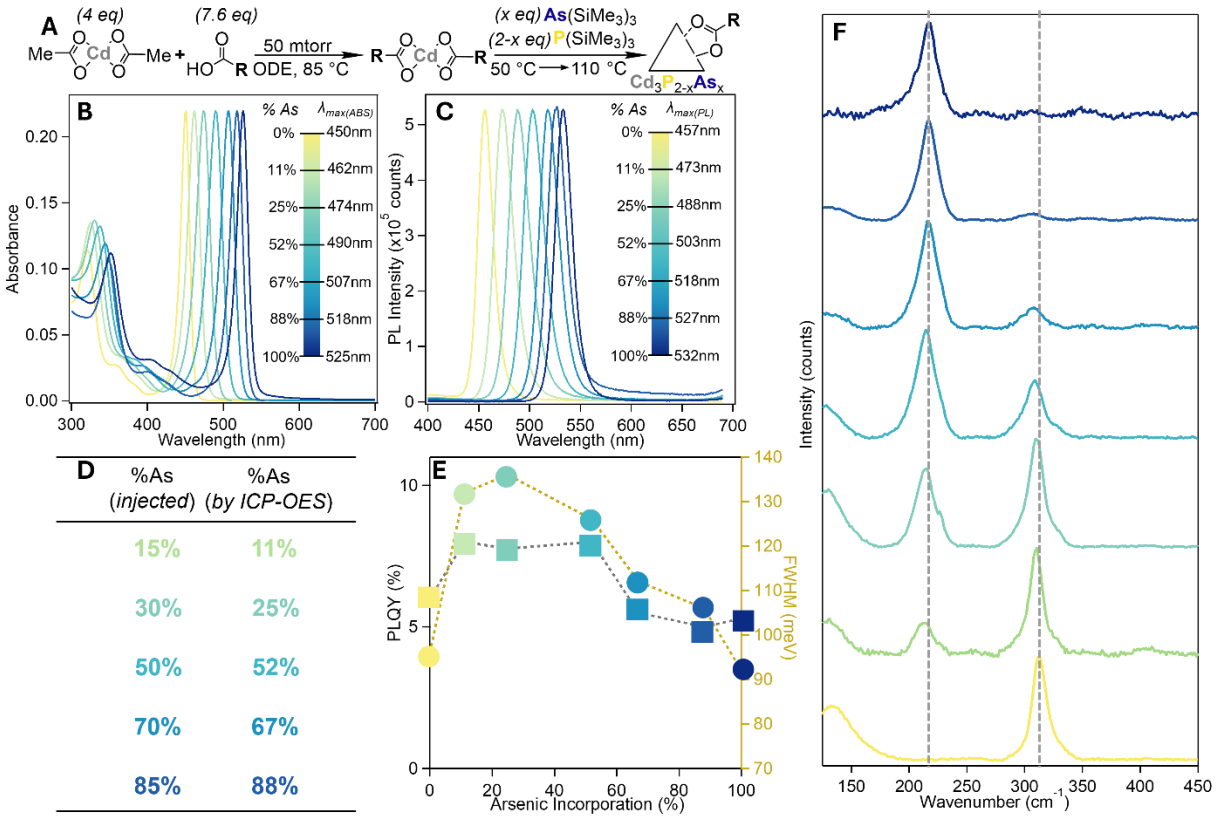

Figure 5.4.1. A) Scheme for the synthesis of continuously tunable $Cd_3P_{2-x}As_x$ clusters via the simultaneous injection of $P(SiMe_3)_3$ and $As(SiMe_3)_3$. B) Absorbance profiles of $Cd_3P_{2-x}As_x$ clusters with varying degrees of As incorporation. C) Photoluminescence spectra of $Cd_3P_{2-x}As_x$ clusters with varying degrees of As incorporation. D) Table comparing the percent $As(SiMe_3)_3$ injected out of total pnictide versus the percent As measured via ICP-OES in the final purified $Cd_3P_{2-x}As_x$ clusters. E) PLQY measurements (squares, left y-axis) and PL FWHM values (circles, right y-axis) for oleate-ligated $Cd_3P_{2-x}As_x$ clusters as a function of %As incorporation. F) Raman spectra for all clusters using λ_{exc} = 785 nm. The 310 cm^{-1} feature is assigned to internal Cd_3P_2 vibrations and the 215 cm^{-1} feature is assigned to internal Cd_3As_2 vibrations.

To further investigate the extent of alloying, ICP-OES measurements were conducted and the experimental percent of As incorporation was determined. The %As measured in the cluster

matched well with the ratio of $P(SiMe_3)_3$ to $As(SiMe_3)_3$ at injection (**Figure 5.4.1D**). Previous studies have concluded that $As(SiMe_3)_3$ is approximately 30x more reactive to metal carboxylates than $P(SiMe_3)_3$[77] and corroborating these observations, during the cluster syntheses, the absorbance features of Cd_3As_2-525 will form immediately upon injection, whereas additional heating is required for Cd_3P_2-450. This higher reactivity would suggest that As would preferentially incorporate into the cluster structure, leading to inflated As percentages. Seeing as the %As at injection matches the %As in the cluster core, it could be that these reactions are approaching quantitative yield where all the pnictide precursor is going towards cluster formation. Otherwise, the high reactivity of the $As(SiMe_3)_3$ would lead to higher %As in the cluster than at injection. The difference in pnictide precursor reactivity could also potentially cause heterostructure formation where the more reactive As preferentially organizes in the center of the cluster and P grows in on the surface.

To investigate this further, we collected Raman spectroscopy to look at the internal vibrations of Cd_3P_2 and Cd_3As_2 units. Previous characterization of microcrystalline Cd_3P_2 and Cd_3As_2 showed peaks at 250.7, 300.8, and 599.1 cm^{-1} for the former and 189.0 and 244.5 cm^{-1} for the latter.[83] It is likely that the small size of the material as well as the possibility of a different crystal phase at the cluster scale would lead to differences in the peak structure. However, this would not influence peak energies to a great degree. In our spectrum, we resolve two peaks, one at 313 cm^{-1} and the other at 217 cm^{-1} (**Figure 5.4.1F**). Due to the cluster morphology likely influencing the peak structure, we assign these features to Cd_3P_2 and Cd_3As_2 vibrations, respectively. Furthermore, the peak intensities follow the expected trend in As incorporation where higher As percentages lead to stronger intensity at 215 cm^{-1} and higher P percentages have the same effect on the 310 cm^{-1} feature. This two-mode behavior, where there are separate features for

the different alloyed materials, can be indicative of heterogeneous alloying.[84–86] However, in many semiconductors systems, homogeneous alloys also show two-mode behavior despite well-mixed alloy domains.[84,87–89] Primarily when the alloy gradient is formed from the anion sublattice is two-mode behavior seen whereas when the cation sublattice is alloyed, the continuous shift of one-mode behavior appears.[90–93] Therefore, the resolution of two discrete peaks in the Raman spectrum of these $Cd_3P_{2-x}As_x$ clusters is not enough to suggest how P and As are arranged in the cluster. However, we note that the Cd_3P_2 feature shifts from 313 cm^{-1} at 0% As incorporation to 305 cm^{-1} at 88% As incorporation. This shifting behavior has been documented in homogeneously alloyed $CdSe_xS_{1-x}$ QDs and attributed to weaker, longer Cd-S bonds that are a function of the lattice parameter of the nanocrystals being dominated by Se with increased incorporation.[84] The same effect, albeit less pronounced, occurs with the Cd_3As_2 feature shifting from 213 cm^{-1} at 11% As incorporation to 217 cm^{-1} for the Cd_3As_2-525 clusters. This can similarly be attributed to weaker, strained Cd-As bonds in a lattice that is primarily Cd_3P_2. Finally, analyzing changes in the peak breadths shows that the FWHMs of the features are the broadest at 52% As incorporation which reflects the most heterogeneous environments of both Cd-P and Cd-As bonds. This trend in bandwidth has also been attributed to the behavior of homogeneous alloying of QDs.[84] Seeing as the Raman peak frequencies and bandwidths follow the trends of uniform alloying, we conclude that these clusters have anion sublattices with homogeneously distributed P and As.

Investigating the PLQY of all oleate-ligated alloy clusters, we find that the brightness is consistent across different alloy percentages (**Figure 5.4.1E**). We measure PLQYs of 6%, 8%, 8%, 8%, 5%, 5%, and 5% in order from Cd_3P_2 to Cd_3As_2. Measured relative to coumarin 500,[94] the value of 6% for Cd_3P_2 clusters matches well with our previous absolute measurements.[49] However, we have previously measured the PLQY of oleate-ligated Cd_3As_2 clusters as 0.5% by integrating

sphere and the value of 5% measured here relative to coumarin 500 is significantly different. Seeing as the photoluminescence of the Cd_3As_2 clusters is more sensitive to oxidation than the Cd_3P_2, we believe that the relative measurements presented herein minimize air exposure and potential photodegradation that can occur during the longer, more intense scans required for absolute PLQY. While alloying introduced continuous tunability to the cluster emission, the PLQYs remained relatively low so we applied our previously developed ligand exchange for monoalkylphosphinates that has been shown to increase PLQYs for Cd_3P_2-450 and Cd_3As_2-525 magic-sized clusters.[49]

5.5 Ligand Exchange of Alloyed CdPAs Clusters

Our previous study found that octadecylphosphinic acid (ODPiA) led to the best optical properties with these clusters so it is the ligand used in this study. The exchange is performed by directly injecting a solution of octadecylphosphinic acid in tetrachloroethylene into a vigorously stirring solution of cluster in toluene. After stirring, the clusters are purified and a second addition is performed. A second purification step results in the final exchanged clusters. The absorbance and photoluminescence of the exchanged clusters are shown as **Figure 5.5.1A** and **Figure 5.5.1B**. There is a ~15 nm red-shift in the absorbance and photoluminescence upon exchange for the octadecylphosphinate. We have previously assigned this shift to a change in the surface dipole due to the electronic differences between carboxylate and phosphinate head groups.[49] This shifts the

available region of emission wavelengths to 469-550 nm, which is still in the blue to green portion of the visible spectrum.

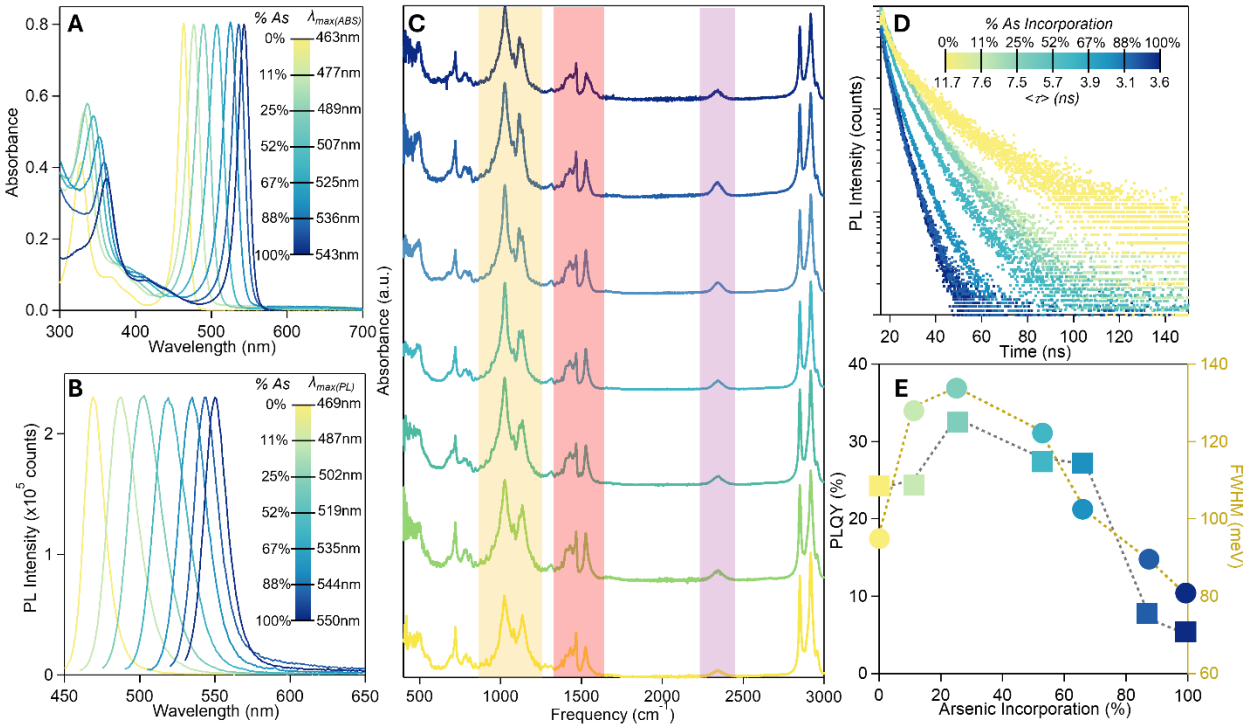

Figure 5.5.1. A) Absorbance profiles of $Cd_3P_{2-x}As_x$ clusters after exchange for octadecylphosphinate with varying degrees of As incorporation. B) Photoluminescence profiles of $Cd_3P_{2-x}As_x$ clusters after exchange for octadecylphosphinate with varying degrees of As incorporation. C) FTIR of $Cd_3P_{2-x}As_x$ clusters showing the magnitude of exchange of oleate (highlighted red) for octadecylphosphinate (P═O and P–O(M) are highlighted yellow and P–H is highlighted purple). D) TRPL spectra of $Cd_3P_{2-x}As_x$ clusters after exchange for octadecylphosphinate. All spectra are fit to a biexponential and the weighted average of the lifetimes is reported for each cluster. E) PLQY measurements (squares, left y-axis) and PL FWHM values (circles, right y-axis) for octadecylphosphinate-ligated $Cd_3P_{2-x}As_x$ clusters as a function of %As incorporation.

It was also determined that complete exchange of oleate for monoalkylphosphinate on the Cd_3As_2 clusters leads to destabilization over time and a loss PLQY. So, to make direct comparisons between the optical performance between clusters, we targeted a partial ligand exchange that would avoid destabilizing clusters with higher As incorporation but would still significantly enhance the PL intensity. The results of the ligand exchange are characterized with FTIR in **Figure 5.5.1C** where the symmetric and asymmetric stretches of the carboxylate are apparent in the 1350-1650 cm^{-1} region (highlighted in red) and the P═O and P–O(M) phosphinate stretching frequencies appear between 900 and 1250 cm^{-1} (highlighted in yellow). The peak intensities across samples match well, confirming similar degrees of exchange from the same procedure (**Figure 5.5.2**). Finally, the characteristic P-H stretch of monosubstituted phosphinates is visible at 2330 cm^{-1} upon exchange (highlighted in purple).

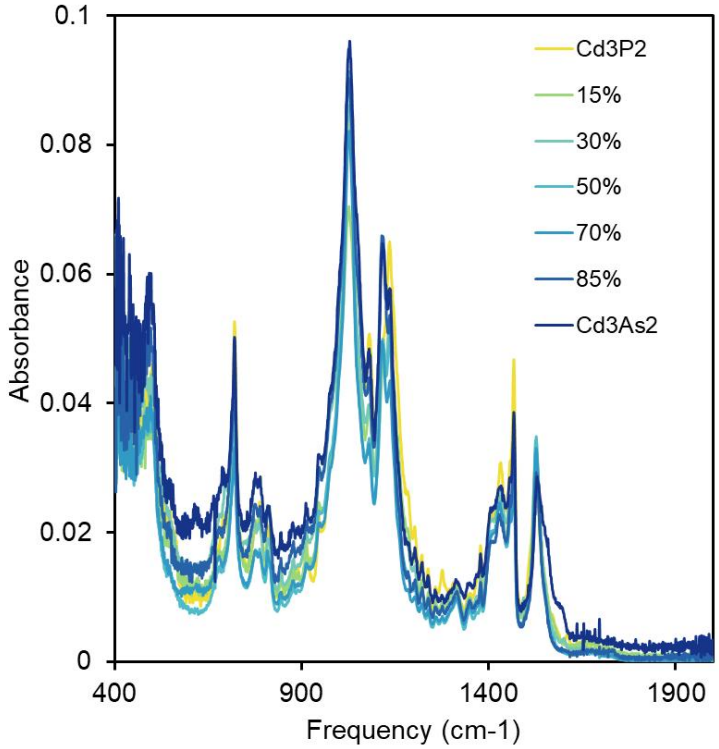

Figure 5.5.2. Overlaid FTIR spectra for all $CdP_{2-x}As_x$ clusters after ligand exchange with ODPiA.

Photophysical characterization of the $Cd_3P_{2-x}As_x$ clusters by time-resolved photoluminescence spectroscopy (TRPL) revealed that the photoluminescence lifetime of the clusters decreased with increasing As content (**Figure 5.5.1D**). Seeing as our structural investigation suggested clusters of similar structure and size, it is likely that the degree of confinement could be the cause for the difference in lifetime. It has been shown that higher degrees of confinement lead to faster radiative and nonradiative recombination rates.[95–98] While the Cd_3P_2-450 and Cd_3As_2-525 have the same structure, the effective mass of the electron for bulk Cd_3As_2 is much lighter, which would cause stronger confinement in Cd_3As_2-525 than Cd_3P_2-450.[99,100] This would mean the intrinsic radiative rate of Cd_3As_2-525 is faster and As incorporation would decrease the photoluminescence lifetime. Furthermore, increasing the As content leads to a more monoexponential decay proving that the decrease in lifetime cannot simply be the result of a new nonradiative state as this would lead to a more complex, multiexponential photoluminescence decay profile. Not only is this trend observed in the TRPL, but we note that the PLQY of the $Cd_3P_{2-x}As_x$-ODPiA clusters does not monotonically decrease with As incorporation indicating the decrease in photoluminescence lifetime isn't simply a result of faster nonradiative decay.

Further investigation shows that after exchange the PLQY of the Cd_3P_2-450 reaches 24%. Interestingly, the smallest As incorporations, 11% and 25% As, lead to an increase in the PLQY reaching 25% and 33% respectively (**Figure 5.5.1E**). The PLQY then decreases to 28% and 27% for As amounts of 52% and 67% before significantly dropping off at the highest levels of incorporation (88% and Cd_3As_2-525, itself) reaching 10% and 13%. The initial increase in the PLQY upon As incorporation can possibly be attributed to the decrease in the radiative rate with higher As percentages. The Cd_3P_2-450 cluster clearly shows biexponential decay indicating a nonradiative process that occurs on the nanosecond timescale. Upon incorporation of As, the PL

decay becomes more monoexponential as the shortened radiative rate outcompetes this nonradiative process. However, further incorporation provokes a new, faster nonradiative process that causes the continuous decrease in PLQY with higher As percentages. It is likely that this process is related to surface As due to the severe drop in PLQY at the highest As percentages. With InAs MSCs, the structure is more prone to 3-coordinate pnictide compared to InP clusters.[30,31,54] This could be the case for II-V clusters as well where Cd_3As_2-525 is more prone to undercoordinated surface atoms thereby opening avenues towards nonradiative recombination.

5.6 Conclusions

Using 4-tert-Butylphenylacetate, we have kinetically-trapped and isolated a new cluster, Cd_3P_2-390. This cluster maintains the impressive peak-to-trough ratio seen with the other II-V clusters and also demonstrates band-edge photoluminescence with a small Stokes shift, albeit the PLQY is significantly lower at <0.1%. Heating Cd_3P_2-390 to 110 °C results in the direct conversion to Cd_3P_2-450 proving that it is an intermediate in the growth of the larger cluster.

Due to the structural homology of Cd_3P_2-450 and Cd_3As_2-525, the simultaneous injection of $P(SiMe_3)_3$ and $As(SiMe_3)_3$ at different ratios result in alloyed $Cd_3P_{2-x}As_x$ clusters that retain the magic-sized structure. This introduces a continuous tunability to the absorbance and emission wavelengths of magic-sized clusters that has previously been inaccessible due to the discrete growth mechanism that is characteristic of the material. A ligand exchange for octadecylphosphinate improves the PLQY of all clusters reaching a peak brightness of 33% from the alloy with 25% As. The photophysical behavior as measured by PLQY and TRPL before and after ligand exchange suggests multiple, complex nonradiative processes that depend upon composition.

5.7 Experimental Methods.

5.7.1 *General Considerations.*

All glassware was dried in a 160 °C oven overnight prior to use. All reactions, unless otherwise noted, were run under an inert atmosphere of nitrogen using a glovebox or using standard Schlenk techniques. *Warning: dimethyl cadmium is a volatile and extremely toxic reactant and was handled with care within a nitrogen glovebox.* Oleic Acid (90%), cadmium acetate dihydrate (98%), octadecene (90%), triethylborane (1.0 M in THF), sodium hypophosphite monohydrate (≥99%), red phosphorus (≥99.99%), calcium hydride (95%), chlorotrimethylsilane (≥99%), naphthalene (99%), sodium metal (ACS reagent, dry), hydrogen peroxide solution (≥30%), and OmniTrace® nitric acid (67-70%) were obtained from Sigma Aldrich. Naphthalene was sublimated prior to use. 4-tert-Butylphenylacetic acid (>98%) and dimethoxyethane (≥99%) were obtained from TCI. Dimethoxyethane was distilled from sodium prior to use. Arsenic powder (99%) and dimethylcadmium (>97%) as a 10 wt% solution in hexanes were obtained from Strem Chemicals and used as received. Potassium hydrogen sulfate was obtained from VWR international. Deuterated chloroform ($CDCl_3$, 99.8% D) was obtained from Cambridge Isotope Laboratories. Tris(trimethylsilyl)arsine ($As(SiMe_3)_3$) and tris(trimethylsilyl)phosphine ($P(SiMe_3)_3$) were prepared according to a literature procedure using either metallic arsenic or red phosphorus.[101] All manipulations were performed under an inert atmosphere of dry N_2 using standard Schlenk line or glovebox techniques unless otherwise indicated. UV-Vis absorbance spectroscopy was carried out using Cary 5000 and Cary 60 spectrophotometers from Agilent Technologies. Steady-state photoluminescence spectroscopy was performed using a Horiba Scientific Fluoromax-4 Spectrofluorometer. Time-resolved photoluminescence spectroscopy was performed using an Edinburgh PLS 1000 Fluorimeter located in the University of Washington's

MEM-C shared user facility. Photoluminescence quantum yield was measured relative to coumarin 500 in methanol.[94] NMR spectra were acquired on 300 and 500 MHz Bruker Avance spectrometers in $CDCl_3$. All FT-IR measurements were acquired in the solid-state on a PerkinElmer Frontier FT-IR spectrometer. ICP-OES was conducted on a Perkin Elmer Optima 8300 inductively coupled plasma-optical emission spectrophotometer. All ICP-OES samples were prepared by digesting ~2 mg of solid sample in 500 µL of H_2O_2 followed by 500 µL of 67% HNO_3 for 24 hours. All Raman spectra were collected with a Renishaw InVia equipped with the Leica DMIRBE inverted optical microscope, exciting at 785 nm, using samples drop cast from solution onto Si wafer. Samples were prepared in a glovebox and remained air-free until mounting on the sample stage of the Raman microscope.

5.7.2 *Synthesis of $CdP_{2-x}As_x$-oleate Nanoclusters.*

Cadmium acetate dihydrate (53.3 mg, 0.2 mmol, 4 eq) is added to an oven-dried 3-neck round bottom flask under positive nitrogen after which it is heated to 40 °C under vacuum to remove water. Oleic acid (107 mg, 0.38 mmol, 7.6 eq) in 1-octadecene (5 mL) is then injected into the flask under positive nitrogen. With stirring at 350 rpm, the temperature is increased to 90 °C under full vacuum to form the cadmium oleate precursor. *Note: During this formation step, it is important to ensure that the cadmium acetate does not agglomerate on the side of the flask thereby hindering its reactivity.* After reacting at 90 °C for 2 hours, the reaction is cooled to 50 °C and placed under positive nitrogen. After the temperature has stabilized, a solution of $P(SiMe_3)_3$ and $As(SiMe_3)_3$ (0.05 mmol total, 1 eq) in 1 mL of toluene is promptly injected into the flask. Immediately after injection, the temperature is set to 110 °C. The reaction is removed from the heat when consecutive aliquots have identical absorbance spectra. The resulting clusters are

precipitated with 12 mL methyl acetate followed by centrifugation at 7830 rpm for 6 minutes. The supernatant is discarded, and the pellet is resuspended in 10 mL of toluene before a second precipitation with methyl acetate. The pellet is dried under vacuum and stored as a solid.

5.7.3 *Ligand Exchange of CdP-oleate for Octadecylphosphinate.*

Purified $CdP_{2-x}As_x$-oleate clusters (5 mg) are dissolved in 5 mL of toluene and placed under stirring at 800 rpm. Separately, 15 mg of octadecylphosphinic acid is dissolved in 3 mL of tetrachloroethylene. A 500 μL portion of the phosphinic acid solution is injected into the $CdP_{2-x}As_x$-oleate cluster solution followed by 30 minutes of stirring at room temperature. The partially exchanged clusters are precipitated with 7.5 mL of acetonitrile followed by centrifugation at 7830 rpm for 6 minutes. The clear supernatant is discarded, and the resulting pellet is resuspended in 5 mL of toluene. This process of phosphinic acid addition, precipitation and resuspension is repeated once more to yield $CdP_{2-x}As_x$-phosphinate clusters.

5.7.4 *Synthesis of Octadecylphosphinic Acid.*

Octadecylphosphinic acid was synthesized according to previous literature reports.[102]

5.7.5 *Synthesis of CdP_{390} Nanoclusters.*

4-tert-Butylphenylacetic acid (77 mg, 0.4 mmol, 8 eq) is dissolved in 2 mL of toluene and to this solution is added a 10 wt% solution of dimethylcadmium in hexanes (570 mg, 0.2 mmol, 4 eq) dropwise. This solution is allowed to stir for 2 hours and then is diluted to a total volume of 6 mL with toluene before being transferred to an oven-dried 3-neck round bottom flask under

positive nitrogen. The solution is heated to 50 °C and $P(SiMe_3)_3$ (15 µL, 0.05 mmol, 1 eq) in 1 mL of toluene is promptly injected into the flask. Immediately after injection, the temperature is set to 75 °C. The reaction is removed from the heat when consecutive aliquots have identical absorbance spectra. The crude reaction is immediately centrifuged at 7830 rpm for 6 minutes to remove any insoluble material. The supernatant is then decanted off and combined with 8 mL of acetonitrile followed by centrifugation at 7830 rpm for 6 minutes. The resulting supernatant is discarded and the white pellet is dried under vacuum and stored as a solid.

5.7.6 *CdP_{390} to CdP_{450} Conversion Reaction.*

CdP_{390} clusters are prepared as described above. Once two consecutive aliquots have identical absorbance spectra, the temperature is increased to 110 °C. Aliquots are continuously measured until the reaction is complete.

5.8 REFERENCES

(1) Jang, E.; Jang, H. Review: Quantum Dot Light-Emitting Diodes. *Chem. Rev.* **2023**, *123* (8), 4663–4692. https://doi.org/10.1021/acs.chemrev.2c00695.

(2) Nguyen, H. A.; Dixon, G.; Dou, F. Y.; Gallagher, S.; Gibbs, S.; Ladd, D. M.; Marino, E.; Ondry, J. C.; Shanahan, J. P.; Vasileiadou, E. S.; Barlow, S.; Gamelin, D. R.; Ginger, D. S.; Jonas, D. M.; Kanatzidis, M. G.; Marder, S. R.; Morton, D.; Murray, C. B.; Owen, J. S.; Talapin, D. V.; Toney, M. F.; Cossairt, B. M. Design Rules for Obtaining Narrow Luminescence from Semiconductors Made in Solution. *Chem. Rev.* **2023**, *123* (12), 7890–7952. https://doi.org/10.1021/acs.chemrev.3c00097.

(3) Moon, H.; Lee, C.; Lee, W.; Kim, J.; Chae, H. Stability of Quantum Dots, Quantum Dot Films, and Quantum Dot Light-Emitting Diodes for Display Applications. *Advanced Materials* **2019**, *31* (34), 1804294. https://doi.org/10.1002/adma.201804294.

(4) Liu, M.; Yazdani, N.; Yarema, M.; Jansen, M.; Wood, V.; Sargent, E. H. Colloidal Quantum Dot Electronics. *Nat Electron* **2021**, *4* (8), 548–558. https://doi.org/10.1038/s41928-021-00632-7.

(5) Liu, Z.; Lin, C.-H.; Hyun, B.-R.; Sher, C.-W.; Lv, Z.; Luo, B.; Jiang, F.; Wu, T.; Ho, C.-H.; Kuo, H.-C.; He, J.-H. Micro-Light-Emitting Diodes with Quantum Dots in Display Technology. *Light Sci Appl* **2020**, *9* (1), 83. https://doi.org/10.1038/s41377-020-0268-1.

(6) Rogers, L. J.; Jahnke, K. D.; Teraji, T.; Marseglia, L.; Müller, C.; Naydenov, B.; Schauffert, H.; Kranz, C.; Isoya, J.; McGuinness, L. P.; Jelezko, F. Multiple Intrinsically Identical Single-Photon Emitters in the Solid State. *Nat Commun* **2014**, *5* (1), 4739. https://doi.org/10.1038/ncomms5739.

(7) Kagan, C. R.; Bassett, L. C.; Murray, C. B.; Thompson, S. M. Colloidal Quantum Dots as Platforms for Quantum Information Science. *Chem. Rev.* **2021**, *121* (5), 3186–3233. https://doi.org/10.1021/acs.chemrev.0c00831.

(8) McKittrick, J.; Shea-Rohwer, L. E. Review: Down Conversion Materials for Solid-State Lighting. *Journal of the American Ceramic Society* **2014**, *97* (5), 1327–1352. https://doi.org/10.1111/jace.12943.

(9) Heindel, T.; Kim, J.-H.; Gregersen, N.; Rastelli, A.; Reitzenstein, S. Quantum Dots for Photonic Quantum Information Technology. *Adv. Opt. Photon., AOP* **2023**, *15* (3), 613–738. https://doi.org/10.1364/AOP.490091.

(10) Lin, S.; Yan, C.; Zhu, J.; Lu, Y.; Peng, X. Nucleation and Growth of Monodisperse CdTe and CdTe/ZnSe Core/Shell Nanocrystals: Roles of Cationic Precursors, Ligands, and Solvents. *J. Am. Chem. Soc.* **2025**, *147* (15), 12962–12972. https://doi.org/10.1021/jacs.5c02597.

(11) Cao, X.; Li, J.; Qian, X.; Li, C.; Peng, X. Nucleation and Growth of Monodisperse and Monocrystalline Wurtzite CdSe Nanocrystals: Zinc Alkanoates as Neutral Ligands. *J. Am. Chem. Soc.* **2025**, *147* (4), 3679–3691. https://doi.org/10.1021/jacs.4c15987.

(12) Wang, Y.; Zhang, J.; Chen, Z.; Zhou, X.; Lei, H.; Qin, H.; Peng, X. Ultra-Narrow Homogeneous Photoluminescence Line Width of Zinc-Blende CdSe-Based Core/Shell Nanocrystals: Dominating Role of Lattice–Ligands Interface. *J. Am. Chem. Soc.* **2025**, *147* (31), 28044–28055. https://doi.org/10.1021/jacs.5c08004.

(13) Chu, D. B. K.; Owen, J. S.; Peters, B. Nucleation and Growth Kinetics from LaMer Burst Data. *J. Phys. Chem. A* **2017**, *121* (40), 7511–7517. https://doi.org/10.1021/acs.jpca.7b08368.

(14) McMurtry, B. M.; Qian, K.; Teglasi, J. K.; Swarnakar, A. K.; De Roo, J.; Owen, J. S. Continuous Nucleation and Size Dependent Growth Kinetics of Indium Phosphide Nanocrystals. *Chem. Mater.* **2020**, *32* (10), 4358–4368. https://doi.org/10.1021/acs.chemmater.0c01561.

(15) P. Campos, M.; Roo, J. D.; W. Greenberg, M.; M. McMurtry, B.; P. Hendricks, M.; Bennett, E.; Saenz, N.; Y. Sfeir, M.; Abécassis, B.; K. Ghose, S.; S. Owen, J. Growth Kinetics Determine the Polydispersity and Size of PbS and PbSe Nanocrystals. *Chemical Science* **2022**, *13* (16), 4555–4565. https://doi.org/10.1039/D1SC06098H.

(16) Zherebetskyy, D.; Scheele, M.; Zhang, Y.; Bronstein, N.; Thompson, C.; Britt, D.; Salmeron, M.; Alivisatos, P.; Wang, L.-W. Hydroxylation of the Surface of PbS Nanocrystals Passivated with Oleic Acid. *Science* **2014**, *344* (6190), 1380–1384. https://doi.org/10.1126/science.1252727.

(17) Liu, H.; Liu, Z.; Pu, C. Size Focusing of Colloidal Quantum Dots under High Monomer Concentration. *Nano Res.* **2022**, *15* (8), 7622–7630. https://doi.org/10.1007/s12274-022-4340-4.

(18) Owen, J. S.; Chan, E. M.; Liu, H.; Alivisatos, A. P. Precursor Conversion Kinetics and the Nucleation of Cadmium Selenide Nanocrystals. *J. Am. Chem. Soc.* **2010**, *132* (51), 18206–18213. https://doi.org/10.1021/ja106777j.

(19) Frenette, L. C.; Krauss, T. D. Uncovering Active Precursors in Colloidal Quantum Dot Synthesis. *Nat Commun* **2017**, *8* (1), 2082. https://doi.org/10.1038/s41467-017-01936-z.

(20) Park, J.; Jayaraman, A.; Schrader, A. W.; Hwang, G. W.; Han, H.-S. Controllable Modulation of Precursor Reactivity Using Chemical Additives for Systematic Synthesis of High-Quality Quantum Dots. *Nat Commun* **2020**, *11* (1), 5748. https://doi.org/10.1038/s41467-020-19573-4.

(21) Tonti, D.; Mohammed, M. B.; Al-Salman, A.; Pattison, P.; Chergui, M. Multimodal Distribution of Quantum Confinement in Ripened CdSe Nanocrystals. *Chem. Mater.* **2008**, *20* (4), 1331–1339. https://doi.org/10.1021/cm071439u.

(22) Wang, F.; Richards, V. N.; Shields, S. P.; Buhro, W. E. Kinetics and Mechanisms of Aggregative Nanocrystal Growth. *Chem. Mater.* **2014**, *26* (1), 5–21. https://doi.org/10.1021/cm402139r.

(23) Souza Junior, J. B.; Mouriño, B.; Gehlen, M. H.; Moraes, D. A.; Bettini, J.; Varanda, L. C. Acid Selenites as New Selenium Precursor for CdSe Quantum Dot Synthesis. *Heliyon* **2024**, *10* (1), e23837. https://doi.org/10.1016/j.heliyon.2023.e23837.

(24) Moscheni, D.; Bertolotti, F.; Piveteau, L.; Protesescu, L.; Dirin, D. N.; Kovalenko, M. V.; Cervellino, A.; Pedersen, J. S.; Masciocchi, N.; Guagliardi, A. Size-Dependent Fault-Driven Relaxation and Faceting in Zincblende CdSe Colloidal Quantum Dots. *ACS Nano* **2018**, *12* (12), 12558–12570. https://doi.org/10.1021/acsnano.8b07092.

(25) Baek, H.; Kang, S.; Heo, J.; Choi, S.; Kim, R.; Kim, K.; Ahn, N.; Yoon, Y.-G.; Lee, T.; Chang, J. B.; Lee, K. S.; Park, Y.-G.; Park, J. Insights into Structural Defect Formation in Individual InP/ZnSe/ZnS Quantum Dots under UV Oxidation. *Nat Commun* **2024**, *15* (1), 1671. https://doi.org/10.1038/s41467-024-45944-2.

(26) Abécassis, B.; W. Greenberg, M.; Bal, V.; M. McMurtry, B.; P. Campos, M.; Guillemeney, L.; Mahler, B.; Prevost, S.; Sharpnack, L.; P. Hendricks, M.; DeRosha, D.; Bennett, E.; Saenz, N.; Peters, B.; S. Owen, J. Persistent Nucleation and Size Dependent Attachment Kinetics Produce Monodisperse PbS Nanocrystals. *Chemical Science* **2022**, *13* (17), 4977–4983. https://doi.org/10.1039/D1SC06134H.

(27) Baletto, F.; Ferrando, R. Structural Properties of Nanoclusters: Energetic, Thermodynamic, and Kinetic Effects. *Rev. Mod. Phys.* **2005**, *77* (1), 371–423. https://doi.org/10.1103/RevModPhys.77.371.

(28) Busatto, S.; de Mello Donega, C. Magic-Size Semiconductor Nanostructures: Where Does the Magic Come From? *ACS Mater. Au* **2022**, *2* (3), 237–249. https://doi.org/10.1021/acsmaterialsau.1c00075.

(29) Wang, J.; Mbah, C. F.; Przybilla, T.; Apeleo Zubiri, B.; Spiecker, E.; Engel, M.; Vogel, N. Magic Number Colloidal Clusters as Minimum Free Energy Structures. *Nat Commun* **2018**, *9* (1), 5259. https://doi.org/10.1038/s41467-018-07600-4.

(30) Sandeno, S. F.; Krajewski, S. M.; Beck, R. A.; Kaminsky, W.; Li, X.; Cossairt, B. M. Synthesis and Single Crystal X-Ray Diffraction Structure of an Indium Arsenide Nanocluster. *ACS Cent. Sci.* **2024**, *10* (3), 744–751. https://doi.org/10.1021/acscentsci.3c01451.

(31) Gary, D. C.; Flowers, S. E.; Kaminsky, W.; Petrone, A.; Li, X.; Cossairt, B. M. Single-Crystal and Electronic Structure of a 1.3 Nm Indium Phosphide Nanocluster. *J. Am. Chem. Soc.* **2016**, *138* (5), 1510–1513. https://doi.org/10.1021/jacs.5b13214.

(32) Ma, F.; Abboud, K. A.; Zeng, C. Precision Synthesis of a CdSe Semiconductor Nanocluster via Cation Exchange. *Nat. Synth* **2023**, *2* (10), 949–959. https://doi.org/10.1038/s44160-023-00330-6.

(33) Mech, S. A.; Gibson, J. O.; Ma, F.; Dobrzycki, L. M.; Zeng, C. From Magic Size to Atomic Precision: Facile Synthesis of a CdTe Semiconductor Nanocluster. *J. Am. Chem. Soc.* **2025**, *147* (9), 7507–7512. https://doi.org/10.1021/jacs.4c16188.

(34) Beecher, A. N.; Yang, X.; Palmer, J. H.; LaGrassa, A. L.; Juhas, P.; Billinge, S. J. L.; Owen, J. S. Atomic Structures and Gram Scale Synthesis of Three Tetrahedral Quantum Dots. *J. Am. Chem. Soc.* **2014**, *136* (30), 10645–10653. https://doi.org/10.1021/ja503590h.

(35) Bootharaju, M. S.; Baek, W.; Deng, G.; Singh, K.; Voznyy, O.; Zheng, N.; Hyeon, T. Structure of a Subnanometer-Sized Semiconductor Cd14Se13 Cluster. *Chem* **2022**, *8* (11), 2978–2989. https://doi.org/10.1016/j.chempr.2022.06.025.

(36) Ma, F.; Ivanov, S. A.; Dobrzycki, L. M.; Zeng, C. Programmable Synthesis of Atomically Precise Semiconductor Artificial Atoms. *Nat. Synth* **2025**, 1–12. https://doi.org/10.1038/s44160-025-00823-6.

(37) Evans, C. M.; Guo, L.; Peterson, J. J.; Maccagnano-Zacher, S.; Krauss, T. D. Ultrabright PbSe Magic-Sized Clusters. *Nano Lett.* **2008**, *8* (9), 2896–2899. https://doi.org/10.1021/nl801685a.

(38) Beecher, A. N.; Dziatko, R. A.; Steigerwald, M. L.; Owen, J. S.; Crowther, A. C. Transition from Molecular Vibrations to Phonons in Atomically Precise Cadmium Selenide Quantum Dots. *J. Am. Chem. Soc.* **2016**, *138* (51), 16754–16763. https://doi.org/10.1021/jacs.6b10705.

(39) Xie, Y.; Yu, S.; Zhang, L.; Du, N.; Yang, M. Radiative and Non-Radiative Decay Kinetics of (CdSe)N (N = 3 and 4) Clusters. *J. Chem. Phys.* **2019**, *151* (6), 064306. https://doi.org/10.1063/1.5109068.

(40) Kelley, A. M. Exciton-Optical Phonon Coupling in II-VI Semiconductor Nanocrystals. *J. Chem. Phys.* **2019**, *151* (14), 140901. https://doi.org/10.1063/1.5125147.

(41) Lin, C.; Gong, K.; Kelley, D. F.; Kelley, A. M. Size-Dependent Exciton–Phonon Coupling in CdSe Nanocrystals through Resonance Raman Excitation Profile Analysis. *J. Phys. Chem. C* **2015**, *119* (13), 7491–7498. https://doi.org/10.1021/acs.jpcc.5b00774.

(42) Jasrasaria, D.; Weinberg, D.; Philbin, J. P.; Rabani, E. Simulations of Nonradiative Processes in Semiconductor Nanocrystals. *J. Chem. Phys.* **2022**, *157* (2), 020901. https://doi.org/10.1063/5.0095897.

(43) Vasilevskiy, M. I.; Anda, E. V.; Makler, S. S. Electron-Phonon Interaction Effects in Semiconductor Quantum Dots: A Nonperturabative Approach. *Phys. Rev. B* **2004**, *70* (3), 035318. https://doi.org/10.1103/PhysRevB.70.035318.

(44) Jasrasaria, D.; Rabani, E. Interplay of Surface and Interior Modes in Exciton–Phonon Coupling at the Nanoscale. *Nano Lett.* **2021**, *21* (20), 8741–8748. https://doi.org/10.1021/acs.nanolett.1c02953.

(45) Calvin, J. J.; Ben-Moshe, A.; Curling, E. B.; Brewer, A. S.; Sedlak, A. B.; Kaufman, T. M.; Alivisatos, A. P. Thermodynamics of the Adsorption of Cadmium Oleate to Cadmium Sulfide Quantum Dots and Implications of a Dynamic Ligand Shell. *J. Phys. Chem. C* **2022**, *126* (30), 12958–12971. https://doi.org/10.1021/acs.jpcc.2c04223.

(46) Klein, M. D.; Bisted, C. H.; Dou, F. Y.; Sandwisch, J. W.; Cossairt, B. M.; Khalil, M. Measuring Relative Energies of Ligand Binding Conformations on Nanocluster Surfaces with Temperature-Dependent FTIR Spectroscopy. *J. Phys. Chem. C* **2023**, *127* (34), 16970–16978. https://doi.org/10.1021/acs.jpcc.3c03951.

(47) Kennehan, E. R.; Munson, K. T.; Doucette, G. S.; Marshall, A. R.; Beard, M. C.; Asbury, J. B. Dynamic Ligand Surface Chemistry of Excited PbS Quantum Dots. *J. Phys. Chem. Lett.* **2020**, *11* (6), 2291–2297. https://doi.org/10.1021/acs.jpclett.0c00539.

(48) You, H.; Liu, Z.; Zhu, K.; Wang, Q.; Liu, Z.; Li, P.; Hu, X.; Duan, J.; Li, Y.; Dai, N.; Hou, X. Unraveling the Role of Ligands Adsorption/Desorption on Photoluminescence Blinking in Single Water-Soluble InP-Based Quantum Dots. *Nano Lett.* **2025**, *25* (33), 12446–12454. https://doi.org/10.1021/acs.nanolett.5c01971.

(49) Sandeno, S. F.; Harvey, S. M.; Lin, V. N.; Cossairt, B. M. Narrow Blue Emission from Cadmium Phosphide Clusters Enhanced through Phosphinate Ligation. *Nano Lett.* **2025**. https://doi.org/10.1021/acs.nanolett.5c01891.

(50) Mule, A. S.; Mazzotti, S.; Rossinelli, A. A.; Aellen, M.; Prins, P. T.; van der Bok, J. C.; Solari, S. F.; Glauser, Y. M.; Kumar, P. V.; Riedinger, A.; Norris, D. J. Unraveling the Growth Mechanism of Magic-Sized Semiconductor Nanocrystals. *J. Am. Chem. Soc.* **2021**, *143* (4), 2037–2048. https://doi.org/10.1021/jacs.0c12185.

(51) Pun, A. B.; Mazzotti, S.; Mule, A. S.; Norris, D. J. Understanding Discrete Growth in Semiconductor Nanocrystals: Nanoplatelets and Magic-Sized Clusters. *Acc. Chem. Res.* **2021**, *54* (7), 1545–1554. https://doi.org/10.1021/acs.accounts.0c00859.

(52) Mazzotti, S.; Mule, A. S.; Pun, A. B.; Held, J. T.; Norris, D. J. Growth Synchronization and Size Control in Magic-Sized Semiconductor Nanocrystals. *ACS Nano* **2023**, *17* (14), 13232–13240. https://doi.org/10.1021/acsnano.3c00585.

(53) Ripberger, H. H.; Sandeno, S. F.; Eagle, F. W.; Nguyen, H. A.; Cossairt, B. M. Structure and Reactivity of II–VI and III–V Magic-Sized Clusters: Understanding and Expanding the Scope of Accessible Form and Function. *Acc. Mater. Res.* **2024**, *5* (6), 726–738. https://doi.org/10.1021/accountsmr.4c00064.

(54) Sandeno, S. F.; Schnitzenbaumer, K. J.; Krajewski, S. M.; Beck, R. A.; Ladd, D. M.; Levine, K. R.; Dayton, D.; Toney, M. F.; Kaminsky, W.; Li, X.; Cossairt, B. M. Ligand Steric Profile Tunes the Reactivity of Indium Phosphide Clusters. *J. Am. Chem. Soc.* **2024**, *146* (5), 3102–3113. https://doi.org/10.1021/jacs.3c10203.

(55) Shin, J.; Choi, M.; Shim, D.; Ziehl, T. J.; Park, S.; Cho, E.; Zhang, P.; Lee, H.; Kang, J.; Jeong, S. Unveiling the Nanocluster Conversion Pathway for Highly Monodisperse InAs

Colloidal Quantum Dots. *JACS Au* **2024**, *4* (3), 1097–1106. https://doi.org/10.1021/jacsau.3c00809.

(56) Vossmeyer, T.; Katsikas, L.; Giersig, M.; Popovic, I. G.; Diesner, K.; Chemseddine, A.; Eychmueller, A.; Weller, H. CdS Nanoclusters: Synthesis, Characterization, Size Dependent Oscillator Strength, Temperature Shift of the Excitonic Transition Energy, and Reversible Absorbance Shift. *J. Phys. Chem.* **1994**, *98* (31), 7665–7673. https://doi.org/10.1021/j100082a044.

(57) Leemans, J.; Respekta, D.; Bai, J.; Braeuer, S.; Vanhaecke, F.; Hens, Z. Formation of Colloidal In(As,P) Quantum Dots Active in the Short-Wave Infrared, Promoting Growth through Temperature Ramps. *ACS Nano* **2023**, *17* (20), 20002–20012. https://doi.org/10.1021/acsnano.3c05138.

(58) Kim, S.-W.; Zimmer, J. P.; Ohnishi, S.; Tracy, J. B.; Frangioni, J. V.; Bawendi, M. G. Engineering InAsxP1-x/InP/ZnSe III−V Alloyed Core/Shell Quantum Dots for the Near-Infrared. *J. Am. Chem. Soc.* **2005**, *127* (30), 10526–10532. https://doi.org/10.1021/ja0434331.

(59) Zhao, T.; Oh, N.; Jishkariani, D.; Zhang, M.; Wang, H.; Li, N.; Lee, J. D.; Zeng, C.; Muduli, M.; Choi, H.-J.; Su, D.; Murray, C. B.; Kagan, C. R. General Synthetic Route to High-Quality Colloidal III–V Semiconductor Quantum Dots Based on Pnictogen Chlorides. *J. Am. Chem. Soc.* **2019**, *141* (38), 15145–15152. https://doi.org/10.1021/jacs.9b06652.

(60) Kim, S.-W.; S, S.; Lee, B. Y. InAsxSb1−x Alloy Nanocrystals for Use in the near Infrared. *Chem. Commun.* **2006**, No. 46, 4811–4813. https://doi.org/10.1039/B611099A.

(61) Chung, Y.-C.; Yang, C.-H.; Zheng, H.-W.; Tsai, P.-S.; Wang, T.-L. Synthesis and Characterization of CdSxSe1−x Alloy Quantum Dots with Composition-Dependent Band

Gaps and Paramagnetic Properties. *RSC Adv.* **2018**, *8* (52), 30002–30011. https://doi.org/10.1039/C8RA06007J.

(62) Ingole, P. P.; Markad, G. B.; Saraf, D.; Tatikondewar, L.; Nene, O.; Kshirsagar, A.; Haram, S. K. Band Gap Bowing at Nanoscale: Investigation of CdSxSe1–x Alloy Quantum Dots through Cyclic Voltammetry and Density Functional Theory. *J. Phys. Chem. C* **2013**, *117* (14), 7376–7383. https://doi.org/10.1021/jp400021u.

(63) Schlenskaya, N. N.; Yao, Y.; Mano, T.; Kuroda, T.; Garshev, A. V.; Kozlovskii, V. F.; Gaskov, A. M.; Vasiliev, R. B.; Sakoda, K. Scroll-like Alloyed CdSxSe1–x Nanoplatelets: Facile Synthesis and Detailed Analysis of Tunable Optical Properties. *Chem. Mater.* **2017**, *29* (2), 579–586. https://doi.org/10.1021/acs.chemmater.6b03876.

(64) Saenz, N.; S. Hamachi, L.; Wolock, A.; H. Goodge, B.; Kuntzmann, A.; Dubertret, B.; Billinge, I.; F. Kourkoutis, L.; A. Muller, D.; C. Crowther, A.; S. Owen, J. Synthesis of Graded CdS 1−x Se x Nanoplatelet Alloys and Heterostructures from Pairs of Chalcogenoureas with Tailored Conversion Reactivity. **2023**. https://doi.org/10.1039/D3SC03384H.

(65) S. Hamachi, L.; Yang, H.; Plante, I. J.-L.; Saenz, N.; Qian, K.; P. Campos, M.; T. Cleveland, G.; Rreza, I.; Oza, A.; Walravens, W.; M. Chan, E.; Hens, Z.; C. Crowther, A.; S. Owen, J. Precursor Reaction Kinetics Control Compositional Grading and Size of CdSe 1−x S x Nanocrystal Heterostructures. *Chemical Science* **2019**, *10* (26), 6539–6552. https://doi.org/10.1039/C9SC00989B.

(66) Pan, Z.; Zhao, K.; Wang, J.; Zhang, H.; Feng, Y.; Zhong, X. Near Infrared Absorption of CdSexTe1–x Alloyed Quantum Dot Sensitized Solar Cells with More than 6% Efficiency and High Stability. *ACS Nano* **2013**, *7* (6), 5215–5222. https://doi.org/10.1021/nn400947e.

(67) Song, X.; Ma, Z.; Li, L.; Tian, T.; Yan, Y.; Su, J.; Deng, J.; Xia, C. Aqueous Synthesis of Alloyed CdSexTe1-x Colloidal Quantum Dots and Their In-Situ Assembly within Mesoporous TiO2 for Solar Cells. *Solar Energy* **2020**, *196*, 513–520. https://doi.org/10.1016/j.solener.2019.12.049.

(68) Zou, H.; Liu, M.; Zhou, D.; Zhang, X.; Liu, Y.; Yang, B.; Zhang, H. Employing CdSexTe1–x Alloyed Quantum Dots to Avoid the Temperature-Dependent Emission Shift of Light-Emitting Diodes. *J. Phys. Chem. C* **2017**, *121* (9), 5313–5323. https://doi.org/10.1021/acs.jpcc.6b12129.

(69) Kong, X.; Deng, Y.; Zou, Y.; Ge, J.; Wang, Y. Anion Exchange in Semiconductor Magic-Size Clusters. *J. Am. Chem. Soc.* **2024**, *146* (8), 5445–5454. https://doi.org/10.1021/jacs.3c12853.

(70) Gao, D.; Hao, X.; Rowell, N.; Kreouzis, T.; Lockwood, D. J.; Han, S.; Fan, H.; Zhang, H.; Zhang, C.; Jiang, Y.; Zeng, J.; Zhang, M.; Yu, K. Formation of Colloidal Alloy Semiconductor CdTeSe Magic-Size Clusters at Room Temperature. *Nat Commun* **2019**, *10* (1), 1674. https://doi.org/10.1038/s41467-019-09705-w.

(71) Yang, Y.; Huang, R.; Liu, Y.; Zhang, C.; Sapelkin, A. V.; Chen, X.; Yu, K. Monomer Substitution Assisted CdTeSe Magic-Size Cluster Development from CdTe and CdSe Prenucleation Clusters in Dispersion at Room Temperature. *Chem. Mater.* **2025**, *37* (8), 2855–2866. https://doi.org/10.1021/acs.chemmater.5c00030.

(72) Yang, J.; Münzer, F.; Baek, W.; Fainblat, R.; Chang, H.; Bacher, G.; Hyeon, T. Chemical Synthesis, Doping, and Transformation of Magic-Sized Semiconductor Alloy Nanoclusters. *J. Am. Chem. Soc.* **2017**, *139* (19), 6761–6770. https://doi.org/10.1021/jacs.7b02953.

(73) Wang, R.; Calvignanello, O.; Ratcliffe, C. I.; Wu, X.; Leek, D. M.; Zaman, Md. B.; Kingston, D.; Ripmeester, J. A.; Yu, K. Homogeneously-Alloyed CdTeSe Single-Sized Nanocrystals with Bandgap Photoluminescence. *J. Phys. Chem. C* **2009**, *113* (9), 3402–3408. https://doi.org/10.1021/jp810325z.

(74) Wang, R.; Ratcliffe, C. I.; Wu, X.; Voznyy, O.; Tao, Y.; Yu, K. Magic-Sized Cd3P2 II−V Nanoparticles Exhibiting Bandgap Photoemission. *J. Phys. Chem. C* **2009**, *113* (42), 17979–17982. https://doi.org/10.1021/jp907642b.

(75) Harris, D. K.; Allen, P. M.; Han, H.-S.; Walker, B. J.; Lee, J.; Bawendi, M. G. Synthesis of Cadmium Arsenide Quantum Dots Luminescent in the Infrared. *J. Am. Chem. Soc.* **2011**, *133* (13), 4676–4679. https://doi.org/10.1021/ja1101932.

(76) Huang, M.; Hickey, S. G.; Höfer, B.; Ding, F.; He, S.; Schmidt, O. G.; Eychmüller, A.; Miao, S. Band-Emission Evolutions from Magic-Sized Clusters to Nanosized Quantum Dots of Cd3As2 in the Hot-Bubbling Synthesis. *J. Phys. Chem. C* **2015**, *119* (28), 16390–16395. https://doi.org/10.1021/acs.jpcc.5b04437.

(77) Harris, D. K.; Bawendi, M. G. Improved Precursor Chemistry for the Synthesis of III–V Quantum Dots. *J. Am. Chem. Soc.* **2012**, *134* (50), 20211–20213. https://doi.org/10.1021/ja309863n.

(78) Zanin, I. E.; Aleinikova, K. B.; Antipin, M. Yu.; Afanasiev, M. M. The Structure of the Compound Cd3P2. *J Struct Chem* **2006**, *47* (1), 78–81. https://doi.org/10.1007/s10947-006-0268-x.

(79) Ali, M. N.; Gibson, Q.; Jeon, S.; Zhou, B. B.; Yazdani, A.; Cava, R. J. The Crystal and Electronic Structures of Cd3As2, the Three-Dimensional Electronic Analogue of Graphene. *Inorg. Chem.* **2014**, *53* (8), 4062–4067. https://doi.org/10.1021/ic403163d.

(80) Almin, K. E. The Crystal Structure of CdSb and ZnSb. *Acta Chemica Scandinavica* **1948**, *2*, 400–407. https://doi.org/10.3891/ACTA.CHEM.SCAND.02-0400.

(81) Tiwari, N.; Liang, Q.; Fedin, I. Cd3P2 QDs Emitting in the SWIR through Overgrowth of Cadmium Phosphide Clusters. *Nanoscale* **2025**. https://doi.org/10.1039/D5NR00002E.

(82) Stein, J. L.; Steimle, M. I.; Terban, M. W.; Petrone, A.; Billinge, S. J. L.; Li, X.; Cossairt, B. M. Cation Exchange Induced Transformation of InP Magic-Sized Clusters. *Chem. Mater.* **2017**, *29* (18), 7984–7992. https://doi.org/10.1021/acs.chemmater.7b03075.

(83) Wei, S.; Lu, J.; Yu, W.; Zhang, H.; Qian, Y. Isostructural Cd3E2 (E = P, As) Microcrystals Prepared via a Hydrothermal Route. *Crystal Growth & Design* **2006**, *6* (4), 849–853. https://doi.org/10.1021/cg049589u.

(84) Mukherjee, P.; Lim, S. J.; Wrobel, T. P.; Bhargava, R.; Smith, A. M. Measuring and Predicting the Internal Structure of Semiconductor Nanocrystals through Raman Spectroscopy. *J. Am. Chem. Soc.* **2016**, *138* (34), 10887–10896. https://doi.org/10.1021/jacs.6b03907.

(85) Lebedev, A. I.; Saidzhonov, B. M.; Drozdov, K. A.; Khomich, A. A.; Vasiliev, R. B. Raman and Infrared Studies of CdSe/CdS Core/Shell Nanoplatelets. *J. Phys. Chem. C* **2021**, *125* (12), 6758–6766. https://doi.org/10.1021/acs.jpcc.0c10529.

(86) Tschirner, N.; Lange, H.; Schliwa, A.; Biermann, A.; Thomsen, C.; Lambert, K.; Gomes, R.; Hens, Z. Interfacial Alloying in CdSe/CdS Heteronanocrystals: A Raman Spectroscopy Analysis. *Chem. Mater.* **2012**, *24* (2), 311–318. https://doi.org/10.1021/cm202947n.

(87) Neto, E. S. F.; da Silva, S. W.; Morais, P. C.; Vasilevskiy, M. I.; Pereira-da-Silva, M. A.; Dantas, N. O. Resonant Raman Scattering in CdSxSe1−x Nanocrystals: Effects of Phonon

Confinement, Composition, and Elastic Strain. *Journal of Raman Spectroscopy* **2011**, *42* (8), 1660–1669. https://doi.org/10.1002/jrs.2918.

(88) Hung, L. X.; Bassène, P. D.; Thang, P. N.; Loan, N. T.; Marcillac, W. D. de; Dhawan, A. R.; Feng, F.; Esparza-Villa, J. U.; Hien, N. T. T.; Liem, N. Q.; Coolen, L.; Nga, P. T. Near-Infrared Emitting CdTeSe Alloyed Quantum Dots: Raman Scattering, Photoluminescence and Single-Emitter Optical Properties. *RSC Adv.* **2017**, *7* (76), 47966–47974. https://doi.org/10.1039/C7RA06500K.

(89) Cheetham, K. J.; Krier, A.; Patel, I. I.; Martin, F. L.; Tzeng, J.-S.; Wu, C.-J.; Lin, H.-H. Raman Scattering in InAsxSbyP1−x−y Alloys Grown by Gas Source MBE. *J. Phys. D: Appl. Phys.* **2011**, *44* (8), 085405. https://doi.org/10.1088/0022-3727/44/8/085405.

(90) Alhaddad, T.; Shoker, M. B.; Pagès, O.; Postnikov, A. V.; Torres, V. J. B.; Polian, A.; Le Godec, Y.; Itié, J. P.; Broch, L.; Bouzourâa, M. B.; En Naciri, A.; Diliberto, S.; Michel, S.; Franchetti, P.; Marasek, A.; Strzałkowski, K. Raman Study of Cd1−xZnxTe Phonons and Phonon–Polaritons—Experiment and Ab Initio Calculations. *J. Appl. Phys.* **2023**, *133* (6), 065701. https://doi.org/10.1063/5.0134454.

(91) Davydov, V. Yu.; Goncharuk, I. N.; Smirnov, A. N.; Nikolaev, A. E.; Lundin, W. V.; Usikov, A. S.; Klochikhin, A. A.; Aderhold, J.; Graul, J.; Semchinova, O.; Harima, H. Composition Dependence of Optical Phonon Energies and Raman Line Broadening in Hexagonal Al x Ga 1 − x N Alloys. *Phys. Rev. B* **2002**, *65* (12), 125203. https://doi.org/10.1103/PhysRevB.65.125203.

(92) Azhniuk, Y. M.; Gomonnai, A. V.; Lopushansky, V. V.; Hutych, Y. I.; Turok, I. I.; Zahn, D. R. T. Resonant Raman Scattering Studies of Cd1-xZnxS Nanocrystals. *J. Phys.: Conf. Ser.* **2007**, *92* (1), 012044. https://doi.org/10.1088/1742-6596/92/1/012044.

(93) Hernández, S.; Cuscó, R.; Pastor, D.; Artús, L.; O'Donnell, K. P.; Martin, R. W.; Watson, I. M.; Nanishi, Y.; Calleja, E. Raman-Scattering Study of the InGaN Alloy over the Whole Composition Range. *J. Appl. Phys.* **2005**, *98* (1), 013511. https://doi.org/10.1063/1.1940139.

(94) Rohwer, L. S.; Martin, J. E. Measuring the Absolute Quantum Efficiency of Luminescent Materials. *Journal of Luminescence* **2005**, *115* (3), 77–90. https://doi.org/10.1016/j.jlumin.2005.01.013.

(95) Leistikow, M. D.; Johansen, J.; Kettelarij, A. J.; Lodahl, P.; Vos, W. L. Size-Dependent Oscillator Strength and Quantum Efficiency of CdSe Quantum Dots Controlled via the Local Density of States. *Phys. Rev. B* **2009**, *79* (4), 045301. https://doi.org/10.1103/PhysRevB.79.045301.

(96) De Mello Donegá, C.; Koole, R. Size Dependence of the Spontaneous Emission Rate and Absorption Cross Section of CdSe and CdTe Quantum Dots. *J. Phys. Chem. C* **2009**, *113* (16), 6511–6520. https://doi.org/10.1021/jp811329r.

(97) Underwood, D. F.; Kippeny, T.; Rosenthal, S. J. Ultrafast Carrier Dynamics in CdSe Nanocrystals Determined by Femtosecond Fluorescence Upconversion Spectroscopy. *J. Phys. Chem. B* **2001**, *105* (2), 436–443. https://doi.org/10.1021/jp003088b.

(98) Klimov, V. I.; McBranch, D. W. Femtosecond 1 P -to- 1 S Electron Relaxation in Strongly Confined Semiconductor Nanocrystals. *Phys. Rev. Lett.* **1998**, *80* (18), 4028–4031. https://doi.org/10.1103/PhysRevLett.80.4028.

(99) Jay-Gerin, J.-P.; Aubin, M. J.; Caron, L.-G. Energy-Band Structure and Electron Mobility of Cadmium Phosphide at Low Temperatures. *Phys. Rev. B* **1978**, *18* (10), 5675–5684. https://doi.org/10.1103/PhysRevB.18.5675.

(100) Sankar, R.; Neupane, M.; Xu, S.-Y.; Butler, C. J.; Zeljkovic, I.; Panneer Muthuselvam, I.; Huang, F.-T.; Guo, S.-T.; Karna, S. K.; Chu, M.-W.; Lee, W. L.; Lin, M.-T.; Jayavel, R.; Madhavan, V.; Hasan, M. Z.; Chou, F. C. Large Single Crystal Growth, Transport Property and Spectroscopic Characterizations of Three-Dimensional Dirac Semimetal Cd3As2. *Sci Rep* **2015**, *5* (1), 12966. https://doi.org/10.1038/srep12966.

(101) Gary, D. C.; Cossairt, B. M. Role of Acid in Precursor Conversion During InP Quantum Dot Synthesis. *Chem. Mater.* **2013**, *25* (12), 2463–2469. https://doi.org/10.1021/cm401289j.

(102) Dhaene, E.; Pokratath, R.; Aalling-Frederiksen, O.; Jensen, K. M. Ø.; Smet, P. F.; De Buysser, K.; De Roo, J. Monoalkyl Phosphinic Acids as Ligands in Nanocrystal Synthesis. *ACS Nano* **2022**, *16* (5), 7361–7372. https://doi.org/10.1021/acsnano.1c08966.

Chapter 6. CONCLUSIONS AND FINAL OUTLOOK

6.1 KEY FINDINGS

There are two main conclusions to be drawn from the work presented in this dissertation. The first is focused on the relation between conversion and the structure of magic-sized clusters. The second is focused on cluster functionalization pathways that can adapt to the metastability of these materials to preserve atomic precision.

Firstly, we have demonstrated the ligand sphere as a synthetic handle for controlling the reactivity of MSCs. Altering the steric pressure significantly changes the reactivity with external precursors. This knowledge was leveraged to synthesize and isolate a new cluster compound, $In_{26}P_{23}(O_2CR)_{39}$, which was characterized by SCXRD. This structure provides insight into the growth of InP and related MSCs, showing that growth can be stepwise and involve other intermediates that can be stabilized and isolated. Furthermore, the new structure is homologous to a previously characterized $Cd_{14}Se_{13}$ cluster;[1] both exhibit an $M_{14}E_{13}$ cage structure built upon an icosahedral anion sublattice. The structural similarities here show that nanoscale stability can follow the same rules across materials from different families.

Secondly, the ubiquitous InAs cluster present as an intermediate in InAs QD reactions has been fully structurally characterized as $In_{26}As_{18}(O_2CR)_{28}(PR'_3)_3$. The anisotropic, distorted wurtzite stack is a stable crystalline motif that explains the cluster's higher thermal stability. We find that the same icosahedral symmetry and $M_{14}E_{13}$ cage structure are present in this cluster as well.

These studies have suggested that nanoscale atomic precision in binary semiconductors with 4-coordinate crystal structures is based on an icosahedral anion sublattice, which results in an $M_{14}E_{13}$ cage. The presence of this motif could potentially be due to the low SA:V of an

icosahedron, but can also simply arise from the 4-coordinate geometry, causing 12 vertices during cluster growth. The structural perturbations upon the growth of this underlying cage, seen through the different metal-anion stoichiometries, can be rationalized through differences in cation-richness requirements and reactivity differences. The atomic precision of InP requires 4-coordinate P likely dictated by the X-type ligand sphere. As seen with CdSe, the structure is nearly identical, but the stoichiometry is different due to the ligation by L-type TMEDA. With InAs, the substantially lower electronegativity of As relaxes the 4-coordinate requirement in the face of X-type ligation, allowing for a more pnictide-rich stoichiometry. Beyond the differences in stoichiometry, the $In_{26}As_{18}$ structure is much more anisotropic when compared to InP and CdSe structures, which is likely due to the increased reactivity of the $As(SiMe_3)_3$. This more pronounced reactivity leads to complete precursor consumption upon injection, and the subsequent growth is therefore more controlled, resulting in a structure with clearer crystalline motifs. While a full rubric cannot be developed from these examples, they provide the basis of how bonding, surface chemistry, and reactivity synergistically combine to result in molecular structures.

Along with these structural investigations, new routes for the functionalization of MSCs have been developed that can enhance properties without compromising metastability. In the first case, Cd_3P_2 clusters can be ligated with monoalkylphosphinates through ligand exchange, and the increased binding affinity greatly enhances the PLQY. This method can also be applied to the related Cd_3As_2 clusters to increase brightness. This work was continued by leveraging the structural similarities of the II-V clusters to generate alloyed $Cd_3P_2As_{2-x}$ clusters with continuously tunable emission. These two routes circumvent the two biggest challenges facing cluster optical properties: dim and discrete emission. The combination of these two routes of functionalization improves the behavior, potentially enabling the use of clusters as classical or quantum emitters.

6.2 Final Outlook

In general, the structural work presented here has offered a route towards understanding how and why MSCs form in particular structures. One of the characteristics of these materials that has been mostly left uninvestigated is the lattice chirality. The cage structure generates two enantiomers, but crystallization always yields a racemic mixture. Developing a procedure to isolate a specific enantiomer, whether through synthetic design or purification, could open impactful avenues for chiral nanomaterials. While this has been investigated for a long time with metallic clusters, there exists only one example of enantiomer separation in semiconductor MSCs with $Cd_{28}S_{17}$.[2]

This analysis has also led to questions about the Cd_3P_2 cluster structure. When so many MSCs show the emission that is consistent with self-trapping, why does this particular structure have strong, narrow emission? It is likely that these unique emission characteristics require some amount of lattice periodicity to add rigidity and avoid structural distortions. It is then highly likely that the structure is a subunit of the Hausmannite-like lattice of the bulk material. The size of the subunit is approximately 1.5 nm based on PDF analysis, but the surface structure remains unknown. While complete refinement by SCXRD is still possible, creative solutions must be developed to address the strong aggregation that occurs if long-chain oleate ligands are not used. The structural characterization of this cluster could provide deep insight into the emissive behaviors of MSCs.

The monoalkylphosphinate ligand class has proven to be a very useful tool due to its mimicry of carboxylate binding behavior. However, it is unlikely to be a fully generalizable route for enhancing cluster emission. The diversity in stoichiometry and structure of clusters manifests as a wide range of emission profiles, driven by very complex photophysical mechanisms. This

means not every cluster radiatively recombines or nonradiatively recombines through the same route as the II-V clusters. For example, $In_{37}P_{20}$ shows self-trapping characteristics, and ligation with phosphinate likely will not improve the rate of self-trapping, a mechanism that is dependent upon structural distortions. In many cases, the surface chemistry of clusters must be tailored to radiative mechanisms to dramatically enhance the emission.

Furthermore, despite complete ligation of the Cd_3P_2 cluster, which leads to 26% PLQY, the majority of recombination remains nonradiative. The lack of trap emission suggests that this loss occurs through vibrations. The idea of encapsulating these clusters (and others) in an inorganic matrix to minimize vibrational losses is a possible route to truly achieving high emission efficiency. This would also protect pnictide atoms from oxidation, which is most likely the basis for quenching when exposed to air. The challenge here would be to complete the encapsulation without disturbing the structure, as the added rigidity of the matrix would force a stringent framework for atomic arrangements. While a sincere challenge to synthesis and fabrication, this encapsulation could result in impressive emission characteristics without degradation.

6.3 REFERENCES

(1) Bootharaju, M. S.; Baek, W.; Deng, G.; Singh, K.; Voznyy, O.; Zheng, N.; Hyeon, T. Structure of a Subnanometer-Sized Semiconductor Cd14Se13 Cluster. *Chem* **2022**, *8* (11), 2978–2989. https://doi.org/10.1016/j.chempr.2022.06.025.

(2) Xu, C.; Zhang, Z.; Zhou, Z.; Han, H. A Chiral CdS Magic-Size Cluster with Enantiomerically-Biased Crystallization. *J. Am. Chem. Soc.* **2025**, *147* (21), 17890–17901. https://doi.org/10.1021/jacs.5c02549.

APPENDIX A: CRYSTALLOGRAPHY DETAILS

Full crystallographic data for the $In_{26}P_{13}(O_2CCH_2C_6H_5C(CH_3)_3)_{39}$ cluster.

Empirical formula	C480 H595 F4 In26 O79 P13	
Formula weight	11092.45	
Temperature	100(2) K	
Wavelength	0.71073 Å	
Crystal system	Monoclinic	
Space group	P 21/n	
Unit cell dimensions	a = 44.699(3) Å	a= 90°.
	b = 24.8681(14) Å	b= 107.109(3)°.
	c = 49.437(3) Å	g = 90°.
Volume	52521(5) $Å^3$	
Z	4	
Density (calculated)	1.403 Mg/m^3	
Absorption coefficient	1.221 mm^{-1}	
F(000)	22448	
Crystal size	0.320 x 0.130 x 0.100 mm^3	
Theta range for data collection	0.947 to 25.027°.	
Index ranges	-53<=h<=53, -29<=k<=29, -58<=l<=58	
Reflections collected	181658	
Independent reflections	92324 [R(int) = 0.0559]	
Completeness to theta = 25.027°	99.5 %	

Refinement method	Full-matrix least-squares on F^2
Data / restraints / parameters	92324 / 49441 / 6275
Goodness-of-fit on F^2	1.162
Final R indices [I>2sigma(I)]	R1 = 0.1391, wR2 = 0.2798
R indices (all data)	R1 = 0.1749, wR2 = 0.2963
Largest diff. peak and hole	2.337 and -1.440 e.Å^{-3}

Full crystallographic data for the $In_{26}As_{18}(O_2CCH_2C_6H_5)_{24}(P(CH_2CH_3)_2C_6H_5)_3$ cluster.

Empirical formula	C222 H213 As18 In26 O48 P3	
Formula weight	8075.70	
Temperature	100(2) K	
Wavelength	0.71073 Å	
Crystal system	Monoclinic	
Space group	P 2_1/c	
Unit cell dimensions	a = 36.969(3) Å	a= 90°.
	b = 20.6296(18) Å	b= 103.421(4)°.
	c = 36.014(4) Å	g = 90°.
Volume	26716(4) Å^3	
Z	4	
Density (calculated)	2.008 Mg/m^3	
Absorption coefficient	4.489 mm^{-1}	
F(000)	15368	
Crystal size	0.070 x 0.060 x 0.050 mm^3	

Theta range for data collection	1.133 to 24.407°.
Index ranges	-44<=h<=44, -24<=k<=24, -43<=l<=43
Reflections collected	43904
Independent reflections	43904 [R(int) = 0.2442]
Completeness to theta = 24.407°	99.9 %
Refinement method	Full-matrix least-squares on F^2
Data / restraints / parameters	43904 / 10248 / 2775
Goodness-of-fit on F^2	1.091
Final R indices [I>2sigma(I)]	R1 = 0.1409, wR2 = 0.2368
R indices (all data)	R1 = 0.3388, wR2 = 0.2802
Largest diff. peak and hole	2.610 and -1.360 e.$Å^{-3}$

VITA

Soren grew up in Bellingham, Washington and was originally exposed to the scientific method while working in the garage with his father. He attended Whitman College for his undergraduate degree where he majored in chemistry with a minor in computer science. While there, he worked under Professor Mark Hendricks researching phase-selective synthesis of copper, zinc, and nickel sulfide nanocrystals using substituted thioureas to control growth kinetics. Upon developing a fascination with the nucleation and growth of inorganic colloids, Soren pursued a PhD in the lab of Professor Brandi Cossairt to investigate cluster formation during nanocrystal synthesis. His doctoral research focused on the synthesis, structural characterization, and functionalization of metal pnictide magic-sized clusters. Outside of lab, Soren spends time outside by running, bikepacking, hiking, and camping.